Atmospheric circulation and the surface mass balance in a regional climate model of Antarctica.

Atmospheric circulation and the surface mass balance in a regional climate model of Antarctica.

Dissertation

zur Erlangung des Doktorgrades
in der Wissenschaftsdisziplin Physik der Atmosphäre

eingereicht an der
Mathematisch-Naturwissenschaftlichen Fakultät
der Universität Potsdam

von
Ksenia Glushak

Stiftung Alfred-Wegener-Institut für Polar- und Meeresforschung
Forschungsstelle Potsdam, Telegrafenberg A43,
14473 Potsdam

Potsdam, Dezember 2007

I dedicate this piece of work to my beloved family. My parents Dina and Nicolay and grandparents Galina, Boris, Zachar and Tomara who brought me up as a respectable, decent person and always believed in me. My sister Elena, who taught me to dream big and never give up. My ”big brother” Michail, who supported and protected me.

Love is all around.

Contents

Chapter 1

Introduction

Understanding the Earth's climate system, particularly climate variability presents one of the most difficult and urgent challenges in science. The Antarctic is the principal region of radiative energy deficit and atmospheric cooling and because of this, its role in the global climate system is crucial. Through a net heating of the tropics and a cooling of the polar regions, the zonal mean radiative heating of the atmosphere generates a meridional energy gradient. It subsequently influences global circulation; this occurs through the meridional energy gradient between the pole and the tropical region and on time scales ranging from the synoptic to seasonal and decadal scales.

The ice sheet in Antarctica is an important element of the global water cycle. By storing large volumes of fresh water as ice or ice lakes, and by sometimes also releasing that water, it can affect the sea level, global ocean circulation, and hence the Earth's climate.

The goal of this dissertation is to improve our understanding of the key processes and decadal scale changes that occur in Antarctica and that also control the regional climate. Potentially, such processes and changes have global implications and consequences.

Before it is possible to accurately assess the role of the Antarctic in the global climate system, it is necessary to understand the key processes of the regional and meso-scale meteorology and dynamics. Projections of the state of global change must accurately account for Antarctic atmospheric processes whose effects are transmitted to the rest of the planet via atmospheric and oceanic circulation patterns and currents. In addition, the processes by which tropical latitudes impact the Antarctic are not fully understood.

The main features of the Antarctic climate are as follows: low surface temperature, strong surface inversion, persistent strong low-level wind (also known as katabatic wind) and low precipitation rate. The Antartic's main processes make an investigation of this region's climate a real challenge. Antarctic's remote location, its distance from other continents, its high topography and the sparse observational data available for it do not make the task at hand any easier.

To model atmospheric and surface processes at the regional scale requires a sufficient horizontal and vertical resolution. This is, especially the case in mountain regions that are situated along steep topographic gradients and is also the case in areas that have complicated land-sea contrasts or areas where there is a presence of sea-ice; all of which are characteristics of Antarctica. Present-day coarse resolution global circulation models and the re-analysis products poorly represent the hydrological cycle on a regional scale. Regional climate models can realistically describe the regional distribution of precipitation and accumulation patterns.

Instrumental records show an increase of approximately 0.6 $^{\circ}C$ in the averaged global surface air temperature in the 20th century(the average of near surface air temperature over land and sea surface temperature). The IPCC (Intergovernmental Panel on Climate Change) projects a 1.4 to 5.8 $^{\circ}C$ increase in the global average surface temperature in the 21st century. Despite this, recent studies (Comiso, 2000; Doran et al., 2002; Chapman and Walsh, 2005) reveal a net surface cooling over the Antarctic continent. Also, because the Antarctic ice sheet contains 70% of the fresh water, which can be released due to increases in temperature, another pressing and global question is the rise of sea levels. Therefore, it is worth investigating the net mass balance accumulation trend. Davis et al. (2005) used satellite radar altimetry measurements from 1992 to 2003 to determine that, on average, the elevation of about 8.5 million square kilometers of the Antarctic interior has been increasing. The increasing elevation was then linked to increases in snowfall, which was translated into a mass gain of 45±7 billion tons per year, tying up enough moisture to lower sea level by 0.12±0.02 millimeters per year.

Natural climate variability is also likely to affect future Antarctic climate evolution. This is because, recently observed climate changes over southern latitudes can be at least partially attributed to changes in the atmospheric circulation regime, especially to regime changes of the Antarctic Oscillation (AAO). Some attempts have been done to detect the causes of this oscillation (Thompson and Solomon, 2002; Cai et al., 2003; Fogt and Bromwich, 2005), but until now, not all of the underlying mechanisms that control the AAO have been known. In addition, it is difficult to distinguish between forced and internal (unforced) climate variations, because the climate system is extremely complex due to the nonlinear interactions between and within its subsystems. Therefore, small changes within the climate system, whatever their reason is, may have large effects on the entire atmospheric circulation and consequently elicit strong regional climate changes. Thus, for detailed investigation of the processes taking place over the most southern continent, it is very essential to use models.

The general objective of this dissertation is to implement and validate the regional climate model, HIRHAM, with a 50 km horizontal resolution for the Antarctic area. The simulated atmospheric fields have been compared with objective analyses from the following: the European Center for Medium Range Weather Forecasts (ECMWF), radiosonde, satellite and observational data at selected stations. As mentioned before, due to the sparse observations the quality of the data is very poor which in turn influences the quality of the ECMWF analyses. In order to realistically simulate monthly to decadal mean fields of the atmosphere, climate models have to resolve the physics of the climate system on small and short time scales. This is because many of the physical processes, such as atmospheric convection, radiation and surface evaporation, are highly non-linear and cannot be represented properly by using averaged fields. The complexity of the above-mentioned processes makes it a challenge.

Therefore, the main objectives of this work are the following:

* To apply the regional climate model HIRHAM to the Antarctic area.
* To validate the model, by attracting the maximum available observational data (re-analysis, station, radiosonde and satellite data).
* To study the sensitivity of the HIRHAM simulation to a change in cloud cover, stability function in planetary boundary layer and the lateral boundary conditions.
* To identify decadal scale process (for example the recent temperature and net mass balance trends).
* To investigate the response of the Antarctic climate to mid-latitude changes via global teleconnection patterns.

This thesis is organized in the following way. **Chapter 2** introduces Antarctic's climate. **Chapter 3** describes the main components of the HIRHAM model, which is used as an investigation tool in this study. **Chapter 4** presents detailed description of the data used for the model validation. **Chapter 5** and **Appendix A** are dedicated to the validation of the HIRHAM model with the ERA40, the NCEP re-analysis data and as well as the radiosonde, satellite and station data. Sensitivity studies with the changed HIRHAM cloud cover, the revised stability function in the PBL and the variation in the width of the relaxation zone are also discussed. **Chapter 6** examines the surface net mass balance of the Antarctic continent. **Chapter 7** presents studies of the decadal-scale processes. On the basis of the Antarctic Oscillation index **Chapter 8** deals with natural climate variability in Antarctica. Conclusions and perspectives are presented in **Chapter 9**.

Chapter 2

Climate of Antarctica

The Antarctic continent and its surrounding Southern Ocean are probably the world's least known regions. The Antarctic region has two important roles in the global climate system. First, it maintains the global heat balance and second, it has a significant effect in the net water budget. Since moisture transport is also part of the heat balance, the two main roles mentioned above are closely linked.

As Fig. 2.1 shows, the Antarctic ice sheet consists of three distinct zones - East Antarctica, West Antarctica and the Antarctic Peninsula. The largest is East Antarctica and it is dominated by the high Antarctic plateau which rises inland of the coast. Here, except for the narrow coastal strip, the elevation of the huge mass of ice is above 2 *km* and the elevation of small areas of the plateau can extend to just above 4 *km*. The surface is not smooth but often covered by sastrugi, which are ridges several centimeters high formed by wind erosion and snow deposition. West Antarctic has an average elevation of 850 *m*. Although generally lower than East Antarctic, some areas elevate more than 2000 *m* on the plateau, reaching up to more than 4000 *m*. The Transantarctic Mountains, which stretch from Victoria Land to the Ronne Ice Shelf, separate East and West Antarctica and rise to a maximum elevation of 4528 *m*. The third area is the Antarctic Peninsula that extends northwards from the main mass of the Antarctic continent. The Peninsula is a narrow mountainous barrier with an average width of 70 *km* and a mean height of 1500 *m*. The Peninsula's highest point is just over 3000 *m* (King and Turner, 1997).

The development of the atmospheric circulation in the southern hemisphere is prompted by three main parameters: the asymmetry of the Antarctic continent, the asymmetry of the locations of the three continents further north and finally, the main ocean climatological parameters (such as the sea surface temperature and sea-ice distribution).

The mean sea level pressure distribution from the ERA40 re-analysis data (European Center for Medium-Range Weather Forecasts (ECMWF)) is shown in Fig. 2.2. The circumpolar trough is a dominant characteristic of the large-scale pressure pattern over the Southern Hemisphere. The averaged sea level pressure patterns show a pronounced zonal structure with three minima occurring over the Indian, Pacific and Atlantic Oceans and also, the high pressure zone over

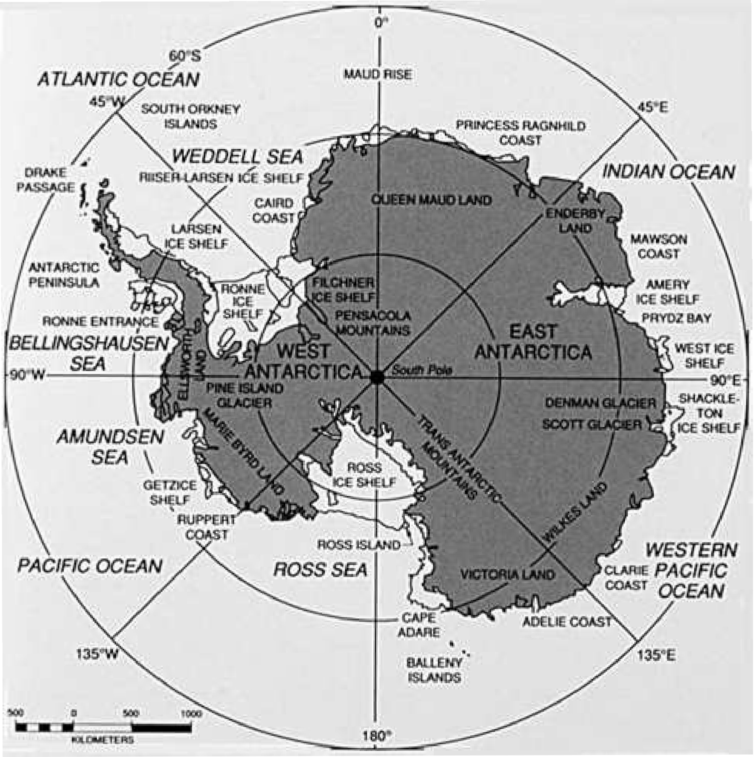

Figure 2.1: *The regions in Antarctica.*

the continent. The circulation over the Antarctic continent can be presented as follows: due to the Coriolis acceleration, cold air at the surface flowing outwards from the polar cell turns towards the west, to form strong southeasterly to easterly surface winds by the edge of the domain around the Antarctic circle. With strong westerly winds prevailing north of 60 °S, from the general circulation in the three-cell structure of the Earths atmosphere, a strong cyclonic vorticity at the surface naturally occurs between the polar cell and the prevailing westerly's around the Antarctic domain.

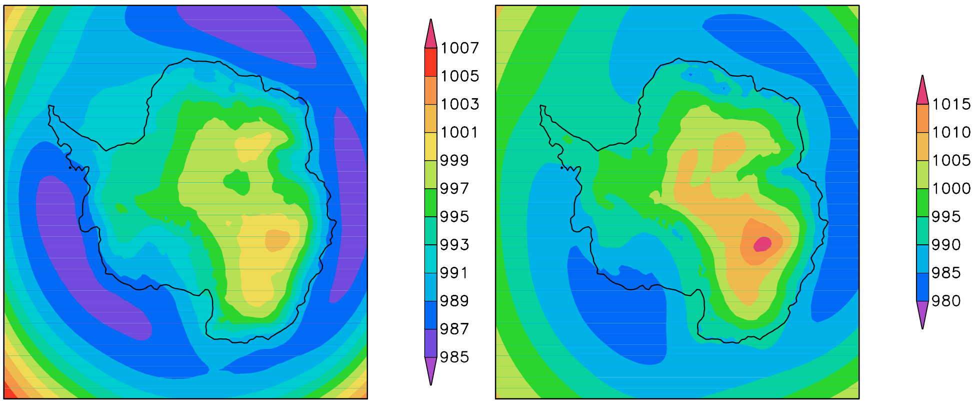

Figure 2.2: *MSLP (hPa) in austral summer (DJF) (left) and austral winter (JJA) (right) for the period 1958-1998. ERA40 re-analysis .*

As the cold air from the south moves over the warmer, oceanic surface to the north there occurs strong baroclinic instabilities and convection; together with the high cyclonic vorticity, result in the formation of mesoscale and synoptic scale cyclonic systems around the edge of the Antarctic domain. These synoptic low-pressure centers tend to move with the westerly's around the Antarctic region and to also drift southwards into the edge of the polar cell region. Throughout the year, the net radiative heat loss is balanced by the meridional heat transport of the atmosphere, with net inflow at upper levels, subsidence over the continent and net flow outwards near the surface. In addition to this general circulation pattern, the synoptic scale eddies which move around the continent and give rise to horizontal advection through the troposphere with flow inwards to the Antarctic on the eastern side of the low pressure centers and outflow on the western sides, with intense mixing of heat and moisture (Giovinetto et al., 1997; Hogan, 1997). The greater radiation loss in winter is associated with the following three changes over the continent: greater cooling, larger horizontal temperature gradients and more intense circulation with stronger winds.

The 2 *m* temperature during austral summer and winter, averaged from 1958 to 1998, is shown in Fig. 2.3.

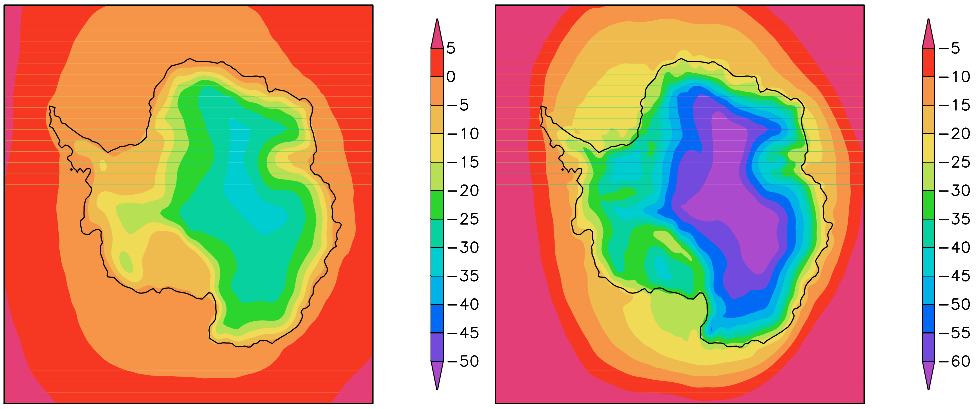

Figure 2.3: *2 m temperature (°C) in austral summer (DJF) (left) and austral winter (JJA) (right) for the period 1958-1998. ERA40 re-analysis .*

The 2 *m* temperature pattern shows the zonal structure over the oceans and the minimum value over the high Antarctic Plateau. During the austral winter, inland temperature can reach -65 °*C*. To a far lesser extent, the radiation deficit is also redressed by heat storage within the snow (Carroll, 1982), and also by, the convective fluxes of heat from leads and polynyas. The low amount of cloud and air moisture over the interior also plays an important role in radiation loss, since cloud cover reduces the incoming solar shortwave radiation and reflects the outgoing longwave radiation back towards the surface.

The fact that the Antarctic consists of a large, high mass of ice centered close to the South Pole has a huge impact on the atmospheric circulation of the Southern Hemisphere. Depressions moving southwards from mid-latitudes tend to become slow-moving or as they come up against the steep orography of the Antarctic coastal region, to start to track towards the east in the Antarctic coastal region. There are therefore few active depressions over the Antarctic interior, although some depressions do penetrate to the South Pole or even Vostok station when the mid-tropospheric flow is especially meridional.

Such a kind of condition is perfect for developing katabatic winds, which are a well-known characteristic of the Antarctic continent. The cold and dense surface air tends to downslope reaching a maximum speed in coastal areas (Renfrew and Anderson, 2002). These areas are favored for the development of coastal polynyas (Wendler et al., 1997). Another important factor for developing katabatic winds is surface orography. The katabatic wind is often observed in the Antarctic valleys where confluence occurs, due to a funneling effect (Nylen et al., 2004). The intensity of the katabatic air movement depends on the cyclonic activity over the ocean and in the vicinity of the coast.

The vertical extent of katabatic winds is determined by the thickness of the layer in which the air is cooled by radiation. Therefore, katabatic winds are always accompanied by an inversion over the ice surface. The level of the wind's minimum intensity (300 - 500 m) coincides with the upper limits of the inversion. Owing to inversions at the ice surface and also to the small parameter of roughness of the snow cover over Antarctica, the coefficient of turbulent exchange is low in spite of high wind speed. At the coastal areas the mixture of the strong katabatic flow and the favourable synoptic system gives rise to the blizzard (Bintanja, 2001b). The blizzard is a strong turbulent snow transport and it is, well known in the coastal areas; it creates difficulty for realistic measurements of precipitation. The climate on the continental coastal regions is dominated by high precipitation and strong storms. Due to the proximity of the sea, most of the snow that falls in Antarctica falls within 200 km of the coast; hence this region experiences the highest accumulation of snow. Since not much precipitation can reach the high Antarctic plateau, the inland part of the continent is commonly referred to as a polar desert. In coastal areas, most precipitation falls as snow, but is highly variable depending on location. Over the Antarctic plateau precipitation falls as ice crystals or ”diamond dust”. For the inner part and central part of Antarctica, the model simulated net accumulation rate calculated as ”Precipitation minus Evaporation” varies from 50 $mm/year$ to 1500 to 2000 $mm/year$, respectively (Vaughan et al., 1999).

The most remarkable feature of the Southern Ocean is the strong seasonal cycle of sea-ice and surface temperature change. The sea-ice plays an interactive role in the heat exchange between the ocean and the atmosphere. The seasonal mean of sea-ice averaged over the period 1958 to 1998 and the seasonal standard deviation are shown in Fig. 2.4 to Fig. 2.5. As it was during the winter season, the seasonal difference is evident when Antarctica almost doubles in size due to increasing sea-ice cover. The maximum in standard deviation shows the areas with the highest sea-ice variability during winter and summertime. During the austral summer, maximum values can be found along the West Antarctic Peninsula and Adélie Land. During

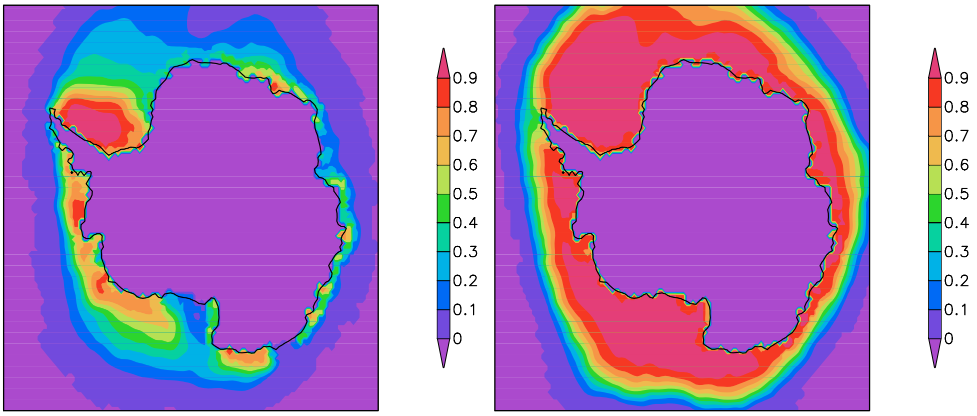

Figure 2.4: *Sea-ice distribution austral summer (DJF) (left) and austral winter (JJA) (right), averaged over 1958 - 1998. ERA40 re-analysis.*

the wintertime, the areas with a higher sea-ice variability are further from the continent and are located at the winter edge of the ice.

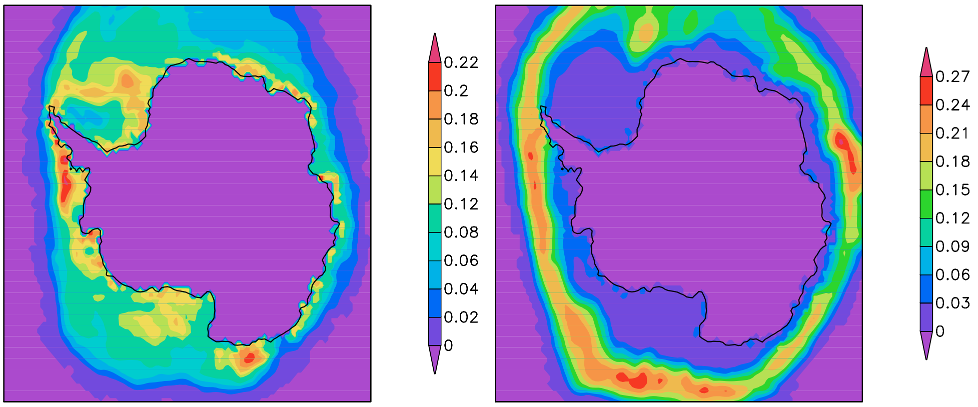

Figure 2.5: *Standard deviation of sea-ice cover austral summer (DJF) (left) and austral winter (JJA) (right),1958 - 1998.*

The seasonal difference is evident, as during the winter season, when Antarctica almost doubles in size due to increasing sea-ice cover. The maximum in standard deviation shows the areas with the highest sea-ice variability during the winter and summertime. The maxima are located at 75 °E and 165 °W. There is a connection between the El-Niño phenomenon (abnormal warming of the sea-surface temperature in the tropical-latitudes of the Pacific Ocean) and the West Pacific Ocean sector in the southern latitudes. Chapter 8 will further discuss the detailed mechanism of the interaction between high southern latitudes and low latitudes. There are different types of sea-ice that can be found in Antarctica. For example, pack ice is multi-year sea-ice, that is, frozen sea water that is a year old or older; it froze and formed elsewhere and later floated off with the winds and currents. Another type is fast-ice: at the end of the winter, rising oceanic swells and increasing temperatures cause the stable winter sea-ice to break-up and begin to drift away from where it formed. Therefore, this year's fast-ice becomes next year's pack-ice, with a portion of it melting and disappearing completely. The thickness of Antarctic ice is typically between one and two meters.

At the continent, the snow blanket covering the surface plays an important role in the heat balance. As shown in Fig. 2.6, the high albedo value, which on average is 80 %, means that most of the solar radiation during the summer period reflects back into the atmosphere and only a relatively small part is absorbed. In summer, each of the four radiation terms (downward and upward shortwave, downward and upward longwave radiation) are in the range of 100 to 400 W/m^2. Thus, generally exceeding the order of the sensible and latent heat fluxes by at least an order of magnitude (Carroll, 1982).

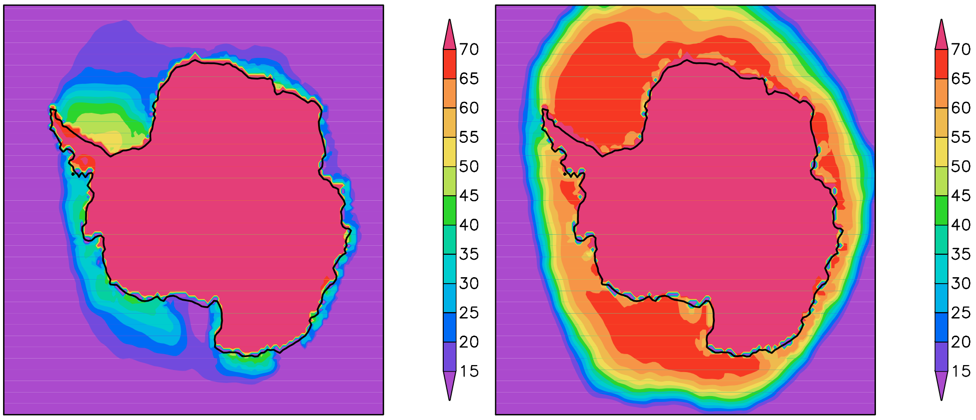

Figure 2.6: *Albedo (%) austral summer (DJF) (left) and austral winter (JJA) (right), averaged over 1958 - 1998. HIRHAM simulation.*

Chapter 3

HIRHAM model description

Taking into account our recent understanding about the climate of Antarctica, much progress has been made during the last two decades exploiting a model hierarchy, ranging from simple, hybrid and intermediate to fully coupled ocean-atmosphere models.

The regional climate model HIRHAM used in this study was developed by Christensen and van Meijgaard (1992); Christensen et al. (1996). Later the model was adapted to the Arctic conditions by Dethloff et al. (1996); Rinke et al. (1997, 1999). The dynamical part of HIRHAM is based on a limited-area model HIRLAM (Machenhauer et al., 1998) and the physical parameterisations are taken from the general circulation model ECHAM4 and include radiation, cumulus convection, land surface processes, planetary boundary layer turbulence, gravity wave drag and condensation (Roeckner et al., 1992, 1996).

The standard model version has a horizontal resolution of $0.5 \times 0.5\ ^\circ$ in a latitude - longitude grid. In the vertical, a hybrid sigma coordinate when the 19 or 25 levels HIRHAM versions are used. The top of the model is at about 10 *hPa*. The HIRHAM is a standard primitive equation Eulerian staggered grid point model.

3.1 Governing equations

The HIRHAM is a hydrostatic model. The dynamical part of HIRHAM is based on the prognostic momentum, thermodynamic and moisture equations. Two metric coefficients (h_x; h_y) have been used in the model equations for any orthogonal coordinate systems or map projections with axes (x,y). On the Earth's surface, a distance ΔX, ΔY can be written as:

$$\Delta X = r h_x \Delta x \quad and \quad \Delta Y = r h_y \Delta y \tag{3.1}$$

The Earth is nearly a sphere, and so it is natural to employ spherical coordinates. In rotated spherical coordinates, the metric coefficients are calculated based on the longitude, latitude of the Earth. Thus,

$$\Delta X = rcos\lambda\Delta\phi \quad and \quad \Delta Y = r\Delta\lambda, \tag{3.2}$$

where r is the radius, ϕ is the longitude and λ is the latitude of the Earth. In Cartesian coordinates, the model governing equations for horizontal momentum and thermodynamics are:

$$\frac{\partial u}{\partial t} = (f+\xi)v - \dot{\eta}\frac{\partial u}{\partial \eta} - \frac{R_d T_u}{rh_x}\frac{\partial lnP}{\partial x} - \frac{1}{rh_x}\frac{\partial}{\partial x}(\Phi+E) + PH_u + K_u \tag{3.3}$$

$$\frac{\partial v}{\partial t} = -(f+\xi)u - \dot{\eta}\frac{\partial v}{\partial \eta} - \frac{R_d T_v}{rh_y}\frac{\partial lnP}{\partial y} - \frac{1}{rh_y}\frac{\partial}{\partial y}(\Phi+E) + PH_v + K_v, \tag{3.4}$$

$$\frac{\partial T}{\partial t} = -\frac{u}{rh_x}\frac{\partial T}{\partial x} - \frac{v}{rh_y}\frac{\partial T}{\partial y} - \dot{\eta}\frac{\partial T}{\partial \eta} + \frac{kT_v\omega}{(1+(\delta-1)q_v)P} + PH_T + K_T, \tag{3.5}$$

where

$$\xi = \frac{1}{rh_x h_y}\left(\frac{\partial}{\partial x}(h_y v) - \frac{\partial}{\partial y}(h_x u)\right), \tag{3.6}$$

$$E = \frac{1}{2}\left(u^2+v^2\right), \tag{3.7}$$

$$\dot{\eta} = \frac{\partial \eta}{\partial t}, \tag{3.8}$$

where u, v are the zonal and meridional wind components, T the air temperature, f the Coriolis force, $R_d = 287.05J/kgK$ the dry air gas constant, Φ geopotential height, $k = 0.4$ is von Kármán's constant, T_v the virtual air temperature, PH_u, PH_v, PH_T are the tendencies from the physical parameterisation, K_u, K_v, K_T are the tendencies from the horizontal diffusion. The $\eta-$coordinate was defined in order to remove or reduce the errors that are known to occur when computing the pressure gradient force, advection, and horizontal diffusion along steeply sloped terrain. The water vapour and cloud water equations are:

$$\frac{\partial q_v}{\partial t} = -\frac{u}{rh_x}\frac{\partial q_v}{\partial x} - \frac{v}{rh_y}\frac{\partial q_v}{\partial y} - \dot{\eta}\frac{\partial q_v}{\partial \eta} + PH_{q_v} + K_{q_v}, \tag{3.9}$$

$$\frac{\partial q_w}{\partial t} = -\frac{u}{rh_x}\frac{\partial q_w}{\partial x} - \frac{v}{rh_y}\frac{\partial q_w}{\partial y} - \dot{\eta}\frac{\partial q_w}{\partial \eta} + PH_{q_w} + K_{q_w}, \tag{3.10}$$

where q_v is the water vapour mixing ratio, $q_w = q_l + q_i$ is the cloud water mixing ratio including the liquid q_l and the solid fraction q_i. The hydrostatic equation is:

$$\frac{\partial \Phi}{\partial P} = -\frac{R_d T_v}{P} \tag{3.11}$$

The continuity equation is:

$$\frac{\partial}{\partial \eta}\left(\frac{\partial P}{\partial t}\right)+\bigtriangledown\cdot\left(\vec{V}_h\frac{\partial P}{\partial \eta}\right)+\frac{\partial}{\partial \eta}\left(\dot{\eta}\frac{\partial P}{\partial \eta}\right)=0, \tag{3.12}$$

where $\vec{V}_h$ is the horizontal wind vector and the definition of the divergence operator is

$$\bigtriangledown\cdot\vec{V}_h=\frac{1}{rh_xh_y}\left(\frac{\partial}{\partial x}(h_yu)+\frac{\partial}{\partial y}(h_xv)\right). \tag{3.13}$$

The surface pressure tendency equation was calculated by integrating the continuity equation, using as boundary conditions $\dot{\eta}=0$ at $\eta=0$ and $\eta=1$:

$$\frac{\partial P_s}{\partial t}=-\int_0^1\bigtriangledown\cdot\left(\vec{V}_h\frac{\partial P}{\partial \eta}\right)d\eta. \tag{3.14}$$

The pressure coordinate vertical velocity is:

$$\omega=\frac{\partial P_s}{\partial t}+\int_\eta^1\bigtriangledown\cdot\left(\vec{V}_h\frac{\partial P}{\partial t}\right)d\eta+\vec{V}_h\cdot\bigtriangledown P \tag{3.15}$$

and the equation for $\dot{\eta}$ is

$$\dot{\eta}\frac{\partial P}{\partial t}=\left(1-\frac{\partial P}{\partial P_s}\right)\frac{\partial P_s}{\partial t}+\int_\eta^1\bigtriangledown\cdot\left(\vec{V}_h\frac{\partial P}{\partial \eta}\right)d\eta. \tag{3.16}$$

A detailed description of the model governing equations can be found in Dorn (2002) and Saha (2006).

3.2 Boundary relaxation

Regional climate models are often used to dynamically produce a high-resolution analysis of the atmosphere. When the dynamical downscaling technique is used with re-analyses, such as those of the NCEP and ECMWF, all the regional details are simulated by the regional model without an input of direct regional-scale observations. The regional model is only driven by the global re-analysis on coarse grids. Downscaling techniques are supposed to retain all the large-scale information that has been well resolved in the global re-analysis data assimilation. Downscaling techniques are also supposed to add the smaller-scale information that the coarse-resolution global data assimilation model could not generate. However, regional models have to deal with the problem of mathematically ill posed lateral boundary conditions. The inconsistencies between the model solution and the driving coarse model field along the boundaries effectively produce undesirable noise, and often, instabilities. The lateral boundary relaxation method of Davies (1976) is used in the HIRHAM model to alleviate such errors in a buffer zone that covers 10 grid points along the model boundary. Fields f_k with superscript HIRHAM and ERA40, are representing the model values and lateral forcing values respectively.

$$f_k = \alpha_k * f_k^{ERA40} + (1-\alpha_k)\, f_k^{HIRHAM} \tag{3.17}$$

The coefficient α_k is the relaxation weight, which linearly joins the boundary forcing data with the model data within the relaxation zone.

$$\alpha_k = 1 - tanh(ak) \tag{3.18}$$

where a is a constant and depends on the number of relaxation points. The α_k values are presented in Tab. 5.5. Moisture and cloud water are relaxed according to an ”inflow/outflow” scheme, since the model experiments revealed that the standard relaxation procedure gives spurious precipitation in the entire relaxation zone. In an ”inflow/outflow” scheme the moisture fields are only linked to the boundary fields at the outermost points in the inflow case and extrapolated based on the four nearest neighboring points located upstream and inside the model domain in the outflow case. The model was driven 4 times per day: at 06, 12, 18 and 00 hours. At the lower boundary, the model was forced by the ERA40’s daily sea surface temperature and sea-ice fraction.

3.3 Initialisation of the prognostic variables

In general the wind and mass fields that form the data base for numerical weather prediction cannot be prescribed with sufficient accuracy. This implies the excitation of high-frequency oscillations with excessive amplitudes in the solution of the model equations. In order to remove these spurious oscillations, the data fields must be initialised before the model is integrated. The implicit form of nonlinear normal mode initialisation (INMI) has become the most widely used initialisation technique. The early formulation of the method for global or hemispheric models was soon followed by applications to limited-area models (Temperton, 1988).

The INMI is based upon the linear analysis of the equations that describe the motion of the atmosphere. The solution to the linearised system of equations can be decomposed into a linear combination of independent eigenfunctions called normal modes. These modes can be split into two groups: modes of meteorological significance with low frequencies, and fast modes, these are generally regarded as noise. The principal goal of the initialisation is to adjust initial mass and wind fields so that the excitation of the fast modes may be suppressed while the slow meteorological modes are preserved. The model prognostic variables are only initialised once by the ERA40 data for temperature, specific humidity, and wind and surface pressure.

3.4 Vertical, horizontal and time discretisation

3.4.1 Vertical discretisation

The HIRHAM model uses a hybrid sigma-pressure coordinate system $\eta(P, P_s)$, with terrain-following sigma surfaces near the ground transitioning to constant pressure surfaces near the top of the domain. Combining sigma and constant pressure is an improvement over constant pressure because it takes advantage of the terrain-following nature of sigma coordinates and avoids intersection of layers with model terrain. This is a monotonic function of pressure P and also depends on surface pressure P_s where : $\eta(0, P_s) = 0$ and $\eta(P_s, P_s) = 1$ In our research the 19 and 25 level HIRHAM versions were used. In these cases, these levels are defined by the pressures of the interface between "half levels" and the "half level" pressures are given by:

$$P_{m+1/2} = A_{m+1/2} + B_{m+1/2} * P_s \qquad m = 1...19/25 \tag{3.19}$$

The values of the constants A and B for the 19 and 25 level HIRHAM versions are calculated using a reference sea level pressure P_s=1015 *hPa* and are shown in Appendix B Tab. B.1. The prognostic variables of temperature, pressure etc. are calculated on "full levels":

$$P_m = \frac{1}{2} * \left(P_{m+1/2} + P_{m-1/2}\right) \tag{3.20}$$

3.4.2 Horizontal discretisation

The numerical solution requires the domain to be discretised and for the governing equations to be reduced to their finite difference equivalents. Fig. 3.1 shows the numerical grid employed for spatial discretisation. The grid is a so-called Arakawa *C* grid, which belongs to the class of staggered grids. In the *C* grid, quantities such as p_s - surface pressure, T -temperature, q - specific humidity, q_L - specific liquid water are defined at the center of the grid, while the east-west components of velocity u, is displaced half a grid space to the west of the center and the north-south component v displaced half a grid space to the south of the center. HIRHAM has a horizontal grid size of 0.5° by 0.5°, which corresponds to approximately 50 *km*. The centered difference scheme is used here for the horizontal discretisation of model equations. In Cartesian coordinates for variable F and horizontal distance $\triangle x$ between two grid points along the $x - axis$, the first-order derivative of F with respect to x and with truncation error δx^2 is presented by:

$$\frac{\partial F}{\partial x} \simeq \frac{F(x + \triangle x) - F(x - \triangle x)}{2 \triangle x} \tag{3.21}$$

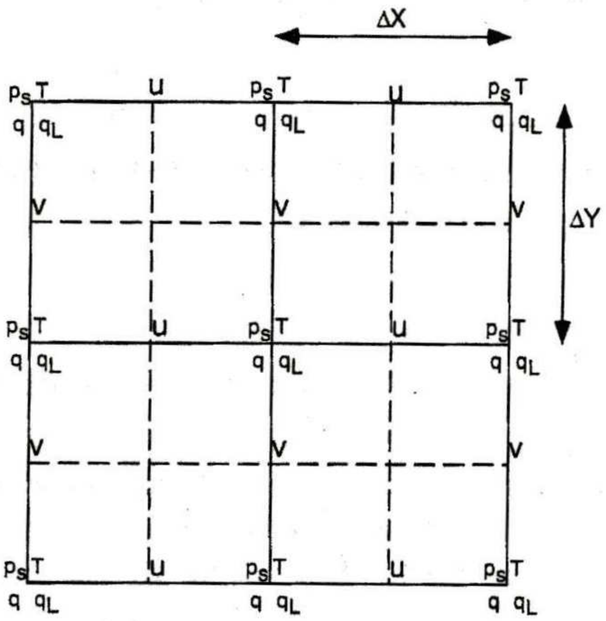

Figure 3.1: *Horizontal Arakawa "C" grid.*

and the second-order derivative of F with truncation error δx^2 is represented by:

$$\frac{\partial^2 F}{\partial x^2} \simeq \frac{F(x+\triangle x) - 2F(x) + F(x-\triangle x)}{(\triangle x)^2}. \tag{3.22}$$

3.4.3 Time discretisation

For the time discretisation of the prognostic model equations, the semi-implicit second-order accuracy "leap-frog" scheme was used. An equation with a prognostic variable ψ can be written as

$$\frac{\partial \psi}{\partial t} = F \tag{3.23}$$

Using the semi-implicit scheme, ψ at the future time step $n+1$ can be written as

$$\psi^{n+1} = \psi^{n-1} + 2\Delta t \cdot \left(F^n - S_\psi\right), \tag{3.24}$$

where F_n represents the local temporal derivative of ψ, S_ψ is the semi-implicit correction term and formulation of this quantity varies from one equation to the other. The explicit formulation of time derivative of ψ, is used as a first approximation while subscript 'e' denotes the explicit term. Therefore, from equation 3.23 we get the following:

$$\psi_e^{n+1} = \psi^{n-1} + 2\Delta t \cdot F^n. \tag{3.25}$$

Now using equations (3.24) and (3.25), we have the complete solution for ψ at the future time step $n+1$

$$\psi^{n+1} = \psi_e^{n+1} - 2\Delta t \cdot S_\psi. \tag{3.26}$$

Finally, a time filter is for the values ψ at the n^{th} time step (this value in the next time step will be treated as $(n-1)^{th}$ time step value) is

$$\psi_f^n = \psi^n + \varepsilon_f \left(\psi_f^{n-1} + \psi^{n+1} - 2\psi^n \right), \tag{3.27}$$

where subscript f represents the time filtered value and $\varepsilon_f = 0.05$.
The time step is 240 *sec* and 120 *sec* for the 19 and 25 vertical level model versions, respectively.

Horizontal diffusion schemes have been common features of numerical models. The reason for keeping them in models is to maintain a balance of kinetic energy in the simulated atmosphere between its generation through conversion of available potential energy and its dissipative transformation into thermal energy. A linear fourth-order horizontal diffusion scheme is applied, but in mountainous regions it is switched off for the temperature and humidity. This is done to avoid spurious mixing of air masses from different pressure levels that will cause unphysical precipitations. Another additional smoothing was done by Shapiro's filter (Shapiro, 1970). It was done to prevent reflection of gravity waves from the upper boundary. The filter was applied to temperature, wind and specific humidity prognostic variables.

3.4.4 Model setup for Antarctica

For the Antarctic climate simulation an integration domain south of 55 °S was chosen with: 122×110 grid points in a horizontal resolution of $0.5^\circ \times 0.5^\circ$, corresponding to grid elements of approximately 50×50 *km*. The grid is made by rotating a regular latitude-longitude grid from the equator to the south pole. The model topography is shown in Fig. 3.2 and the integration area including the Antarctic continent and surrounding parts of the Southern Ocean are shown in Fig. 3.3.

One of the main components of further successful inquiry is the correct choice of the size and proper setup of the grid domain (Rinke and Dethloff, 2000). For example, the amount of clouds and precipitation we get in the result depends on cyclonic movement and also, how much cyclones penetrate the integration area. The choice of this area location was based on previous experience in the Arctic area as well as the region's features (Dethloff et al., 1996).

3.5 Parameterisations

In climate models, complex relationships between grid and sub-grid scale processes are often represented using simple approximations where one parameter is estimated based on an

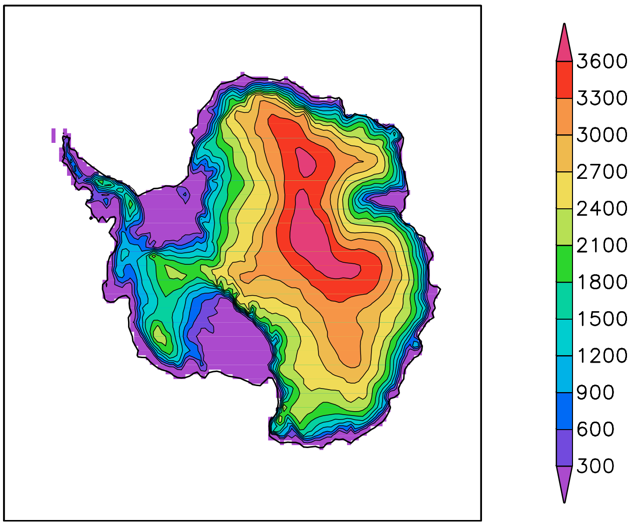

Figure 3.2: *Antarctic orography (m) in 50 × 50 km model horizontal resolution.*

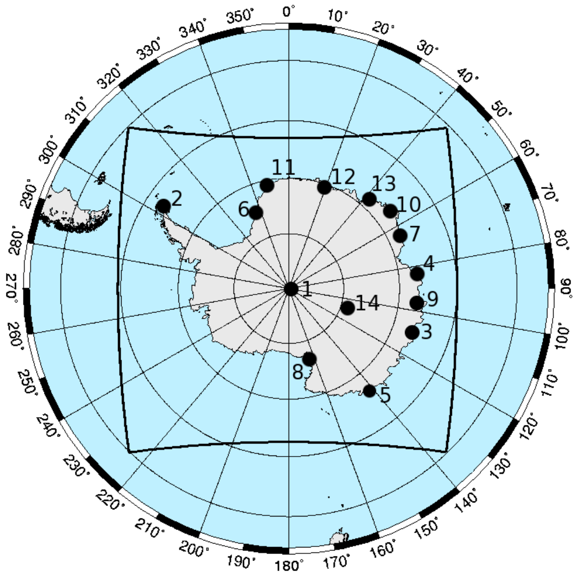

N	*Station*	*Longitude*	*Latitude*	*Elevation(m)*
1	Amundsen-Scott	0 °E	90 °S	2880
2	Bellingshausen	58.9 °W	62.2 °S	16
3	Casey	10.5 °E	66.3 °S	42
4	Davis	78.0 °E	68.6 °S	13
5	Dumont-Durville	140.0 °E	66.7 °S	43
6	Halley	26.4 °W	75.5 °S	30
7	Mawson	62.9 °E	67.6 °S	16
8	McMurdo	166.7 °E	77.9 °S	24
9	Mirny	93.0 °E	66.5 °S	30
10	Molodezhnaya	45.9 °E	67.7 °S	40
11	Neumayer	8.4 °W	70.7 °S	50
12	Novolazarevskaya	11.8 °E	70.8 °S	119
13	Syowa	39.6 °E	69.0 °S	29
14	Vostok	106.9 °E	78.5 °S	3420

Figure 3.3: *HIRHAM grid and location of the observation stations used in the model validation (left). The names and elevation of the stations are posted in Tab.3.2 (right)*

.

assumed relationship to another parameter. Physical processes play an important role in the atmosphere. These processes occur both on horizontal and vertical scales, which are resolved and unresolved by the numerical model. Even in very high-resolution models, the physics of unresolved scales have important impacts on the evolution of the state of the atmosphere (Dethloff et al., 2001). Physics such as short and long wave radiation, turbulence (including gravity wave drag), deep and shallow convection, cloud and precipitation generation and air-sea/air-land interactions need to be parameterised. Parameterisations are formulas (empirical or derived from physical hypothesis) by means of prognostic and diagnostic model variables, calculating the effect of sub-grid scale physics on the resolved scales.

The following processes are parameterised in the HIRHAM model:

- *short-wave and long-wave radiation.* The principal quantity determined in the radiation calculation is the temperature tendency, i.e. the atmospheric heating or cooling rate. It is related to the flux divergence according to

  $$\frac{\partial T}{\partial t} = \frac{g}{C_p}\frac{\partial F}{\partial p} \tag{3.28}$$

  where F is the net total radiative flux composed of shortwave and longwave fluxes, g and C_p are the constant of gravity, and the space heat of air, respectively. Every two hours, the model calculates the radiative transfer equations. Radiation parameterisation is calculated based on Morcrette (1990). Four spectral intervals are used in the shortwave radiation and six in the longwave radiation.

  To take into account the change in temperature and the solar zenith angle between the time when the full radiation is calculated, effective transmissivity τ_e and emissivity ε_e are defined at each model level such that:

  $$F_T = \varepsilon_e \cdot \sigma \cdot T^4 \tag{3.29}$$

  $$F_S = \tau_e \cdot S_0, \tag{3.30}$$

  where F_T and F_S are the net longwave and shortwave fluxes, respectively. σ is the Stefan-Bolzman constant and S_0 is the solar flux at the top of the atmosphere. The values ε_e and τ_e are fixed between the full radiation time steps and the net fluxes are recomputed at every time step using Eq. 3.29 and Eq. 3.30 with the correct temperature and solar zenith angle. Further details can be found in Fortman (2004).

  Cloud optical properties include cloud emissivity and optical thickness. The emissivity ε of clouds in the terrestrial region is described by:

  $$\varepsilon = 1 - e^{-\frac{k \cdot m \cdot d}{\bar{\mu}}} \tag{3.31}$$

  where k = 0.084 $m^2 g^{-1}$ is the mass absorption coefficient (Stephens, 1978), d is the geometrical cloud thickness and m is the water or ice content in gm^{-3}. Optical thickness δ, single scattering albedo $\tilde{\omega}$, and back-scattering coefficient β are the optical parameters considered in transfer of solar radiation. For both cloud phases, the parameterisation of Stephens (1978) is adopted:

  $$log(\delta) = \begin{cases} 0.2633 + 1.7095 \cdot ln\left[log(m \cdot d)\right] & (\lambda < 0.685\mu m) \\ 0.3492 + 1.6518 \cdot ln\left[log(m \cdot d)\right] & otherwise \end{cases}$$

Single scattering albedo and back-scattering coefficients are taken from (Kerschgens et al., 1978).

* *Land surface processes*. The land surface parameterisation scheme comprises the evolution of soil temperature profile, soil moisture, surface water vapor flux, planetary boundary layer, momentum and heat transfer and snow pack over land. If there is snow on the ground surface, then the snow surface temperature, otherwise ground surface temperature act as an interface between atmosphere and soil. In the presence of snow pack over land that has a depth exceeding 9 m water equivalent, the surface is considered to be covered with ice. Therefore, soil temperature equations are solved with the characteristic of ice.

These areas are prescribed in the model and identified as glaciers. For snow depth deeper than 0.025 m, an extra heat conduction equation evolves according to

$$\frac{\partial T_{S_n}}{\partial t} = \frac{F_S}{\rho_{S_n} \cdot C_{S_n} \cdot S_n}, \tag{3.32}$$

where T_{S_n} is temperature in the middle of snow pack, F_S is sum of radiative and turbulent fluxes at the surfaces, $\rho_{S_n} C_{S_n}$ is heat capacity of snow per unit volume equal to $0.6345 \times 10^6 Jm^{-3}K^{-1}$ computed using snow density ρ_{S_n} of 300 kg m^{-3} and S_n is depth of the snow pack. The skin temperature of the snow, which serves as an interface to the atmosphere, is obtained through a linear extrapolation from the snow layer and the upper soil layer. This temperature may not exceed the snowmelt temperature. If $T_{S_n} > 273.16\,K$, the energy is first used to warm the soil underneath and only if both the snow temperature and the upper soil temperature reach the melting point will, further energy be used to melt the snow.

* *boundary layer processes*. Vertical diffusion: turbulent surface fluxes are calculated from the Monin-Obukhov similarity theory (Louis, 1979) and with a higher order closure scheme for the transfer coefficients of momentum, heat, moisture and cloud water within and above PBL. According to the Monin-Obukhov similarity theory, the gradients of the wind u and internal energy ($s = C_p \cdot T + g \cdot z$) are assumed to be universal functions of the stability parameter.

$$\frac{kz}{u_\star} \cdot \frac{\partial u}{\partial z} = \phi_m \left(\frac{z}{L}\right) \tag{3.33}$$

$$\frac{kz}{s_\star} \cdot \frac{\partial s}{\partial z} = \phi_h \left(\frac{z}{L}\right) \tag{3.34}$$

where $u_\star$ is the surface friction velocity, z is the height and L is the Monin-Obukhov length :

$$L = \frac{s \cdot u_\star^2}{k \cdot g \cdot s_\star}, \tag{3.35}$$

where ϕ_m and ϕ_h are universal flux profile functions for momentum and heat, k is von Karman's constant and ($u_\star$, $s_\star$) are derived from the surface turbulent fluxes.

$$\rho \cdot u_\star^2 = \rho \cdot C_m \cdot \mid u \mid^2 \tag{3.36}$$

$$\rho \cdot u_\star \cdot s_\star = \rho \cdot C_h \cdot \mid u \mid \cdot (s - s_S) \tag{3.37}$$

Equations 3.28 and 3.29 can be integrated over the lowest model layer, and L eliminated using Eq. 3.20 in order to derive C_m and C_h. However, such expression cannot be analytically obtained because of the complicated form of ϕ_m and ϕ_h. C_m and C_h are approximated by following analytical expressions, Louis (1979):

$$C_m = \left(\frac{k}{ln \frac{z}{z_0}} \right)^2 \cdot f_m \left(Ri, \frac{z}{z_0} \right) \tag{3.38}$$

and

$$C_h = \left(\frac{k}{ln \frac{z}{z_0}} \right)^2 \cdot f_h \left(Ri, \frac{z}{z_0} \right) \tag{3.39}$$

The empirical functions f_m and f_h must have the correct behaviour near neutrality and in the asymptotic cases of high stability or instability. In the highly stable case, when Richardson number $Ri \geq 0$, the stability functions f_m and f_h are parameterised as follows:

$$f_m = \frac{1}{1 + (2 \cdot b \cdot Ri) / \left(\sqrt{1 + d \cdot Ri} \right)}, \tag{3.40}$$

$$f_h = \frac{1}{1 + (3 \cdot b \cdot Ri) / \left(\sqrt{1 + d \cdot Ri} \right)} \tag{3.41}$$

with b=5, d=5.

The buoyancy flux is formulated in terms of cloud-conservative variables by including the impact of cloud processes in the buoyancy term. This is achieved by modifying the Richardson number into a so-called moist Richardson number

$$Ri = \frac{g}{\theta_v} \cdot \frac{(A \triangle \theta_l + \theta B \triangle q_t) \triangle z}{(\triangle u)^2 + (\triangle v)^2}, \tag{3.42}$$

where g is the gravity constant, θ_l refers to a cloud water potential temperature, $q_t = q_l + q_v + q_i$ is the total water content, specific as well as held in clouds and θ and θ_v are the usual potential and virtual potential temperatures defined without the liquid water term. The two numerical constants A and B are based on Deardorff (1980). The eddy diffusion coefficients are calculated as functions of the turbulent kinetic energy.

To define the top of the boundary layer two levels are computed. First level above the dynamical height (Ekman layer height).

$$h_{dyn} = 0.5 \cdot (u_{\star}/f) \tag{3.43}$$

where f is Coriolis parameter. Second, a dry convective level, h_{cnv}, is defined as the lowest level for which the static stability $s > s_{NLEV}$. The top of the planetary boundary layer is then given by:

$$h_{pbl} = max\left(h_{dyn}, h_{cnv}\right) \tag{3.44}$$

The above formulation takes into account early morning cases (where the dry convective boundary layer starts to develop), where considering $h_{cnv} = h_{dyn}$ would give too strong vertical constraint for the turbulent diffusion.

* *mountain wave drag*. Orographic forcing is prescribed by a sub-grid scale orographic variance. Surface stress due to gravity waves is calculated from linear theory and dimensionality considerations. And, the vertical structure of momentum flux is calculated from a local wave Richardson number. It is very suitable to use a high resolution climate model is for a detailed description of the interaction between the surface and the atmosphere that occurs through surface turbulent fluxes of moisture and heat. The fluxes to and from the surface are caused by the atmospheric vertical temperature and humidity gradients. The strength of the turbulent fluxes is a function of the surface roughness. The surface roughness length is geographically prescribed over land while, over ocean it is calculated from the Charnock formula. And, over sea-ice a constant value of 0.001 m has been used. The roughness length over land plays the most significant role in the steep edges of the ice sheet. Based on the experiments conducted in the Arctic integration domain over the high topography of Greenland and also, the results of van Lipzig (1999), we implemented the new roughness length for the land, which was reduced to 3 m to constrain it to values smaller than the altitude of the lowest model level as shown in Fig. 3.4.

* *cloud microphysics*. The cloud scheme is based on Sundqvist (1978). Subgrid-scale condensation and cloud formation is taken into account by specifying appropriate thresholds for relative humidity depending on altitude and static stability. The mass flux convection scheme is after Tiedtke (1989). The cloud scheme has three types of convection, deep, shallow, and midlevel and includes an unsaturated downdraft. Deep convection is driven by moisture convergence in the entire column of air. Shallow convection is driven by moisture convergence in the boundary layer and midlevel convection occurs when there is upward motion creating conditional instability. A bulk entraining plume-type cloud model is used for all convective types, and different entrainment and detrainment rates are used for the different types of convection. The updraft mass flux is proportional to boundary layer moisture convergence for the shallow and deep convection and the up-

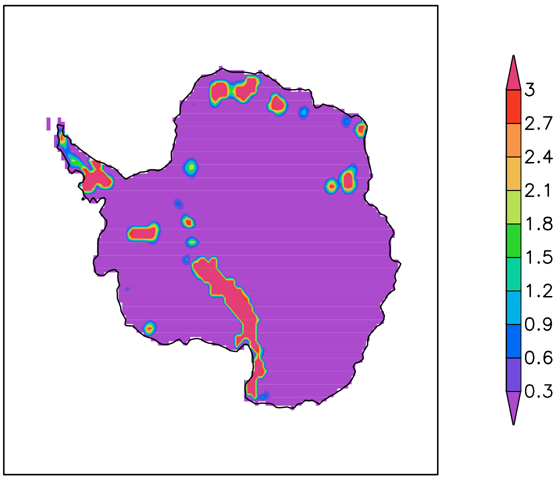

Figure 3.4: *The reduced surface roughness length (m)*

ward motion in the midlevel convection, while the height of convection is dependent on the buoyancy of the plume. The convective cloud water detrained at the top of cumulus clouds is used as a source term in the stratiform cloud water equation (Roeckner et al., 1996). For the stratiform clouds water content is calculated from a budget equation including sources and sinks due to phase changes and precipitation formation by coalescence of cloud droplets and gravitational settling of ice crystals (Sundqvist, 1978).

The cloud cover fraction C_i at each model level (i = 1...$nlev$) is parameterised as a nonlinear function of the grid cell mean relative humidity U_i at this level. For $U_{c,i} < U_i \le U_{sat}$, where $U_{c,i}$ is a height-dependent threshold for cloud formation and U_{sat} = 1 the saturation humidity, the cloud cover fraction is given by

$$C_i = 1 - \sqrt{1 - \frac{U_i - U_{c,i}}{U_{sat} - U_{c,i}}} \tag{3.45}$$

For $U_i \le U_{c,i}$, the respective layer is cloudless (C_i = 0). The height dependence of $U_{c,i}$ is prescribed as

$$U_{c,i} = U_{c,top} + \left(U_{c,surf} - U_{c,top}\right) exp\left(1 - \left(\frac{p_{surf}}{p_i}\right)^{N_c}\right) \tag{3.46}$$

where p_i is the pressure, p_{surf} the surface pressure, $U_{c,top}$ = 0.4 and $U_{c,surf}$ = 0.99 are the thresholds at the top of the atmosphere and at the surface, respectively, and N_c = 4 is a fitting parameter. In the current model setup, there is no distinction between convective and stratiform clouds, and (3.46) is used for all cloud types except for marine stratus clouds under a low-level inversion (below the pressure level $p_c \approx 735$ hPa).

The total cloud cover in a vertical column C_{tot}, in which the overlap of clouds at different levels have to be taken into account, is computed as

$$C_{tot} = \prod_{i=1}^{nlev} \frac{1 - max(C_{i-1}, C_i)}{max(1 - C_{i-1}, \varepsilon)} \tag{3.47}$$

where the levels are numbered from top (i = 1) to bottom (i = nlev), and $C_0 \equiv 0$. ε is a pure security parameter to avoid division by zero. This assumption for the total cloud cover represents a type of maximum random overlap. With this approach, vertically continuous clouds are assumed to be overlapped to their maximum possibility, while clouds at different heights, that are separated by an entirely cloud-free model level, are randomly overlapped.

* *surface processes*. The land surface scheme considers the heat and water budgets in the soil, snow cover and land and the heat budget of permanent land and sea-ice. The albedo of snow and ice surfaces is a function of surface temperature. In snow covered areas, the surface albedo is modified according to :

$$\alpha_{surf} = \alpha_{Sb} + (\alpha_S - \alpha_{Sb}) \cdot \frac{S_n}{S_n + S_n^\star} \tag{3.48}$$

where α_S is snow albedo, α_{Sb} is background albedo, S_n is simulated snow depth, $S_n^\star$ is critical snow depth (=0.01 m). The albedo of snow and ice surface (α_S) is a function of surface type (t_S) and surface temperature (T_S). For $T_S \geq T_m = 273.15K$ (i.e. for melting of snow or ice), α_S is fixed at a relatively small value, $\alpha_S = \alpha_{S_{min}}(t_S, \alpha_f)$, whereas α_S is large, $\alpha_S = \alpha_{S_{max}}(t_S, \alpha_f)$, for a cold surface ($T_S \leq T_0 = 263.15K$) according to Robock (1980). In the temperature range $T_0 < T_S < T_m$, $\alpha_S = \alpha_S(T_S, t_S, \alpha_f)$ is obtained by linear interpolation

$$\alpha_S = \alpha_{S_{max}} - (\alpha_{S_{max}} - \alpha_{S_{min}}) \cdot \frac{T_S - T_0}{T_m - T_0}. \tag{3.49}$$

For glacier ($\alpha_f = 0$), $\alpha_{max} = 0.8$ and $\alpha_{min} = 0.6$.

The detailed description of some of the parameterisation schemes implemented in the HIRHAM and experiments with the HIRHAM model over the Arctic area can be found in Dethloff et al. (1996); Rinke et al. (1997, 1999); Dethloff et al. (2001); Dorn (2002); Saha (2006); Rinke et al. (2006).

Chapter 4

Datasets and comparison periods

Re-analysis products are designed to obtain global, homogeneous and selfconsistent datasets of the atmospheric dynamics and also, to do this on the longest time scale allowed by the currently available instrumental data. In a re-analysis, a consistent state-of-the-art atmospheric forecast model and data assimilation scheme are run on a historical archive of meteorological observations. Thus, removing spurious climate change caused by updates in the model code. However, variations in the amount and type of data may still cause significant ”jumps” in the re-analysis climate, this is especially true for data-sparse regions like Antarctica (Marshall et al., 2002; Bromwich and Fogt, 2004).

4.1 ERA40 and NCEP-NCAR re-analyses datasets

Several gridded datasets have been used for the HIRHAM model validation. Among the several available re-analyses, the most comprehensive are those of the National Center for Environmental Prediction / National Center for Atmospheric Research (further NCEP) and the European Center for Medium-Range Weather Forecast (ECMWF) 40-years re-analysis (ERA40). Therefore, in this study they are compared with each other, with observational data and are used for the model validation. To compare model output with the station data, the variable was linearly interpolated from the HIRHAM grid to the station location. In order to carry out direct comparisons between the re-analysis and model simulation result, the re-analysis data were interpolated to the HIRHAM grid.

The online NCEP re-analysis data are commonly available on a 2.5° by 2.5° degree grid. The NCEP re-analysis (Kistler et al., 2001) covers the period 1948 to 2005, with a monthly update. It is based on a numerical weather prediction model with T62 spectral resolution, which corresponds approximately to 209 *km* and has 28 sigma levels (17 standard pressure levels) in the vertical. The monthly mean is calculated on every 6 hours model output. The ERA40 re-analysis (Uppala et al., 2005) covers the period September 1957 to August 2002 and has a horizontal resolution T106 which corresponds $1.125\ ^\circ \times 1.125\ ^\circ$ ($\approx$ 125 *km*). Vertical resolution is 60 vertical levels (23 standard pressure levels). Compared to the use of satellite retrievals by the NCEP series of re-analyses, satellite radiances are assimilated into the ERA40. The ERA40 represents the presatellite era better than the NCEP (Bromwich and Fogt, 2004). Marshall and Harangozo (2000) and Hines et al. (2000) found that in the NCEP data, there were large erroneous biases in the winter mean sea level pressure and in the 500 *hPa* geopotential height fields over the Southern Ocean and near Antarctica. These errors were related to the re-analysis assimilation schemes in data-sparse regions. Operational data such as the ERA40 re-analysis data have been provided by the ECMWF. The ERA40 is a result of a 3D-Var data assimilation system being applied to past observational data. Those observations include satellite data, radiosonde data, etc. Some of the Antarctic data were included in the ERA40. For example: Antarctic surface data (1947 to 2006) from the British Antarctic Survey, Australian Antarctic surface and radiosonde data (1947 to 2006) from the Australian Bureau of Meteorology and automatic Antarctic stations from Wisconsin University (1980 to 2006), (http://www.ecmwf.int/research/era). The NCEP and ERA40 re-analysis data for the 1958 to 1998 period were used for validation of the HIRHAM model. Additionally, operational data (OD) from ECMWF were used in the model validation. The spectral resolution used here is T106, which approximately corresponds a horizontal resolution of 125 *km*. The OD are available from October 1998 to the present. The current operational model has 60 model levels which are converted to 21 pressure levels. The monthly means for the period January 2000 to December 2001 were used for the investigation.

4.2 Radiosonde data

The Antarctic stations can be classified into two types: manned and unmanned stations. Manned stations usually provide more accurate data than unmanned stations do. This is in the former, the attention needed for the proper maintenance of instruments in polar environments is afforded and the sensors are calibrated on a regular basis. The unmanned stations, usually called the automatic weather stations (AWS), have been used to supplement the small number of manned stations and to obtain a better general overview of the continent (Stearns and Wendler, 1988). The station observations (both surface and upper air) for Antarctica were obtained from the British Antarctic Survey (BAS) READER (Reference Antarctic Data for Environmental Research) project website (http://www.antarctica.ac.uk/met/READER/). The dataset includes the long-term-operated stations around the Antarctic continent, (Turner et al., 2004). Temperature, mean sea level pressure, station level pressure and 10 *m* wind are the primary data included in the READER database. Using 6-hourly surface data, the monthly means were recomputed from the synoptic reports. To be included in the READER project the surface station observations must extend for at least twenty-five years. AWS were also included in the READER project. In this work, monthly mean data from 14 stations were used for the model validation:

the names and locations can be found in Tab. 3.2. The vertical profiles of the wind speed from Neumayer station, (Alfred Wegener Institute for Polar and Marine Research, Bremerhaven) were used for the model validation. Vaisala radiosondes were launched at Neumayer station during the period 1991 - 1998. In addition to wind speed and direction, the radiosondes measure profiles of temperature and relative humidity, as a function of pressure. For the Vaisala radiosondes, Vaisala reports that the temperatures are accurate to 0.1 to 0.2 K. The relative humidity values with respect to water are accurate to ± 3 %.

4.3 AVHRR data

Satellite thermal infrared data provide relatively accurate surface temperatures because the infrared emissivities of most of the Antarctic's surfaces are spatially uniform and close to unity. However, since infrared radiation is sensitive to clouds, surface measurements can only be derived during cloud-free conditions. In the processing of Antarctic data, a special cloud-masking technique had to be utilised because snow-covered surfaces and clouds have similar infrared signatures. The Advanced Very High Resolution Radiometer (AVHRR) data have been evaluated by Comiso (2000). The dataset provides detailed information about the distribution of surface temperature and has been successfully used to identify cooling trends in Antarctica (Comiso, 2000). These were recently confirmed by studies using $in-situ$ data (Doran et al., 2002). The National Oceanic and Atmospheric Administration (NOAA) AVHRR aboard satellites is a cross track scanner operating at the following wavelengths: 0.58 - 0.68 mm (channel 1), 0.73 - 1.1 mm (channel 2), 3.5 - 3.9 mm. The monthly temperature mean data are available for the time period August 1981 to December 2004. These data are gridded with a horizontal resolution of 12.5 km. The data were received via personal communication from J. Comiso (Cryospheric Sciences Branch, NASA Goddard Space Flight Center, Greenbelt, MD). To compare the model simulations to the AVHRR data, the satellite data were interpolated to the HIRHAM horizontal grid.

4.4 Total water vapour data

Melsheimer and Heygster (2005) pursued research into the retrieval of advanced data products derived from polar-orbiting meteorological satellites for enhanced moisture analyses and subsequent numerical climate simulations. Melsheimer and a group of scientists at the University of Bremen are evaluating the utility of high resolution and, satellite-derived moisture data in numerical weather prediction models. Total water vapour retrieved from the AMSU-B (Advanced Microwave Sounding Unit B) sensor on NOAA's (National Oceanic and Atmospheric Administration) new generation polar orbiting satellites, NOAA-15, NOAA-16 and NOAA-17 might also be used with regional models for water cycle investigations. Modern computer technology developed in the last decade now makes it feasible to fully utilise the volumes of remotely sensed data collected from meteorological satellite systems in operational and, mesoscale forecast models. Along with global coverage, low earth orbiting satellites have the advantage of being able to carry microwave instruments. Retrieval in the microwave spectral region is critical in obtaining the vertical structure of atmospheric temperature and water vapour. The frequencies and numbering of the AMSU-B channels are shown in the following table Tab. 4.1.

AMSU-B	16	17	18	19	20
Frequency [GHz]	89	150	183.3 ±1	183.3±3	183.3±7

Table 4.1: *AMSU-B channels and frequencies*

The basic idea (Miao et al., 2001) is to use three channels where the surface emissivity is similar but the water vapour absorption is different, such as the three AMSU-B channels centered on the 183.3 GHz water vapour line (Tab. 4.1). The retrieval algorithm has a limitation (personal communication with Melsheimer C.). Because of channel saturation, if the TWV is larger than 6 kg/m^2 the algorithm cannot determine TWV from AMSU data. The actual limit depends weakly on the temperature and humidity profile. For the years 1999 to 2003, the retrieved data for the Arctic region was successfully validated against the NCEP re-analysis. The monthly means of the total water vapour fields for the Antarctic region are available for the year 2000. The horizontal resolution is 0.5×0.5 ° latitude-longitude grid. For precise intercomparison, the TWV data were regridded to the HIRHAM grid.

Chapter 5

Model validation

Often the numerical models simulating the climate state contain biases compared to the observations. The performance of one model differs from the other in space and time. The discrepancy may arise from different parameterisations of physical processes, different initial and boundary conditions and different numerical schemes. To evaluate the quality of the HIRHAM model simulation different gridded datasets, observation station and remote sensing data were used. The Antarctic is a data-poor region. Due to the sparse observational network in the Antarctic, the spatial interpolation of the observed data may contain biases or smooth out the local profiles. Furthermore, the Antarctic's observation stations hold only a limited number of directly measured climate variables. While comparing a model simulation with station measurements, station data may not be representative of that area, which is resolved in the model by 50 $\times$50 *km* grid box. The model evaluation is a very important step and should be done before proceeding with other model applications. The vertical and horizontal structures of the main meteorological parameters were checked out. To make the conclusions from the just mentioned calculations more precise, the root-mean-square error and correlation coefficient were also calculated. The first HIRHAM model run for the Antarctic integration area was carried out with 19 vertical levels in the atmosphere. After a successful 1 year run with this version of the HIRHAM model, in order to start the long-term climate run (1958 - 1998) we introduced the version of the HIRHAM model with 25 vertical levels. The vertical resolution was increased from 19 to 25 levels to better represent the processes in the planetary boundary layer. Thus, the model's lowest level was located at 12 *m* above the ground. For all of the model simulations, the HIRHAM's staggered "Arakawa *C*" horizontal grid was set to a resolution of 50 *km*. The pressure at the model top was set to 10 *hPa*. The 40 years (1958 - 1998) HIRHAM simulation has been performed. The model was initialized and forced at the lateral and lower boundaries with European Center for Medium-Range Weather Forecasts (ECMWF) ERA40 re-analysis. The ERA40 data have a horizontal resolution of $1.125\ ^\circ \times 1.125\ ^\circ$ ($\approx$ 125 *km*). The input data were transferred to the model's area by using a boundary relaxation procedure within the 10 outermost points.

In the following parts of this chapter, the climate of Antarctica will be described through a discussion of the key meteorological parameters in the region.

5.1 Mean sea level pressure

Averaged over a period of 40 years, Fig. 5.1 and Fig. 5.2 show the seasonal structure of the Antartic mean sea level pressure (MSLP) during summer and winter. South of the subtropical high, the mean pressure drops steeply to its lowest values in the circumpolar trough between 60 °S and 70 °S. There are three low pressure systems, whose positions do not change too much with the seasons. Climatologically, these minima include the Amundsen Sea Low, a low in the eastern Weddell Sea, and in the longitudes of Wilkes and Adélie Lands (over the Ross Sea), as visible in HIRHAM simulation (middle) in Fig. 5.2. Scientists have studied the regional influences on cyclones in high latitudes. For example, Carrasco and Bromwich (1993) have examined the frequent mesoscale cyclones over the Ross Sea. They found that cyclogenesis is associated with both local baroclinic zones and the intensity of the katabatic wind that blows from Terra Nova Bay. The circumpolar trough is a dominant characteristic of the large-scale weather pattern over the southern hemisphere. The averaged sea level pressure patterns show a pronounced zonal structure (e.g. HIRHAM simulation in Fig. 5.1). A comparison of the simulated pressure patterns with ERA40 re-analysis for the austral summer, presented in Fig. 5.1 shows that the simulations are in good agreement with the observed pressure patterns. The difference between re-analysis and HIRHAM simulation or ”bias” is defined as ”ERA40 minus HIRHAM simulations”. The largest difference reaches 7 *hPa* (Fig. 5.1, right) and it appears over the Eastern part of the Antarctica. During the austral summer HIRHAM overestimates MSLP in the internal part of the continent, but in the coastal area and over the Southern Ocean the difference ”ERA40-HIRHAM” is within ± 2 *hPa*. The difference over the Ross Ice Shelf and Ronne Ice Shelf appears due to the varying representation of the land-sea mask in the HIRHAM model and the ERA40 re-analysis.

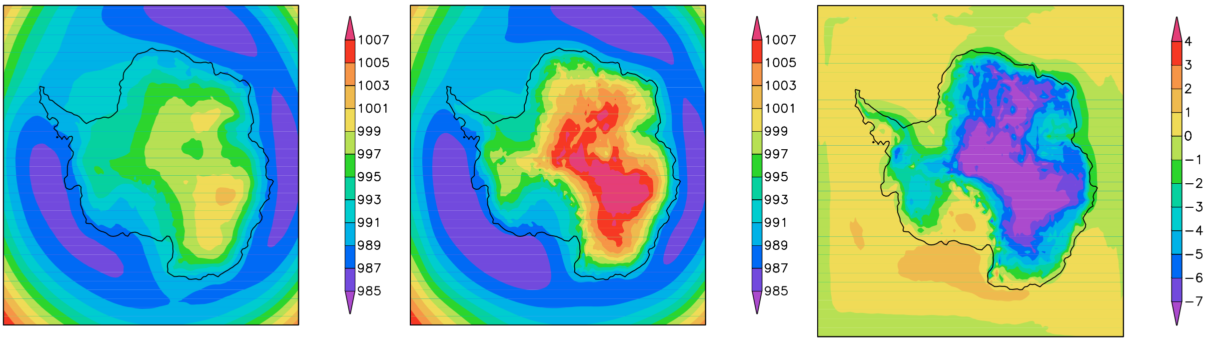

Figure 5.1: *Mean sea level pressure (hPa) in austral summer (DJF), for the period 1958-1998. ERA40 (left), HIRHAM (middle), difference ”ERA40 minus HIRHAM” (right).*

Fig. 5.2 shows that during the austral winter (JJA) the stronger anticyclone appears over the continent. It's maximum value is more than 1015 *hPa*. The main difference between the simulation and the re-analysis occurs over the highest part of the continent. This bias exists throughout the period that the long-term simulation covers, thus suggesting that the representation of small-scale features may be the source of a systematic bias between the re-analyses and the HIRHAM model. The HIRHAM simulated MSLP horizontal structure is in a good agreement with re-analysis and the difference decreases from 7 *hPa* to 4 *hPa*, relative to the summer period. During the winter season sea-ice extend is doubled in size, therefore no difference can be observed over the Ross and Ronne Ice Shelves. We calculated the standard deviation (SD) for the main meteorological parameters according Eq. A.1 (Appendix A) for the ERA40 data and the HIRHAM simulation. This was done to monitor the location of maxima and minima changes in MSLP. Hereafter, the *rmse* index was used to show how consistent agreement between observational data and the data from the model simulation. The SD term is used to show how to spread the data from the mean value within one array of data, such as is the case in the HIRHAM's simulation or in the ERA40. The SD of the sea level pressure's field can be used as an indicator of synoptic activity. High SDs are associated with large pressure anomalies caused, for example, by the passage of cyclones. During both the austral summer and winter, strong changes, from 4 to 6 *hPa*, in the MSLP occurred in the Bellingshausen, Amundsen and part of the Ross Sea sector. Over the continent, changes in the MSLP were smaller and ranged between 3 to 4 *hPa*. These maxima and minima correspond to the permanent low pressure systems in circumpolar vortices and anticyclones over the continent which can be observed over the entire year.

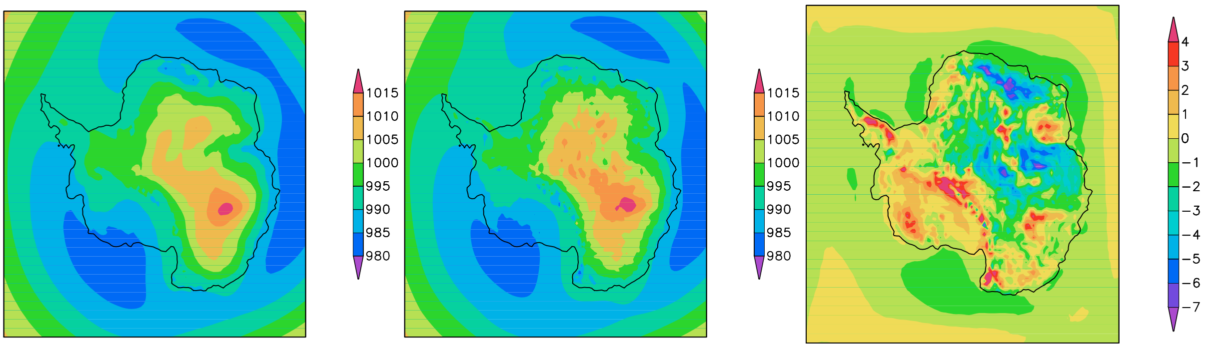

Figure 5.2: *Mean sea level pressure(hPa) in austral winter (JJA), for the period 1958-1998. ERA40 (left), HIRHAM (middle), difference "ERA40 minus HIRHAM" (right).*

Further comparisons were made between the model output and the observation station data. For a precise confrontation, the model output was linearly interpolated to the station location. The topography of the Antarctic continent is mainly responsible for the variety of regional climates that can be found. For this investigation, we chose 9 stations spread out around the continent and that held available data. Based on locations and similar regional features (e.g. high plateau stations, coastal stations), the stations were divided into two groups. Descriptions and detailed analyses of weather in the coastal regions of Antarctica are important not only for considering local characteristics but also for understanding the large scale circulation over Antarctica. Also, two short runs were carried out to test the model output depending on the boundary data. The first run, covering the period January 1997 - August 2002, HIRHAM was driven by ERA40. The second run, covering the period July 1999 - April 2005, HIRHAM was driven by Operational Data (OD, ECMWF). 2000 and 2001 are the only overlapping years. Fig. 5.3 - Fig. 5.6 present the intercomparison for those years. Meanwhile, the stations' locations and elevations are shown in Tab. 3.2. The annual oscillations of MSLP for Novolazarevskaya and Syowa station are shown in Fig. 5.3. A gap in the black line indicates that the data are missing during some months (e.g. Novolazarevskaya station from December 2000 to May 2001). For both stations, the simulation data reveal annual variations in the atmospheric pressure similar to the other Antarctic coastal stations. A strong variability between 980 *hPa* and 998 *hPa* occurs during the year, with two minima in April and October.

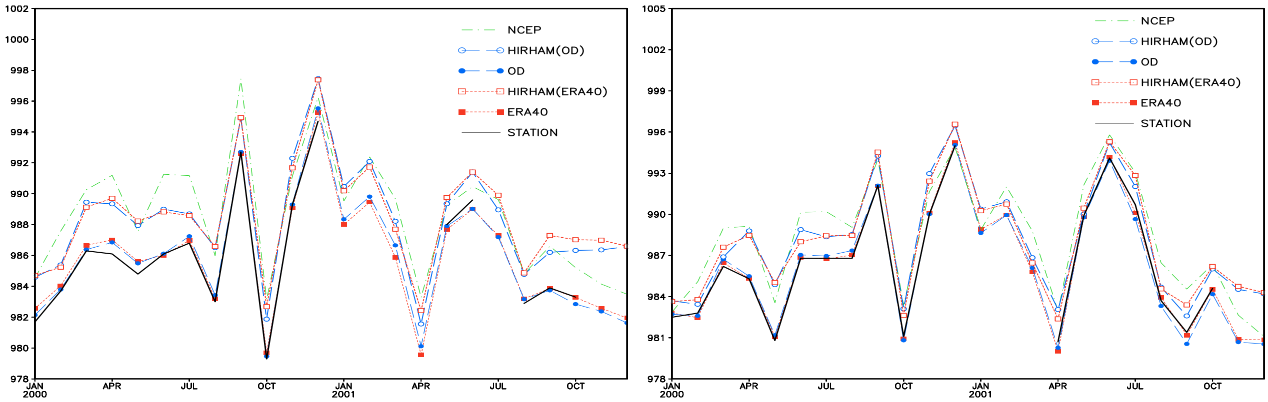

Figure 5.3: *MSLP (hPa) in 2000 - 2001, NCEP, HIRHAM(OD) - (HIRHAM driven by Operational Data), OD - Operational Data), HIRHAM(ERA40) - (HIRHAM driven by ERA40), ERA40, station data. Novolazarevskaya (left) and Syowa (right) station. Y-axis – pressure levels (hPa).*

As ECMWF products assimilate surface pressure from the Antarctic stations, we should expect a good agreement between ERA40, OD and the station data. NCEP has a bigger bias relative to observational data. HIRHAM overestimates MSLP by 4 *hPa*, this is within the acceptable range for the regional climate model, as presented in Fig. 5.3. The disparity in MSLP can be related to the differences between the model's and the real stations' elevation. Mirny station is situated on the coast of Cape Davis and Casey station is on the coast of Wilkes Land (East Antarctica). The annual MSLP cycle for both stations is shown in Fig. 5.4. The wind and weather regimes at the Casey are strongly modified by the close proximity of Law Dome. Both stations show the sudden change in MSLP during austral summer December 2000 - February 2001. The amplitude of such a "jump" was 7 *hPa* and 8 *hPa* for Casey and Mirny station, respectively. Both the re-analysis and the HIRHAM simulation captured this jump very well. The similarity in the annual oscillation, as explained above, proves that there is a strong relationship

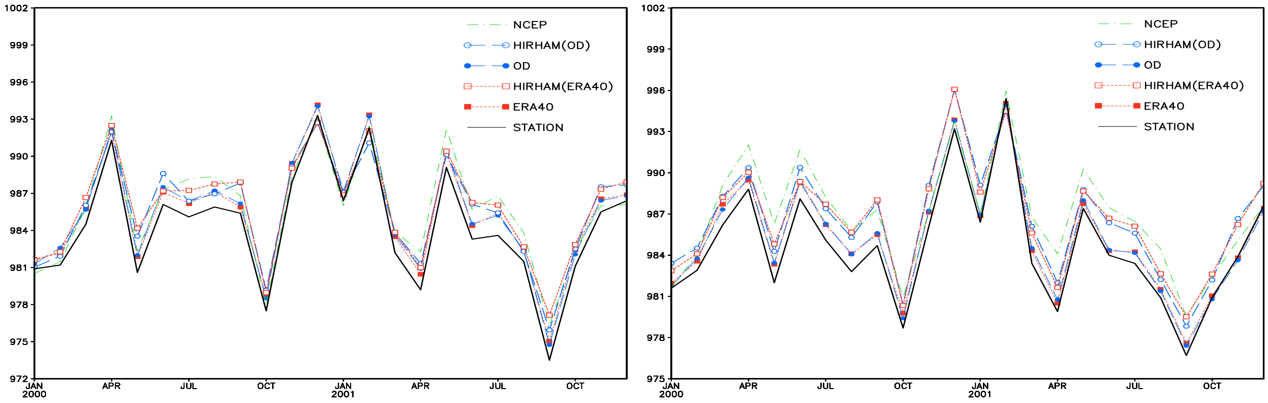

Figure 5.4: *As in Fig. 5.3 but for Casey (left) and Mirny (right).*

between an anomaly in MSLP and the station location.

Dumont-Durville station is located on Adélie Land, a well-known place for strong katabatic wind. Observations showed that the principal triggering factor for katabatic storms is the passage of a depression in the area (Wendler et al., 1993). The depressions generally move from the west around the Antarctic creating in the coastal area a pressure gradient that induces the katabatic wind. Therefore, the proper simulation of the katabatic wind is very essential for the climate simulation for Antarctic continent. Fig. 5.5 shows a graph of the MSLP for McMurdo and Dumont-Durville stations. For October, 2000 both stations show the deep minimum in MSLP. The re-analyses and HIRHAM simulation show the good agreement in MSLP with observational data. By following the annual cycle, as indicated in Fig. 5.5 (left), one can conclude that relative to the stations' values, HIRHAM slightly overestimates the MSLP while the driving data (ERA40) slightly underestimate it.

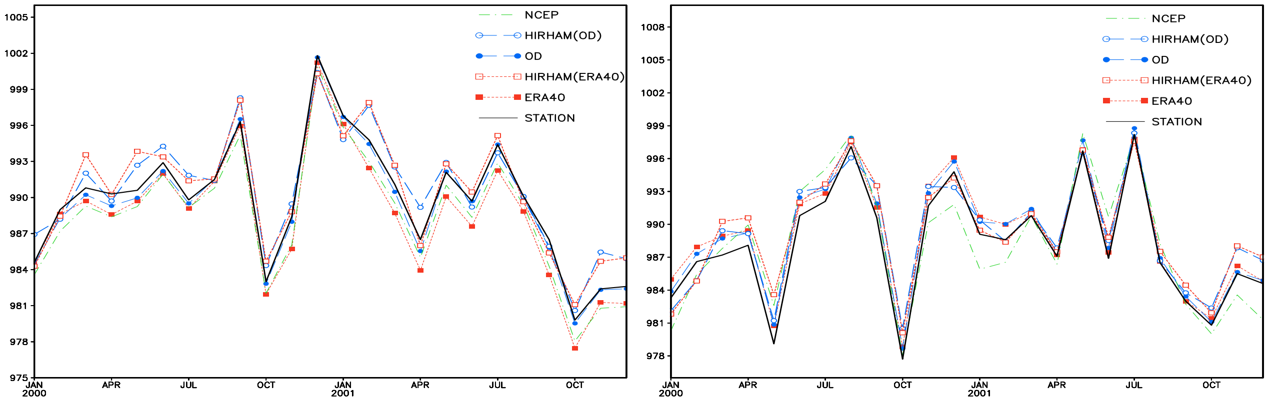

Figure 5.5: *As in Fig. 5.3 but for McMurdo (left) and Dumont-Durville (right).*

Halley Station is situated on the Brunt Ice Shelf. In general, the weather at the Halley is controlled by large synoptic scale systems that form in the circumpolar trough. These track south into the Weddell Sea or the lee lows, which form on the east side of the Peninsula, and then move slowly across the Weddell Sea. Neumayer station is situated on the Ekström Ice Shelf.

During the summer season, the weather is dominated by low pressure systems that move across the northern Weddell Sea from the Antarctic Peninsula. These low pressure systems move in an easterly direction and last between two to seven days. The simulated MSLP patterns, as shown in Fig. 5.6, are in agreement with the stations observation. With the exception of the results at the Halley station in September, 2000, where the difference between the model simulation and station data reached 6 *hPa*, the difference between the simulated MSLP and the station observations lies within ± 2 *hPa*. Accepting this jump the model simulation is in agreement with both the re-analyses and the station data.

Unfortunately, only two manned inland stations provide data. The data from these stations were used for the model evaluation that took place over the central part of Antarctica (the rest of the stations were located in the coastal zones). The Amundsen-Scott and Vostok stations are situated over 2000 *m* above sea level. The Amundsen-Scott station is dominated by the plateau high and it experiences periodical influences of modified maritime air from the Bellingshausen Sea and, the Weddell Sea. Furthermore, on rare occasions, the Amundsen-Scott station also experiences residual moisture from the Atlantic Ocean via the Dronning Maud Land. Thus, the South Pole and Vostok stations are representative of continental stations and, the Halley and Casey stations are typical of coastal Antarctic stations (which are more exposed to low level easterly's than to the westerly's that the Bellingshausen station so often experiences (Turner and Pendlebury, 2004). Surface pressure from both stations is shown in Fig. 5.7. Due to high station elevation, only surface pressure has been recorded.

The surface data were not available for NCEP, ERA40 and OD data, so hereafter only observations and HIRHAM simulated surface pressure are presented. The month-to-month simulated pattern looks similar to the station data. However, for the Amundsen-Scott station data the monthly mean difference is high. One explanation for this is the difference in elevation between the model' and the real station. The Amundsen-Scott station elevation in the model is 2665 *m*, which is about 215 *m* below the real value. For Vostok station the difference is 115 *m*. Taking into account the dry adiabatic lapse-rate (since the atmosphere is mostly unsaturated

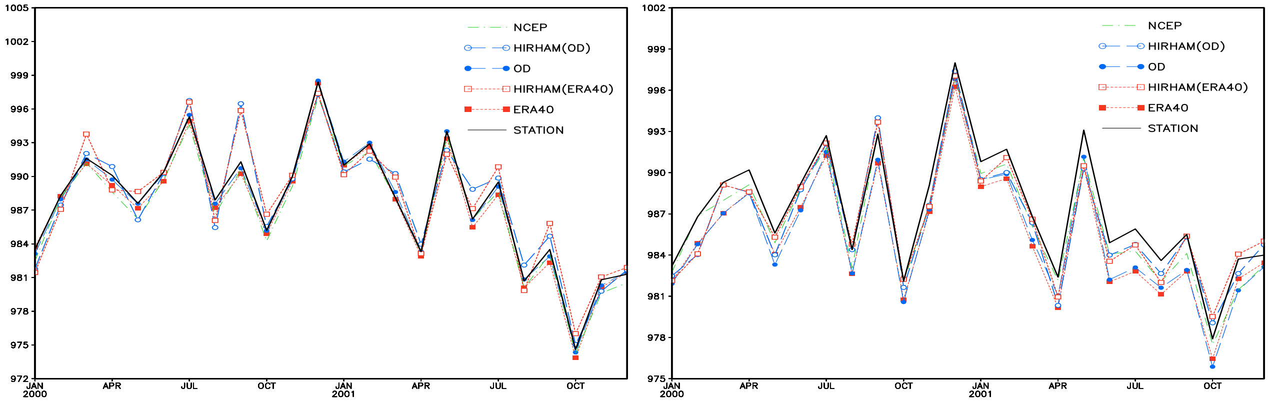

Figure 5.6: *As in Fig. 5.3 but for Halley (left) and Neumayer (right).*

over the Antarctic Plateau) the difference between the station and model elevation was recalculated in terms of pressure and this corresponds 12 *hPa* and 6 *hPa* for Amundsen-Scott and Vostok station, respectively. Thus, the model results agree reasonably well with the station data.

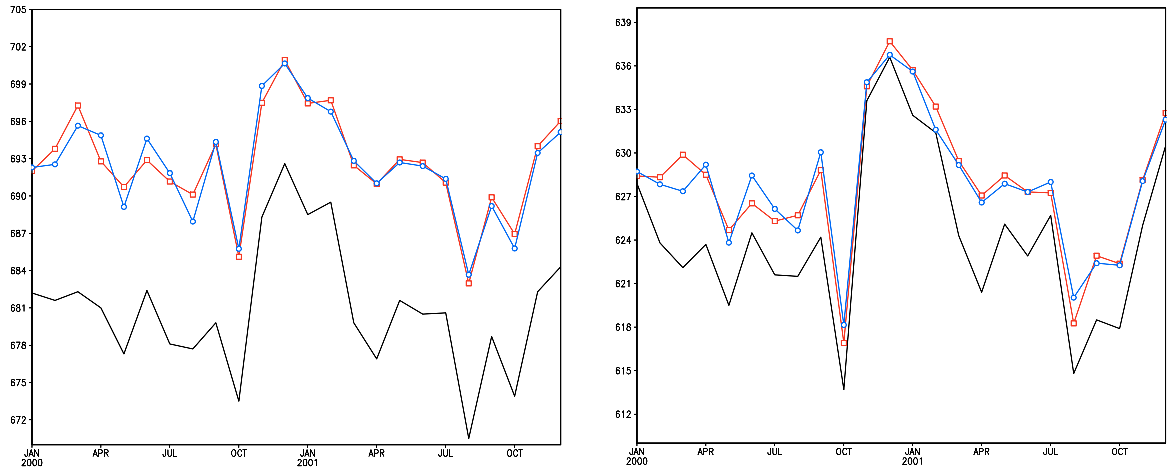

Figure 5.7: *Surface pressure (hPa) for Amundsen-Scott (left) and Vostok (right), HIRHAM(ERA40) (red), HIRHAM(OD) (blue), station data (black). Y-axis – pressure levels (hPa).*

Statistics from monthly averaged model output, re-analyses and station data for the MSLP fields were examined. In each case, the correlation coefficient, bias, and *rmse* are calculated from the station observations and the values of both, the model and the re-analyses. In the following equation, bias refers to the "long-term mean observed value *minus* the long-term mean HIRHAM (or re-analysis)".

$$bias = \bar{X}_{STATION} - \bar{X}_{HIRHAM;ERA40;NCEP} \tag{5.1}$$

(where X is pressure, temperature, etc.) The root-mean-square (*rmse*) error has been calculated to characterize the spread and the consistency among the model's simulation (re-analyses) and observational data. A small *rmse* value, along with a small bias, indicates an agreement amongst the model (re-analyses) data and the observational data, it also shows that they capture the processes that govern the variable. A large *rmse* value indicates in the simulation a disagreement with the observational data as well as showing that it is unreliable. The *rmse* was calculated as :

$$rmse = \sqrt{\frac{\sum_{k=1}^{N}(X_k - Y_k)^2}{N}} \tag{5.2}$$

and the correlation index:

$$r(X,Y) = \frac{\sum_{k=1}^{N}(X_k - \bar{X}) * (Y_k - \bar{Y})}{\sqrt{\sum_{k=1}^{N}(X_k - \bar{X})^2 * \sum_{k=1}^{N}(Y_k - \bar{Y})^2}} \tag{5.3}$$

where X_k is simulated pressure (2 m temperature, 500 hPa geopotential height, etc.), $\bar{X}$ is the mean value (calculated over the given period), Y_k is station pressure (2 m temperature, etc.), $\bar{Y}$ is the observed mean value and N is the month number included in statistical calculations. Many intercomparisons between different re-analyses have already been done. For example, Bromwich and Fogt (2004) used the ERA40 and the NCEP re-analyses. Their results showed that compared to the NCEP, the ERA40 follows observation more closely. However, a more detailed look at the presatellite era (before 1979's) reveals many shortcomings in the ERA40, particularly in the austral winter. Bromwich and Fogt (2004) investigated the period between 1958 to 1998.

Mean sea level pressure 1981 - 1998									
	BIAS			RMSE			CORRELATION		
	I	II	III	I	II	III	I	II	III
Bellingshausen	-0.53	-0.76	0.04	1.2	1.46	0.41	0.98	0.97	0.99
Casey	-1.63	-1.12	-3.51	1.95	2.54	5.38	0.98	0.91	0.76
Davis	-0.92	0.04	-0.88	1.2	2.06	2.38	0.98	0.91	0.9
Dumont-Durville	-1.32	-0.74	-1.62	2.01	2.44	3.86	0.96	0.91	0.82
Halley	0.32	0.47	0.12	1.77	2.35	1.75	0.94	0.9	0.94
Mawson	-2.21	-0.89	-3.02	2.52	1.98	4.28	0.97	0.93	0.85
Mirny	-1.85	-0.54	-1.81	2.01	2.21	3.82	0.98	0.91	0.81
Molodezhnaya	-2.42	-0.33	-0.97	2.62	1.76	1.95	0.97	0.93	0.93
Neumayer	-0.82	-0.26	-0.7	2.00	2.66	2.51	0.93	0.86	0.88
Novolazarevskaya	-1.78	-0.19	-2.23	2.07	2.11	3.32	0.98	0.9	0.87
Syowa	-1.32	0.04	-0.56	1.69	1.8	1.83	0.97	0.93	0.93
AVERAGE	-1.32	-0.39	-1.38	1.91	2.12	2.86	0.97	0.91	0.88

Table 5.1: *Statistical measures of mean sea level pressure (hPa) , I - HIRHAM, II - ERA40, III - NCEP.*

In our study, statistical calculations were carried out for a shorter period, in such way that the data from a maximum number of stations were available. Statistics were calculated for 11 stations and listed in Tab. 5.1. The Amundsen-Scott station was not included in the calculations since it lies well above sea level and therefore doesn't record MSLP. Statistics cover an 18 year period for all stations. The results show that the HIRHAM overestimates MSLP (except Halley stations), and that is in agreement with a 2 year annual patterns for the years 2000 and 2001 in Fig. 5.3 - Fig. 5.7. *Rmse* values show that the monthly mean values from the model simulation and the observational data are quite close to each other. The correlation index is sufficiently high for all datasets, but HIRHAM has the highest one 0.97. The NCEP correlation index is a bit lower but nonetheless, it is in agreement with Bromwich and Fogt (2004). An agreement between horizontal patterns, year-to-year variability in conjunction with high correlation index between the simulated MSLP and the observational data (or re-analysis) proves that the HIRHAM model simulates MSLP with sufficient accuracy.

5.2 Geopotential height

The Antarctic continent has a very high elevation above the sea level. 500 *hPa* standard isobaric level is the first level which lies everywhere above the continent. The continent's radiative cooling and katabatic winds are partly responsible for a pronounced circumpolar vortex developing in the middle and upper troposphere. The close coupling of the upper tropospheric circulations with the Antarctic terrain implies a significant scale interaction occurs in the higher southern latitudes. The shallow continental scale drainage flow appears to be essential in prescribing large scale circulations. Formulation of the energy exchanges between the Antarctic continent and the overlying atmosphere including a depiction of the katabatic wind regime is very important in the climate model in order to properly simulate the large-scale tropospheric circulations in the southern hemisphere. The attendant meridional mass transport provided by the katabatic wind regime may form a significant component of the heat flux in the lower atmosphere and thereby help alleviate the intense baroclinicity in the coastal periphery of the continent (Parish and Bromwich, 1991).

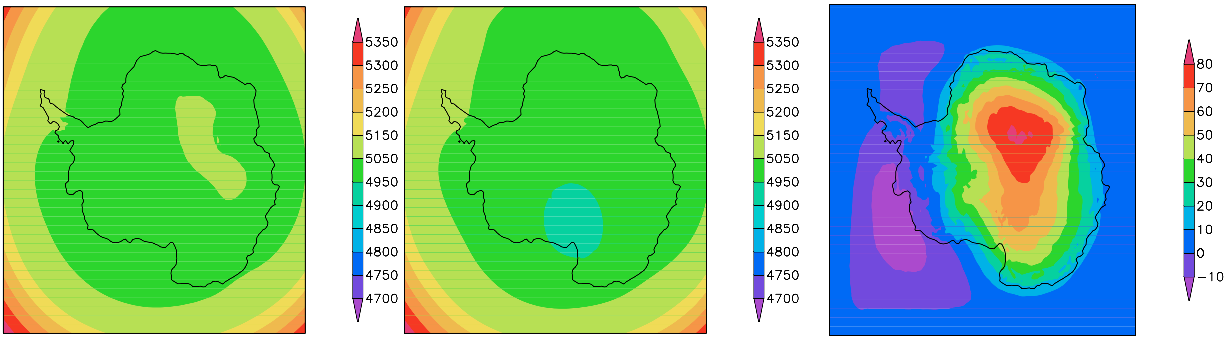

Figure 5.8: *500 hPa geopotential height (gpm) in austral summer (DJF), for the period 1958 - 1998. ERA40 (left), HIRHAM (middle), difference "ERA40 minus HIRHAM", (right).*

The summer and winter mean 500 *hPa* geopotential height fields are shown in Fig. 5.8 and Fig. 5.9, respectively. During the austral summer the HIRHAM's 500 *hPa* level represents a uniform pattern with a shifting minimum toward the Ross Ice Shelf, whereas the ERA40 data have one maximum over the Antarctic plateau. During summer, the HIRHAM shows stronger anticyclonic circulations over the continent. This difference can be noticed through all of the tropospheric levels. Generally the agreement with re-analysis is slightly better for Western Antarctica than what it is for Eastern Antarctica. During winter, the geopotential height simulated by HIRHAM is in a better state of agreement with the ERA40 data. The minimum of 500 *hPa* height is located at about 4800 *m* and it is shifted from the central part of the continent to the coastal area. Pohlmann and Greatbatch (2006) found the difference for 500 *hPa* level between NCEP and ERA40 re-analysis about 30 *gpm* during the winter and summer seasons. Bromwich and Fogt (2004) show the negative correlation for 500 *hPa* standard isobaric level between station data and ERA40 re-analysis. The biggest difference was observed in presatellite era, and the better agreement was found after 1979. Taking this into account, we can expect that the HIRHAM already has an artificial bias introduced by the driving data. The difference between the HIRHAM simulation and the ERA40 reveals a wavenumber 1 pattern. It evidences that the biggest difference occurs on a planetary scale.

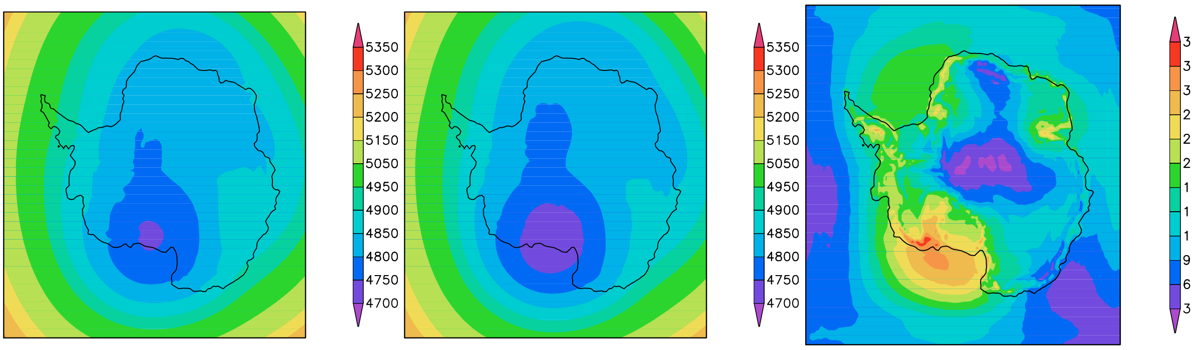

Figure 5.9: *500 hPa geopotential height (gpm) in austral winter (JJA), for the period 1958 - 1998. ERA40 (left), HIRHAM (middle), difference "ERA40 minus HIRHAM", (right).*

The main statistical indices for 500 *hPa* height were calculated for a precise intercomparison between the HIRHAM simulation, the re-analyses data and observational data and shown in Tab. 5.2. Appendix A, Fig. A.2 shows the horizontal structure of SD. The maximum SD can be observed over the Pacific Ocean with 50 *gpm* during the summer and with 70 *gpm* during the winter. For the austral summer, the minima SD, 20 *gpm*, is located along the Antarctic

500 *hPa* geopotential height, 1983 - 1998									
	BIAS			RMSE			CORRELATION		
	I	II	III	I	II	III	I	II	III
Amundsen-Scott	15.68	-9.44	22.13	42,14	53,27	39,07	0.91	0.87	0.95
Casey	9.28	-5.56	-2.62	15,73	37,14	23,66	0.99	0.92	0.96
Davis	2.70	-13.79	-5.49	18,67	43,9	20,38	0.97	0.9	0.98
Dumont-Durville	14.19	0.53	20.04	36,12	37,25	36,37	0.94	0.91	0.95
Halley	14.29	3.93	12.04	26,17	34,14	22,46	0.95	0.91	0.98
Mawson	1.9	-15.2	-1.62	18,01	38,21	21,47	0.98	0.92	0.97
McMurdo	38.11	5.57	26.24	56,87	62,34	50,52	0.88	0.82	0.93
Mirny	10.69	-2.63	2.43	19,31	39,16	22,03	0.98	0.9	0.97
Molodezhnaya	12.21	-4.39	2.94	17,4	38,79	11,87	0.98	0.95	0.99
Neumayer	13.27	1.93	14.09	23,61	32,09	23,03	0.97	0.91	0.98
Novolazarevskaya	18.23	3.4	24.43	43,14	57,64	50	0.89	0.85	0.9
Syowa	7.04	-10.03	5.19	18,98	35,63	17,33	0.98	0.93	0.98
Vostok	22.09	-2.88	40.98	28,78	44,98	17,34	0.96	0.9	0.99
AVERAGE	13.82	-3.73	12.37	28.07	42.66	27.35	0.95	0.89	0.96

Table 5.2: *Statistical measures of 500 hPa height (gpm), I - HIRHAM, II - ERA40, III - NCEP.*

Peninsula and in Indian Ocean's western sector. During the winter season, SD minimum values can be found along the eastern coast. As previously mentioned, for the MSLP, smaller values in *bias* along with smaller *rmse* show a better agreement between the two datasets. For all stations, the HIRHAM model underestimates the height of the 500 *hPa* level. This is in agreement with the MSLP as shown in Tab. 5.1. Consequently, a stronger anticyclone over the continent can be observed in the model simulation. Higher correlation indices show a good agreement between the real data and the model simulation. Apparently, the increasing horizontal resolution relative to the driving data, improves the representation at the surface level as well as in processes attendant to higher levels. The higher correlation index supports this with 0.95 and 0.89 for HIRHAM and ERA40, respectively.

5.3 Air temperature

The Antarctic continent is one of the coldest places on our planet. Low temperatures in the Antarctic's interior are caused by a combination of different factors: high elevation, high latitude, high surface albedo and consequently a negative radiation budget which forces a strong surface-based temperature inversion. During winter, in the central part of the continent, the surface temperature can reach -70 $^\circ C$.

For the years 1958 to 1998 and also, for the austral summer season (DJF), the horizontal pattern of 2 m temperature was averaged. The results are shown in Fig. 5.10. While, the main structure between both of the datasets looks similar, during the austral summer the HIRHAM model is much colder than the ERA40. Over the Antarctic plateau, the minimum value for the HIRHAM simulation is -50 $^\circ C$; over the unfrozen parts of the Southern Ocean, the maximum value is approximately 5 $^\circ C$. Over the coastal areas the differences lie within the range $\pm$ 4 $^\circ C$. Over Eastern Antarctica, the highest part of the continent, HIRHAM is by 12 $^\circ C$ colder than what the re-analysis showed. The results for the bias derive from either a radiation deficit or a cloud cover overestimation. The HIRHAM model overestimates the cloud cover that occurs over the inner part of continent during the austral summer (this will be shown later in Fig. 5.33). Hence, smaller amount of solar radiation can reach the surface, and warm it up. Over the inner part of the continent, the radiation cooling (as a consequence of cloud cover overestimation), may be the reason for the MSLP overestimation in the HIRHAM simulations. During the winter season, the role of cloud cover is inversed, effectively keeping the continent warm. Another reason for the surface temperature bias can be connected with overestimation of MSLP as it was shown in Fig. 5.1. The strong and steady anticyclone that moves over the continent partially blocks the influx of relatively warm and humid air that comes from the Southern Ocean.

Over the 40 year period, the winter mean of 2 m temperature was calculated (the results are shown in Fig. 5.11). Apparently, during winter the horizontal structure in the HIRHAM and the ERA40 are in a better agreement than what they are during summer. Over the Eastern

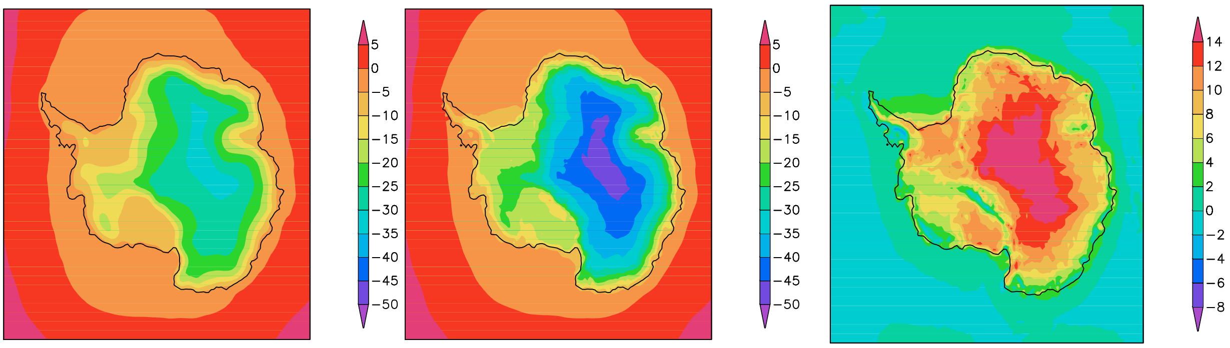

Figure 5.10: *2 m temperature (°C) in austral summer (DJF), averaged for the period 1958-1998. ERA40 (left), HIRHAM (middle), difference "ERA40 minus HIRHAM" (right).*

Antarctica, the difference between the model output and the ERA40 decreased to 4 °*C*. During the winter months, in the inner part of the continent 2 *m* temperature drops down to -60 °*C*. Due to the expansion of the sea-ice cover during winter, areas with a positive temperature are far further away from the coastal line than what they are during the summer season. Thus, during the winter season, the influence of the Southern Ocean on the Antarctic's climate decreases significantly.

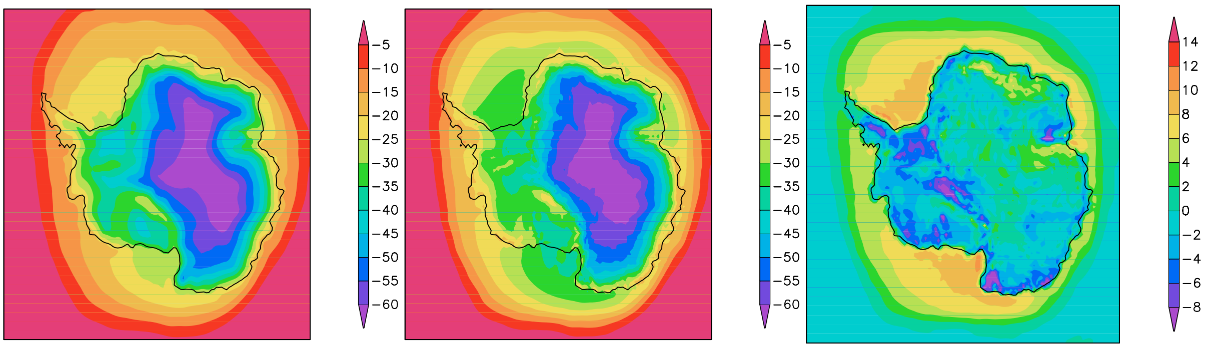

Figure 5.11: *2 m temperature (°C) in austral winter (JJA), for the period 1958-1998. ERA40 (left), HIRHAM (middle), difference "ERA40 minus HIRHAM" (right).*

For 2000 - 2001, the simulated 2 *m* temperature was validated against the NCEP, the ERA40 re-analysis, OD, AVHRR (Advanced Very High Resolution Radiometer) and the observational data. Like how we saw in the MSLP case, the HIRHAM model was driven by OD. It is therefore denoted as HIRHAM(OD). The HIRHAM model that was driven by ERA40 data is denoted as HIRHAM(ERA40). Chapter 4.3 already discussed the horizontal resolution and retrieval algorithm of AVHRR data. Now, it is important to note that the surface temperature retrieved from the AVHRR's data was based on a cloud-free reading. To compare AVHRR, HIRHAM and the other gridded dataset with the observational data, it was first necessary to conduct a linear interpolation to the station's location.

For "year-to-year cycle" validation of the model simulations, we chose 8 coastal and 2 interior stations, and all of these had data available to us (shown in Fig. 5.12 - Fig. 5.16). A gap in the black line indicates that data are missing during some months (e.g. Novolazarevskaya station has some data missing from December, 2000 to May, 2001). Over the two year period, Fig. 5.12 shows duration of 2 m temperature at the Syowa and the Novolazarevskaya stations. These results potentially indicate that the duration of 2 m temperature at the aforementioned stations occurs on an annual basis. The annual cycles for all of the stations reveal that the Antarctic's temperature oscillates dramatically between summer and winter. The continent hits its minimum temperatures from June to September and its maximum temperatures from November to February. The HIRHAM model has a lower surface temperature compared to the driving and observational data. For example, in the summer season the bias is 5 - 7 $^{\circ}C$ while for the the period of the winter season it is only 2 - 4 $^{\circ}C$. At the coastal stations this difference is significantly smaller than in the central part of the continent. Apparently, the model simulates the synoptic scale processes with sufficient accuracy and so enough cyclones can penetrate the continent. The disparity between the AVHRR's data and observational data is connected to the differences between the surface and the 2 m temperature and the "cloud-free case" of an algorithm limitation.

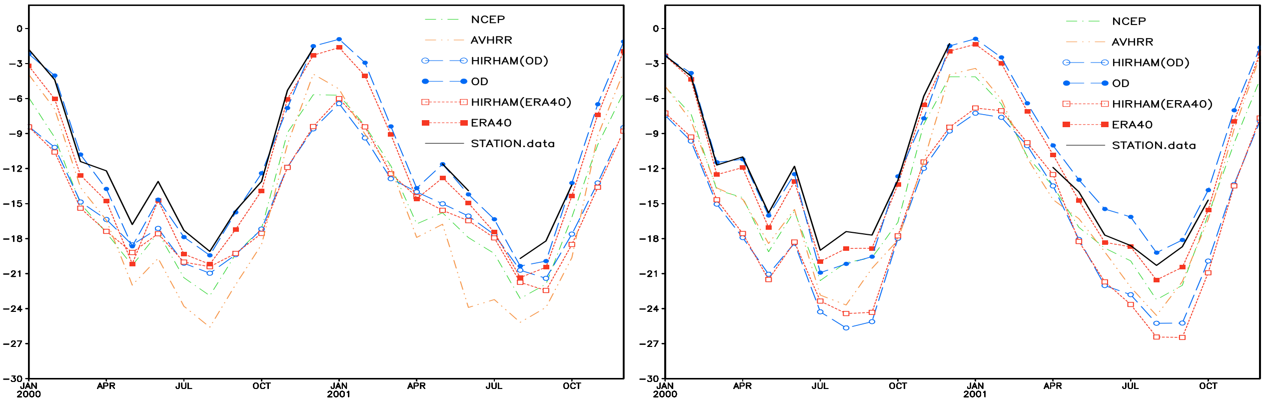

Figure 5.12: *2 m temperature ($^{\circ}C$) in 2000 - 2001, NCEP, AVHRR, HIRHAM(OD) - (HIRHAM driven by Operational Data), OD - Operational Data, HIRHAM(ERA40) - (HIRHAM driven by ERA40), ERA40, station data. Novolazarevskaya (left) and Syowa (right) station. Y-axis – temperature (°C).*

The 2 m temperature for Casey and Mirny is shown in Fig. 5.13. At the Casey station the HIRHAM(ERA40) is very similar to the driving data. However, there is a bigger difference up to 7 $^{\circ}C$ between the HIRHAM(OD) and the operational data. Since it passed additional assimilation procedures, the ERA40 re-analysis closely represents the real data than OD. The errors in OD can appear due to observational problems, or wrongly transmitted information. Looking at Fig. 5.13 during transition seasons, strong temperature gradients in all datasets can be observed; negative, during the austral autumn 15 $^{\circ}C$ and positive, during the austral spring 10 $^{\circ}C$. During the winter and summer, the change in amplitude of 2 m temperature is slightly smaller 5 - 7 $^{\circ}C$. At the Mirny station the difference between HIRHAM (OD) and observational data is smaller than what it is between the observational data and the HIRHAM model that is driven by the ERA40. When compared to the other datasets, the HIRHAM(ERA40) model shows the lowest temperature. On average, the model bias for the summer season is 7 $^{\circ}C$ and 3 $^{\circ}C$ for the winter season. Over a two year course, Fig. 5.14 shows the 2 m temperature experienced at McMurdo and Dumont-Durville stations' for the period January 2000 to December 2001. At the McMurdo station, winter lasted 5 months (May through to September). Dumont-Durville station's winter was 10 $^{\circ}C$ warmer than McMurdo station's winter. The preconditions for these warm winter temperatures are strong winds; due to forced mixing, these limit the intensity of the surface inversion. At the Dumont-Durville station the data show that no systematic trend exists during the winter. Warm and cold spells can occur during any part of the winter. Looking at this disparity, the HIRHAM model at the McMurdo station is almost 8 $^{\circ}C$ colder than the observational and driving data. Similarly, at the Dumont-Durville station, both of the HIRHAM's outputs are warmer than those of the re-analysis. Yet, the HIRHAM outputs are still colder than the observational data. As such, one issues that has come out of this intercomparison is this: the scale of the bias between model simulations and the observational data strongly depends on the station location and hence climate regional features. In contrast to this,

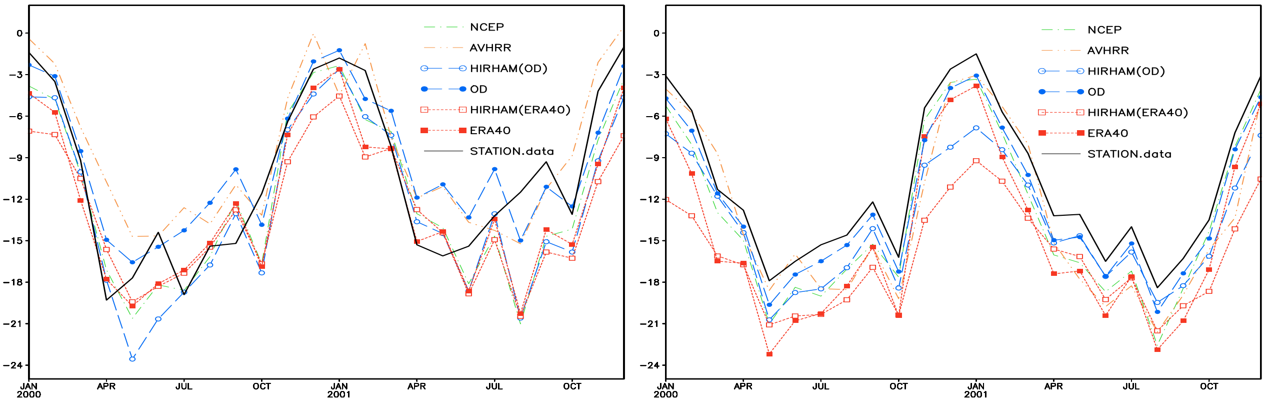

Figure 5.13: *As in Fig. 5.12 but for Casey (left) and Mirny (right) station.*

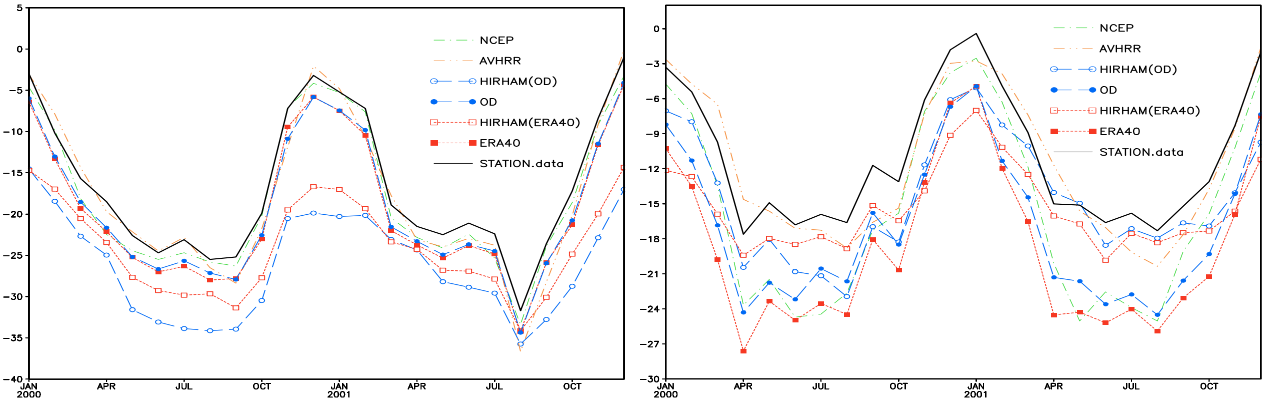

Figure 5.14: *As in Fig. 5.12 but for McMurdo (left) and Dumont-Durville (right) station.*

Fig. 5.15 shows that the observation data is colder than both the re-analyses and the HIRHAM model simulated data, but HIRHAM has the smallest bias of 2 $^\circ C$. The HIRHAM model that is driven by ERA40 data captures small month-to-month oscillations in 2 m temperature (for example, September 2000 or June 2001 at the Halley station). For both stations presented in Fig. 5.15 the HIRHAM model's two years course is in agreement with the observational data.

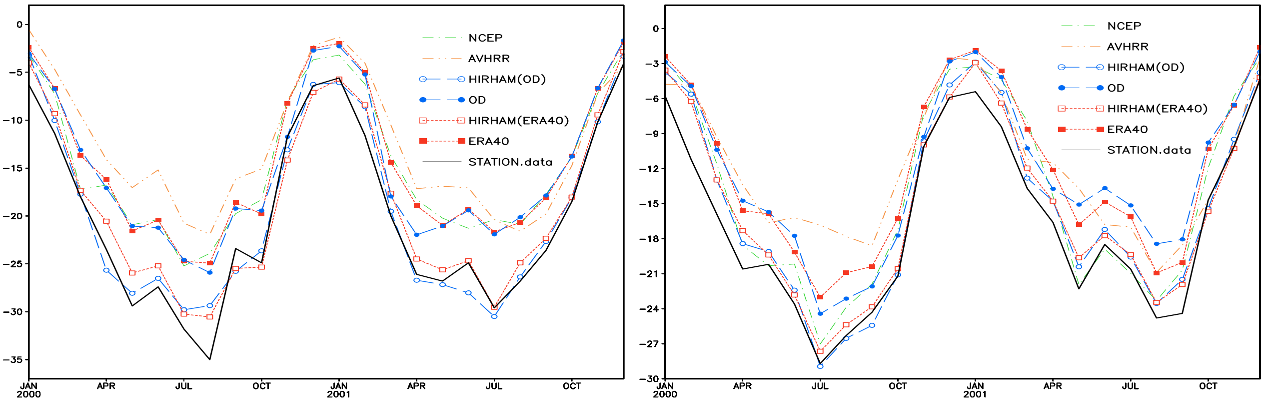

Figure 5.15: *As in Fig. 5.12 but for Halley (left) and Neumayer (right) station.*

In Fig. 5.16, the coldest stations are presented. Amundsen-Scott station's minimum temperature reached -62 $^\circ C$. During the transition period and the austral winter, the model output is in agreement with the observational data. When the austral summer arrives, a strong cold bias appears and, the HIRHAM simulation underestimates 2 m temperature meanwhile, all of the re-analyses overestimate 2 m temperature. The same situation occurs at the Vostok station. In both cases the summer bias reaches 12 $^\circ C$. There are three sources for the summer bias in the HIRHAM simulation and they are follows: a cloud cover overestimation over the Antarctic's plateau, the MSLP overestimation and the difference in elevation over the highest part of the continent, all of which demand a closer examination. We propose that increased horizontal resolution can lead to a better representation of the surface's fluxes. Additional experiments should be carried out with an improved snow-albedo scheme, as it was shown in Dethloff et al. (2006) for the Arctic area. For the inner part of the Antarctic, only a small amount of data is available. We calculated the monthly average for a 2 m temperature at the Amundsen-Scott and the Vostok stations over a period of 40 years. The results are shown in Fig. 5.17. The regional features for the Vostok and the Amundsen-Scott stations are similar. Both stations are located in the inner part of the continent, far away from the Southern Ocean. Also, they are elevated more that 2500 m above sea level, for more information, see Tab. 3.2. The mean temperature's slow fall during the austral winter is determined by the outgoing radiation. This means that as long as the sun remains below the horizon, the temperature will continue to fall at a slow rate. During the winter months, the phenomenon of the *coreless winter* (surface temperature remain relatively the same from the beginning of the winter to the end) is observed in the data for both stations. At the surface, this phenomenon is explained by a state of equilibrium wherein the surface's heat loss is balanced by an atmospheric longwave back radiation, a vertical eddy flux,

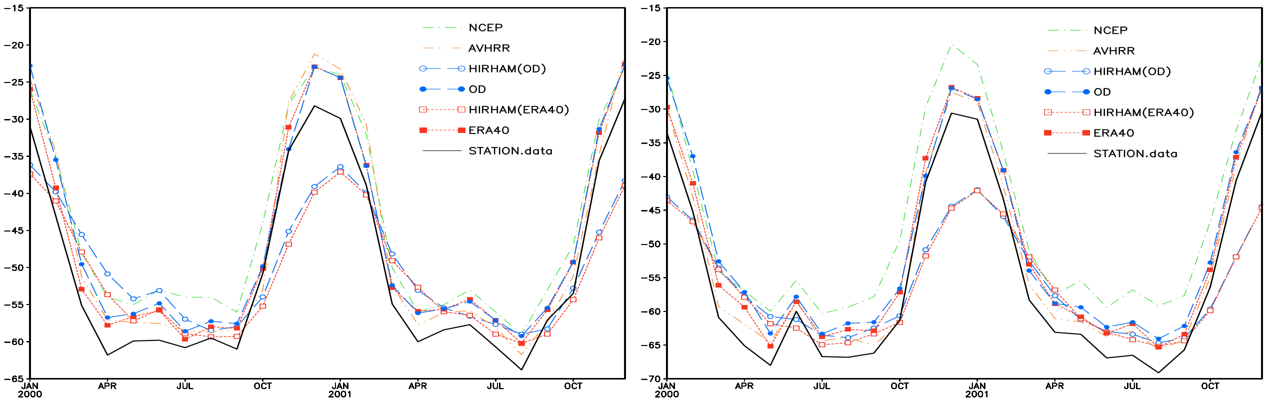

Figure 5.16: *As in Fig. 5.12 but for Amundsen-Scott (left) and Vostok (right) station.*

a conduction from the ground, and a heat of sublimation. This implies that at the surface level, a decrease in temperature and also, a decrease in how long it takes to cool down, is dependant on the trend of the temperature above the surface inversions, or in other words, on a coreless winter in the troposphere. The HIRHAM model simulates this phenomenon for both stations.

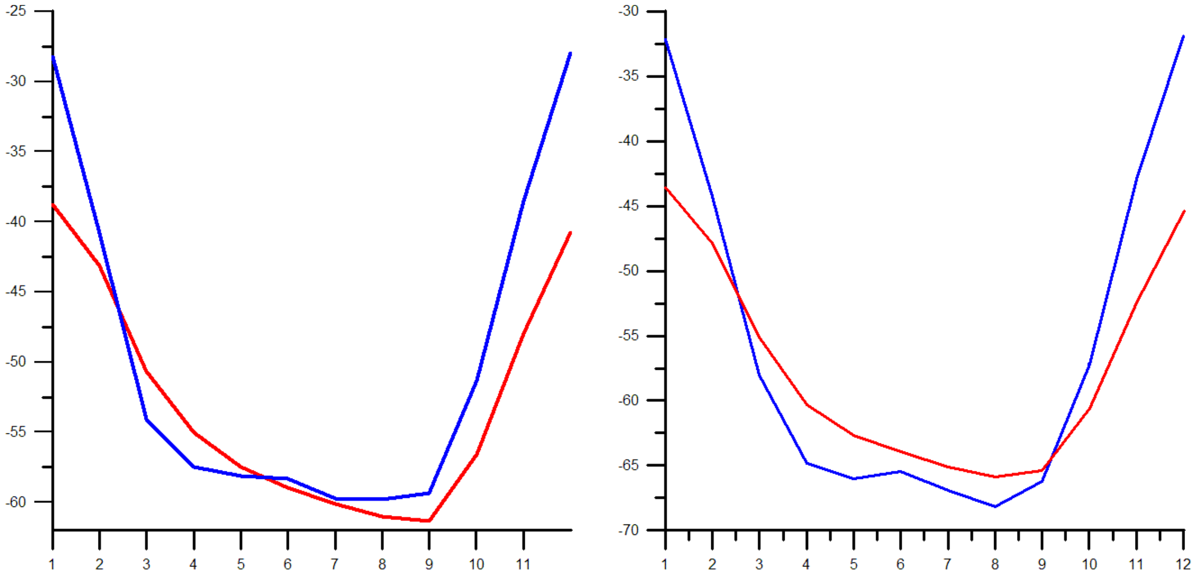

Figure 5.17: *2m temperature (°C) for Amundsen-Scott (left) and Vostok (right) station, monthly mean for the period 1958 - 1998, HIRHAM (red), station observation (blue). Y-axis – temperature (°C).*

The lengths of surface air temperature records as well as MSLP around Antarctica varied from one station to another because of differences in setup and operation times. The following stations have relatively long and reliable measurements: South Pole, Halley, Vostok and McMurdo stations. Other manned stations that were established at much later dates are the Neumayer and Mirny stations. Some statistical parameters were calculated for the 2 m temperature. For example of these calculations, see Tab. 5.3 (for the 18 year period), and SD over the 40 years are shown in Appendix A Fig. A.3. During the winter season, the horizontal pattern from the SD closely follows the distribution of sea-ice. During the summer season and over most of the Antarctica, ERA40 has a higher SD of 1.2 - 1.5 °C than HIRHAM simulations of 0.6 - 1.2 °C , which means less changes during the warm season in the model output. Based on the table data, the average bias for the HIRHAM model is 3.75 °C. The results also show that only for Halley station both re-analyses and the HIRHAM are warmer then observational data. The HIRHAM correlation index is 0.94.

2 *m temperature*, 1981-1998									
	BIAS			RMSE			CORRELATION		
	I	II	III	I	II	III	I	II	III
Amundsen-Scott	2.99	-5.2	-3.79	6.15	6.03	4.82	0.94	0.98	0.98
Bellingshausen	0.12	-0.51	0.34	1.28	0.91	1.21	0.96	0.97	0.94
Casey	3.93	3.5	3.65	4.99	4.94	5.21	0.85	0.84	0.85
Davis	5.75	0.71	4.00	5.89	1.24	4.16	0.98	0.99	0.98
Dumont-Durville	3.92	7.74	5.94	4.58	7.99	6.80	0.95	0.98	0.97
Halley	-0.12	-5.27	-3.93	1.95	5.58	4.52	0.97	0.98	0.97
Mawson	6.49	6.85	7.55	6.76	7.04	7.94	0.97	0.99	0.98
McMurdo	6.39	5.57	4.35	9.04	7.99	7.33	0.70	0.80	0.80
Mirny	4.65	3.43	2.70	5.12	3.69	3.23	0.97	0.99	0.97
Molodezhnaya	5.30	1.97	1.45	5.55	2.54	2.00	0.97	0.98	0.98
Neumayer	0.03	-4.59	-2.32	1.59	4.86	3.05	0.97	0.98	0.97
Novolazarevskaya	5.86	3.51	5.98	6.11	3.84	6.25	0.97	0.98	0.97
Syowa	5.16	0.98	3.69	5.38	1.40	3.85	0.97	0.99	0.99
Vostok	1.97	-5.45	-5.50	2 years are missing					
AVERAGE	3.75	0.95	1.72	4.95	4.46	4.64	0.94	0.96	0.95

Table 5.3: *Statistical measures of 2 m temperature (°C), I - HIRHAM, II - ERA40, III - NCEP*

To resume, 2 *m* simulated temperature is in agreement with the station data. The difference between the ERA40 re-analysis and the HIRHAM model's output for the austral winter is ± 4 °C. Over the inner part of the continent, for the austral summer HIRHAM is colder than the re-analysis by 12 °C. Relaying on different aspects of this summer bias some conclusions can now be made about the cause of the this temperature underestimation. In the HIRHAM model simulation, there are three sources that contribute to the summer temperature bias: an overestimation of cloud cover over the Antarctic plateau, an overestimation of the MSLP and also, a difference in elevation in the highest parts of the continent. The creation of the negative temperature bias is explained by a shortage of incoming solar radiation, which is due to an overestimation of cloud cover during the summer season. The cloud overestimation problem is known from the HIRHAM simulation over the Arctic area (Rinke et al., 1997). In order to attain a better representation of the cloud cover over Europe, Meinke et al. (2006) adopted the nudging technique (von Storch et al., 2000) for his regional climate model. Such a method can be applied in a simulation of the Antarctic climate and it will be aid to better represent the local orography and feedback mechanisms in the lower troposphere.

5.3.1 Surface temperature based on the satellite measurements

The next step toward validating the model was to comprehensively compare the satellite data and the model simulations. Satellite-based temperatures (hereafter referred as AVHRR data) are referred to as surface temperature (Comiso, 2000). The data were received via personal communication with J. Comiso (Cryospheric Sciences Branch, NASA Goddard Space Flight Center, Greenbelt, MD). The AVHRR data's resolution is 12.5 by 12.5 *km*. The retrieval's algorithm assumes "clear-sky" conditions. Surface temperature monthly mean averaged over 1982-1998 were available. The validation of winter and summer season mean (calculated from monthly mean) was carried out.

Before the intercomparison started, the satellite data were interpolated to the HIRHAM model's grid. Fig. 5.18 shows the average surface temperature during the austral summer and for the years 1982 to 1998. Discussing the differences between the HIRHAM simulations and the AVHRR data we have to keep in mind that the AVHRR surface temperatures are intended only for cloud-free-sky atmosphere. The monthly mean of the AVHRR data is consistent with the weather station data - the difference is within ± 3 °*C*. During the summer, the satellite-derived temperatures tended to be lower than the 2 *m* air temperatures. This pattern does not hold for the rest of the year (Comiso, 2000). During summer, the HIRHAM model strongly underestimates the surface temperature. In the HIRHAM simulation, the minimum value over the Eastern Antarctica is about -50 °*C*. AVHRR data show the lowest temperature -40 °*C* at the same place as in the HIRHAM simulation, but the area is notably smaller.

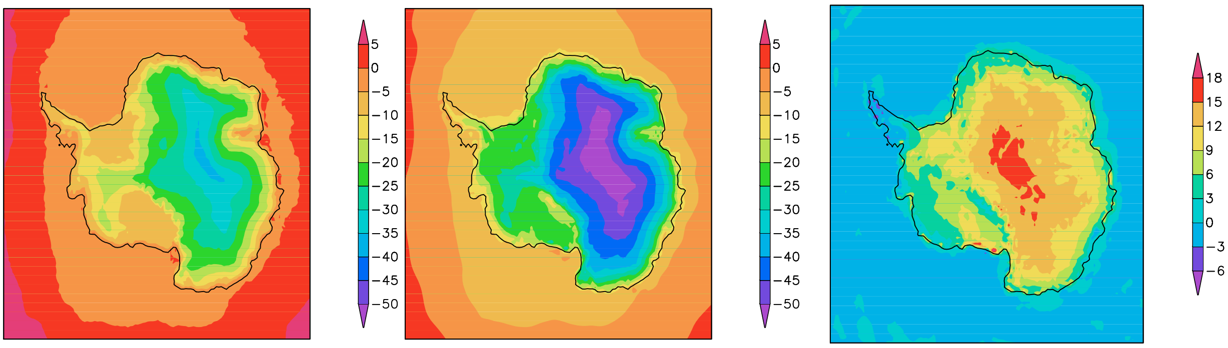

Figure 5.18: *Surface temperature (°C) in austral summer (DJF), for the period 1982 - 1998. AVHRR (left), HIRHAM (middle), difference "AVHRR minus HIRHAM" (right)*

During winter, as shown in Fig. 5.19, the surface temperature within a 3 °*C* agreement with Comiso (2000). The 2 *m* temperature and surface temperature are usually close to each other when the air temperature is below freezing temperature. The cold temperature of Antarctica's interior does not allow water vapour to remain in the air and this, can inhibit cloud formation. At the South Pole, clear sky conditions are typically observed during the winter season. In such conditions, there is an agreement between the HIRHAM simulation and the AVHRR data. During the summer season the agreement between the observational data, the AVHRR data and the

HIRHAM simulation becomes weaker. This is because along the coasts, disturbances become more frequent. Cloudy sky conditions are more frequent due to the maritime influence and polar circulation patterns. The cloud cover hits its peak during the austral spring and summer, while it is at its lowest during the winter months (King and Turner, 1997). This explains why during the summer the differences between the HIRHAM model and the AVHRR data are greater than during the winter. Following Comiso (2000) estimations, differences in the surface air temperature between the station data and the satellite data are within ± 3 °*C*. During the austral winter the differences between the HIRHAM and the AVHRR data are within that range. In the following section, the vertical temperature structure is examined.

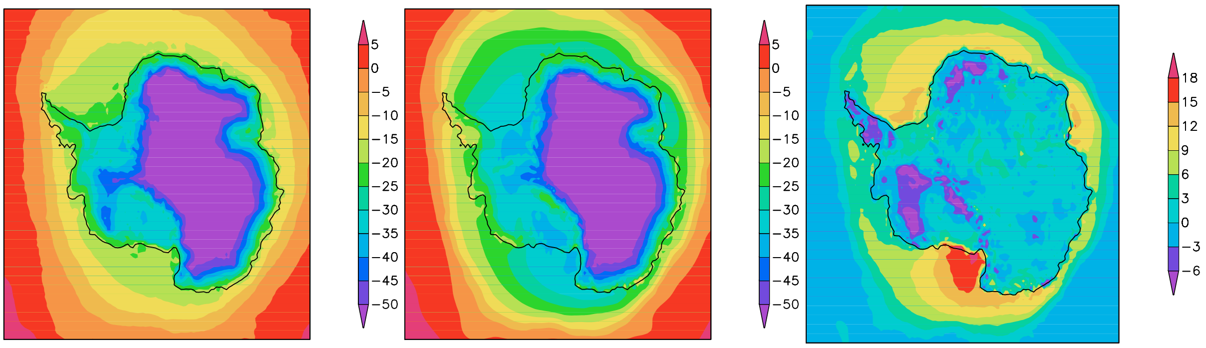

Figure 5.19: *Surface temperature (°C) in austral winter (JJA), for the period 1982 - 1998. AVHRR (left), HIRHAM (middle), difference "AVHRR minus HIRHAM" (right)*

5.3.2 Vertical temperature structure

To validate the modeled vertical structure, we used radiosonde data taken from the READER project (c. details in Chapter 4.2). This dataset is a collection of the radiosonde data from various manned stations around the Antarctic continent. The periods in which the measurements were taken differ from station to station. The Antarctic's temperature and, geopotential height were interpolated to standard isobaric levels. These are available online at (*http : //www.antarctica.ac.uk/met/READER/*). The annual temperature mean for the NCEP re-analysis, the HIRHAM(ERA40), the HIRHAM(OD) and the station data were plotted on standard isobaric levels. This is shown in Fig. 5.20 and Fig. 5.21. Since, the vertical profiles look similar and the difference is small for the different stations, only 2 coastal and 1 inner stations are shown here. The HIRHAM model data show consistency with the observational data. The differences between the two HIRHAM outputs, which were driven by the re-analysis and the operational data, are not significant and lie within ± 2-5 °*C*. At the surface level, a bigger bias can be observed between the NCEP and observational data. At 600 *hPa*, the HIRHAM model simulation gets closer to the NCEP data and at higher pressure levels the NCEP already shows signs of having a smaller bias than the HIRHAM model. Apparently, HIRHAM's results are better in the lowest levels and it better represents the surface processes. Therefore, the

HIRHAM also better represents lower part of the atmosphere (planetary boundary layer). The proper simulation of the atmosphere vertical structure is essential for a correct representation of the surface-low level troposphere feedback mechanism. Fig. 5.21 shows the Amundsen-Scott station's vertical temperature profiles. The surface pressure is about 500 *hPa*, which is why only the upper part of the atmosphere is presented here. The agreement between all datasets are quite good and constant bias 5 °*C* presents at all standard isobaric levels. The tropopause lies near 300 hPa in this sounding, which is typical for the concerned period. Above 300 *hPa* the observational data can be assumed as doubtful, since the measurements were carried out in a cold heavy Antarctic conditions and the accuracy of these measurements become smaller.

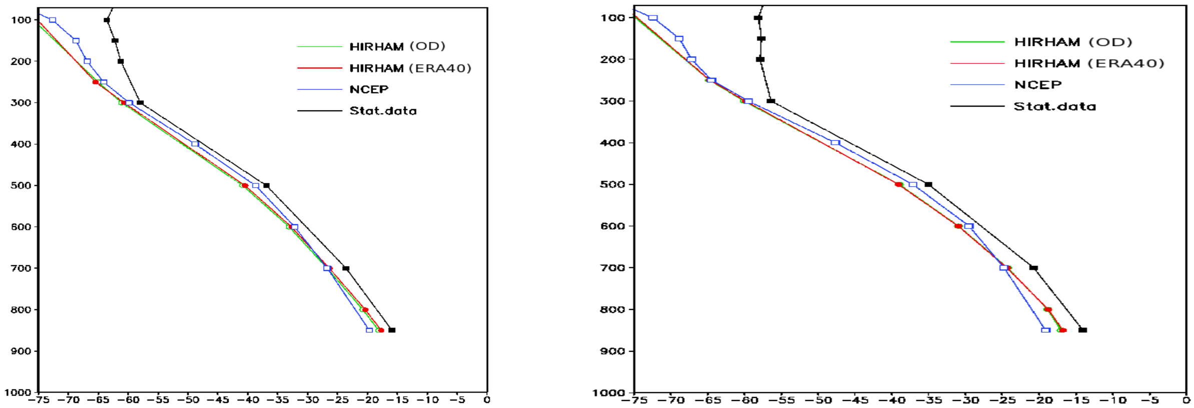

Figure 5.20: *Annual average temperature (°C) during the year 2000, NCEP, HIRHAM(OD) - (HIRHAM driven by Operational Data), HIRHAM(ERA40) - (HIRHAM driven by ERA40), station data. Novolazarevskaya (left) and Syowa (right) station. Y-axis – pressure levels (hPa).*

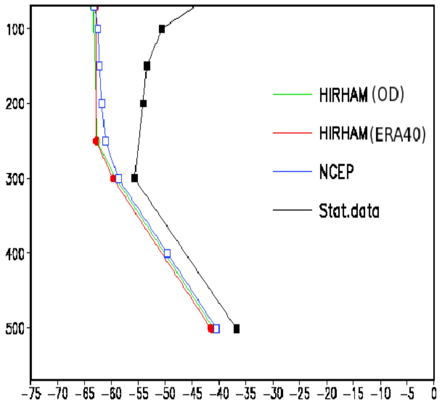

Figure 5.21: *As in Fig. 5.20 but for Amundsen-Scott station.*

5.3.3 Surface temperature inversion

For a long amount of time, it has been known that strong surface inversions exist over the Antarctic plateau and also, that they play an important role in the formation of near-surface wind and the atmospheric radiation redistribution. Surface inversion strength (depth) is defined as the temperature difference between the surface and the warmest temperature in the lower troposphere. It exists because of the small amount of solar energy absorbed by the surface and also, because of the smaller emissivity of the atmosphere, that is, smaller when compared to the surface. Inversions are associated with stably stratified and, persistent conditions that decouple the surface from the lower troposphere above the inversion. They influence the magnitude of heat and moisture fluxes through openings in the sea-ice, the depth of vertical mixing in the boundary layer, cloud formation, surface wind velocity, and lead formation. Unfortunately, meteorological stations that provide radiosonde data are sparsely distributed across the Antarctic, and therefore provide little information on the spatial distribution of temperature inversions.

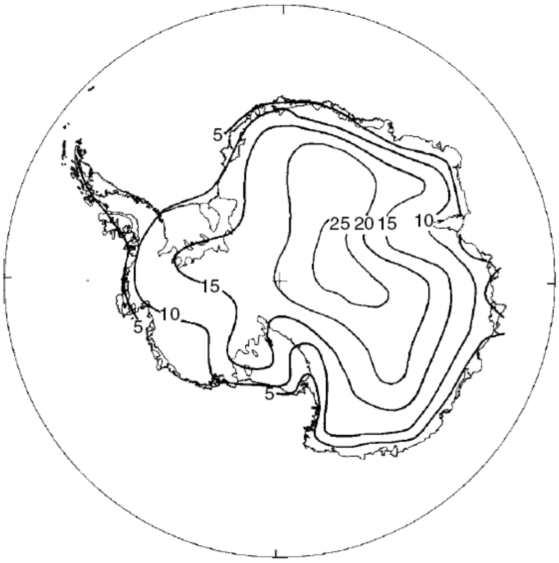

Figure 5.22: *The strength of the surface inversion (°C) from Phillpot and Zillman (1970) in austral winter (JJA).*

Connolley (1996) calculated that in winter months, the interior of the Antarctic ice sheet the surface temperature inversion is about 25 $°C$. It is well known that the Antarctic temperature inversion is strongest during the winter and that it is greatly reduced during the summer (Turner et al., 2006). The inversion strength analysis (Phillpot and Zillman, 1970) was calculated based on $in-situ$ upper-air data, which was collected during the International Polar Year (1957) and later is shown in Fig. 5.22. The HIRHAM simulation result is shown in Fig. 5.23. Both fields have the same basic distribution of inversion strength, of which the maximum values occur over the high plateau of East Antarctica. Although it should be noted that the inversion strength in the HIRHAM simulation is slightly smaller, than what it was computed from the $in-situ$ data. This difference caused by the different time periods used in the model simulations and presented by $in-situ$ data. Therefore, this is a very good result for the regional model. There is a definite seasonal variation of inversion strength. During the summer period and in the Eastern part of Antarctica, the surface inversion becomes smaller: it is simulated to be between 9 to 18 $°C$.

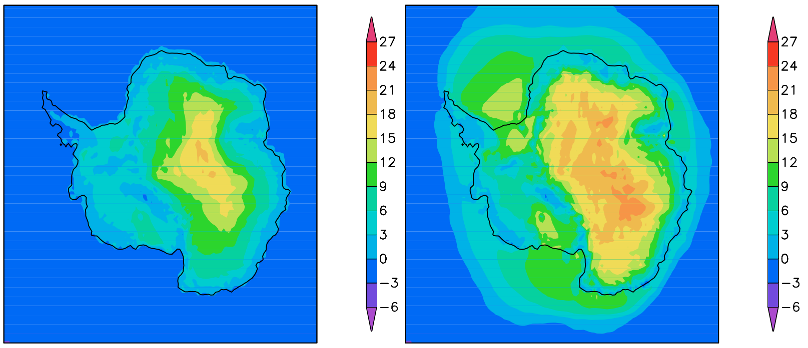

Figure 5.23: *The strength of the surface inversion ($^\circ C$) in HIRHAM in austral summer (DJF) (left) and austral winter (JJA) (right), for the period 1958-1998.*

Over a span of 10 years, Hudson and Brandt (2005) calculated the mean of the inversion strength during summer at the Amundsen-Scott station. The maximum value found was $7.5\ ^\circ C$. By looking at a different parts of the continent, different results are found. For example, if we consider Vostok station, it can be noticed that because it is situated on flat surfaces it subsequently does not experience strong katabatic winds. In contrast, the Dumont-Durville base is situated at the coastal line near a steep ice slope and here; strong katabatic winds vertically mix the cold air through a deep layer. As a result, a strong temperature inversion cannot be maintained there for a long time. There is a strong connection between low level wind field and the strength of the temperature inversion.

A few places over Antarctica are well known for having a stronger surface wind. For example, this is case in Adèlie Land area and in the Mizuho station. We show the temperature and wind profiles for the former mentioned part of the Antarctica in Fig. 5.24 and for the latter in Fig. 5.25.

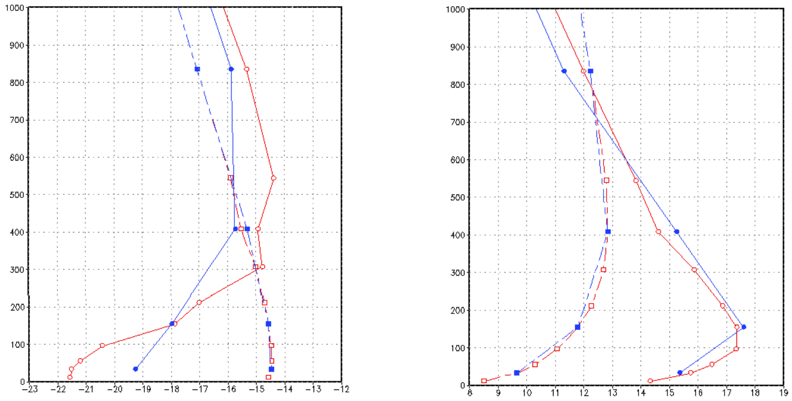

Figure 5.24: *Vertical temperature profile ($^\circ C$) (left), vertical profile of the wind speed, (m/s), (right) in the lowest 1000 m. Blue line is 19 vertical levels, red line is 25 vertical levels HIRHAM. Solid line is HIRHAM, dashed line is ERA40 for the Adéle Land area, November 1997. Y-axis – height (m).*

The strong stability in the lower troposphere is associated with a pronounced radiation inversion in the temperature profiles. For a better representation of the planetary boundary layer, the vertical model resolution has been increased from 19 to 25 levels. Fig. 5.24 shows the vertical temperature and wind speed profiles found in the lowest 1000 meters. The comparative analysis has been carried out for November 1997, when simulation data for both vertical of the HIRHAM versions were available. In the lowest hundreds meters, katabatic wind is seen in the vertical profile as increased wind speed. The vertical wind profile is well reproduced by both of the model versions (that had different vertical resolutions). Already with 19 vertical levels, a lower tropospheric inversion is simulated. Furthermore, the maximum speed for the katabatic wind is simulated at about 150 *m*. Figures 5.24 and 5.25 clearly show that compared to the 25 vertical level version of the HIRHAM model, the 19 vertical level version of the model simulates a higher wind speed and a less intense temperature inversion. The ERA40 data, which is indicated by dashed lines, are unable to resolve the inversion and the low-level katabatic wind jets that we saw in the HIRHAM simulations.

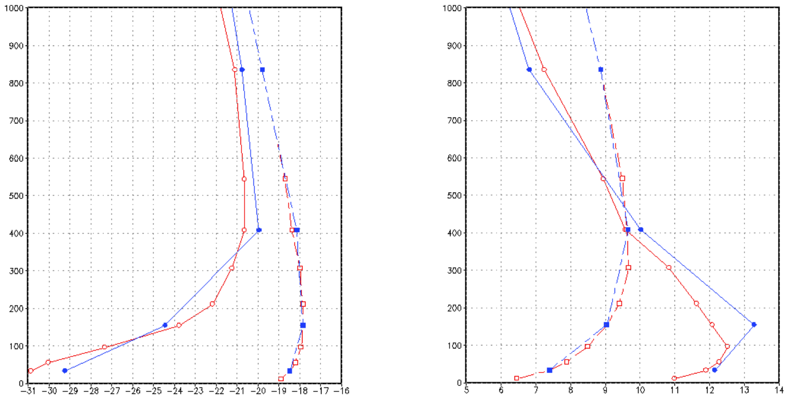

Figure 5.25: *Vertical temperature profile (°C), (left), vertical profile of the wind speed, (m/s), (right) in the lowest 1000 m. Blue line is 19 vertical levels, red line is 25 vertical levels HIRHAM. Solid line is HIRHAM, dashed line is ERA40 for the Mizuho station, November 1997. Y-axis – height (m).*

In conclusion, the HIRHAM model simulates the stable boundary layer with sufficient accuracy. To simulate the climate of Antarctica with high accuracy the planetary boundary layer must be resolved with a higher vertical resolution. As experiments clearly show, an increased vertical resolution better represents the processes in the boundary layer. For a better evaluation of the temperature profile, additional observational data are necessary.

5.4 Wind

As described in van den Broeke et al. (1997), the strong surface wind is one of the Antarctica's permanent features. Fig. 5.26 shows the lowest model level wind, which is located at 12 *m* above the surface. Averaged over 40 years, the austral summer mean for the ERA40 re-analysis and the HIRHAM simulation are presented for the intercomparison. The arrows indicate the wind direction and the colours indicate the wind speed. The first glance reveals that the HIRHAM simulates stronger wind fields over the coastal line. The maximum simulated wind speed, 12 m/s, can be observed over the Adélie Land. The orography at that region creates the perfect conditions for the katabatic wind formation. The large interior basin and a relatively small confluence zone is in the coastal area. Due to the funneling effect, the intensities and durations can be sustained all year around (Wendler et al., 1997). The lower wind speed, 3 m/s, is located over the high Antarctic plateau. Around the continent the zonal circulation prevails. The major difference between the ERA40 and the HIRHAM is located along the coastline. The HIRHAM overestimates the re-analysis by 2 to 4 m/s. Fig. 5.27 shows the winter climatologic mean for the wind speed and direction for both the HIRHAM and the ERA40 re-analysis.

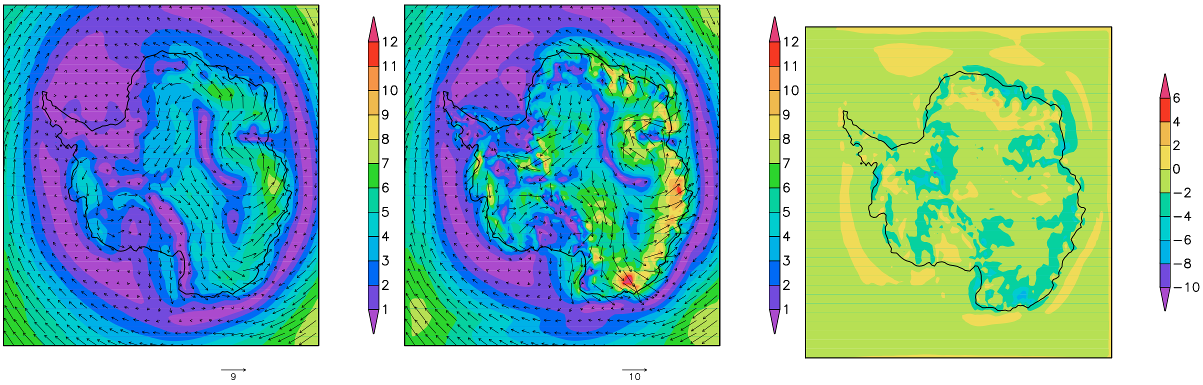

Figure 5.26: *The lowest model level (12 m) wind speed (color shaded) (m/s) and direction in austral summer (DJF), for the period 1958-1998. ERA40 (left), HIRHAM (middle), difference "ERA40 minus HIRHAM" (right).*

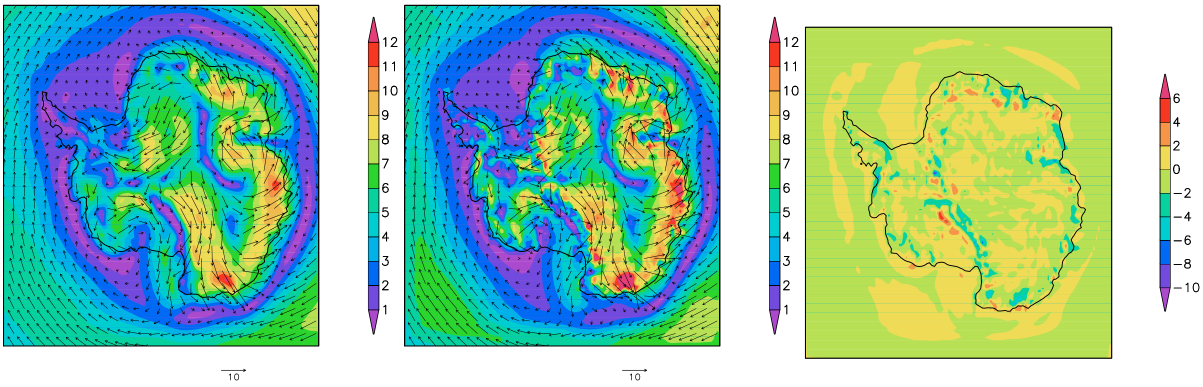

Figure 5.27: *The lowest model level (12 m) wind speed (color shaded) (m/s) and direction in austral winter (JJA), for the period 1958-1998. ERA40 (left), HIRHAM (middle), difference "ERA40 minus HIRHAM" (right).*

Relative to the austral summer, the mean wind speed over the continent increased by 2 - 4 m/s. Over the inland part, the inter-seasonal variability appears to be small but it appears to be bigger along the coastal line. As cold low-level air flows from the high plateau to the sea, both of the ERA40 and the HIRHAM mesoscale simulations clearly produce the continent-scale drainage flow over East Antarctica. The flow is deflected to the left by the Coriolis force producing a net easterly component to the flow over Antarctica.

Additionally, oscillations for 10 *m* wind speed were calculated over a period of 4 years. This was done for the different stations around the continent and the results are shown in Fig. 5.28 to Fig. 5.31. The ERA40 data are shown for the model's lowest level which is located at 12 *m* above the surface. Taking into account the stable boundary layer we can expect small differences between the 12 and 10 *m* high wind speed. Wind speed is a difficult parameter for accurate measuring. It is hard to expect a high accuracy in the difference between model output and observational data. Nonetheless, if HIRHAM correctly captures the main synoptic scale processes, we should at least expect a good agreement in the year-to-year oscillations. Fig. 5.28 shows the wind speed for Novolazarevskaya and Syowa stations.

At the Novolazarevskaya station the modeled wind speed (1 - 8 m/s) is much smaller than the measured wind speed (6 - 16 m/s). This station is located on a nunatak (at the grounding line) and, about 75 *km* from a large range (with rock outcrop). A nunatak is a mountain-top that is not covered by land ice and that protrudes out of a surrounding glacier. In the regional climate models, the sub-grid-scale orography's drag and its effect on the large-scale flow is taken into account by a formulation that uses an effective roughness length (derived from the variance of the sub-grid-scale orography). The maximum value for the roughness length is 3 *m* and it is located at the Novolazarevskaya station. Taking this assumption into account, the surface wind speed shows a lower value. Therefore, an evaluation of the model in a region with such a complex orography is difficult. At the Novolazarevskaya station, it is observed that the maximum wind speed occurs in the winter and the minimum wind speed occurs in the summer. Compared to the observational data and the NCEP re-analysis, the HIRHAM simulation has the lowest wind speed, but it nevertheless captures local features and it closely follows the driving data. At the Syowa station, the observed wind speed is about 4 - 12 m/s. The HIRHAM and the ERA40 data slightly underestimate the observed 10 *m* wind speed by 2 - 4 m/s, while the NCEP data show the highest value. The same bias was found for the rest of the stations (see Fig. 5.29 to Fig. 5.30). In November 1996, an interesting feature was noticed at the Halley station: for this

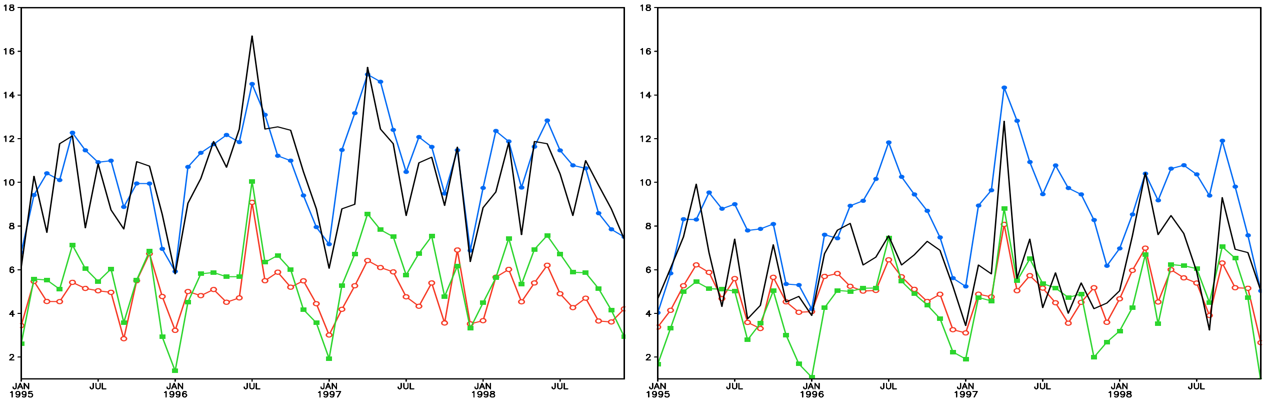

Figure 5.28: *10 m wind speed (m/s) for Novolazarevskaya (left) and Syowa (right), HIRHAM (red), NCEP (blue), observational data (black). The lowest model level wind (12 m) ERA40 (green, m/s).*

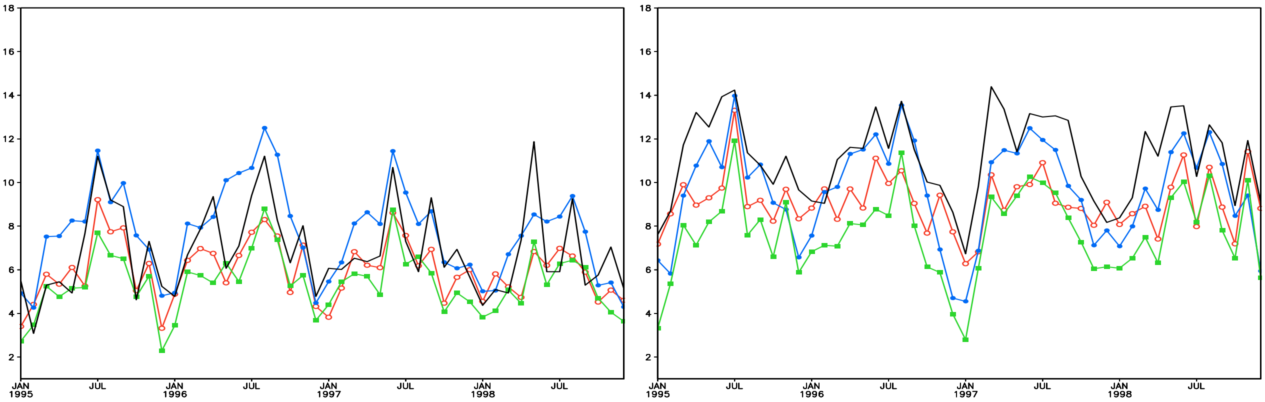

Figure 5.29: *10 m wind speed (m/s) for Casey(left) and Mirny (right), HIRHAM (red), NCEP (blue), observational data (black). The lowest model level wind (12 m) ERA40 (green, m/s).*

month, all of the datasets showed the maximum wind speed. The NCEP, the ERA40 re-analysis data, as well as, the HIRHAM simulations have a spike with a 9 m/s amplitude. However, the HIRHAM's results are closer to the real data. By looking at Fig. 5.29 and Fig. 5.30, another conclusion can be made. The HIRHAM model is in agreement with the driving re-analysis and the station data.

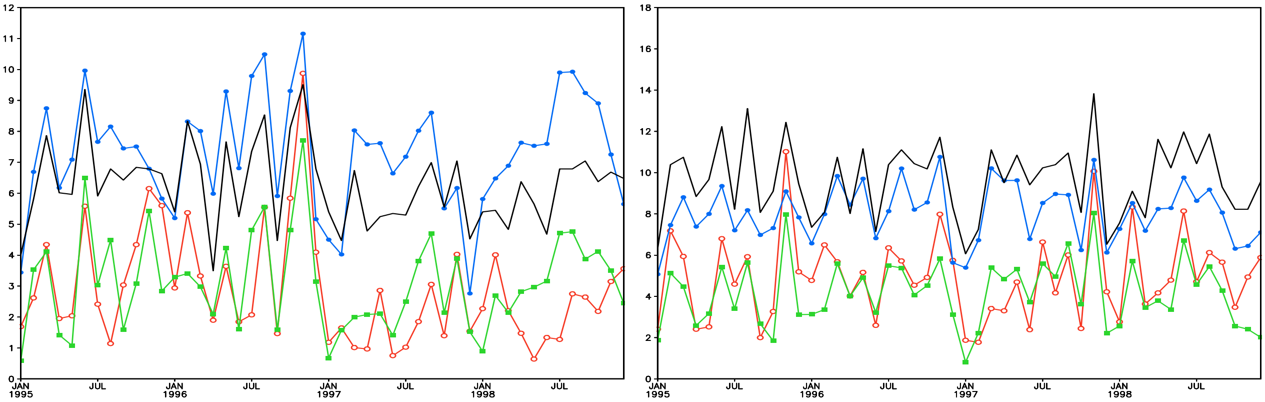

Figure 5.30: *10 m wind speed (m/s) for Halley(left) and Neumayer(right), HIRHAM (red), NCEP (blue), observational data (black). The lowest model level wind (12 m) ERA40 (green, m/s).*

In contrast to the coastal stations, inner stations have a lower maximum wind speed (see Fig. 5.31). Following observational data, the maximum value for both stations is 7 m/s. In the inner part of the continent, the low wind speed values maintain the strong surface inversion. At the Amundsen-Scott station, the NCEP and the ERA40 re-analysis slightly overestimate the observational data. Meanwhile, the HIRHAM model shows lower values and more stable course with a less pronounced change between summer and winter. The bias between the model output and the observational data lies within 1 - 3 m/s. This small underestimation of the low level wind speed could be an additional component in the strong and cold summer temperature bias. Thus, it maintains the artificial strong surface inversion, which is due to the low mixing rate.

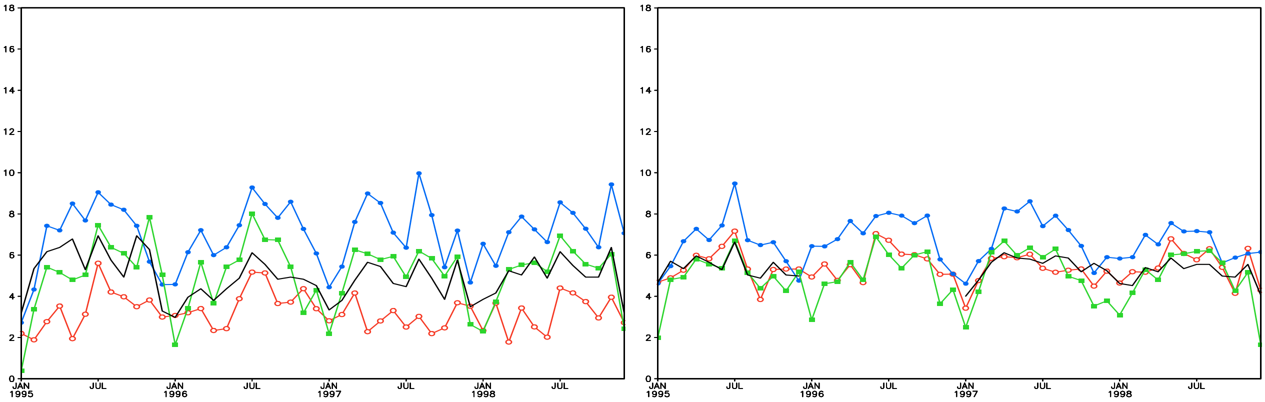

Figure 5.31: *10m wind speed (m/s) for Amundsen-Scott (left) and Vostok (right), HIRHAM (red), NCEP (blue), observational data (black). The lowest model level wind (12 m) ERA40 (green, m/s).*

For Neumayer station in year 1997, the vertical profiles of the temperature and wind speed in the lowest 2400 *m* are shown in Fig. 5.32. Based on radiosonde data, the seasonal mean was calculated. As it was already seen in 10 *m* wind speed, the HIRHAM model keeps the same negative bias in the vertical profiles. The underestimation of the surface wind causes difficulties in mixing the cold surface air with the inflow of the relatively warm air from the Southern Ocean. With a realistic magnitude, the katabatic wind speed in the lowest 200 - 400 *m* was simulated by HIRHAM. As an example, the austral spring (SON) model wind changes from 6.5 m/s to 9.5 m/s, and the real wind speed changes from 13 to 16 m/s. This hints that the HIRHAM simulation can be improved by a better representation of surface processes.

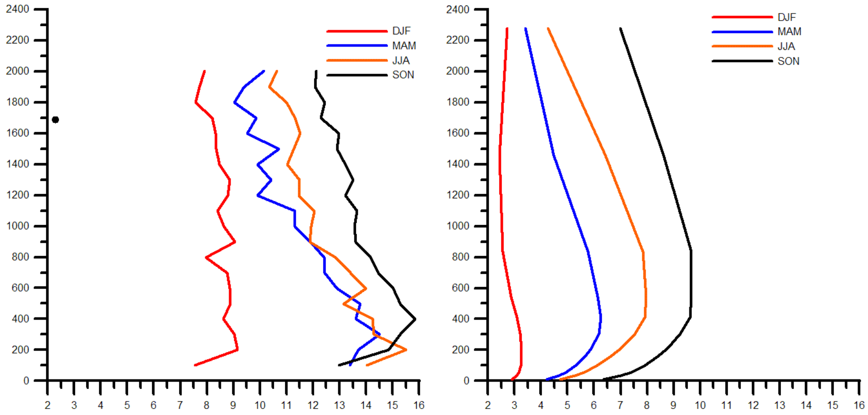

Figure 5.32: *Wind speed (m/s) vertical profiles (lowest 2400 m), Neumayer (left), HIRHAM (right), seasonal mean for 1997. Y-axis – height (m).*

5.5 Cloud cover

Clouds play a key role in the climate system's energy and water cycle. Clouds heavily affect the radiative net balance of the atmosphere by modulating shortwave and longwave radiation. Changes in amounts of cloud condensation affect the vertical stability of the atmosphere. By producing precipitation, clouds form an essential link in the water cycle between the atmosphere and the surface.

In order to account for the effect of clouds in numerical models for climate prediction, cloud processes and their interaction with the environment are usually formulated in terms of cloud cover or cloud systems. In this light, vertical profiles of area averaged cloud parameters like, cloud fraction and cloud liquid water, represent the properties of the cloud ensemble. Over the past decade, scientists have made considerable efforts to comprehensively describe cloud processes in large-scale atmospheric models. Despite these efforts, the parameterisation of cloud processes and their interaction with radiation and convection is still identified as one of the major problems.

Cloud cover at high latitudes is not well known (Hahn et al., 1995; Rossow and Schiffer, 1999). The clouds over continental Antarctica consist primarily of ice crystals (Morley et al., 1989). In the presence of strong temperature inversions in the lower troposphere over much of the Antarctic continent, clouds warm the surface and cool the free atmosphere (Yamanouchi and Charlock, 1995); this climatic effect of cloud cover is rarely found anywhere else. Clouds predominantly are thought to be located at the top of the inversion (Mahesh et al., 2001). A primary source of it is a longwave downwelling radiation. Most regional climate models assume that the fractional cloud coverage is determined by the grid-averaged relative humidity, stability, or resolvable-scale vertical motions. If cloud cover changes in response to a change in relative humidity, then there is an important feedback between changing relative humidity and changing cloud cover. As an example, the relative humidity vertical profile at the Neumayer station is shown in Fig. 6.1. Since cloud cover is a difficult element to measure, for the model validation there are only a few gridded datasets available.

Averaged over 40 years, the HIRHAM model's simulated seasonal mean of cloud cover is shown in Fig. 5.33. Standard deviations for the winter and summer seasons are shown in Fig. A.5, Appendix A. During the austral summer, one maximum in the cloud cover can be seen over the Western coast of the Antarctic Peninsula. It is connected with this region's topography. The high orography of the Antarctic Peninsula acts as a barrier for the cyclones that move in an eastern direction. Therefore, more clouds and a higher precipitation rate are observed along the Western coast of the Antarctic Peninsula than what is observed along Eastern side. Along the Eastern part of Antarctica simulated cloud cover rate of 40 to 60 % can be observed. This result is in agreement with some of the coastal stations' observational data presented by Guo et al. (2003) in Tab. 5.4. The simulation results show that clouds cover most of the Eastern part of Antarctica during the austral winter. It is less realistic because during the cold winter months

Antarctic air can no longer hold so much water vapour. Apparently, the HIRHAM model overestimates the cloud cover over the inner part of the continent. Rinke et al. (1997) presented cloud cover validation in the HIRHAM model for the Arctic area. The intercomparison with observational data revealed that the model overestimated cloud cover during the whole year. The table 5.4 lists the seasonal and annual bias for cloud cover, calculated for year 1993.

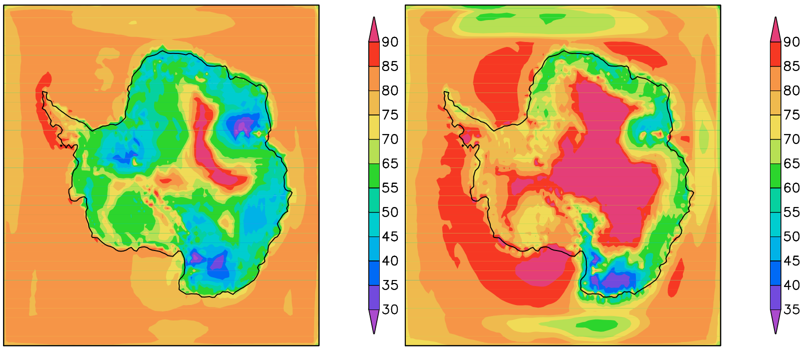

Figure 5.33: *Cloud cover (%) in austral summer (DJF) (left) and in austral winter (JJA) (right), for the period 1958 - 1998. HIRHAM simulations.*

	ANNUAL			DJF			MAM			JJA			SON		
	I	II	III	I	II	III	I	II	III	I	II	III	I	II	III
SP	90	45	45	83	63	20	65	32	33	70	29	41	91	56	35
Casey	63	71	-8	64	78	-14	65	75	-10	64	67	-3	58	63	-5
Davis	55	59	-4	51	60	-9	55	63	-8	60	51	9	52	63	-11
Halley	77	61	16	77	59	18	78	66	12	73	48	25	80	69	11
Mawson	46	47	-1	44	52	-8	49	43	6	52	47	5	40	46	-6
Neumayer	68	59	9	65	64	1	63	51	12	70	51	19	76	70	6
Syowa	65	65	0	70	68	2	65	71	-6	57	54	3	68	69	-1
Vostok	91	20	71	72	17	55	97	15	82	98	16	82	95	33	62
AVER.			16			8.1			15			22.6			11.4

Table 5.4: *Cloud cover in 1993 (%), I - HIRHAM, II - Observations (Guo et al. (2003)), III - "HIRHAM minus Observations".*

The HIRHAM overestimates the cloud cover over the inner part of the continent, as it can be seen for Vostok and Amundsen-Scott stations from Tab. 5.4. For the Amundsen-Scott station, the bias remains throughout all of the seasons, with maximum value showing in the austral winter. During austral autumn and winter, at the Vostok station, for both of the dataset, the cloud cover value almost does not change. For the coastal stations, the bias is not so strong and it lies within an acceptable range. Cloud clover is directly linked to the local circulation. At the coast, it means that enough cyclones, which are very important for the precipitation distribution, penetrate to the continent.

In the next chapter the model validation of the radiation fluxes (net shortwave radiation, net longwave radiation, sensible and latent heat flux) is presented.

5.6 Surface radiation budget

The Antarctic continent is a region where energy radiated to space is greater than energy absorbed from the Sun. Due to this disproportion, the near-surface atmosphere is often stably stratified. This is particularly true over the high-elevation areas of the Antarctic Plateau. Under these conditions, the processes in the stable boundary layer often dominate the transfer of energy in the forms of radiation, sensible and latent heat, and momentum between surface and atmosphere. Parish (1988) found that processes in the lowest few hundred meters are the dominant factors determining atmospheric flows over Antarctica.

The surface energy balance equation is given as:

$$\downarrow SW + \uparrow SW + \downarrow LW + \uparrow LW + H_s + H_l + G = 0 \tag{5.4}$$

where $\downarrow SW$ is shortwave (SW) downwelling flux, $\uparrow SW$ is the SW upwelling flux reflected from the surface, $\downarrow LW$ is the longwave (LW) downwelling flux, $\uparrow LW$ is the longwave upwelling flux, H_s is the sensible heat flux, H_l is the latent heat flux and G is upward heat flux through the snowpack. The last term is insignificant and can therefore be neglected, Carroll (1982). In contrast, the net value of the LW radiation flux plays a very important role in the energy balance. The horizontal pattern of the net LW radiation is shown in Fig. 5.34 and Fig. 5.35. The winter and summer mean was calculated for the year 1997 based on the monthly means. The net LW radiation balance shows the difference between the incoming LW and the outcoming LW radiation. The ERA40 data have a more uniform structure than what does have the HIRHAM output, isolines mostly follow the orography of the continent. The minimum value for the ERA40 reanalysis, is located over the Eastern part of Antarctica and it is about 30 W/m^2 higher than the HIRHAM simulations, this is probably due to difference in cloud cover. The difference

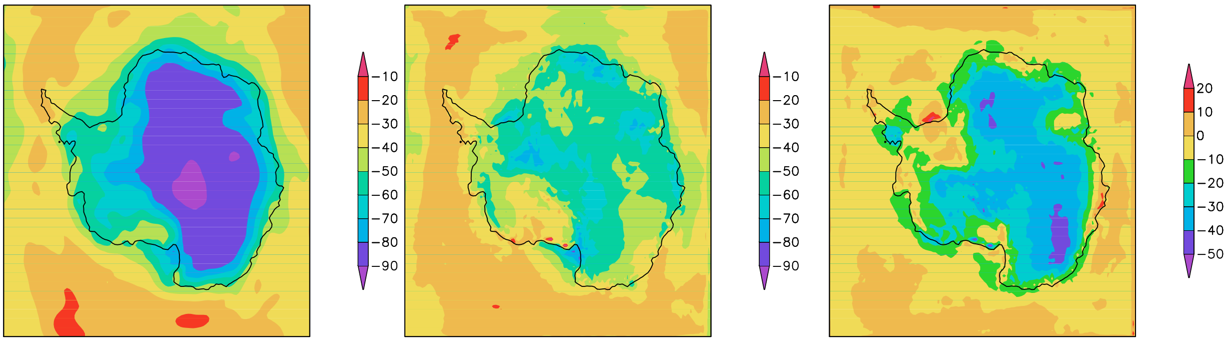

Figure 5.34: *Net longwave radiation at the surface (W/m^2) in austral summer (DJF), 1997. ERA40 (left), HIRHAM (middle), difference "ERA40 minus HIRHAM" (right).*

between the incoming and the outcoming LW radiation is essential for the surface temperature. This is especially true during the cold and long winter season. During the winter months the situation remains the same, although the difference between the model simulation and the re-analysis decreases to 5 - 10 W/m^2, this is shown in Fig. 5.35. It means that compared to the re-analysis data, the HIRHAM model accumulates more radiation energy. This accumulation can be connected with an overestimation of cloud cover, since it keep the outgoing LW radiation. Unfortunately, there is no other available gridded dataset for the radiation fluxes. More data, such as radiation fluxes derived from satellite data, would have produced a better model validation and a more detailed investigation. The SD of the LW and the SW radiations, calculated over 40 years for the summer and winter season, are shown in Appendix A, Fig. A.4. The net short wave radiation supplies most of the energy directed towards the surface. It is also the only heating source for the inner part of the frozen Antarctic. Any decrease in surface solar irradiance tends to cool the surface, whereas an increase in clouds increases the downward thermal infrared irradiance and this, has a warming influence on the surface. During the winter months the Sun is below the horizon and so throughout this period there is no income of solar radiation at all. However, during the summer months the incoming radiation is more than 400 W/m^2 on the Antarctic plateau. Despite this, due to reflection (surface albedo is about 85% most of time) the net SW radiation at the surface does not reach more than 80 W/m^2 (see Fig. 5.36). The positive net SW radiation balance means that the surface gets more SW radiation than what was reflected back into the atmosphere. Around Eastern Antarctica, the HIRHAM model mean value is lower by 20 W/m^2. The explanation for this is an overestimation of cloud cover (for summer season). This effectively blocked the surface from the incoming solar radiation and kept the surface colder than what it is in reality. For at least two reasons, the reflected solar radiation in the model is too low: a too-low surface albedo and a negatively biased incoming solar radiation. Apparently, there are biases in clear-sky fluxes, clouds, and/or cloud-radiation interactions.

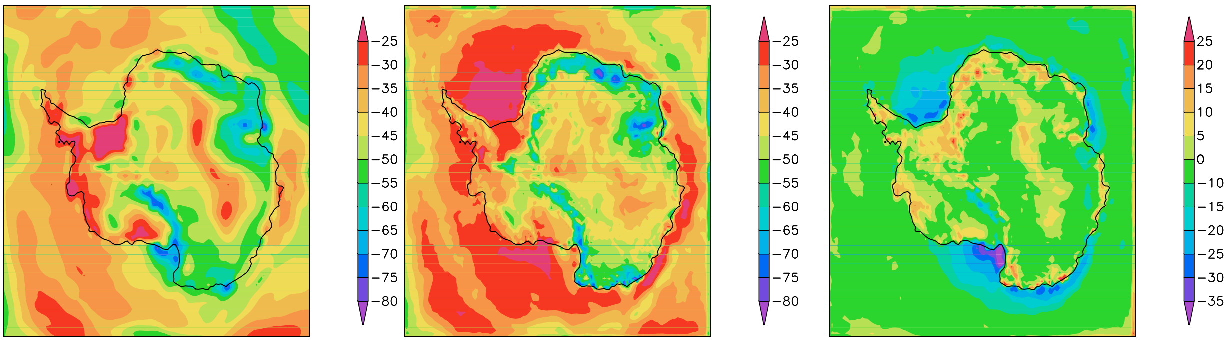

Figure 5.35: *Net longwave radiation at the surface (W/m^2) in austral winter (JJA), 1997. ERA40 (left), HIRHAM (middle), difference "ERA40 minus HIRHAM" (right).*

In Antarctica, there have been very few direct measurements of the atmospheric fluxes of latent and sensible heat. The horizontal and temporal resolution of the existing measurements

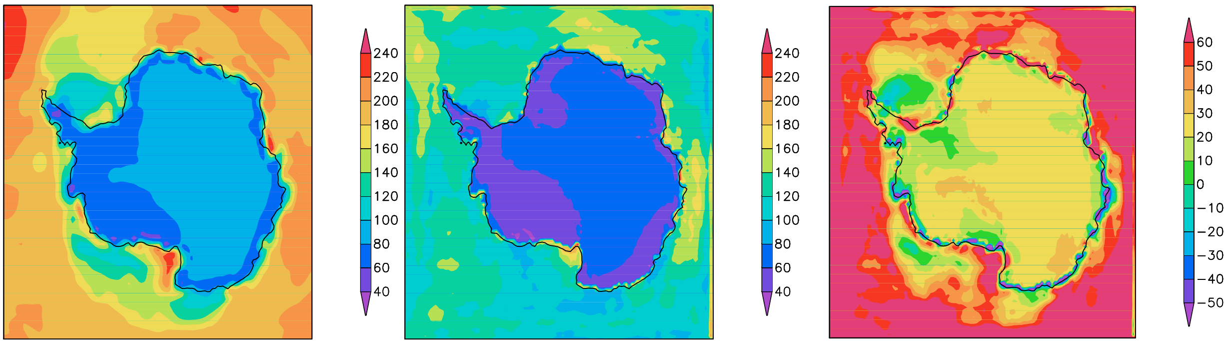

Figure 5.36: *Net shortwave radiation at the surface (W/m^2) in austral summer (DJF), 1997. ERA40 (left), HIRHAM (middle), difference "ERA40 minus HIRHAM" (right).*

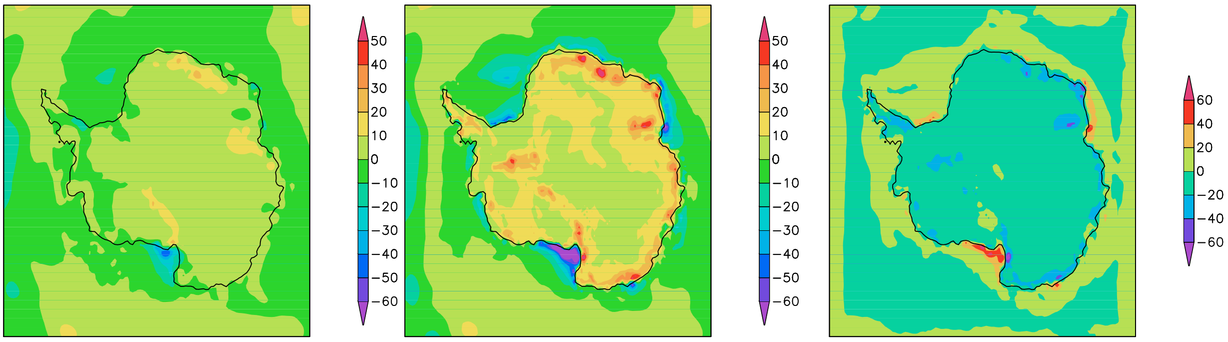

Figure 5.37: *Sensible heat flux at the surface (W/m^2) in austral summer (DJF), 1997. ERA40 (left), HIRHAM (middle), difference "ERA40 minus HIRHAM" (right).*

(King et al., 1996) is not sufficient for the purpose of directly validating a regional model. The highly stable stratification of the boundary layer restricts turbulent transport, as such, the summer means of sensible heat flux are only between 10 - 20 W/m^2, Fig. 5.37 - Fig. 5.38.

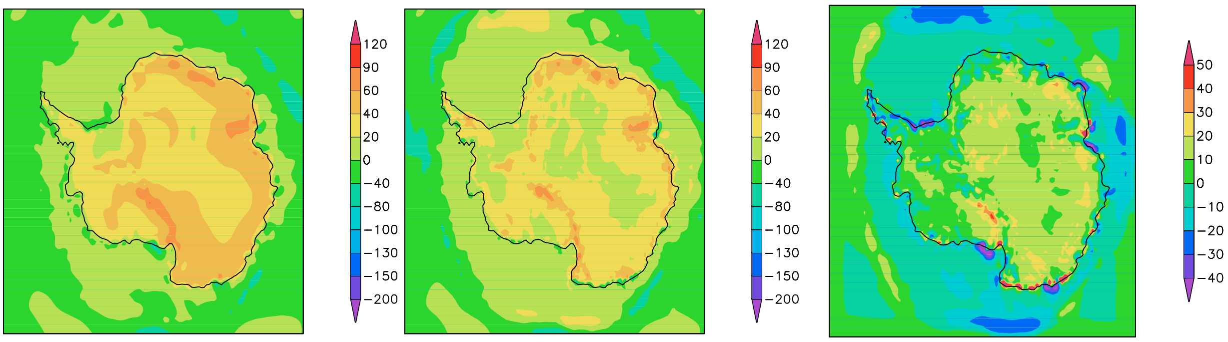

Figure 5.38: *Sensible heat flux at the surface (W/m^2) in austral winter (JJA), 1997. ERA40 (left), HIRHAM (middle), difference "ERA40 minus HIRHAM" (right).*

In the HIRHAM model, the seasonal difference is not as significant as in the ERA40 data. The winter mean values over the continent stay between 20 - 40 W/m^2. The heat fluxes from the surface to the atmosphere, via evaporation/sublimation or condensation/deposition, are very important in the warm regions. In the Antarctic area, it is not that significant since most of time the surface temperature is below freezing point. The model latent heat flux summer and winter means are shown in Fig. 5.39 and Fig. 5.40. Since the presence of open water leads to evaporation, the latent heat flux is closely connected with the sea-ice mask. Therefore during the winter season the horizontal structure closely follows the sea-ice mask. As was mentioned, before, only a few observational data are available for the radiation fluxes.

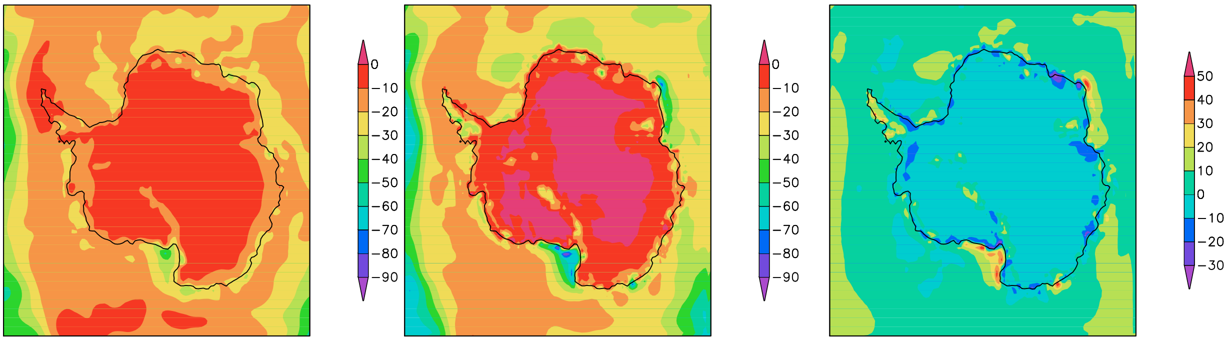

Figure 5.39: *Latent heat flux at the surface (W/m^2) in austral summer (DJF), 1997. ERA40 (left), HIRHAM (middle), difference "ERA40 minus HIRHAM" (right).*

Fig. 5.41 shows the radiation fluxes data that had been measured at the South Pole station (Dutton et al., 1989). This data were received between April 1986 - December 1987 from satellite observation by Pavolonis and Key (2003).

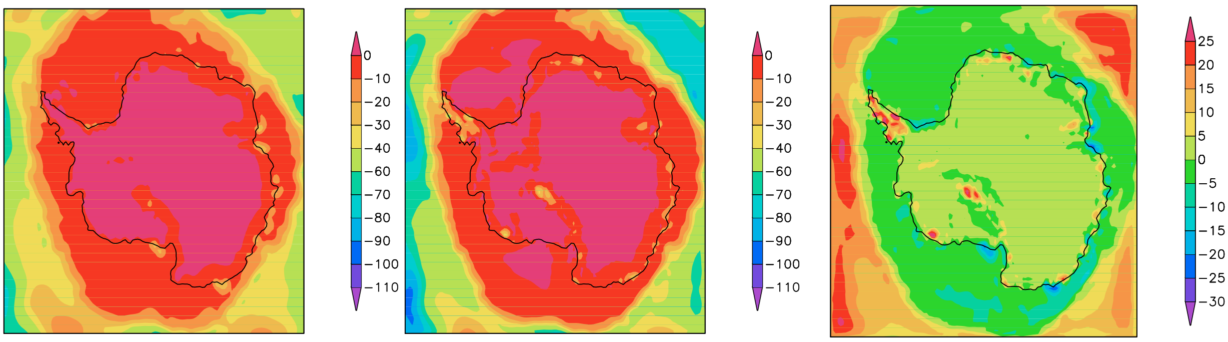

Figure 5.40: *Latent heat flux at the surface (W/m^2) in austral winter (JJA), 1997. ERA40 (left), HIRHAM (middle), difference "ERA40 minus HIRHAM" (right).*

The approximate absolute errors in the measurements reported by Dutton et al. (1989) are 2% for the SW measurements and 5% for the LW measurements. Radiation fluxes from the newly extended AVHRR (Advanced Very High Resolution Radiometer) Polar Pathfinder (APP-x) dataset were retrieved in order to improve our knowledge of the Antarctic's surface energy balance (Maslanik et al., 1997) (see Fig. 5.41). The standard APP products include the following: spectral radiance, viewing and illumination geometry, three cloud masks, clear sky surface temperature and albedo sampled at a 5 *km* resolution and into two daily composite images covering both of the polar regions. The retrieved cloud and surface parameters are then used as inputs to *FluxNet*, a neural network implementation of the two-stream radiative transfer model

Streamer (Key and Schweiger, 1998) intended for the calculation of the radiative fluxes. For the algorithm details see Key (2002).

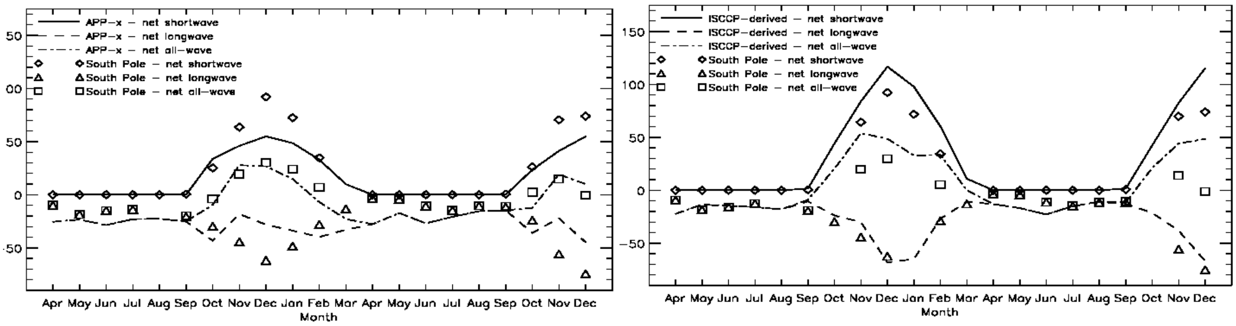

Figure 5.41: *Comparison of the surface net shortwave, longwave, and all-wave radiative fluxes from the APP-x dataset (left) and the ISCCP-derived dataset (right) and the net fluxes based on surface measurements (Dutton et al., 1989) made at South Pole Station (April 1986 - December 1987) from Pavolonis and Key (2003).*

The International Cloud Climatology Project (ISCCP) cloud product is the second satellite dataset (Schiffer and Rossow, 1983). Five geostationary and two polar orbiting satellites collect data. The data is then processed into global cloud datasets. The latest series of ISCCP datasets is the D-series (Pavolonis and Key, 2003). As with the calculation of radiative fluxes based on the APP-x data, cloud, atmospheric, and surface parameters from the ISCCP 3-hourly dataset (D1) were used as input to *FluxNet*. For more information concerning the ISCCP D1 dataset, see Rossow et al. (1996). The HIRHAM model simulated net radiation fluxes are shown in Fig. 5.42.

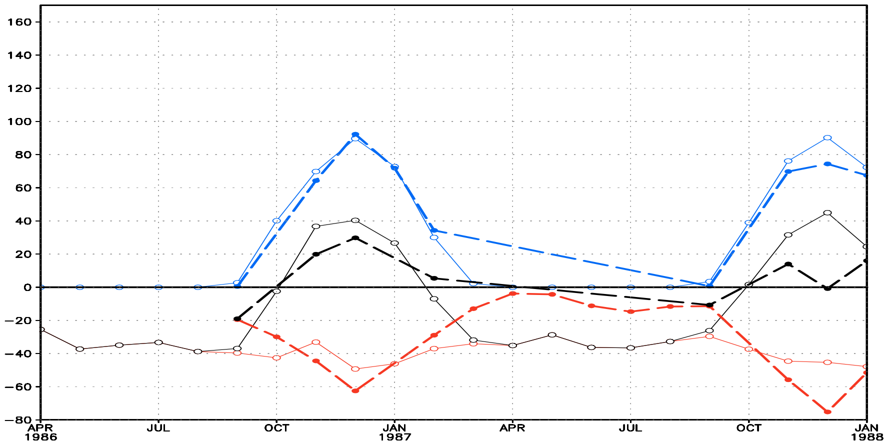

Figure 5.42: *Comparison of the surface net shortwave(blue), longwave (red) and all-wave radiative fluxes (black) from the HIRHAM (solid line) and observational data (dashed line) for South Pole Station (April 1986 - December 1987), (Dutton et al., 1989).*

The HIRHAM model simulation results for the net short wave radiation are the closest to observational data. Longwave radiation is simulated with sufficient accuracy and the accent in October to November 1986. APP-x dataset show the same splash as what the HIRHAM model does. Compared to the observational data, the HIRHAM has a lower net LW radiation flux during the winter, but already during next spring the situation becomes vice versa.

The same satellite datasets were used for the annual cycle radiation fluxes model validation at the Neumayer station for 1993 (see Fig. 5.43 and Fig. 5.44 for the results). In January 1993, the difference between the HIRHAM simulation and the observational data (75 W/m^2) for the net SW radiation is larger than what it is between either of the following: "the ISCCP and the observational data" (45 W/m^2) and "the APP-x minus observation" (5 W/m^2). The difference in the net SW radiation is caused by the difference in solar zenith angle between the location where the measurements were taken and the solar zenith angle used in the APP-x or ISCCP data (Pavolonis and Key, 2003). During the transition seasons the differences become smaller, reaching zero during the polar night. The highest annual amplitude is revealed in the model simulation of 140 W/m^2 and minimum annual amplitude is revealed in the APP-x data of 60 W/m^2. The model bias can be explained by the difference between the model and Neumayer station's real orography at and consequently, the strong dependence between the net SW radiation and the surface slope. Compared to the net SW radiation shown in Fig. 5.44, the simulated net LW radiation is in better agreement with observational data. The annual net LW radiation amplitude is 30 W/m^2 and it is smaller than what was recorded for the net SW radiation. Compared to the APP-x or ISCCP derived data for the austral summer (-40 W/m^2), the HIRHAM simulations show that for the same period, the lowest net LW radiation value is -50 W/m^2.

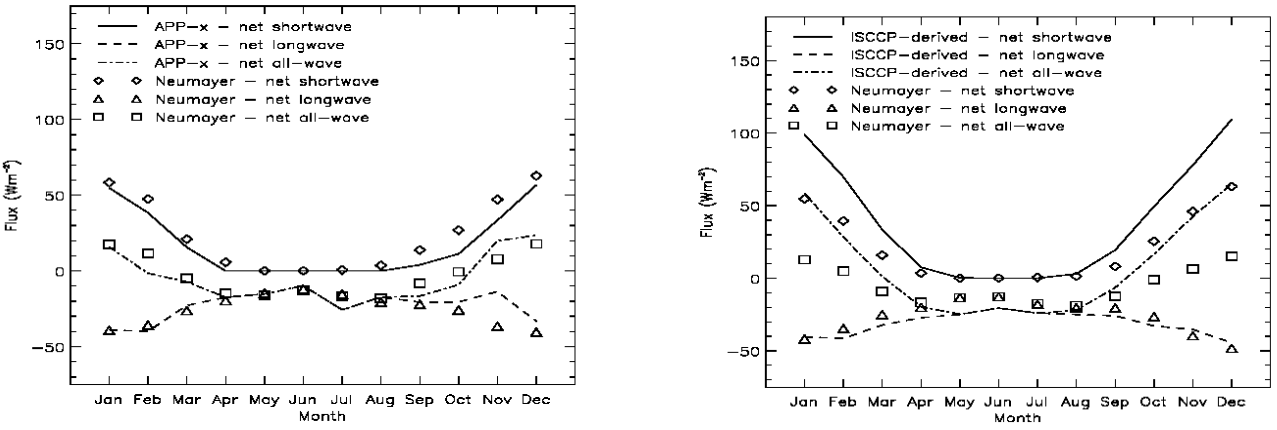

Figure 5.43: *Comparison of the surface net shortwave, longwave, and all-wave radiative fluxes from the APP-x dataset (left) and the ISCCP-derived dataset (right) and the net fluxes based on surface measurements made at Neumayer Station (1993). (Pavolonis and Key, 2003).*

Due to the strong overestimation of the net SW radiation, the total simulated radiation balance during the summer season is strongly positive 60 W/m^2. During the austral winter the

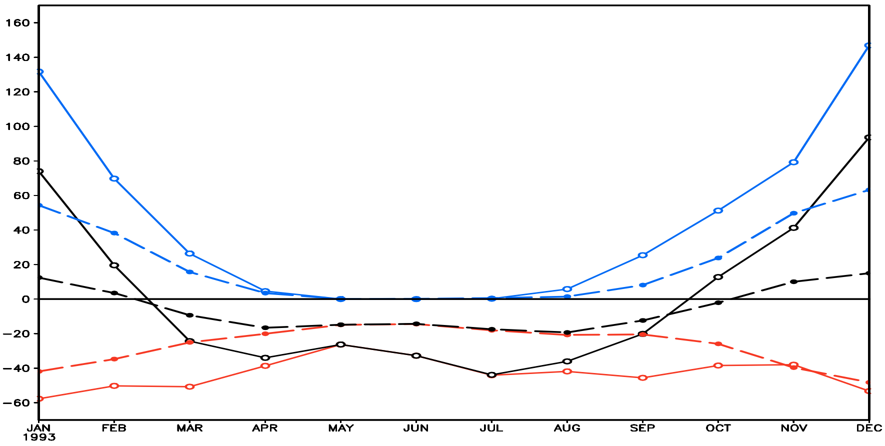

Figure 5.44: *The net SW (blue) (W/m^2), net LW (W/m^2) (red) and all-wave radiative fluxes (W/m^2) (black). HIRHAM simulation (solid line), observational data (dashed line). Neumayer station, 1993.*

total simulated radiation balance is negative -30 W/m^2. The observation shows that the summer net balance is slightly above zero (10 W/m^2) and that it is almost constant (-20 W/m^2) during winter. The net radiation fluxes do not give us the needed understanding of the key processes responsible for the radiation balance over Antarctica. Also, the radiation fluxes data from two stations are not enough for an accurate model validation. HIRHAM's simulated separated downward and separated upward components for the SW and the LW radiation are presented in Fig. 5.45. By following the monthly mean one can see that the HIRHAM model strongly underestimates the incoming solar radiation. The only obstacle in the way of downward shortwave radiation is the cloud cover. The seasonal means of the simulated cloud cover were presented in Tab. 5.4. There is no consistency between the cloud cover overestimation and the downward SW radiation. Apparently, the source of the strong bias is in the surface slope estimation with a big zenith angle, since the biggest difference grows from austral spring to austral summer.

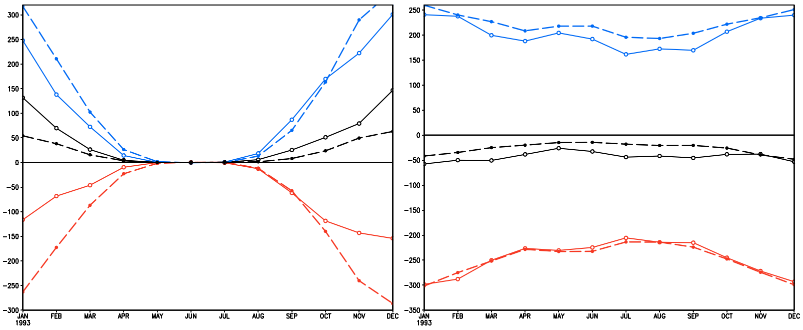

Figure 5.45: *The components (W/m^2) of the SW radiation (left), LW radiation (right) for Neumayer station in 1993. HIRHAM simulation (solid line), observational data (dashed line). In left graph: blue line is downward SW radiation, red line is upward SW radiation, black line is net SW radiation. In right graph: blue line is downward LW radiation, red line is upward LW radiation, black line is net LW radiation.*

A detailed look at the component of the LW radiation in Fig. 5.45 (right) reveals the connection between cloud cover estimation and downward LW radiation. The principal difference between the simulated cloud cover and the observation, that is the difference of 19 % occurs during austral winter. This coincides with a stronger underestimation of the downward LW radiation. Corresponding to the cloud emissivity, the model should now properly simulate the surface temperature. During summer when the difference between the model's cloud cover and the observed value become significantly smaller the downward LW radiation is in better agreement. The outgoing LW radiation is in quite good agreement of 5 W/m^2 with model output. This is true for the entire year. From November to March the model maintains a negative bias in the incoming SW radiation. Also, because the model takes multiple scattering into account, the negative bias in the modeled surface albedo may contribute to the negative bias in the incoming solar radiation. It seems that the albedo parameterisation does not correspond well with the albedo over Antarctica. When the HIRHAM model was used for the Arctic simulations, Box and Rinke (2003) discovered that the parameterisation gives too low albedo values for surface temperatures near the freezing point. van Lipzig (1999) presented the same results in Antarctic simulations with the RACMO model. Without detailed cloud measurements, the rates of a too-low surface albedo and a negatively biased incoming solar radiation on the bias cannot be clarified. Therefore, the detailed investigation of upward and downward components of the net SW and the net LW is essential to build a better understanding of the model radiation budget.

To resume, the mean sea level pressure structure was studied. The results show that the spatial and temporal resolution is in a good agreement with observational and re-analysis data. The HIRHAM correlation index with station data is higher than what the correlation index is from the ERA40 or the NCEP re-analysis. The vertical and horizontal temperature structures are in a good agreement with the observational and radiosonde data. The cold surface summer bias, which is present throughout the validation period, appeared due to cloud cover overestimation.

Indeed, due to cloud cover overestimation, a small bias in radiation fluxes can be observed. The model radiation fluxes were studied by employing two station's observational data and two different satellite datasets. The HIRHAM model's results are very similar to the APP-x data. An underestimation of the surface wind field was discovered. Despite this, the surface inversion depth, which is strongly linked to the wind field, is in a good agreement with the satellite data.

An attempt to investigate the origin of the MSLP and 2 m temperature summer biases was carried out. This was achieved through three sensitivity experiments one was based on a revised stability function PBL, the other was based on an increased threshold relative humidity in cloud cover calculations and the final one was based on a changed relaxation zone size in the boundary area.

5.7 Sensitivity studies with the HIRHAM model

A large summer temperature bias was detected in the HIRHAM simulations. As such, it was necessary to discover how the model's key processes influenced it's temperature evolution. In order to study the processes responsible for the surface temperature and MSLP summer bias in the model climate simulations, a series of sensitivity experiments using the HIRHAM model were conducted.

The revised stability function was introduced to both increase the heat flux towards the surface and to reduce the summer surface temperature bias.

Modeling studies show that the simulated high southern latitude climate is highly sensitive to the radiation parameterisation (Hines et al., 2004). The threshold relative humidity was changed to reduce the cloudiness and to increase the surface temperature during the summer season.

Most regional models predict full field within the regional model domain without any knowledge of large - scale features resolved by the driving global analysis, except in the buffer zone near the lateral boundaries. Therefore, the additional experiment was carried out with the increased/decreased boundary relaxation zone width. The results of the above described sensitivity experiments are further explained below.

5.7.1 Planetary boundary layer

The Antarctic is a place with unique climate features. There exist complex nonlinear feedback mechanisms between the land surface and the atmosphere. During winter and for part of the summer, the Antarctic's intense radiational cooling and highly transmissive atmosphere effectively generates a persistent low-level temperature inversion. This inversion, which is present for almost the entire year, reaches its greatest depth over the higher elevations of the Antarctic's ice sheet. The inversion is not any stronger at the end of the polar night than it is at the beginning. This is because it's equilibrium is reached between the surface's longwave radiation loss decreases as temperature falls while the downward radiation from the inversion layer changes relatively little over time. Over the Antarctic plateau, the stable stratified boundary layer influences the heat exchange between the land surface and the atmosphere. In this case a small amount of vertical mixing takes place and a small amount of heat is transported towards the surface. The surface also gets colder from outgoing longwave radiation. Such conditions further maintain the stable stratification. In the HIRHAM model the use of different planetary boundary layer (PBL) parameterisations leads to different heat and momentum fluxes from the surface to the atmosphere. These differences are of the same order as those that are due to synoptic-scale changes (Dethloff et al., 2001). The strong momentum diffusion combined with weak heat diffusion at high Ri numbers is a feature of the HIRHAM model's stability function. A stability function by Louis et al. (1982) increased the turbulent heat flux towards the surface during stable conditions and improved the winter soil bias in the ECMWF model (Viterbo et al., 1999). We carried out the sensitivity run (SR1) with the new constant d=1, as proposed by (Viterbo et al., 1999), instead of the old (d=5, see section 3.5) in the empirical formulation of the stability parameter:

$$f_m = \frac{1}{1+(2\cdot b\cdot Ri)/\left(\sqrt{1+d\cdot Ri}\right)}, \tag{5.5}$$

$$f_h = \frac{1}{1+(3\cdot b\cdot Ri)/\left(\sqrt{1+d\cdot Ri}\right)}. \tag{5.6}$$

This formulation has very little impact on the surface momentum flux over land, therefore it does have not much of an effect on the large scale circulation. The ratio of momentum and heat diffusion is reduced, effectively increasing the heat flux towards the surface (Viterbo et al., 1999). This sensitivity experiment aimed to show whether or not the new stability function would decrease the summer surface temperature bias in the model simulations. Taking the new parameter into account, a one year HIRHAM test run was carried out. Moreover, the differences between the control run (CR) and SR1 were calculated. The differences in 2 *m* temperature are shown in Fig. 5.46. Negative values indicate an increase in the 2 *m* temperature in the PBL SR1. Looking and comparing the two model versions, there were no remarkable differences in their horizontal distribution of 2 *m* temperature. In both the Antarctic's winter and summer seasons, the differences between the CR and SR1's are generally small (± 1.2 °*C*). The main differences are most likely to be found over the Antarctic plateau, where summer SR1 2 *m* temperature values are up to 1.2 °*C* lower than CR values as well as in the continent's north-east part where relative to CR, SR1 experiences a surface warming of up to 1°*C*. However, in the southern winter, compared to CR, SR1 values over the plateau can be up to 1.2 °*C* higher. While it is not immediately clear which model version is correct, CR is probably closer to reality than what SR1 is because the formers 2 *m* temperature bias is smaller during southern summer.

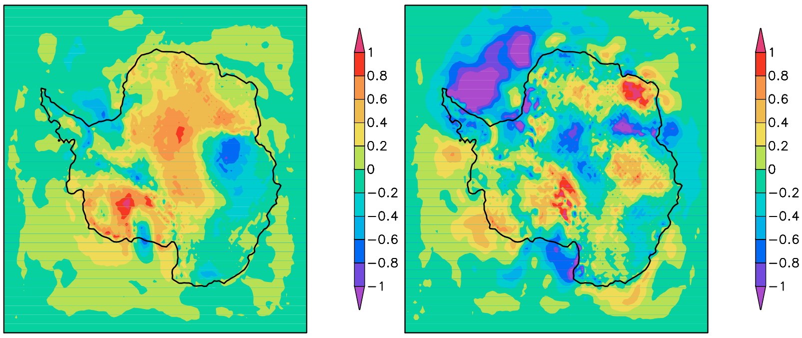

Figure 5.46: *2 m temperature (°C) [control run minus sensitivity run] in austral summer (DJF) (left) and in austral winter (JJA) (right), 1997. HIRHAM simulations.*

In Fig. 5.47, it is possible to see the MSLP differences between CR and SR1. During the summer and winter seasons, the MSLP varies within ± 3 *hPa* between CR and SR1. The strongest surface inversion is observed over the flat Antarctic plateau which is maintained there

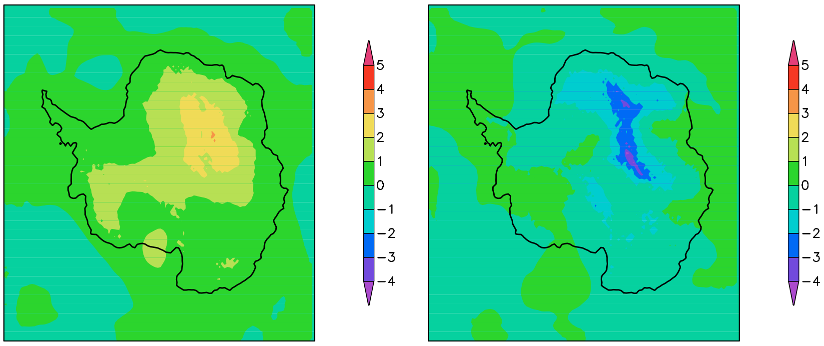

Figure 5.47: *Mean sea level pressure (hPa)[control run minus sensitivity run] (°C) in austral summer (DJF) (left) and in austral winter (JJA) (right), 1997. HIRHAM simulations.*

by the stable stratified PBL. Therefore, the revised stability function introduced the strongest disparity in the MSLP over the Antarctic plateau. Fig. 5.48 shows the difference between CR and SR1 in the total cloud cover and the net shortwave radiation. In this case, in order to show the feedback mechanism in the atmosphere-surface interaction, as demonstrated in the model, only austral summer means were presented. Over most of the Antarctic and during the austral summer the revised stability function increased the simulated cloud cover by 3 up to 12 %. The decreased stability function increased the vertical mixing of the inversion layer. Therefore, more low level clouds developed and reduced the net shortwave radiation by maximum 6 W/m^2 as it is shown in Fig. 5.48 (right). A good example is the Amery Ice Shelf. Stronger winds lead to increased turbulence which in turn, mixed warmer air down and decreased vertical gradients. Inversions under clouds are generally weaker (lower temperature difference) and shallower (lesser depth). An increased downward infrared flux, which occurs under clouds, causes the surface to warm up, or to at least reduce it's cooling rate. Although it is easy to see how wind and longwave flux affects temperature and inversions, the resulting relationships are not as simple as might be expected. During both seasons, in the SR1 the surface fluxes such as sensible heat flux and latent heat flux (not shown here) display only minor changes, within $\pm$ 2 W/m^2. Thus, it decreases the sublimation rate, and the net mass balance (averaged over the grounded ice) was increased from 118.86 $mm/year$ to 120.12 $mm/year$. Fig. 5.49 illustrates the net longwave radiation (LW) difference between CR and SR1. During the summer season in Victoria and Wilkes land, the net surface LW radiation increased in SR1 between 2 and 6 W/m^2. Over the rest of the Eastern part of Antarctica it decreased from 1 to 4 W/m^2. The revised PBL scheme has slightly increased the downward sensible heat flux. This increased sensible heat flux has increased the surface temperature and in turn, it has increased the LW cooling. Once again, this experiment proved the complexity and nonlinear feedback of the atmospheric processes that are taking place in the lowest levels of the Antarctic boundary layer. The simulation results showed that new stability functions only partly decreased the summer surface temperature bias. Therefore, additional experiments were carried out to find out the key processes responsible for the summer temperature bias in the surface temperature and cloud cover.

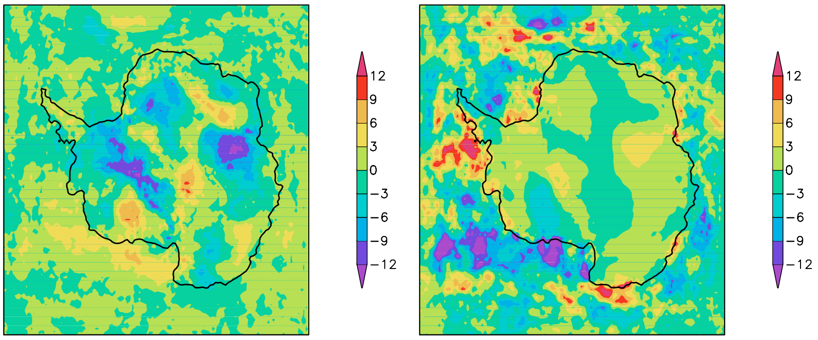

Figure 5.48: *Total cloud cover (%) (left) and net shortwave radiation at the surface (W/m^2) (right) in austral summer (DJF), 1997. [Control run minus sensitivity run], HIRHAM simulations.*

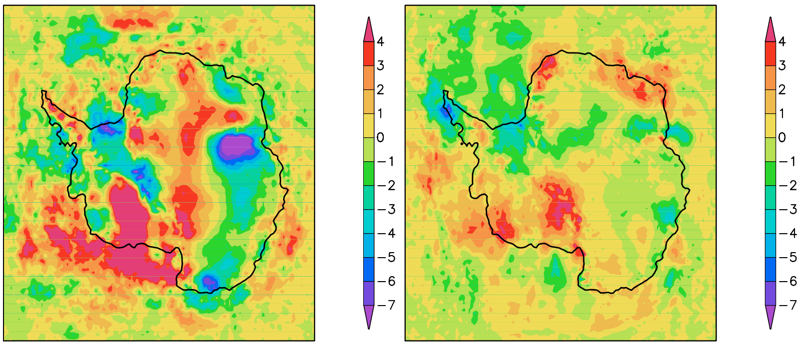

Figure 5.49: *Net longwave radiation at the surface (W/m^2) [control run minus sensitivity run] in austral summer (DJF) (left) and in austral winter (JJA) (right), 1997. HIRHAM simulations.*

5.7.2 Cloud cover

The parameterisation of clouds in climate models is one of the largest sources for uncertainty in the simulation results. Improvement of the model's cloud parameterisation is therefore a challenging but also promising aspect of model development. Clouds influence the energetics of the atmosphere in at least two major ways. Firstly, during a cloud's condensation process the condensed water is removed from the atmosphere through precipitation releasing large amounts of latent heat. Secondly, the scattering, absorption, reflection, and emission of radiation clouds strongly influences atmospheric radiation, and thereby also effects the energy budget of the Earth. The above mentioned results of the HIRHAM simulations using the ECHAM4 physical package exhibits deficiencies in the cloud distribution. The regional climate simulations showed large cold bias in the surface temperature - this is particularly true during the summer months. There are significant deficiencies in the simulation of Antarctic cloud radiative effects. The optical thickness of Antarctic clouds appears to be excessive. This contributes to a warming effect in surface temperature during winter and a deficit in downward shortwave radiation during summer.

The sensitivity experiment with increased threshold relative humidity was carried out in order to reduce the cloud formation. Hypothetically speaking, the summer surface temperature bias will be decreased by increasing the threshold relative humidity. This process should subsequently reduce the cloud cover. These changes affect the vertical distribution of the clouds. Since the relative humidity decreases with the high the main reduction of the clouds is expected to occur in the middle and partly lower part of the troposphere. In a case where there are less clouds, more shortwave radiation may reach the surface and warm it up (that is, during the summer season). Low thick clouds primarily reflect solar radiation and cool the surface of the Earth. High, thin clouds primarily transmit incoming solar radiation; at the same time, they trap some of the outgoing infrared radiation emitted by the Earth and radiate it back downward, thereby warming the Earth's surface. The modified threshold relative humidity was used for one year test run. The simulations have been performed with the unchanged version of HIRHAM and with a modified minimum threshold value for grid-mean relative humidity ($U_{c,top}$). For each grid box, sub-grid cloud formation was included in the large scale cloud scheme by incorporating fractional cloud cover (parameterised as a non-linear function of grid-mean relative humidity). This was done for the so-called ”critical relative humidity”, which has to be exceeded for the condensation process to begin. This profile is set to the value of 0.99 for the lowest atmospheric levels in the model, decreasing to a value of 0.4 in higher levels of the atmosphere. Prognostic variables related to cloud formation are water vapor and total cloud water. For these variables, budget equations are solved. In the sensitivity run the empirical formulation of the cloud cover fraction was similar to section 3.5 but with a different constant value, $U_{c,top}$ =0.99. Fig. 5.50 shows the cloud cover difference ”control HIRHAM run (CR) minus sensitivity run (SR2)” during the summer and winter year of 1997.

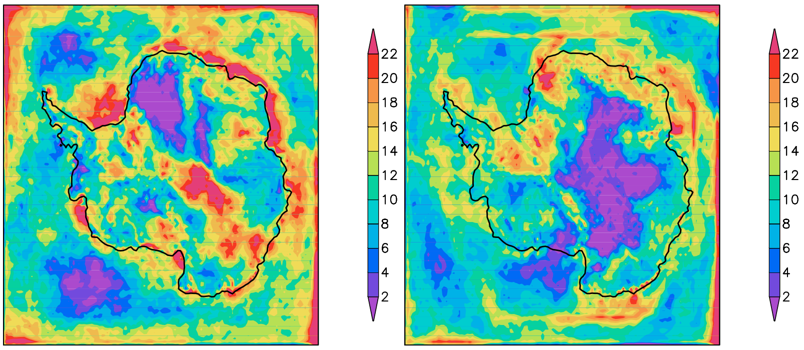

Figure 5.50: *Cloud cover [control run minus sensitivity run] (%)in austral summer (DJF) (left) and in austral winter (JJA) (right), 1997. HIRHAM simulations.*

During the austral summer, relative to CR the total cloud cover in SR2 decreased from 3 % over Queen Maud Land to a maximum of 20 % along the coast and Transantarctic mountains.

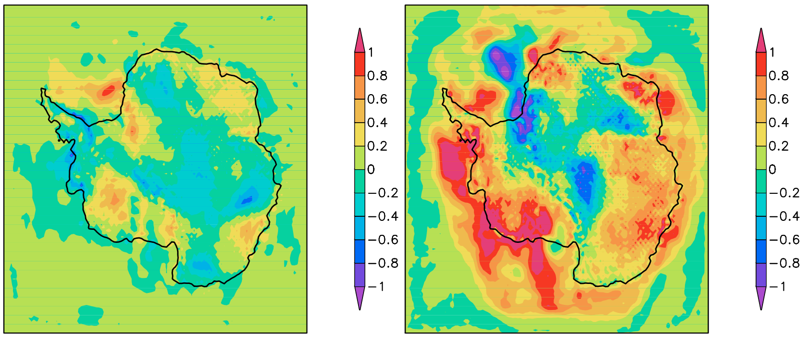

Figure 5.51: *The 2m temperature [control run minus sensitivity run] (°C) in austral summer (DJF) (left) and in austral winter (JJA) (right), 1997. HIRHAM simulations.*

During the summer, the difference between the two model runs had a less uniform horizontal structure that it did during the winter. Throughout the winter, HIRHAM SR2 simulated 2 % fewer clouds over the whole Eastern part of Antarctica and 15 % fewer clouds along the coastline. Clouds influence the radiation budget and therefore both climate and temperature. Clouds reflect a large fraction of solar radiation that, results in a cooling of the surface. On the other hand, clouds inhibit longwave radiation loss from the surface: this can lead to higher surface temperatures. The dominant process depends on many factors including cloud type and thickness, the magnitude of the solar radiation, and the albedo of the underlying surface.

As can be seen in shown in Fig. 5.51 during the summer season the 2 m temperature increased by 0.2 - 0.8 $^{\circ}C$ in SR2, that is, when compared to CR. During the winter months, when clouds keep the continent warm, a reduction in cloud cover leads to the cooling of Victoria and Wilkes Land by 0.2 - 0.8 $^{\circ}C$. In SR2, the net shortwave and longwave radiation at the surface, as well as latent and heat fluxes (not shown) do not change significantly ($\pm$ 1.5 W/m^2). As such, we may conclude that the upper and middle level clouds were decreased by an increased threshold relative humidity. This conclusion is in agreement with the SR1 results. Over the Amery Ice Shelf and during the austral summer, the SR1 showed that due to the revised stability function the cloud cover was increased by 10 %. Hence, the surface temperature was increased by 1 $^{\circ}C$. In the SR2, despite a reduction of cloud cover by almost 20 % there did not appear to be any significant changes in the 2 m temperature. Therefore, one may conclude that the main cloud cover reduction took place in the middle part of the atmosphere. The balance between shortwave and longwave radiation at the surface determines whether clouds will have a cooling or warming effect. Thin clouds increase surface net radiation because they transmit substantial shortwave energy to the surface and also, because they enhance longwave input. Multiple shortwave reflections from clouds are responsible for increased solar insolation on the snow's surface. Therefore, thin clouds over a bright surface increase both shortwave and longwave contributions. To shift the radiation balance, the cloud albedo must increase (by increasing the optical thickness) in order to reduce the shortwave radiation at the surface. The brighter the ice sheet (the higher the surface albedo), the greater cloud optical depth must be in order to have a surface cooling effect (Bintanja and van den Broeke, 1996). Fig. 5.52 shows the MSLP difference between CR and SR2, of HIRHAM simulation, during the summer and winter seasons. During austral summer and winter, the MSLP shows a small difference within ± 1.2 *hPa*. It is slightly smaller than was shown in the sensitivity run with the revised stability function in the PBL scheme. The 500 *hPa* height differences for summer and winter seasons (CR minus SR2) are shown in Fig. 5.53. The summer difference plot indicates the weakening of the polar anticyclone. This tendency is not only observed at the surface, it can also be found in the upper levels of the atmosphere. The 500 *hPa* height simulated in the CR is almost 20 *gpm* higher than the values in SR2. During the winter (JJA), the opposite situation takes place. Cloud reduction leads to a strengthening of the polar anticyclone. This is due to of presence of strong temperature inversions in the lower troposphere over much of the Antarctic continent. That is, clouds warm the surface and cool the free atmosphere. Based on this result, we conclude that the change in one cloud model parameter was not able to improve the summer 2 *m* temperature or to reduce the cold summer bias which is up to 12 °*C* colder than the observations. For the most part, cloud cover reduction have been previously observed at the upper layers of the atmosphere failing to show the direct and strong influence of the clouds on the surface's processes. The reason for the

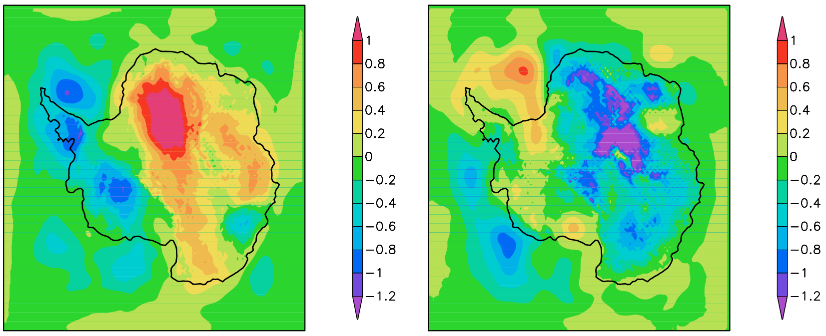

Figure 5.52: *Mean sea level pressure [control run minus sensitivity run] (hPa) in austral summer (DJF) (left) and in austral winter (JJA) (right), 1997. HIRHAM simulations.*

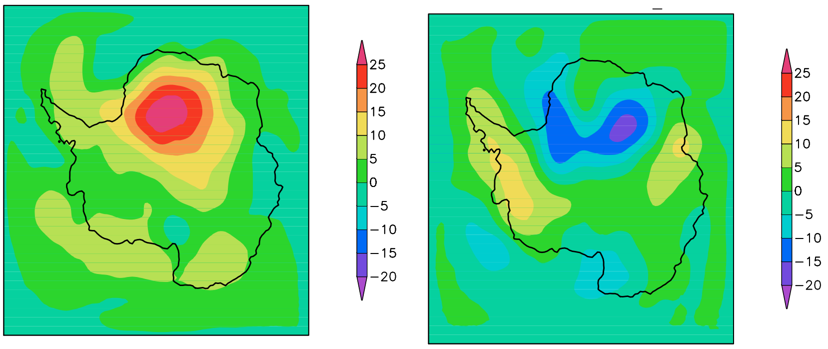

Figure 5.53: *500 hPa geopotential height [control run minus sensitivity run] (gpm) in austral summer (DJF) (left) and in austral winter (JJA) (right), 1997. HIRHAM simulations.*

overestimation of cloud cover during all seasons should be further investigated. The method for calculating the total cloud cover could be another reason for the apparent discrepancy between the observed and simulated tests. In HIRHAM, this is done using the maximum random overlap assumption. With this approach, vertically continuous clouds are assumed to be overlapped to their maximum possibility, while clouds at different heights, that are separated by an entirely cloud-free model level, are randomly overlapped. However, studies by Hogan and Illingworth (2000) indicate that for vertically continuous clouds, the mean overlap is distinctly more random than it is assumed by the maximum-random overlap. For such clouds, this would result in higher values of total cloud cover. Räisänen (1999) studied the effects of vertical resolution on cloudy-sky radiation. Räisänen (1999) showed that both the longwave and the shortwave radiation calculation was sensitive to the cloud overlap assumption. Comparing the 25 level HIRHAM version to the 19 level HIRHAM version, in the latter, the decrease in winter cloud cover is consistent with the decreasing integrated total water and precipitation observed for the winter atmosphere. During the summer, the difference in total cloud cover becomes stronger. Over the continent the 19 level HIRHAM version gives results from 10 % up to 20 % lower than does the 25 level HIRHAM version. Thus, the 2 m temperature over the continent increases by up to 3 $^{\circ}C$. In conclusion, both model versions disagree with observed total cloud cover by simulating too much clouds. One source of the error could be introduced by the maximum-random overlap method to calculate total cloud cover. It would be highly desirable to attain a detailed validation of the vertical structure of the simulated cloud amount. Further experiments with microphysical cloud parameters and a more elaborate cloud parameterisation scheme are also suggested.

5.7.3 Lateral boundary conditions

The utility and use of regional climate models has grown immensely over the years which has made them indispensable tools for climate studies. The seminal work of Denis et al. (2002) clearly establishes the benefit of dynamic downscaling from coarse resolution analysis. They showed that dynamic downscaling has the strong ability to reproduce realistic small scale features. In a related study Antic et al. (2004) showed that complex topography and coastline features have a strong impact on the reproducibility of small scale climate features that an regional climate model can resolve. But with growing use of regional climate models it is also becoming apparent that the regional climate model integrations are limited by the errors in forcing from the lateral boundary conditions (Noguer et al. (1998); Christensen et al. (1998); Misra et al. (2003)). When the dynamical downscaling technique is used with re-analyses, such as with ERA40, all the regional details are simulated by the regional model. This occurs without an input of direct regional-scale observations. What drives the regional model is only the global re-analyses on coarse grids. Downscaling techniques are supposed to retain all the large-scale information that have been resolved well by the global re-analysis data assimilation. Moreover, downscaling techniques add smaller-scale information which could not be generated by the global data assimilation model's coarse-resolution. However, regional models, have to deal with the problem of lateral boundary conditions, which is mathematically ill-posed. The inconsistencies between the model solution and the driving coarse model field along the boundaries produce undesirable noise, and often, instabilities. In buffer zones that cover several grid points, along the model boundary, Davies' lateral boundary relaxation method (1976) can usually alleviate such errors. When producing regional solutions, the regional model is not meant to modify large-scale fields. The differences between the regional model and the provided largescale data are highlighted here: the former better represents topography, surface characteristics, and also quite different representations of subgrid processes. However, the extent to which the regional model deviates from the external data is a matter of debate. Since the external data are usually only provided near the lateral boundaries, large domains will result in a significant regional climate model - forcing differences at the synoptic scale, this is particularly true over the polar regions (Rinke and Dethloff, 2000). The following authors explain the several issues regarding the one-way nested regional climate models: Giorgi and Mearns (1999), Marbaix et al. (2003) and Antic et al. (2004). The ill-posed mathematical formulation of the boundary conditions contributes to an amplification of forecast errors usually attributed to parameterisation errors or any other model formulation errors or inaccuracies. Two sensitivity runs were done for the purpose of better understanding the errors caused by lateral boundary conditions. During the control run surface pressure, horizontal wind, specific humidity and air temperature were relaxed in a 10 point wide boundary zone (hereafter CR_{k10}). The coefficient α_k as described in section 3.2 is the relaxation weight: within the relaxation zone, this joins the boundary forcing data with the model data. α_k is calculated as:

$$\alpha_k = 1 - tanh(ak) \tag{5.7}$$

where a is a constant and k is the number of points in the relaxation zone. $a = 0.5$ when $k = 8$, $a = 0.33$ when $k = 10$ and $a = 0.25$ when $k = 12$. The α_k values for the control and sensitivity runs are shown in Tab. 5.5.

k	0	1	2	3	4	5	6	7	8	9	10	11
α_k (k=8)	1	0,538	0,238	0,095	0,036	0,013	0,005	0,002				
α_k (k=10)	1	0,678	0,417	0,238	0,130	0,069	0,036	0,019	0,010	0,005		
α_k (k=12)	1	0,755	0,538	0,365	0,238	0,152	0,095	0,059	0,036	0,022	0,013	0,008

Table 5.5: *The relaxation weight* α_k.

The first sensitive run was carried out with $k = 8$ (hereafter SR_{k8}) wide boundary zone. Meanwhile, the second sensitivity run was carried out with $k = 12$ (hereafter SR_{k12}) wide boundary zone. Both runs were done for the year 1997. Based on simulation results the seasonal mean

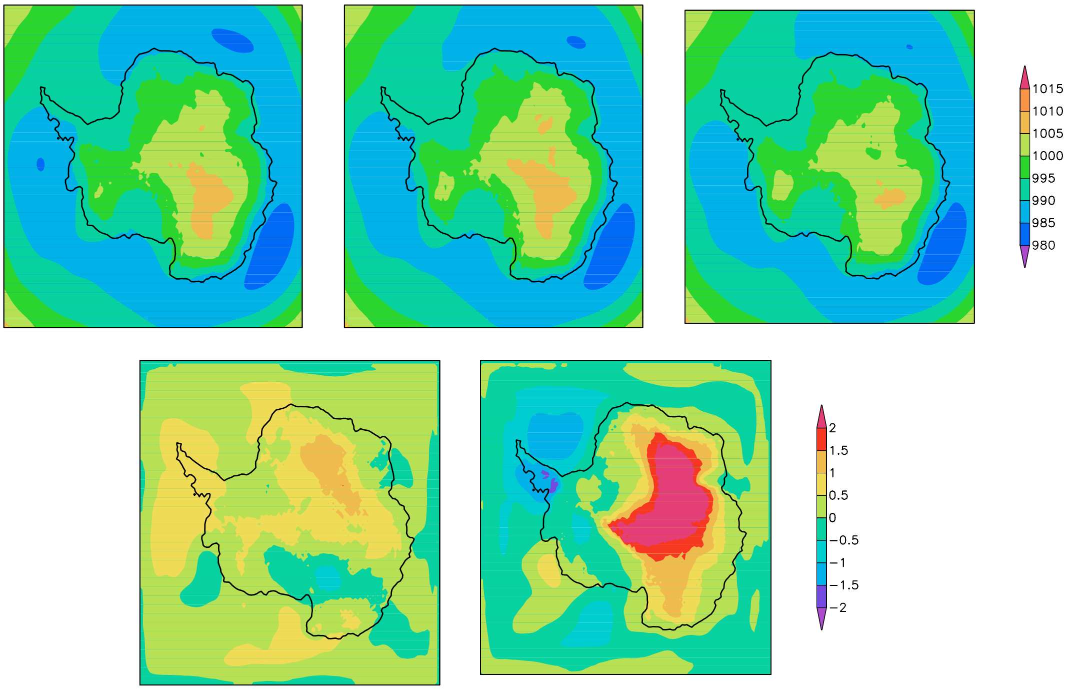

Figure 5.54: *Mean sea level pressure (hPa) in austral summer (DJF), 1997.* SR_{k8} *(left),* CR_{k10} *(middle),* SR_{k12} *(right), (top panel). The mean sea level pressure differences [*$CR_{k10}-SR_{k8}$*, left] and [*CR_{k10}*-*SR_{k12}*, right], bottom panel. HIRHAM simulations.*

was calculated as were the differences between control and sensitivity runs. Fig. 5.54 shows the horizontal patterns of the mean sea level pressure (MSLP). It also illustrates the difference between control and sensitivity runs during the summer season.

Due to a slightly increased or decreased boundary zone width, we should not expect a big difference in the horizontal pattern of MSLP (upper panel). However, the difference becomes visible. SR_{k8} shows lower values in MSLP over the Indian Ocean and Bellingshausen Sea than CR_{k10}. If the lateral boundaries are close to the regional domain grid point, then at this point, an advection of the coarse-resolution circulation may be able to eliminate mesoscale features - this situation can be seen in the SR_{k12} sensitivity run over the Indian Ocean in Fig. 5.54, right. The twelve point thick buffer zone reduced the austral summer MSLP bias over the Antarctic plateau by 2 - 3 hPa. This, is almost 35 % of the MSLP summer bias found in the 40 years HIRHAM simulation. For the long time simulations with a domain over the Arctic, Rinke and Dethloff (2000) also found that most of the contribution to the error in the regional model derives from deviations in the large-scales.

Fig. 5.55 shows the winter (June-July-August) MSLP from the control and sensitivity runs, as well as the differences ($CR_{k10}-SR_{k8}$) and (CR_{k10}-SR_{k12}). The biggest difference between CR_{k10} and sensitivity runs in the MSLP horizontal pattern during austral winter is visible over the Ross Sea; as Fig. 5.55 shows, like in the other two plots, there is no strongly pronounced low pressure center in CR_{k10} . The changes are also visible over the Antarctic Plateau, where the

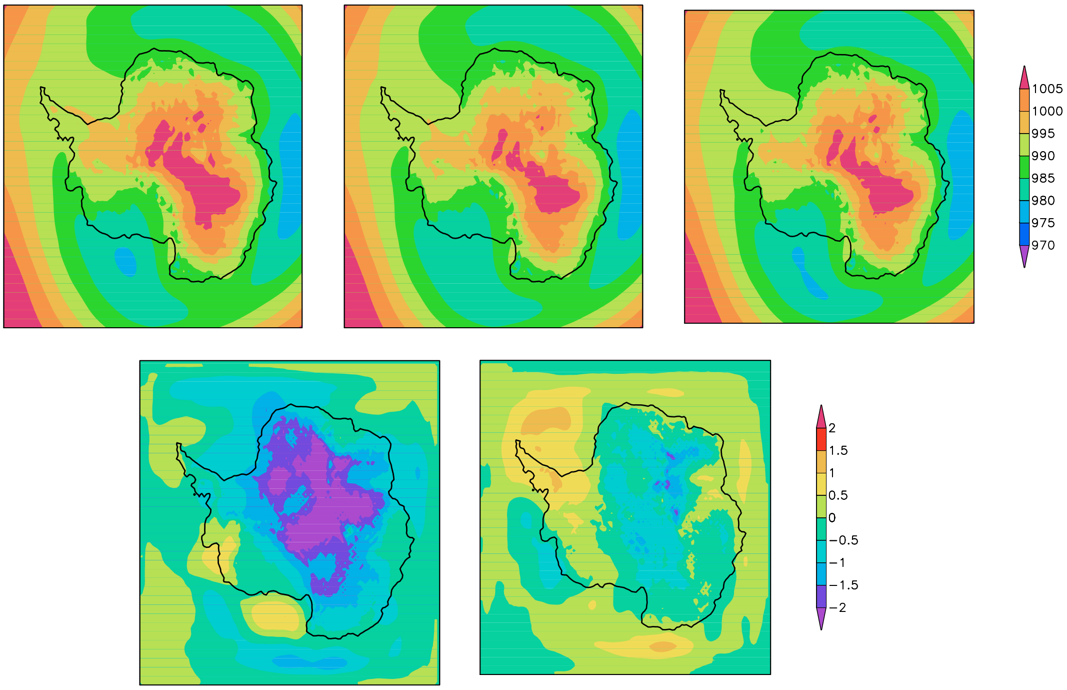

Figure 5.55: *Mean sea level pressure (hPa) in austral winter (JJA), 1997.* SR_{k8} *(left),* CR_{k10} *(middle),* SR_{k12} *(right), (top panel). The mean sea level pressure differences [*CR_{k10} *-* SR_{k8} *, left] and [*CR_{k10} *-* SR_{k12} *, right], bottom panel. HIRHAM simulations.*

SR_{k8} MSLP is higher than the CR_{k10} MSLP by 2.5 hPa and SR_{k12} MSLP is slightly higher than the CR_{k10} by 1 - 1.5 hPa. Regarding the control run, the HIRHAM simulation with the widest lateral boundary conditions did not show differences comparable to those that were observed during the austral summer. The MSLP seasonal mean calculated from the model sensitivity runs for summer and winter showed that the 10 points boundary zone is the best solution for the climate long-term run.

Based on one year simulations, the 2 m temperature seasonal mean was calculated for the three HIRHAM runs. Compared to the MSLP, the surface temperature is a less dependent variable from the lateral boundary condition's uncertainties. Therefore, the 2 m temperature horizontal pattern does not show the considerable disparity between the control and both sensitivity runs. Subsequently, only seasonal differences are presented. Fig. 5.56 shows the HIRHAM 2 m summer and winter temperature differences between CR_{k10} and both sensitivity runs. In section 5.3, the model validation demonstrated that from December to February the model underestimates the 2 m temperature over the Antarctic Plateau (by a maximum of 14 $^{\circ}C$). Neither of the new lateral boundary conditions decreased this austral summer bias. During the austral winter the SR_{k12} sensitivity study shows the stronger horizontal advection of warm air mass from the domain border to the sea-ice edge. On the border between open ocean and the sea-ice, stronger changes occur in its surface temperature and its heat fluxes. During the winter months (June-July-August) the sea-ice edge is located much closer to the lateral boundaries than what

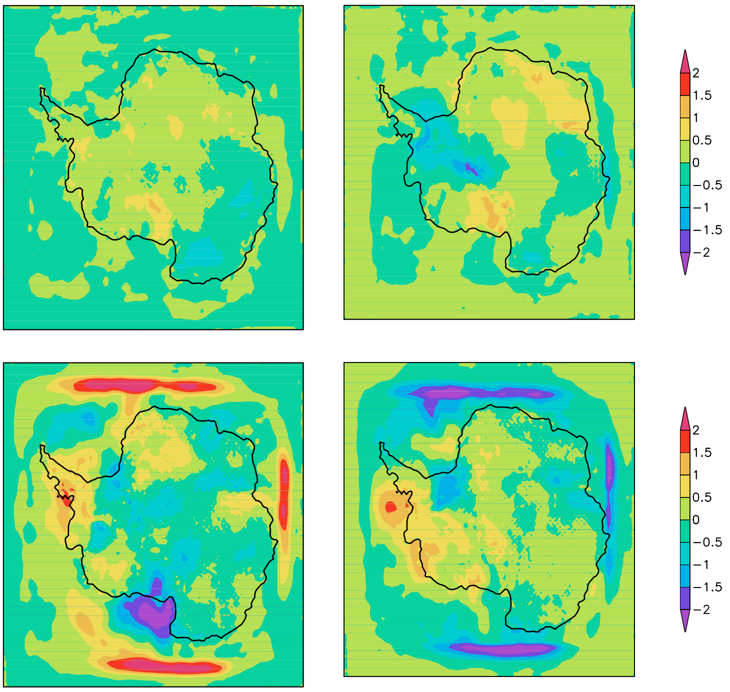

Figure 5.56: *The 2 m temperature (°C) differences [CR_{k10} - SR_{k8} , left] and [CR_{k10} - SR_{k12} , right]. The austral summer (upper panel) and austral winter (bottom panel), 1997. HIRHAM simulations.*

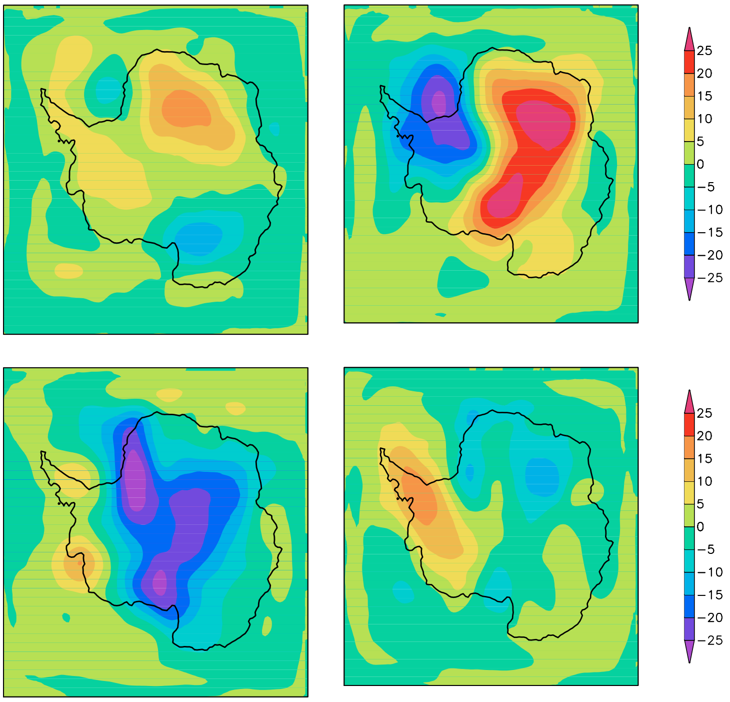

Figure 5.57: *500hPa geopotential height (gpm) differences [CR_{k10} - SR_{k8} , left] and [CR_{k10} - SR_{k12} , right]. The austral summer (upper panel) and austral winter (bottom panel), 1997. HIRHAM simulations.*

it is during the austral summer months (December-January-February). Therefore the boundary zone width plays a more crucial role for the 2 *m* temperature during the winter than what it does during the austral summer. Fig. 5.57 shows the CR_{k10} 500 *hPa* geopotential height minus sensitivity runs. For the summer and winter seasons, in 500 *hPa* height, the SR_{k8} and SR_{k12} differ by more than 20 *gpm* over the Antarctic continent. The differences between the control ans sensitivity runs show opposite features compared to the MSLP pattern. In the austral summer the wider lateral boundary relaxation zone does not decrease the 500 *hPa* geopotential height bias - this is further discussed in section 5.2. One of the explanations for such difference is the prevailing processes over the surface and in the upper levels of the atmosphere. At 500 *hPa* geopotential height the higher wind speed is predominant. Meanwhile, at the surface, the wind speed is significantly weaker. This suggests that, in the case of low relaxation, the problems are caused by fast perturbations in the upper levels (which cannot be damped due to the combination of high wind speed and low relaxation rate.) This conclusion is in agreement with Marbaix et al. (2003).

To resume, three sensitivity runs were carried out to reduce both the summer surface temperature bias and the cloud cover overestimation. The revised stability function proposed by Viterbo et al. (1999) was able to slightly increase the downward heat flux, and thus, only partly decrease the summer surface temperature bias. The increased threshold relative humidity value resulted in the upper and middle layer cloud reduction. This was not enough to increase the downward shortwave radiation in order to warm up the surface and to reduce the strong summer temperature deficit.

The boundary relaxation zone width sensitivity run produced an interesting result. The MSLP summer bias was reduced by 35 % due to the increased relaxation zone in the boundary areas. The MSLP seasonal mean calculated from the model sensitivity runs for summer and winter showed that the 10 points boundary zone is the best solution for the climate long-term run.

Nevertheless, since it represents a realization of only a single year, the model's sensitivity simulation cannot be directly compared to the climatology. However, the consistency of bias for both the surface temperature and the cloud cover indicates the following: in the HIRHAM model, the overestimation of cloud and the underestimation of the surface temperature over the Antarctic plateau are main problems.

Chapter 6

The surface mass balance over Antarctica

In the last few years, one of the most heavily discussed issues has been the global sea level rise. The contribution to sea level rise from the ice sheet in Antarctica over the last few decades is not well established and is also the subject of conflicting assessments. In order to attain a clear understand of the issue at hand, we need to first understand the transformations going on in the Antarctic. The ice sheet can be viewed as a chain mechanism for the income of snow and the output of ice. Through precipitation or snowfall, new snow is constantly added to the ice sheet. Ice is constantly being lost because the ice sheet is simultaneously melting directly into the seas and a small amount of runoff during periods of summer melt, and the calving of icebergs. In our model the last mentioned processes were not included and the main focus was on the atmospheric part. As the main components of the net mass balance over Antarctica, precipitation and evaporation comprise the main accent of our research. After a successful model validation, it is necessary to investigate the key processes that influence the net mass balance over the Antarctic continent in the model.

6.1 Total water vapour

Surface snow accumulation is the most important mass input to the Antarctic ice sheets. As a dominant term among various components of surface snow accumulation (precipitation, sublimation/deposition, snow drift), the precipitation is of particular importance in helping to assess the mass balance of the Antarctic ice sheets and their contribution to global sea level change. In comparison to the current estimations of global sea level rise of (about 1 to 3 $mm/year$), (Cullather et al., 1998), the annual precipitation over the ice sheets can be calculated in terms of an equivalent sea level decrease and is estimated to be quite large (about 8 $mm/year$). Under polar conditions, precise precipitation accumulation is a difficult parameter to measure. The strong wind makes it difficult to make accurate measurements because it is hard to distinguish between clear precipitation that falls down and precipitation that was transported by the wind. In contrast to the gauge measurements, accumulation estimates derived from glaciological methods are usually straightforward and are considered reliable. Unfortunately, one of the strong disadvantages of those data is the horizontal nonuniformity. The high-resolution model can provide us with a better understanding of the polar regions which is suffering from a lack of horizontal uniform data. Relative humidity (RH) is one of the parameters that can describe the amount of water vapour available in the air. We compared the RH's simulated vertical profiles with Neumayer station's observational data. We then linearly interpolated the simulation data to the above-mentioned stations location. The data was obtained from the four closest points to the station. The seasonal mean was calculated on the monthly mean base. The seasonal average, taken over a 17-year period, is shown in Fig. 6.1. The main intercomparison was done within the lowest 2400 *m*. For RH, the HIRHAM model is able to reproduce the radiosonde profile's most important features. However, the model is not able to reproduce the detailed vertical variability at vertical scales, that is, those of which are less than 1 *km*. For both seasons the main profile's structure looks similar. While the HIRHAM model slightly underestimates RH in the lowest 1500 *m*, it overestimates the RH above 1500 *m*. During the austral winter the difference between model simulation and station data slightly decreases because less water vapour is contained in the cold Antarctic air. Apparently, this overestimation, which is cause by sub-grid scale cloud formation, leads to the cloud cover overvalue that occurs during the summer and winter seasons. This conclusion can also explain the cold temperature bias over Antarctica found in the model simulation. Additionally, it again emphasizes the complicity of the atmospheric processes that are included in the model formulation. Due to the lack of RH radiosonde station data, we instead used satellite data in order to further evaluate the model. The vertical integrated humidity (or total water vapor, TWV) was compared to satellite data.

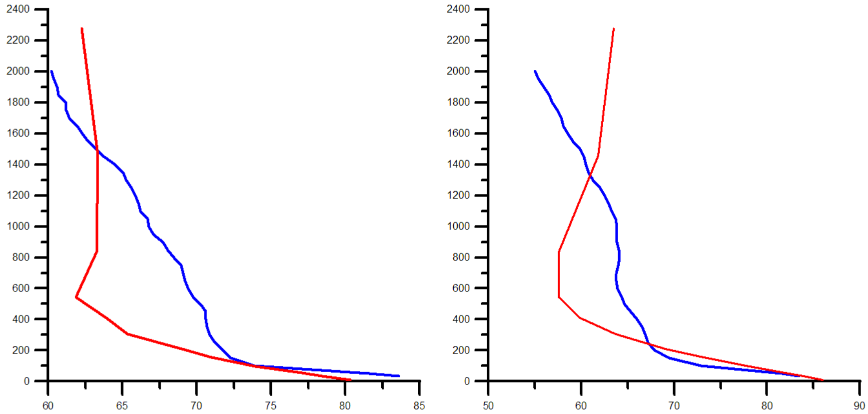

Figure 6.1: *Relative humidity (%) vertical profiles at Neumayer station austral summer (DJF) (left) and austral winter (JJA) (right), 1991-1998. HIRHAM (red), station data (blue). Y-axis – height (m).*

The TWV monthly mean maps obtained from the University of Bremen are based on AMSU-B (Advanced Microwave Sounding Unit B) data (Melsheimer and Heygster, 2005) and a modified version of Miao's algorithm (Miao et al., 2001) and available for the year of 2000. In a latitude-longitude grid which corresponds to 50 *km*, the horizontal resolution is $0.5 \times 0.5\,^{\circ}$. For a detailed intercomparison with simulation data, TWV fields were interpolated to the HIRHAM model's horizontal grid. The summer and winter means are shown in Fig. 6.2 and Fig. 6.3, respectively. As an effect of the retrieval algorithm restriction, there are missing data (this is the case for the Ronne Ice Shelf, for example). If the TWV is larger than 6 kg/m^2, the algorithm cannot determine the TWV from the AMSU data: this is due to channel saturation. The actual limit depends weakly on the temperature and humidity profile. By looking at the horizontal structure, one can say that HIRHAM simulations represent most of the features. These include larger values 2 - 2.5 kg/m^2 over the Antarctic Peninsula as well as along the Antarctic East and West coast. They also include small values over the East Antarctica plateau.

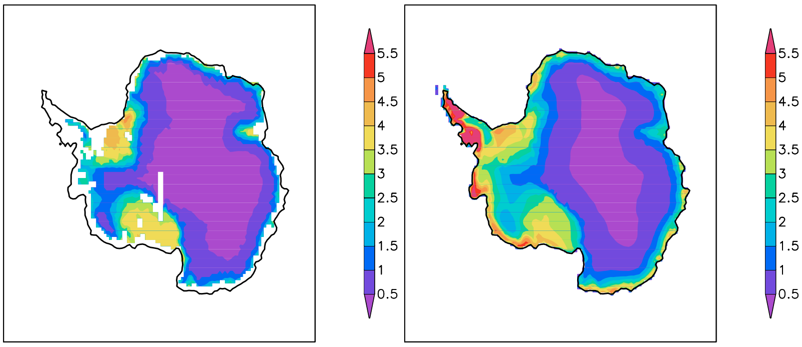

Figure 6.2: *Total water vapour (kg/m^2) in austral summer (DJF) 2000, AMSU-B (left), HIRHAM (right).*

The relatively prevalent precipitable water largely reflects the ability of the warmer atmosphere to hold more water vapour. Over the most of parts of the Antarctic's East, observations and simulations show a mean TWV value of about 0.5 - 1 kg/m^2. For both seasons, the HIRHAM model shows a higher value, of about 0.5 kg/m^2, over the plateau. The considerable deviations that occur along the Antarctic Peninsula during the summer season are caused by the retrieval algorithm restriction and the substantial influence of the Southern Ocean. During the winter seasons, the Antarctic's air is extremely dry. In the upper levels of the atmosphere, air tends to circulate toward Antarctica from lower latitudes. By the time the air descends over the

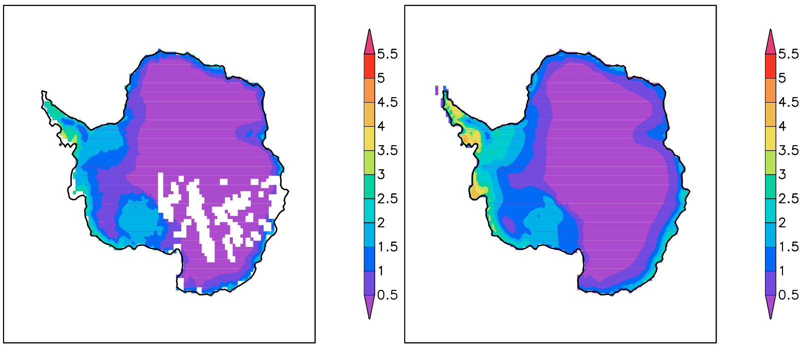

Figure 6.3: *Total water vapour (kg/m^2) in austral winter (JJA), 2000. AMSU-B (left), HIRHAM (right).*

polar central plateau and reaches the atmosphere boundary layer most of the moisture has been removed. In Fig. 6.3, this feature is well presented by the HIRHAM simulation.

6.2 Net surface mass balance

From observations, the annual accumulation over Antarctica is estimated to be between 1500 to 2000 $mm/year$ water equivalent (Vaughan et al., 1999) (this is as shown in Fig. 6.4). Around the grounded ice sheet, the average accumulation value is 149 mm/year. Other than precipitation, the mass budget is also influenced by the fall of ice crystal, evaporation, run-off and snowdrift. Since the most important sources are precipitation (P) and evaporation (E), the net balance has been calculated as ”Precipitation minus Evaporation”, (P - E).

Since the temperatures are usually below the freezing point, the run-off is not too significant. Snowdrift is a more characteristic of the region’s local features. Averaged for the period 1958 to 1998, Fig. 6.5 shows the calculated net balance (P - E) for the ERA40 re-analysis and the HIRHAM simulation (left and middle). It also shows the one-year simulation mean with 19 vertical levels. The model computed net balance maps reveal a high degree of success in simulating the major geographical patterns of net balance and also the absolute value. For the Antarctic Peninsula, which has the largest accumulation rate, the maximum value is approximately 1500 - 1800 $mm/year$. Meanwhile, the minimum values occur over the plateau (about 5 - 50 $mm/year$). The net balance is negative in places with a high orography or some mountain areas, such as the following: Transantarctic Mountains, the Dronning Maud Land, Lambert glacier and Ronne Ice Shelf. Such areas are dubbed as the ”blue ice” places. A detailed description of these places is provided in Chapter 6.3. The location of these places strongly connects

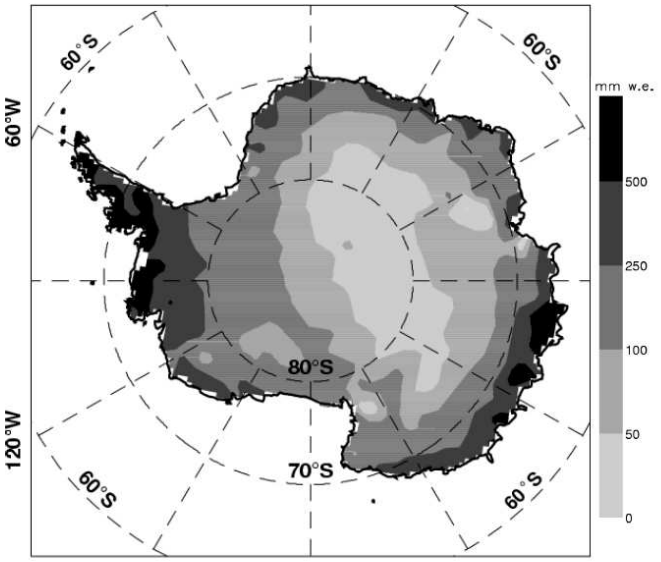

Figure 6.4: *Net balance (mm/year) from (Vaughan et al., 1999).*

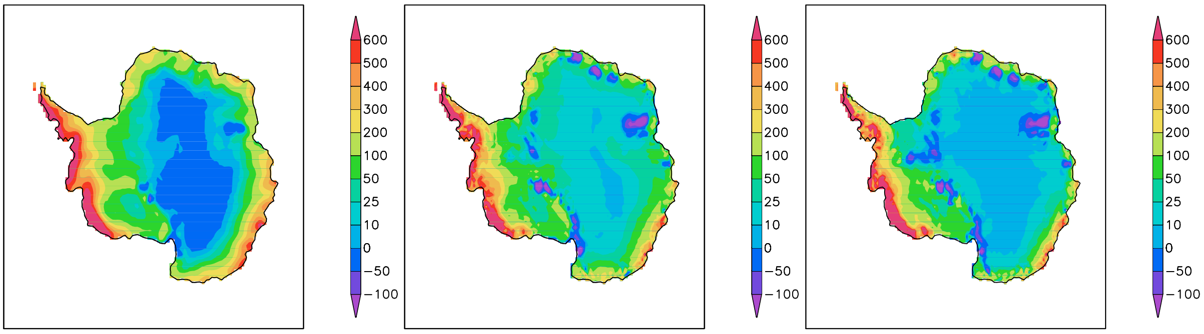

Figure 6.5: *Net balance (mm/year) averaged over 1958 - 1998, ERA40 (left), 25 levels HIRHAM (middle). 19 levels HIRHAM (right), 1997.*

with a maximum in sub-grid scale orography. The connection between the model vertical resolution and the net mass balance is also clearly shown in Fig. 6.5, (see the middle and left panel). Due to the increasing vertical resolution (that added 6 additional levels in the lowest part of the atmosphere) the area with a minimum net mass accumulation is significantly shrinking. In addition to this, the horizontal size of the blue ice areas becomes smaller. Thus, a better representation of the heat and moisture fluxes in the planetary boundary layer, has strongly improved the model simulations results.

The important features of Antarctic continent as surface inversions and katabatic winds play a crucial role in the formation and distribution of the net precipitation. Although precipitation mainly falls as snow, some coastal areas, especially the Antarctic Peninsula can receive rain at any time of the year. The mechanisms by which precipitation is formed and delivered to the Antarctic coast and, in particular, the Antarctic Peninsula are quite different from central Antarctica because of the proximity to the circumpolar trough and the synoptic systems therein (Turner et al., 1998). The high plateau of Antarctica receives a small amount of precipitation and is the world's largest desert (Vaughan et al., 1999). Much of the precipitation that does occur results from a clear sky deposition of ice crystals. To achieve an accurate simulation of local details and regional averages, an improvement in horizontal resolution and hence, topography is essential. Fig. 6.6 shows the difference between the ERA40 data and the HIRHAM simulation, with the precipitation and evaporation components and the total net balance shown separately. The biggest disparity in the precipitation field occurs over the Antarctic Peninsula or, to be more precise over the Western coast. This is a place where cyclones move in an easterly direction and meet with the high 2000 m orography of the Antarctic Peninsula. The HIRHAM overestimates precipitation rates in this area by about 300 - 400 $mm/year$. Meanwhile, ERA40 shows the stronger evaporation over the Antarctic Peninsula. During austral summer, the positive difference "ERA40 - HIRHAM " in the 2 m temperature explains the strong evaporation rate in the re-analysis data over the Antarctic Peninsula. Thus, the disparity in net balance, which is shown in Fig. 6.6 (right), is an issue of the net accumulation main components. Additionally, this disagreement between the model simulation and re-analysis reveals some variance along the East

Antarctic coastline. Here, the ERA40 net balance is higher than the HIRHAM model simulation result. For the HIRHAM and the ERA40 data, the standard deviations (SD) of the precipitation and net mass balance were calculated over 40 years. This was done to show the places with a higher variability in the mass accumulation (c. Appendix A: Fig. A.6 - Fig. A.7). Since most of the cyclones cannot penetrate deep inside the continent, the highest SD can be found in the coastal area. Thus, the Antarctic Peninsula and the coastal areas around the continent influence year-to-year variability with maximum variability seen in West Antarctica. Accumulated precipitations were calculated as a sum of large scale and convective precipitations. Over the vast part of the Antarctic continent convective precipitation does not play a significant role, (total precipitation is presented in Fig. 6.7). Exhaustive studies of the precipitation characteristics over Antarctica are given by Bromwich (1988); Turner et al. (1999); van Lipzig et al. (2002); Bromwich et al. (2004). The precipitation distribution is mostly connected with the orography. The relatively warm and humid air that comes from the Southern Ocean rises up, as soon as it reaches the steep Antarctic continent. Toward the inner part of the continent, the influence of synoptic scale processes decreases and over the cold plateau the precipitation rate reaches a minimum. This is thought to be a result of the limited flux of sensible and latent heat over the interior and the weakening of systems that occurs as a result of being forced to climb over high topography (Simmonds and Law, 1995). Recently, there has been a substantial amount of effort put into the literature to determine the snow accumulation in the polar regions, especially that of Antarctica (Turner et al., 1999; Giovinetto and Zwally, 2000; Bromwich and Fogt, 2004). There are three main techniques for estimating snow accumulation: surface based measurements, remote sensing and climate models. Since the accuracy of those methods varies, the long-term-averaged continent-wide maps of snow accumulation over Antarctica show a broad spectrum of results. The long-term estimates for the grounded ice sheet (GIS) from several studies, range from 119 (van de Berg et al., 2006) to 197 $mm/year$ (Ohmura et al., 1996) (GIS estimates for the conterminous ice sheet, which includes the ice shelves). In general, the studies employing glaciological data are considered to be the most reliable; the study of Vaughan et al. (1999) represents the current best approximation of 149 $mm/year$ for the GIS, although a

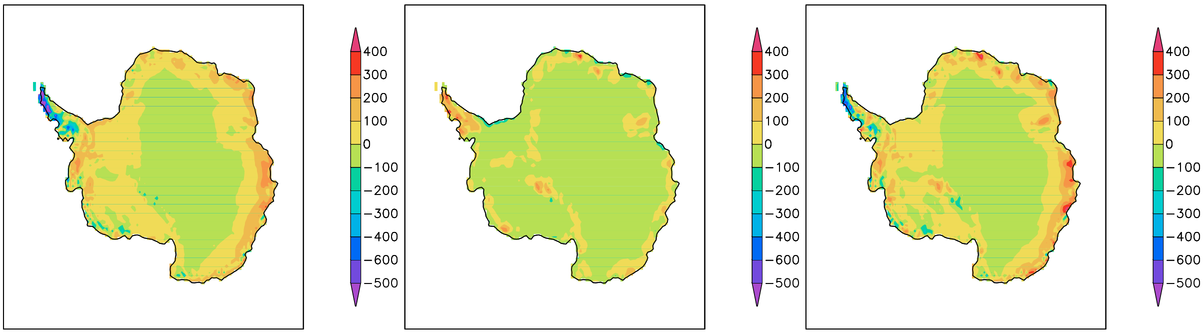

Figure 6.6: *The difference "ERA40-HIRHAM" averaged for the period 1958 - 1998. Accumulated precipitation (mm/year) (left), evaporation (mm/year) (middle), net balance (mm/year), (right).*

recent study of (van de Berg et al., 2006) shows evidence that the Vaughan et al. (1999) dataset underestimated coastal precipitation. The 1997 annual mean net balance was calculated for the 19 and 25 level HIRHAM versions and the ERA40 re-analysis. The accumulation rates are 94.07 $mm/year$, 123.69 $mm/year$ and 142.13 $mm/year$, respectively. The 25 level HIRHAM shows the closest result to the ERA40 re-analysis and is in better agreement with the observed data.

Works by previous authors have shown that prior to the modern satellite era, the ERA40 precipitation estimates for Antarctica are poor (Bromwich and Fogt, 2004; van Lipzig et al., 2002). As a result, we decided to divide the long-term run into two periods: S1 for 1958 to 1977 and S2 for 1978 to 1998. The horizontal structures of accumulated precipitation, evaporation and net balance are shown in Fig. 6.7 to Fig. 6.9.

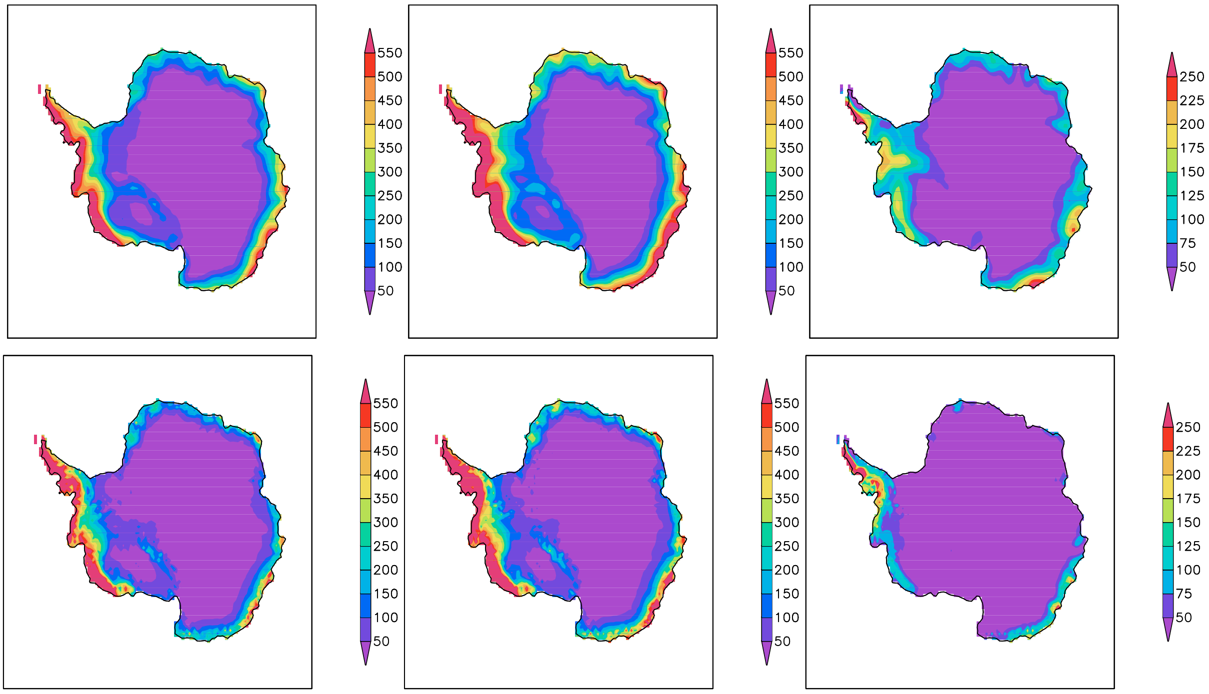

Figure 6.7: *The sum of large scale and convective precipitation (mm/year) in S1 (left), S2 (middle), difference S2-S1 (right). ERA40 (top panel), HIRHAM simulations (bottom panel). S1 – years: 1958-1977, S2 – years: 1978-1998.*

In Fig. 6.7, the spatial pattern for the ERA40 re-analysis is quite similar to the HIRHAM simulated pattern. For both datasets, the maximum values above 500 $mm/year$ can be found over the Antarctic Peninsula and along the coastline of Eastern Antarctica. The minimum value of 50 $mm/year$ appears over the Antarctic Plateau. The biggest difference appears during the S2 period along the coastal line of Wilkes Land and Donning Maud Land. The differences between S2 and S1 are higher for the ERA40 data than what it is for the HIRHAM simulations. Based on a lack of data during the presatellite era, one can see that there is a strong inequality between the S2 and S1 periods (Monaghan et al., 2006). For the ERA40 (top panel) and the HIRHAM (bottom panel), Fig. 6.8 shows the evaporation field averaged over the S1 and S2 periods and it is also shows the difference between them. The re-analysis show a strong 200 *mm/year* maximum value over the Antarctic Peninsula, which is absent in the model simulation, and a minimum over the plateau.

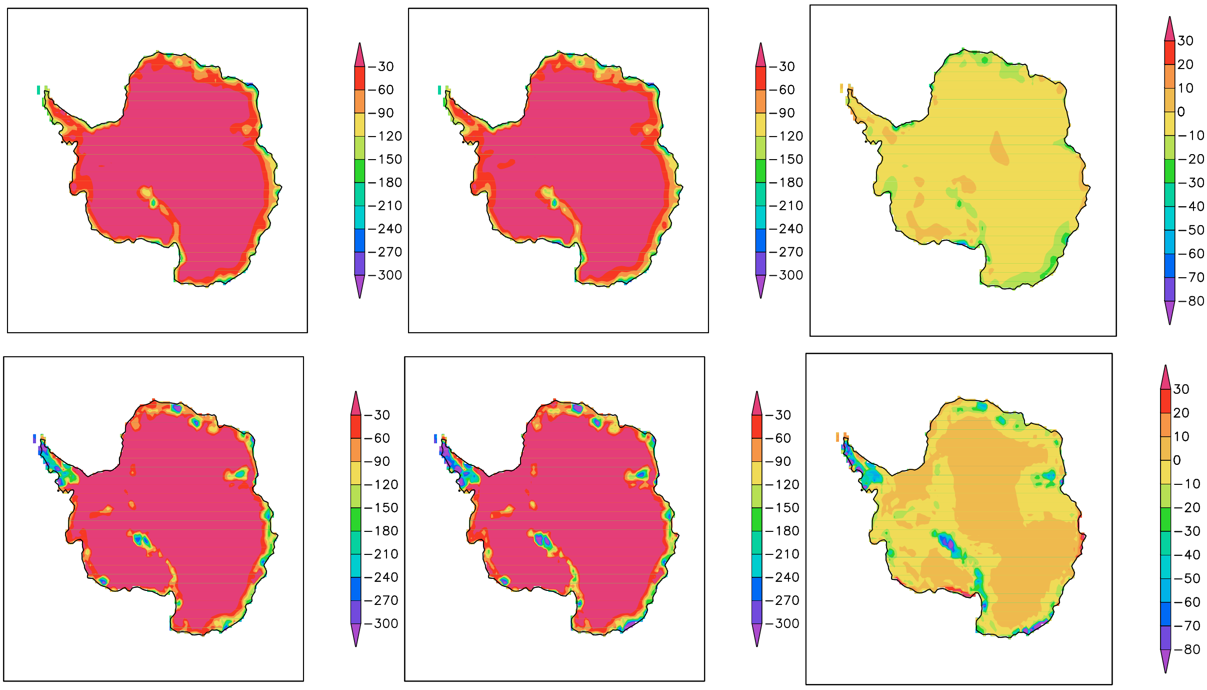

Figure 6.8: *Evaporation (mm/year) in S1 (left), S2 (middle), difference S2-S1 (right). ERA40 (top panel), HIRHAM simulations (bottom panel). S1 – years: 1958-1977, S2 – years: 1978-1998.*

Another maximum, which is present in both datasets, can be seen over the Transantarctic Mountains. The strong evaporation in this area creates an opportunity for the formation of ”blue ice” areas (c. Chapter 6.3). The difference between the second and first period is higher for the HIRHAM simulation than what it is for the ERA40 re-analysis. The evaporation field does not reveal such a big difference between S2 and S1 as what was found in the precipitation field. The re-analysis shows that during the second period the evaporation was weaker than during the presatellite era. The exception to this occurred, one place around the plateau. Fig. 6.9 presents the net accumulation balance for both periods as well as the difference between the HIRHAM simulations and re-analysis. By following the difference in the main net balance components, one can expect a disparity over the Antarctic Peninsula coming from precipitation and also, a disparity over the Antarctic plateau coming from the evaporation component. Since new satellite data was assimilated the artificial deficit over the Antarctic plateau became smaller in the ERA40 dataset during the S2 period. The accumulation rate increased by 10 *mm/year* over the Antarctic plateau and by 55 *mm/year* around the coastline of the continent. In the HIRHAM simulation the highest value for the S2 period can be found over the Antarctic Peninsula and Western Antarctica. By adding more observational data to the ERA40 data during the last 20 years allowed a better representation of the net accumulation balance in the re-analysis and hence in the HIRHAM model simulation. The HIRHAM simulated net balance shows a minimum over the Eastern part of the continent and the maximum accumulation over the Antarctic Peninsula. The temporal structure and the magnitude is in good agreement with Fig. 6.4. The annual mean was calculated for S1, S2 and long-term periods (1958 to 1998) for the HIRHAM and for the ERA40 re-analysis.

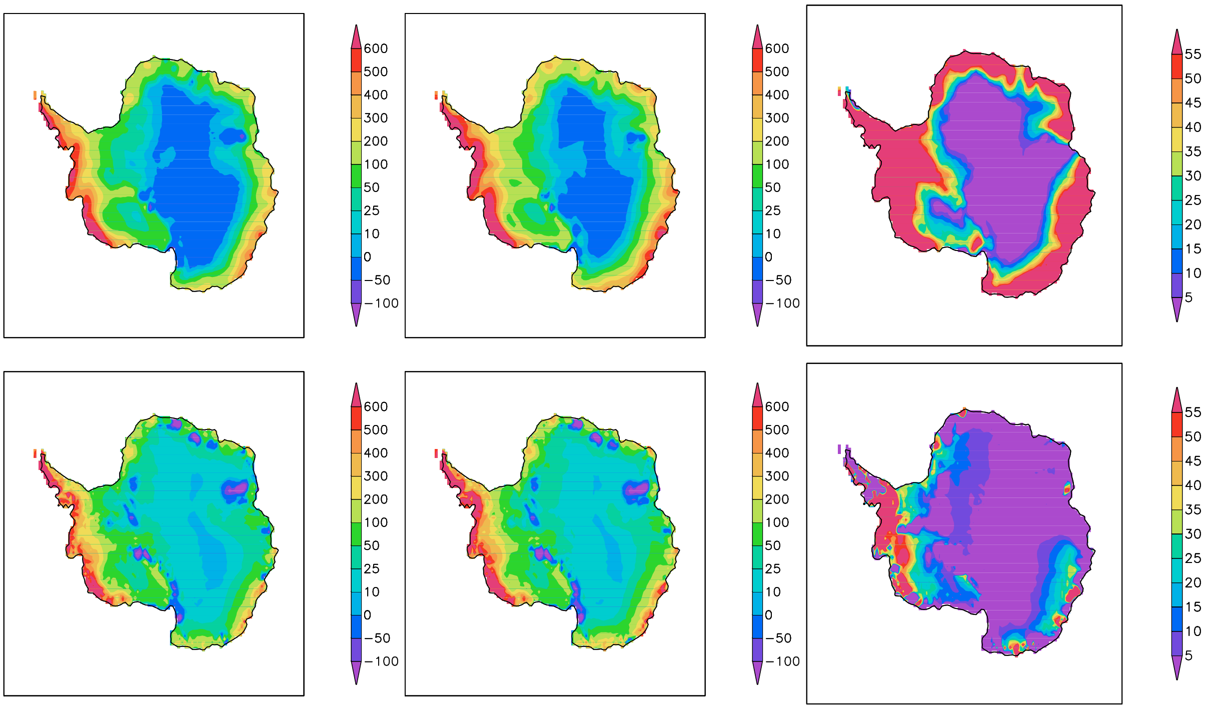

Figure 6.9: *Net balance (mm/year) in S1 (left), in S2 (middle), difference S2-S1 (right). ERA40 (top panel), HIRHAM simulations (bottom panel). S1 – years: 1958-1977, S2 – years: 1978-1998.*

Tab. 6.1 shows for the S1 period, both the HIRHAM and the ERA40 re-analysis give lower values than during the S2. The annual mean of the HIRHAM net accumulation over the 40 years is in a good agreement with the different compilations. Taking into account the HIRHAM cold temperature trend during the summer season, we should expect an increasing precipitation rate with an improved physical parameterisation of such processes. Two such examples are cloud formation and albedo scheme. Also, a partial reduction of ”blue ice” areas leads to an increasing net accumulation balance around the continent. Based on the intercomparison between the S1 and S2 periods, the net balance decadal trend was calculated within the S2 period. The horizontal structure is shown and discussed in Chapter 7.

	period	GIS ($mm/year$)
HIRHAM	1958-1977	95.2
HIRHAM	1978-1998	116.7
HIRHAM	1958-1998	107.2
ERA40	1958-1977	102.7
ERA40	1978-1998	148.9
ERA40	1958-1998	126.3
Van de Berg et al. (2005)	1958-2002	153
Van de Berg et al. (2005)	1958-1979	139
Van de Berg et al. (2005)	1980-2002	166
Vaughan et al. (1999)	variable	149
van Lipzig et al. (2002)	1979-1993	156

Table 6.1: *Long-term accumulation (mm/year) over the grounded ice sheet (GIS) of Antarctica compared to other compilations.*

6.3 Blue ice

The majority of the Antarctic landscape consists of areas with large snow-accumulation and here, the sheet mass balance is positive. However, in the near-coastal area of Dronning Maud Land, there exist alternating patterns of positive and negative mass balance. The negative mass-balance areas are usually seen in the form of exposed blue ice.

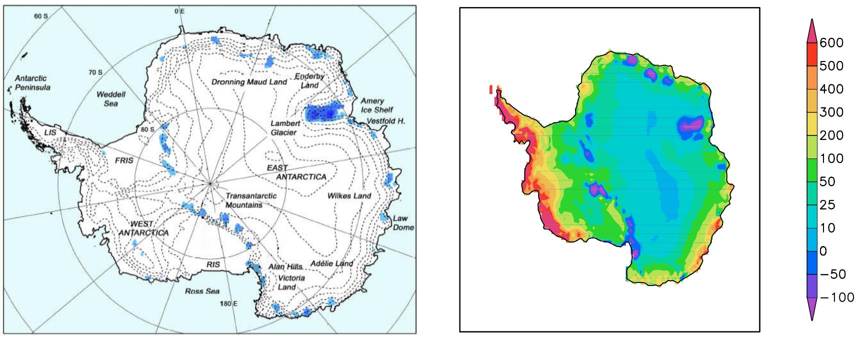

Figure 6.10: *Antarctica with geographical features mentioned in the text. Blue areas indicate areas with 10% "blue ice" areas coverage according to the compilation of van den Broeke et al. (2006) (left). HIRHAM net balance averaged over 1958 - 1998 (mm/year), (right).*

Fig. 6.10 shows the HIRHAM simulated accumulation net balance over the period 1958-1998 as well as the geographical distribution of "blue ice" areas (BIAs) (from AVHRR data) (van den Broeke et al., 2006). The location of the BIAs, which has been simulated by the HIRHAM agrees very well with the satellite data. Although it should be noted that the HIRHAM overestimates the horizontal size of the BIAs. Three factors are necessary for the formation of the BIAs: a nature obstacle (e.g. the Transantarctic mountains, mountains in the Dronning Maud Land), strong surface cooling and strong surface wind, which prevent falling down precipitation from accumulation (Bintanja, 1999; Bintanja and Reijmer, 2001; Bintanja, 2001a; Sinisalo et al., 2003). The Dronning Maud Land was chosen for the detailed investigation of the surface processes in the BIAs. For the period 1958 to 1998, Fig. 6.11 shows the mean value for July average for wind speed and direction. The month of July was chosen as an example of the winter season when maximum wind speed is observed and permanent surface cooling takes place. Since it is calculated over the area with a maximum roughness length, the excessively low wind speed has an artificial bias.

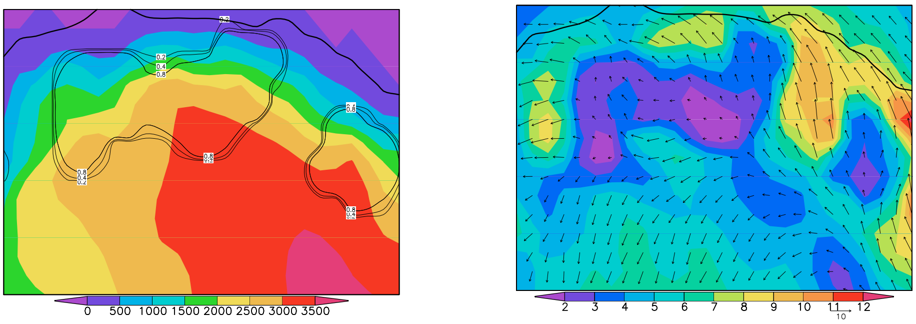

Figure 6.11: *Orography (color shaded, m), roughness length(contour lines, m), left. Wind speed (color shaded; m/s) and wind direction (arrows; m/s), right. July, 1958 - 1998.*

The Dronning Maud Land is a place where within a few hundred kilometers the elevation steeply decreases from 3500 *m* to sea level. At this place, sub-grid orography plays a very important role in the main processes responsible for the strong surface-atmosphere interaction, as for example, latent and heat flux formation.

A high-resolution climate model is a very suitable tool for a detailed description of the interaction between the surface and the atmosphere through surface turbulent fluxes of moisture and heat. These fluxes to and from the surface are caused by the atmospheric vertical temperature and humidity gradients. The strength of the turbulent fluxes is a function of the surface roughness. The roughness length over land plays the most significant role in the steep edges of the ice sheet. Based on experiments in the Arctic integration domain over the high topography of Greenland (Box and Rinke, 2003), the new roughness length for land was implemented, which was reduced to 3 *m* as shown in Fig. 3.4 and Fig. 6.11. This approach is in agreement with van Lipzig (1999).

In HIRHAM, the roughness length for momentum exchange is equal to the roughness length for sensible and latent heat exchange. The turbulent fluxes at the surface are calculated from the Monin - Obukhov similarity theory with the second-order, turbulent kinetic energy closure (Brinkop and Roeckner, 1995). To take into account the effect of small-scale orographic features on the turbulent exchange, an effective roughness length is derived from the variance of the subscale orography, is introduced. By this formulation, the latent heat exchange is enhanced in the mountainous regions; here, the effective roughness length is large and results in a value that is too large for the sublimation. To highlight the link between sensible, latent heat fluxes and

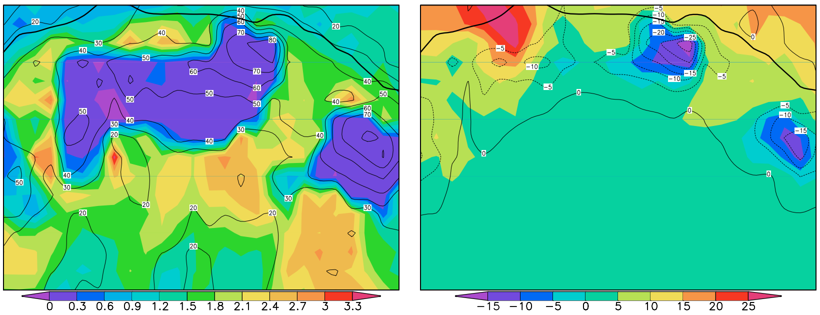

Figure 6.12: *Difference between 2 m temperature and surface temperature (color shaded; °C), sensible heat flux (contour lines; W/m^2), left. Net balance (color shaded; mm/month), latent heat flux (contour lines; W/m^2), right. July, 1958 - 1998.*

net accumulation, Fig. 6.12 presents the monthly mean values over the BIAs. Averaged 1958 to 1998 for the month of July, the accumulated net balance and, the sensible and latent heat fluxes in BIAs are shown in Fig. 6.12. The location of the smallest difference between 2 *m* temperature and surface temperature precisely corresponds with the location of the roughness length and hence the sensible heat flux maxima. The location of the minimum value for latent heat flux coincides with the location of the minimum in the accumulation net balance. Certainly, a better representation of heat fluxes would decrease the blue ice areas and consequently increase the total net balance around the continent.

Chapter 7

Decadal time scale processes over Antarctica

In recent years, various studies have shown evidence of warming and cooling over the Antarctic continent. Most of them used station data, which are generally distributed over the Antarctic Peninsula and the coast of the continent (King and Harangozo, 1998; van den Broeke, 2000). Also, the surface temperature distributions differ from station to station, and the temperature trends can have opposite signs even in adjacent stations (Weatherly et al., 1991). On the other hand, Doran et al. (2002); Chapman and Walsh (2005) showed a net cooling over the Antarctic continent between 1958 and 2000. The temperature, pressure and net accumulation balance trend were calculated based on the 40 year HIRHAM simulation.

7.1 Temperature trend

An analysis of air temperature trends has been carried out for the period from 1958 to 1998. For better understanding of decade scale changes, the long-term run was divided into two periods, S1 for 1958 to 1978 (presatellite era) and S2 for 1978 to 1998.

The forecasting equation for the linear trend is:

$$y(t) = \alpha + \beta * t \tag{7.1}$$

where t is a time index.

$$\alpha = \frac{\sum_{i=1}^{n} y \sum_{i=1}^{n} t^2 - \sum_{i=1}^{n} t \sum_{i=1}^{n} ty}{(n\sum_{i=1}^{n} t^2) - (\sum_{i=1}^{n} t)^2} \qquad t = 1.....n \tag{7.2}$$

$$\beta = \frac{n\sum_{i=1}^{n} ty - \sum_{i=1}^{n} t \sum_{i=1}^{n} y}{(n\sum_{i=1}^{n} t^2) - (\sum_{i=1}^{n} t)^2}, \tag{7.3}$$

where $y(t)$ is an annual mean of the meteorological parameter (e.g. temperature, pressure, net balance etc.), and n is the years number. The parameters α and β represent the "intercept" and "slope" of the trend line.

Fig. 7.1 shows the temperature trend calculated in both periods for ERA re-analysis and the HIRHAM simulation. During the S1, re-analysis data and the spatial patterns of the HIRHAM simulation reveal big negative temperature trend in the Indian Ocean along Mawson coast and in the Pacific Ocean over the Amundsen and Ross Seas. Over the continent the difference between the model simulation and re-analysis becomes more significant. The ERA40 shows a warming of 0.3 $^\circ C/decade$ over most of the Eastern part of Antarctica, while HIRHAM reveals a 0.6 $^\circ C/decade$ cooling. Both datasets show the agreement over Weddell Sea, in effect giving a positive temperature trend of 1.2 $^\circ C/decade$ from the ERA40 and 2.1 $^\circ C/decade$ from the HIRHAM, respectively. In that region, the 1970s were the warmest years in the 20th century. This is connected with the extensive polynya in the Weddell Sea (Enomoto and Ohmura, 1990). During the S2, the difference between the re-analysis and the model simulations becomes smaller. Both show a slight warming of 0.3 - 0.6 $^\circ C/decade$ over most of the Antarctic. The disagreement over the Ross Ice Shelf is connected with a difference in the land-sea mask and hence, sea-ice treatment. The temperature trend for the Antarctic stations is summarized in Tab. 7.1. A big negative temperature trend close to Marie Byrd Land (the Amundsen Sea) during the S1 and strong positive one during S2, can be connected with a phase of the global teleconnection pattern. The regression analysis reveals the strong dependence between SAM (Southern Annual Mode) and MSLP in this sector of the Pacific Ocean. Also, there is a strong dependence between the temperature trend and the beginning and the end of the evaluated period.

During the S1, only eleven out of fourteen stations show the negative temperature tendency. Meanwhile, only four stations in the S2 period show the same result. Apparently, the last quarter of the 20th century was warmer than the previous one. On the highest parts of the glacial plateau (Vostok station 0.08 $^\circ C/decade$) the temperature varies without a distinct trend (Turner et al., 2005). In the years 1958 to 1998, the trend of the mean seasonal values of the air temperature shows great spatial differentiation (as is shown in Fig. 7.2). Such differences are connected with the dependance of the radiation balance on the variability of cloudiness and the albedo of the surface, and on the transformation of pressure fields and changes of the atmospheric circulation (King and Turner, 1997). The seasonal means show that in the model simulation, the 0.3 to 0.6 $^\circ C/decade$ cooling stretching from Dronning Maud Land to South Pole occurs in all seasons of the year. Moreover, the strongest negative temperature trend, as well as the positive one, can be observed during the transition seasons (austral spring and autumn). The biggest difference between the re-analysis and the HIRHAM simulations is observed during austral winter; it lies over the Eastern part of Antarctic. Here, the HIRHAM shows the 0.3 $^\circ C/decade$ negative temperature trend, while the ERA40 data show 1.2 $^\circ C/decade$, which is strong positive.

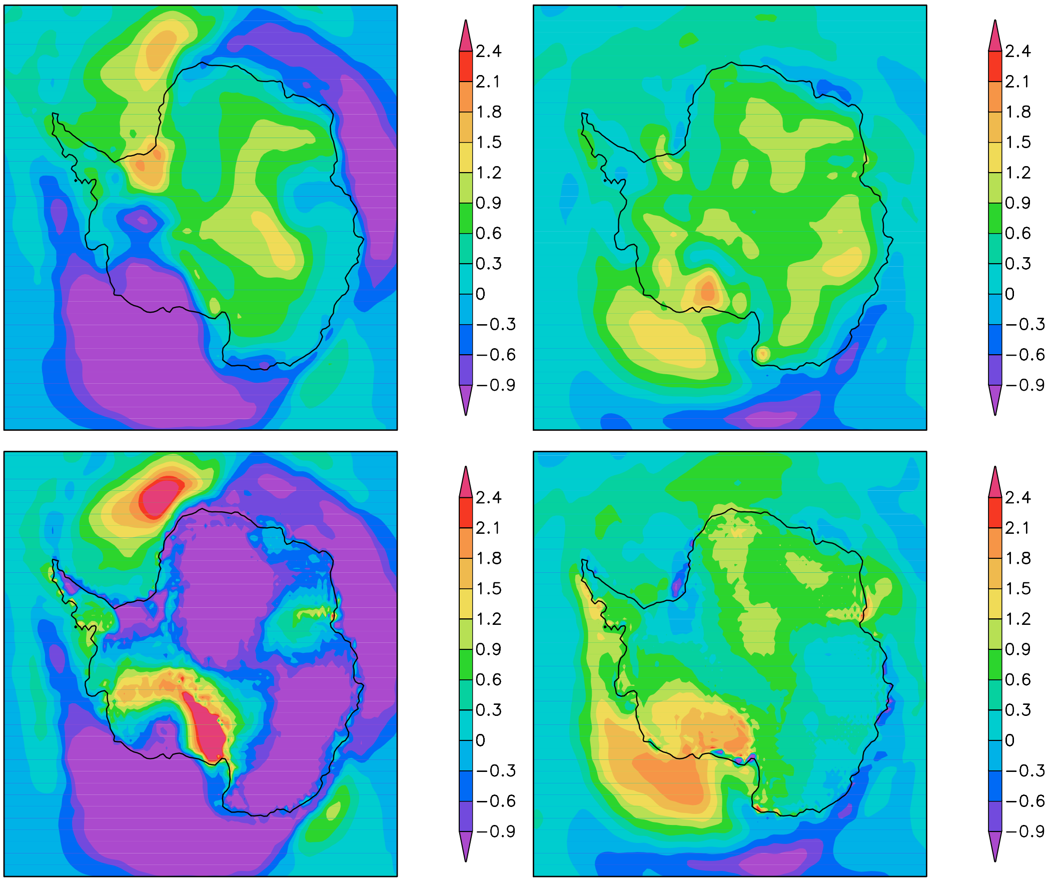

Figure 7.1: *Annual temperature trend (°C/decade) for the S1 period (left) and S2 (right). ERA40 (top panel), HIRHAM (bottom panel). S1 – years: 1958-1977, S2 – years: 1978-1998.*

Chapman and Walsh (2005) calculated the linear trends of annual mean surface air temperature for the period 1958 to 2002 (Fig. 7.3) based on surface stations, automatic weather stations, and ship/buoy observations. During the austral summer and autumn, observational data reveal that the temperature cools from -0.15 to -0.35 $^{\circ}C/decade$ along the Wilkes Land, Eastern coast of Antarctica. Although the cooling is a bit stronger and reaches -0.6 $^{\circ}C/decade$, it is nonetheless well captured by the HIRHAM.

Around the Antarctic continent the seasonal temperature trend is strongly variable. The Antarctic Peninsula region is an example of air temperature increasing in every season, with a special intensification of this feature in the autumn-winter period. A strong warming over the Antarctic Peninsula has been observed over the past 50 years and for the three seasons: summer, autumn and winter. The rapid and consistent warming of the Antarctic Peninsula contrasts with the weak temperature changes observed along the Eastern coast of Antarctica. It is also in contrast with the slight cooling over the eastern Weddell Sea and in central continental Antarctica. This regional contrast is one of the most interesting patterns of global climate change. It is supported by analysis of $in-situ$ data (Turner et al., 2005), satellite measurements (Comiso, 2000), soundings, or re-analysis (Marshall et al., 2002; Doran et al., 2002).

		HIRHAM			ERA40		
	Station	S1	S2	1958 - 1998	S1	S2	1958 - 1998
1	Amundsen-Scott	-1.36	0.45	-0.19	0.71	0.85	1.0
2	Bellingshausen	0.31	0.42	0.64	0.36	0.37	0.49
3	Casey	-0.45	-0.21	0.28	0.02	0.19	0.53
4	Davis	-0.49	0.64	0.32	-0.18	0.45	0.16
5	Dumont-Durville	-0.54	-0.03	0.79	0.05	-0.19	0.96
6	Halley	0.32	0.04	0.47	1.03	0.09	0.53
7	Mawson	-0.28	0.88	0.43	0.35	0.60	0.56
8	McMurdo	0.24	-0.07	0.11	0.85	0.61	0.83
9	Mirny	-0.33	-0.015	-0.31	0.03	0.27	0.34
10	Molodezhnaya	-0.57	0.34	0.19	-0.32	-0.16	0.2
11	Neumayer	-0.78	0.98	0.42	0.10	0.43	0.48
12	Novolazarevskaya	-1.0	0.73	0.20	0.22	0.16	0.77
13	Syowa	-0.51	0.15	0.30	-0.20	-0.35	0.10
14	Vostok	-0.69	0.47	0.08	1.26	0.77	1.0

Table 7.1: *Annual temperature surface trends ($^\circ C/decade$) at selected Antarctic stations.*

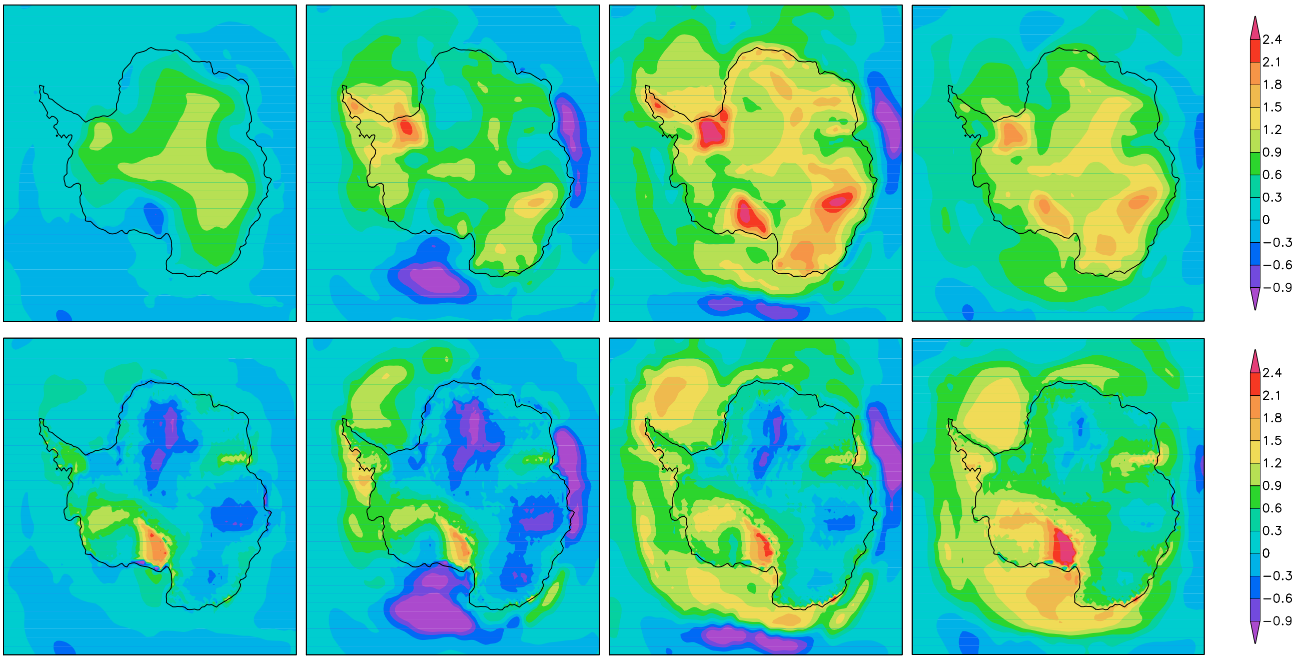

Figure 7.2: *Seasonal temperature trend ($^\circ C/decade$), 1958 - 1998. From left to right: austral summer (DJF), autumn (MAM), winter (JJA), spring (SON). ERA40 (top panel), HIRHAM simulations (bottom panel).*

The HIRHAM shows that the temperature changed more significantly at the coastal stations (for example Dumont-Durville station 0.79 $^\circ C/decade$ in HIRHAM simulations) than what it did for the inland stations (Amundsen-Scott station -0.19 $^\circ C/decade$, Vostok station 0.08 $^\circ C/decade$). Fig. 7.4 shows the linear trend of annual temperature changes for the

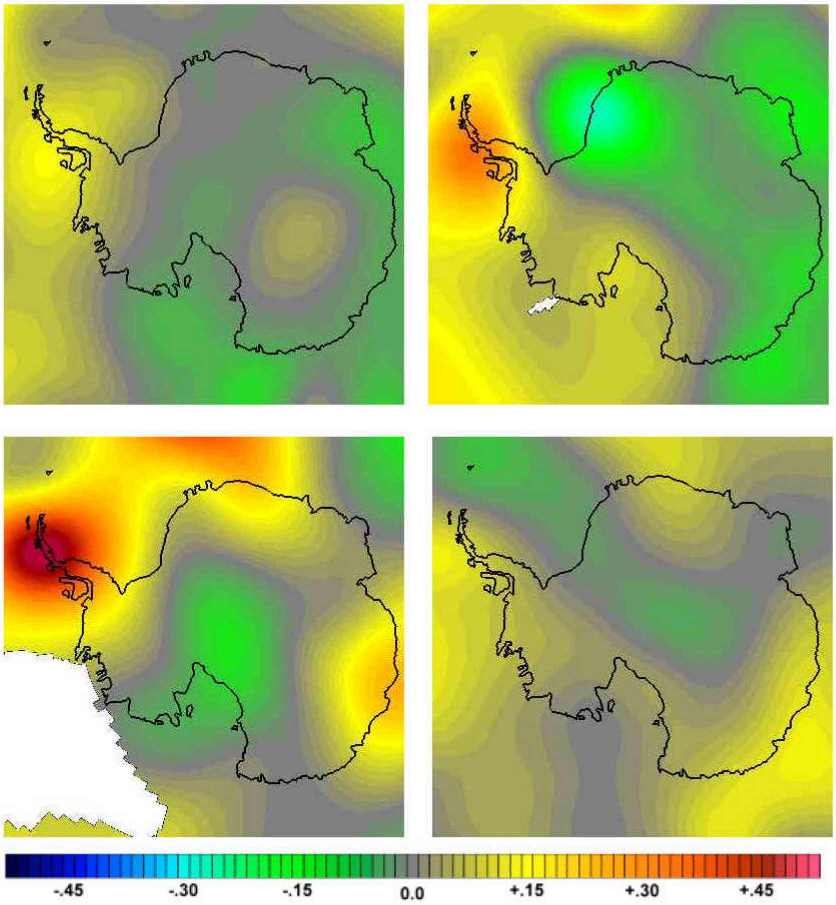

Figure 7.3: *Seasonal temperature trend (°C/decade), 1958 - 2000. Upper panel from left to right: austral summer (DJF), autumn (MAM). Bottom panel from left to right: austral winter (JJA), austral spring (SON) from Chapman and Walsh (2005).*

HIRHAM simulations, the ERA40 and the NCEP re-analysis , as averaged from 1958 to 1998, meanwhile, annual trends calculated from the observational data are averaged from 1958 to 2002 (Chapman and Walsh, 2005). The uncertainty of the temperature trend for the HIRHAM simulation was calculated on the "least-squares-method" (Bevington, 1969) and this is shown in Appendix A Fig. A.8. The NCEP data were available online and interpolated to the HIRHAM grid before the trend calculation.

The HIRHAM simulation and the NCEP re-analysis spatial patterns are in good agreement with observations. The distribution of minima and maxima agrees reasonably well for the HIRHAM and station data. There is a negative temperature trend of about 0.3 $°C/decade$ over the Eastern part of the continent and strong warming from 0.3 $°C/decade$ in observational data and upto 0.6$°C/decade$ for the HIRHAM simulation over the Antarctic Peninsula. In contrary, the ERA40 shows a net warming of 0.9 $°C/decade$ over the high antarctic plateau and 1.2 $°C/decade$ over the Antarctic Peninsula.

Additionally, the model simulated temperature trend was calculated at 500 *hPa* geopotential height, the first isobaric level which lies everywhere above the surface and is shown in

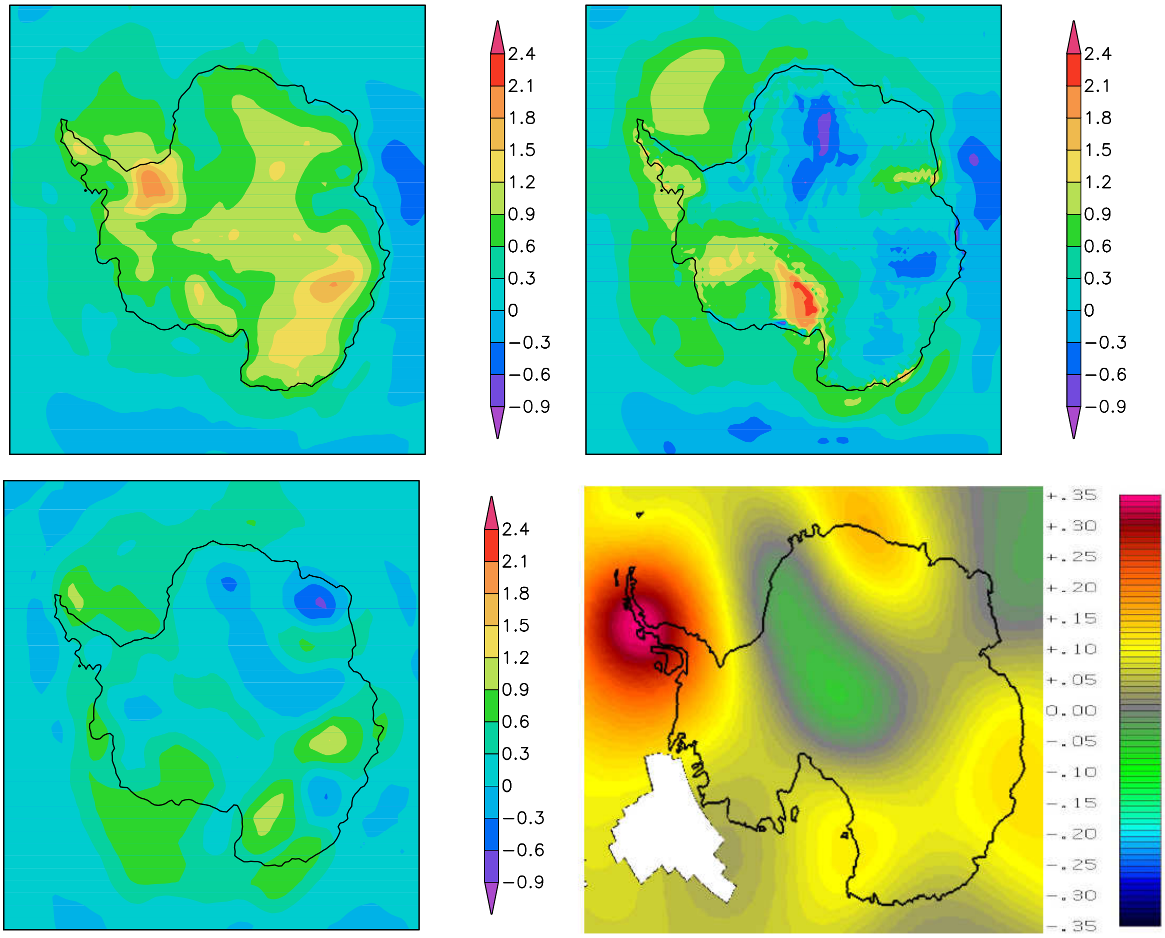

Figure 7.4: *Annual temperature trend (°C/decade) over 1958 - 1998. Upper panel: ERA40 (left) and HIRHAM simulation (right). Bottom panel: NCEP (left) and Chapman and Walsh (2005) over 1958 - 2002 (right).*

Fig. 7.5. Three seasons show the net temperature warming at this level. The horizontal structure reveals that during the S1 period, the lowest warming took place, with a minimum value of 0.3 $°C/decade$ over the entire Eastern part of Antarctica. The strongest positive trend is located over the Southern Ocean, with a maximum of 0.7 $°C/decade$ in the Atlantic Ocean sector. During the S2, this maximum shifted towards the Indian Ocean. The S1 period is characterised by a change in the trend of the temperature from negative at the surface to positive at 500 hPa geopotential height. Apparently, the negative surface temperature trend, as well as the positive temperature trend at 500 hPa, are not just due to changes in the surface processes but are also connected with an AAO (the Antarctic Oscillation) phase. As it will be discussed in the next chapter, the difference between AAO positive and negative phases clearly corresponds to the horizontal pattern of the 2 m temperature and 500 hPa temperature trends. The ERA40 data show the strong warming during the S1 and S2 periods and over the 40 years: the horizontal structure is shown in Fig. 7.6. As one can see, the horizontal structure of the temperature trend above the continent, consists of the alternate weak and strong positive temperature spots with a maximum 0.7 $°C/decade$ over the Eastern part of the continent. Contrary to the negative

HIRHAM 2 *m* temperature trend ERA40 positive one appears on both levels. One may conclude that the HIRHAM temperature trend agrees well with the observation at the surface level and the 500 *hPa* temperature trend.

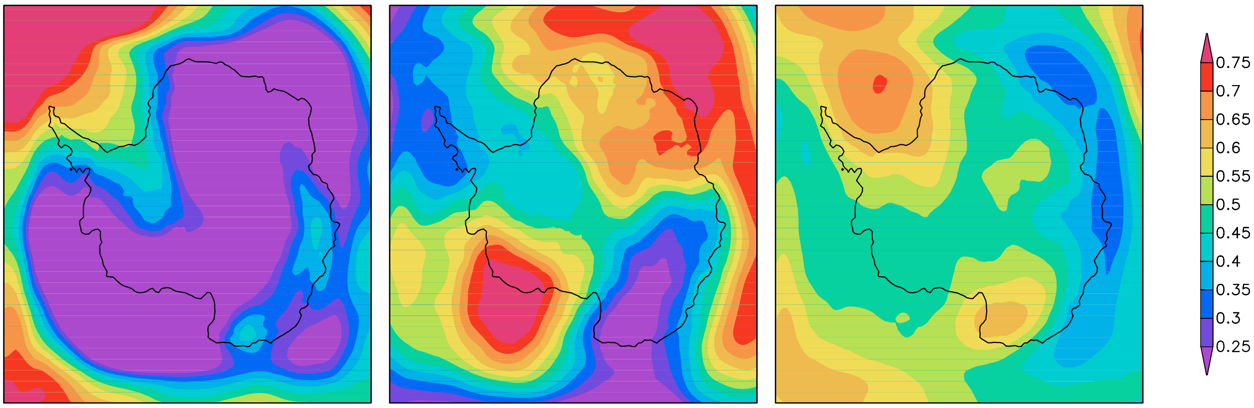

Figure 7.5: *Annual temperature trend at 500 hPa standard pressure level (°C/decade) for the S1 period (left), S2 (middle), 1958 - 1998 (right). HIRHAM simulation, S1 – years: 1958-1977, S2 – years: 1978-1998.*

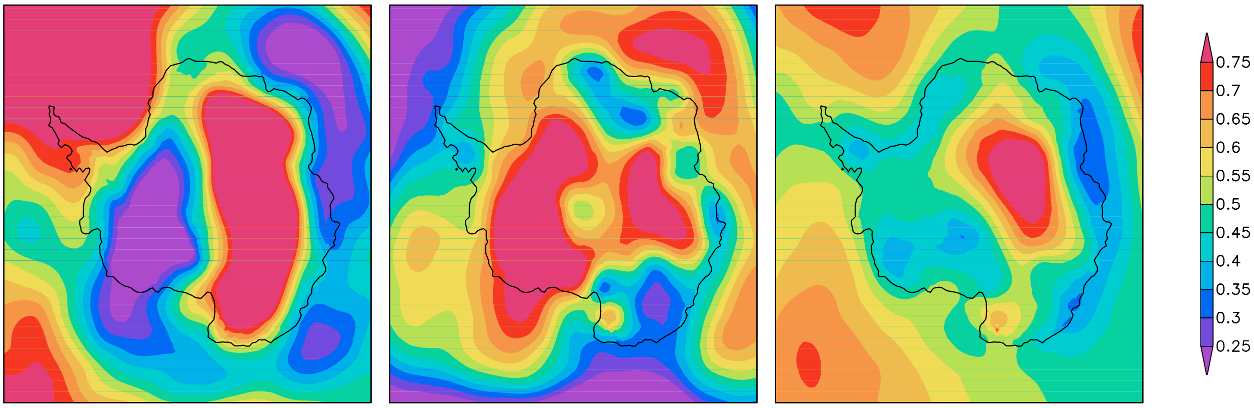

Figure 7.6: *Annual temperature trend at 500 hPa standard pressure level (°C/decade) for the S1 period (left), S2 (middle), 1958 - 1998 (right). ERA40, S1 – years: 1958-1977, S2 – years: 1978-1998.*

7.2 Pressure trend

Mean sea level pressure (MSLP) trends during the S1 and S2 periods, and also over the long-term run for the ERA40 re-analysis and the HIRHAM are shown in Fig. 7.7. During 1958 to 1977 the 1.2 *hPa/decade* negative pressure trend can be observed in both datasets close to Marie Byrd Land, in HIRHAM's case over the entire land area. On the opposite side of the continent, over Filchner Ice Shelf and the Weddell Sea a 0.6 - 0.8 *hPa/decade* positive pressure trend is located.

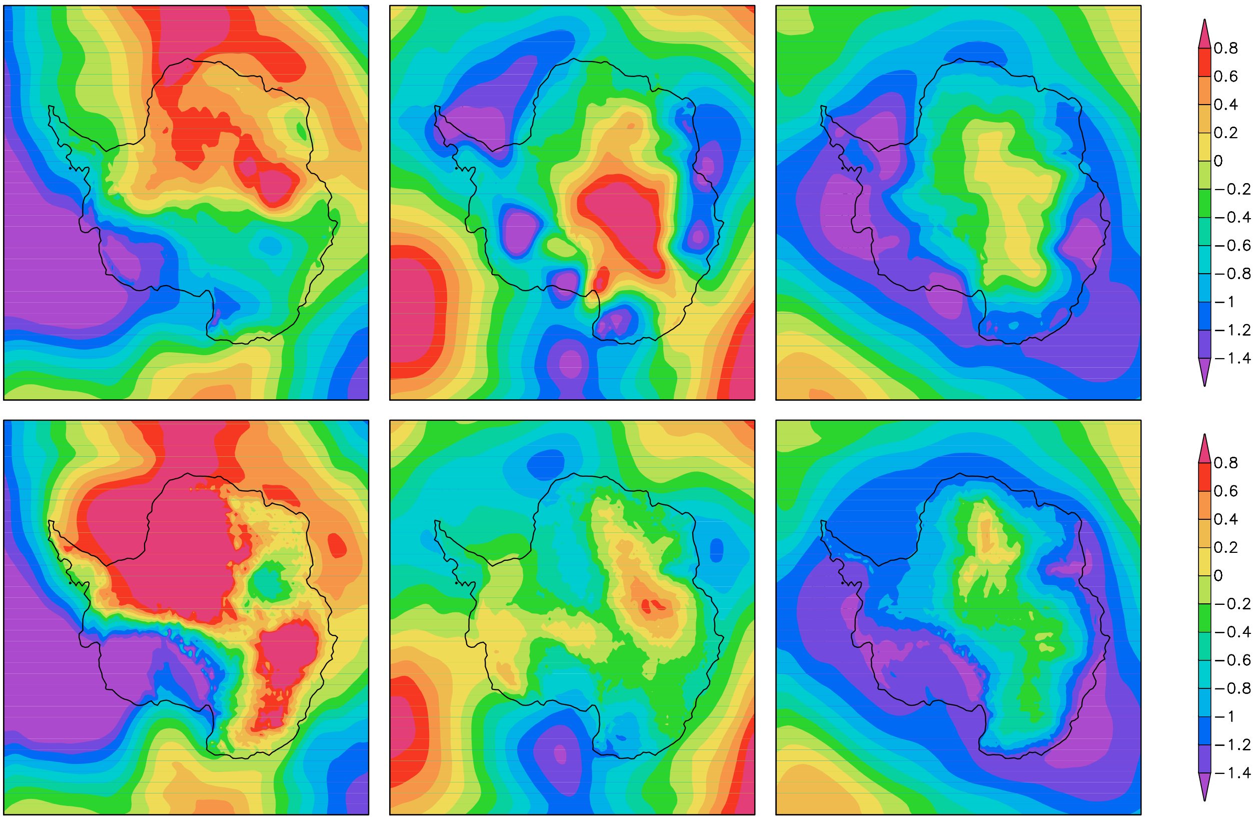

Figure 7.7: *Annual sea level pressure trend(hPa/decade) for the S1 period (left), S2 (middle), 1958-1998 (right). ERA40 (top panel), HIRHAM simulations (bottom panel). S1 – years: 1958-1977, S2 – years: 1978-1998.*

In the ERA40 re-analysis, it spreads from the Atlantic Ocean to the South Pole. During the S2 period less uniform structure appears and more local minima and maxima are revealed mostly over the coastline. The belt with decreasing MSLP surrounds the continent. It makes clear the increasing precipitation during the S2 over the Antarctic coastline, as shown in Fig. 6.7. The MSLP trend for the long-term run is presented in Fig. 7.7 (right). The general patterns are similar for both datasets. A decrease of from -1.2 $hPa/decade$ to -1.4 $hPa/decade$ in pressure occurred along the Antarctic coastline. The negative pressure trend explains the increase in the net accumulation field in coastal areas (i.e. more cyclonic disturbances, more clouds, more precipitation reaching the coast, less intense inversion and rising temperatures). In agreement with that, Turner et al. (2005) evidenced that decreases in the pressure field occur in all of the sectors that cover the Antarctic coastline. Turner's result is based on a 29 year integration from various stations around the Antarctic continent. Over the inner part of the continent, the pressure trend lies within ± 0.2 hPa. Based on the NCEP re-analysis, Simmonds and Keay (2000) analysed the cyclonic density and depth around the Antarctic continent. They reported a negative (positive) trend in the surface pressure south (north) of 40°S, which they attribute to "the high latitude mode (SAM)". The connection between SAM and the pressure field will be discussed in the next chapter.

7.3 Net surface mass balance trend

Fig. 7.8 shows the annual precipitation trends for the following: S1 (left), S2 (middle) and the ERA40 re-analysis and the HIRHAM simulation over the 40 year period (right). During the period S1, Wilkes Land and Dronning Maud Land have a 5 $mm/year^2$ negative precipitation trend. The location of the areas with negative precipitation trend is in a good agreement with the positive sea level pressure trend, effectively clarifying the feedback connection between the dynamics and physics of the atmospheric processes. The maximum precipitation during the S2 and over the 40 years shows a 10 $mm/year^2$ trend over the Antarctic Peninsula and the West Antarctica coastal line. It is in a good agreement with the MSLP and the earlier discussed temperature trends. With the exception of Adélie Land, net precipitations increased from 2.5 up to 5 $mm/year^2$ along the entire Eastern coast during the S2. It is still not clear whether this big difference between S1 and S2 periods is a natural oscillation or an issue of better representation of the re-analysis data during the modern satellite era. Over the inner part of the continent, which is distant from the Southern Ocean, the precipitation trend is not significant. Studies of the atmospheric transport of water vapour to Antarctica have shown that circulation variations are probably the primary source of interannual variability in precipitation (Connolley and King,

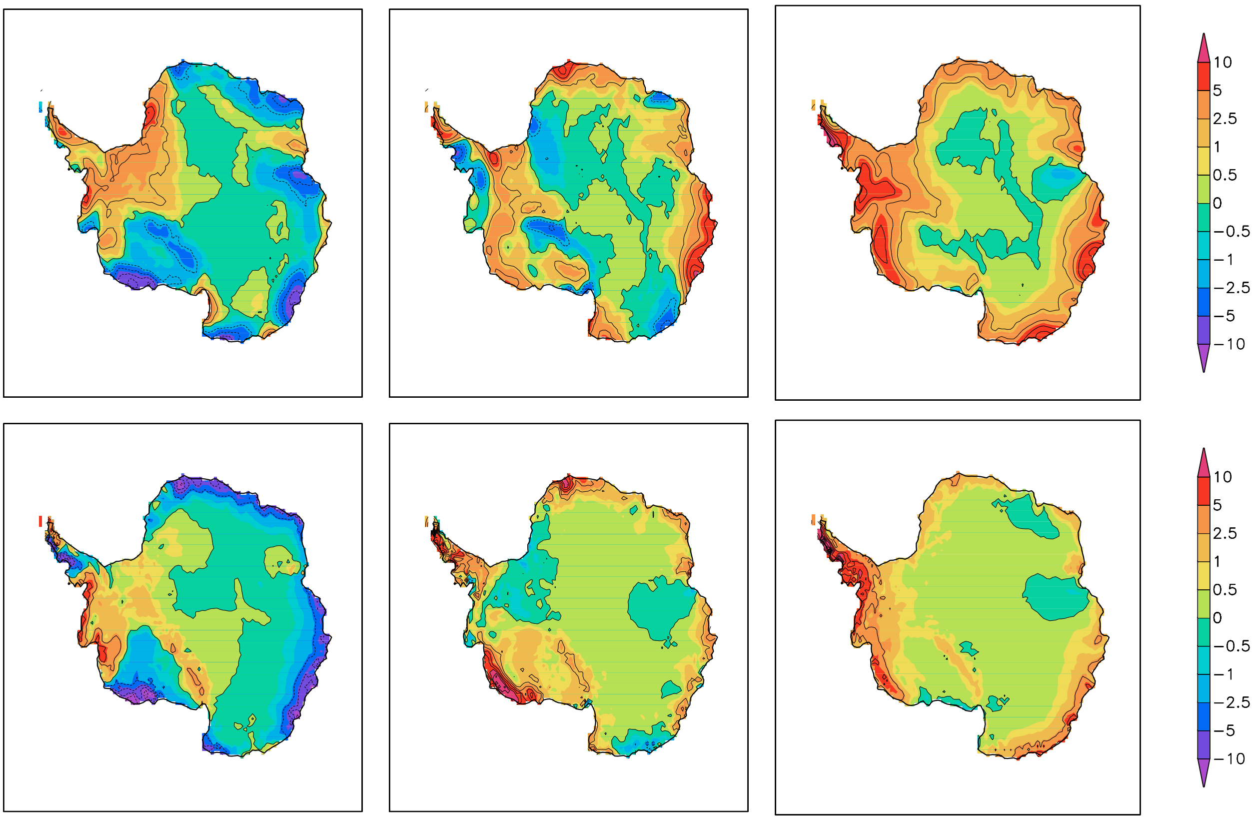

Figure 7.8: *Annual precipitation trend ($mm/year^2$) for the S1 period (left), S2 (middle), 1958 - 1998 (right). ERA40 (top panel), HIRHAM simulations (bottom panel). S1 – years: 1958-1977, S2 – years: 1978-1998.*

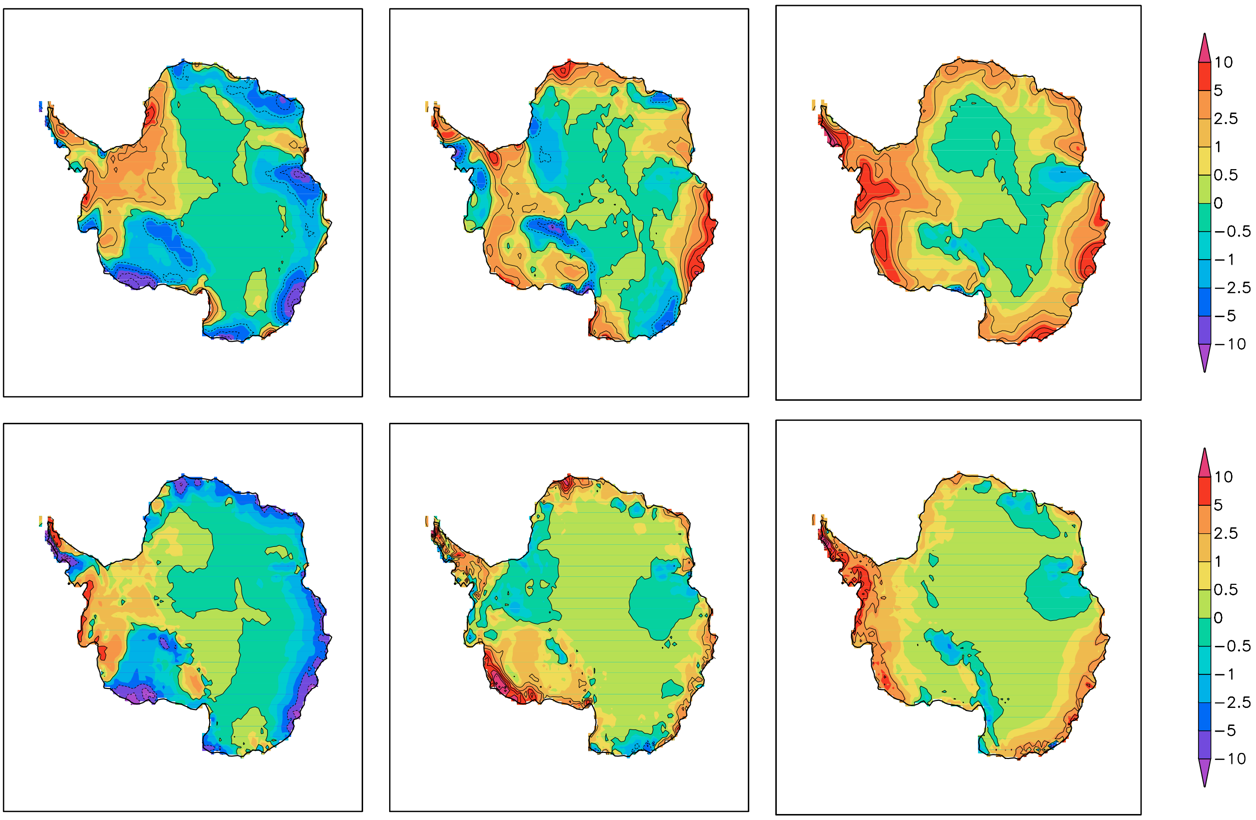

Figure 7.9: *Annual net balance trend (mm/year^2) for the S1 period (left), S2 (middle), 1958 - 1998 (right). ERA40 (top panel), HIRHAM simulations (bottom panel). S1 – years: 1958-1977, S2 – years: 1978-1998.*

1993). Temperature changes alone do not seem sufficient to explain the observed trends and it is likely that concurrent circulation changes have occurred.

Fig. 7.9 shows the net balance trend ($mm/year^2$) calculated over the S1, S2 periods and over the 40 years. Since in the accumulation balance evaporation is a less significant term than precipitation, the spatial patterns of net balance mostly follow the precipitation patterns. The biggest difference between the periods S1 and S2 reveals itself in the coastal areas. The net balance trend has changed from negative during the S1 to positive during the S2 period on the Eastern coastline, which is also in good agreement with the changes in the pressure field. During the 40 year long-term run, over the central part of the continent the net balance doesn't show strong oscillation.

An additional intercomparison between the model simulation result and the satellite data was completed. The net mass balance trend from the HIRHAM simulation was calculated over the period 01.1992 - 12.2001, which is one year shorter than the period used by Davis et al. (2005). Since the driven data is available only until August 2002, the data for 2002 were not included in the calculation. Davis et al. (2005) used satellite radar altimetry measurements from 01.1992 to 12.2002 to determine that, on average, the elevation of about 8.5 million square kilometers of the Antarctic interior has been increasing (Fig. 7.10 (left)). The increasing elevation was

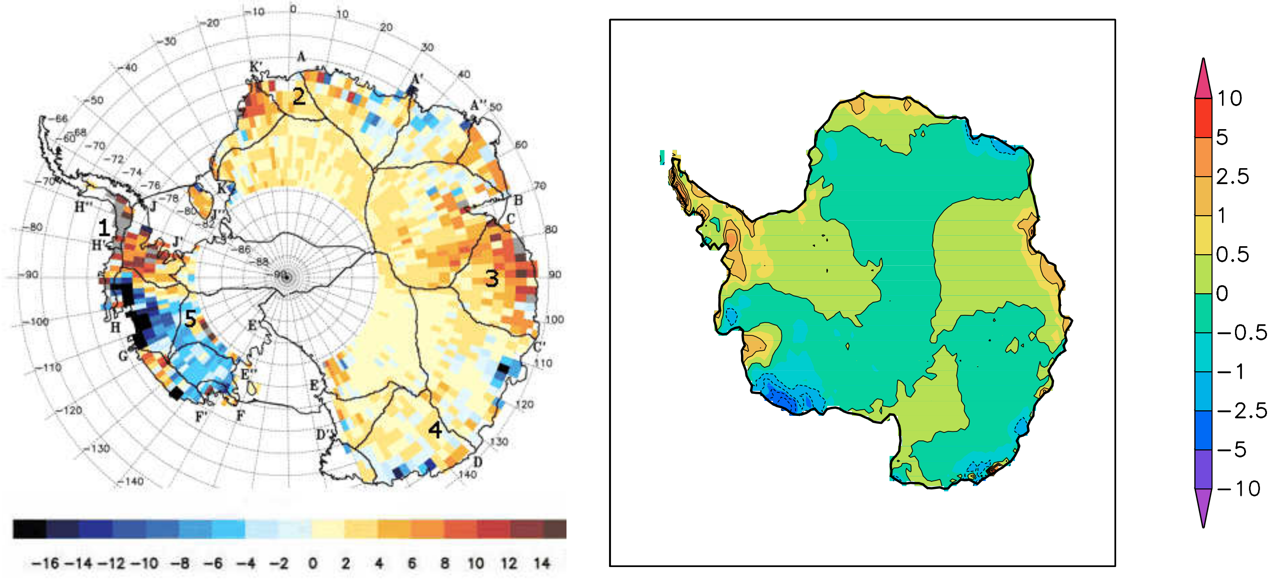

Figure 7.10: *Rate of elevation change (cm/year^2) by altimetry satellite measurements Davis et al. (2005), Jan 1992 - Dec 2002 (left). Annual net balance trend (cm/year^2) for Jan 1992 - Dec 2001, HIRHAM simulation (right).*

then linked to increases in snowfall, which was translated into a mass gain of 45 ± 7 billion tons per year, tying up enough moisture to lower sea level by 0.12 ± 0.02 $mm/year$. The spatial pattern reveals the areas with maximum accumulation (5 $cm/year^2$) in the Antarctic Peninsula (1), Riser-Larsen Ice Shelf (2) and Denman Glacier (3) (for a better understanding, these areas are denoted by numbers from 1 to 5 in Fig. 7.10, left). All of them are well captured by the HIRHAM simulations (Fig. 7.10 (right)). Those areas alternate with sinking areas. Good examples of those areas are Dronning Maud Land (2) and Wilkes Land (4). The HIRHAM reveals a small area with 5 - 10 $cm/year^2$ positive accumulation trend which is also captured by satellite measurements (8 - 10 $cm/year^2$). The HIRHAM slightly underestimates the horizontal size of maximum and minimum accumulation rate areas. But the location and magnitude agree well with Davis et al. (2005).

To resume, in this chapter the temporal variability and change in some of the key meteorological parameters over the Antarctic continent on decadal-scale time periods were investigated. For the period 1958 to 1998, the existing Antarctic surface air temperature records reveal periods of persistent (multi-year) and geographically extensive temperature trends towards cooling in the interior and warming in the coastal regions. The spatial and seasonal patterns of these trends are, however, not quite simple and appear to change with time; that is, the temperature relationship between specific locations is not temporally consistent. The cooling has been modest in coastal East Antarctic regions, but more pronounced at the Amundsen-Scott Base and at the South Pole. The clear decrease in surface pressure at the coastal areas over the full periods of the long-term runs is indicative of the SAM moving towards a high-index state in recent decades. The positive (negative) trend in MSLP closely corresponds to the negative (positive) trend in the accumulation net balance. The Antarctic ice sheet grows over the Eastern part of Antarctica with small exceptions in Dronning Maud Land and Wilkes Land and sinks in the Antarctic Peninsula. Once again, the small negative net balance trend over the Antarctic Peninsula emphasized the complicity of the non-linear system interaction. In areas where one of the main meteorological parameters, temperature, shows a strong positive trend the alternate positive/negative net balance trend can be observed. The global teleconnection between these decadal scale processes and more southern latitudes will be discussed in the next chapter.

Chapter 8

Influence of Antarctic Oscillation (AAO) on the regional Antarctic climate

Certain analyses of long term series of atmospheric circulation data reveal large scale correlations between the flows at remote locations. These fluctuations belong in the low frequency range of timescales, and they have been dubbed ”teleconnections” to stress the correlation at a distance aspect of their nature. Teleconnections are located in particular places, and take the form of ”standing waves”, with fixed nodes and antinodes of low frequency oscillation. They are often orientated in such a way as to indicate connections between the mid-latitude and high latitude low frequency transients. These teleconnections are connected with the propagating Rossby waves. We looked at the atmospheric wave patterns associated with these teleconnections and also looked at ”indices” which are used to determine whether the pattern is in a negative or positive phase. The semi-annual oscillation (SAO) in the middle and more southern latitudes is an important and well known component of the Southern Hemisphere climate. One of the first works on the SAO was completed by van Loon (1967), and a reexamination of the phenomenon and its motives was presented by Meehl (1991). The SAO consists of the twice-yearly contraction and expansion of the pressure trough around Antarctica, in response to differences in heat storage between Antarctica and the surrounding oceans. As a result of the SAO, the surface pressure in middle and high latitudes shows a clear half-yearly wave. The analyses of the mid- and high-latitude records show that this SAO dominates the long-term sea level and geopotential height climatology over southern latitudes poleward of 35 °S. In the midlatitudes (35 °S - 60 °S), the SAO exhibits pressure and geopotential height maxima during the spring and autumn, minima in early winter and summer, and is most pronounced over the three southern oceans. The phase of the SAO reverses poleward of 60 °S, where pressure and geopotential height maxima occur in the solstice seasons (Gong and Wang, 1999; Thompson and Wallace, 2000; Kwok and Comiso, 2002).

The synoptic activity in the Southern Hemisphere, particularly extra tropical cyclone and anticyclone behaviour, is strongly associated with climate variability in the Pacific Ocean. The most commonly known example of this association is the El Niño / Southern Oscillation (ENSO), which is one of the most studied interannual modes of variability in the climate system, with extensive discussion in the literature about its predictability and teleconnection effects on temperature and precipitation anomalies over the globe (Karoly, 1989; Guo et al., 2004). The El-Niño phenomenon is an abnormal warming of surface ocean waters in the eastern tropical Pacific. Climate modeling studies are a crucial tool for evaluating the linkages between the Antarctic region and lower latitudes. Since the HIRHAM grid covers a smaller area than needed in global teleconnection research, we instead used this: the 1958 to 1998 monthly mean Antarctic Oscillation index (AAO) based on the first principal component of the NCEP 850 *hPa* extratropical height field (20 °S - 90 °S adapted from Thompson and Wallace (2000), data are available online: *http://www.jisao.washington.edu/aao/*). Genthon et al. (2005) calculated the AAO index based on the ERA40 and NCEP data and showed that the difference in indices was not significant. Therefore, in our work we used the NCEP AAO index, available on-line. It is important to note that the year-round monthly mean AAO data have been used to obtain the year leading pattern of the AAO. The AAO index is shown in Fig. 8.1. High AAO is associated with a low pressure over Antarctica (strong westerly winds, stronger jet, a strong circumpolar vortex, poleward storm track and low amplitude Rossby waves) and a high pressure over mid-latitudes. The forcing of the AAO is still the subject of great debate. There are three leading ideas: increasing of the greenhouse gases (Cai et al., 2003), variability in the ozone layer (Thompson and Solomon, 2002) and changes in tropical sea surface temperature in the Pacific Ocean (Fogt and Bromwich, 2005). Fogt and Bromwich (2005) suggest that ENSO

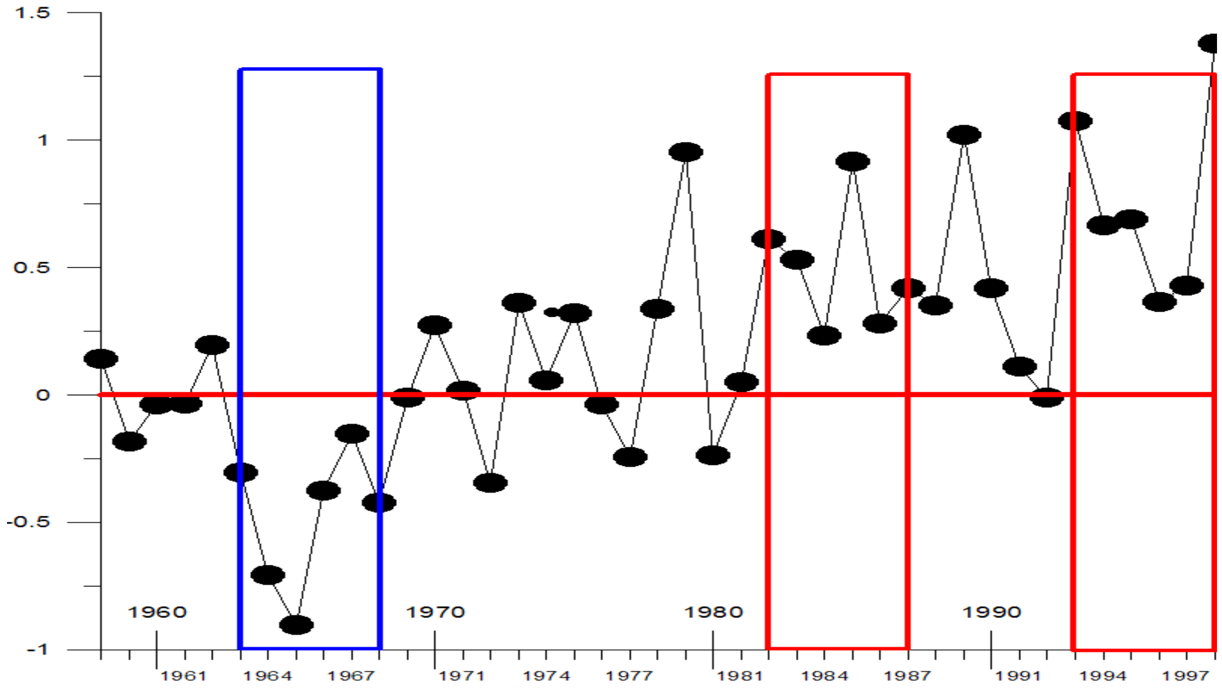

Figure 8.1: *Time series of yearly mean AAO index, 1958 - 1998. NCEP data. Left – AAO^{-} years: 1963-1968, middle – AAO^{+1} years: 1982-1987, right – AAO^{+2} years: 1993-1998.*

and the AAO are related, the decadal variability of the ENSO teleconnection being governed by the coupling with the AAO. For the detailed investigation of global teleconnection, two positive and one negative AAO phase periods were chosen. The first (negative) is denoted AAO^{-} and covered the years from 1963 to 1968, the second (positive) is denoted AAO^{+1} and covers the period from 1982 to 1987 and the third (positive) is denoted AAO^{+2} and covers the years from 1993 to 1998. Recently, the AAO has been shown to have a trend towards its positive polarity (Thompson and Solomon, 2002; Marshall, 2003).

8.1 Mean sea level pressure

The seasonal mean of the main climate generative meteorological fields were calculated for those six years phases. They include: sea level pressure, 2 *m* temperature, 500 *hPa* geopotential height, precipitation and the net mass balance. Fig. 8.2 to Fig. 8.4 show the MSLP horizontal pattern of positive and negative AAO phases and the difference between them for the ERA40 and HIRHAM simulations.

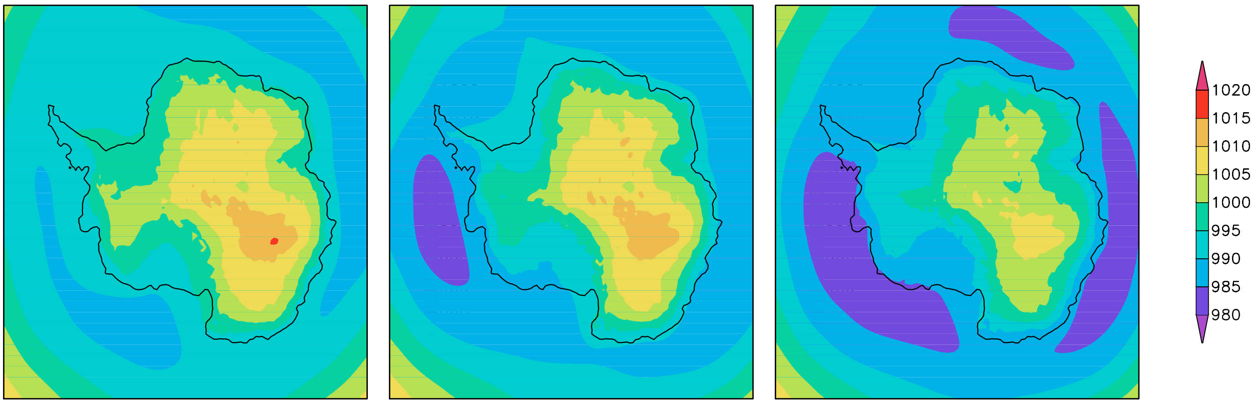

Figure 8.2: *Mean sea level pressure (hPa) in austral summer (DJF), HIRHAM simulation. Left – AAO^{-} years: 1963-1968, middle – AAO^{+1} years: 1982-1987, right – AAO^{+2} years: 1993-1998.*

The horizontal structure of MSLP in Fig. 8.2 and Fig. 8.3 , clearly defines the circumpolar vortex around the continent, with minimum values over the Pacific, Indian and Atlantic Oceans. The main difference between positive and negative phases is deep in the circumpolar vortex; it is increased from AAO^{-} to AAO^{+2}. During the AAO^{+2}, a strong El-Niño phenomenon was observed in the eastern Pacific. The difference between AAO^{+1} and AAO^{+2} can be connected with a strong ozone reduction, effectively increasing greenhouse gases or El-Niño phenomena. Disparities between the HIRHAM simulation and the ERA40 data are mostly concentrated over the high Antarctic plateau, where the HIRHAM shows 1000 - 1010 *hPa* and the ERA40 data show smaller values 995 to 1005 *hPa*. Fig. 8.4 shows the difference " AAO^{+1} minus AAO^{-} " and " AAO^{+2} minus AAO^{-} ", left and right, respectively for the HIRHAM (top panel) and ERA40 data (bottom panel). Regions over which the difference is statistically significant (at the

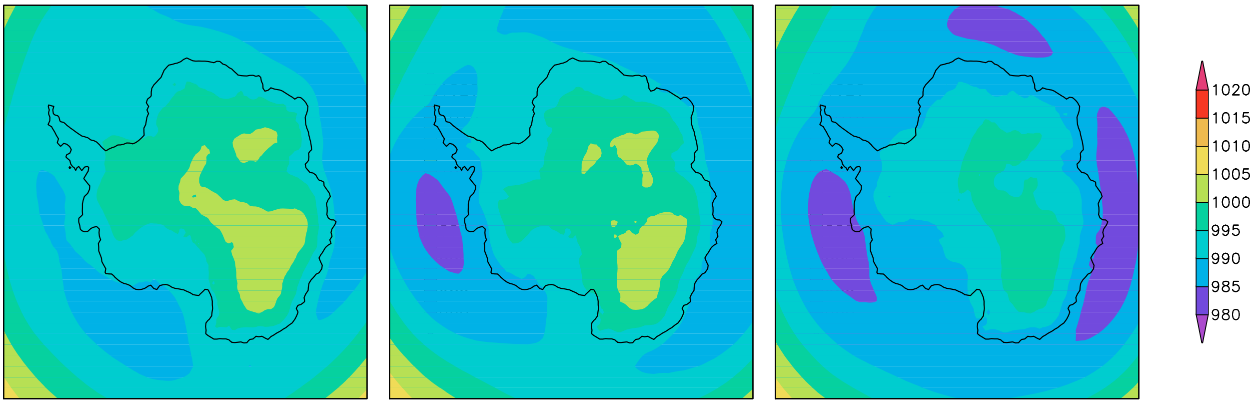

Figure 8.3: *Mean sea level pressure (hPa) in austral summer (DJF), ERA40.
Left – AAO^{-} years: 1963-1968, middle – AAO^{+1} years: 1982-1987, right – AAO^{+2} years: 1993-1998.*

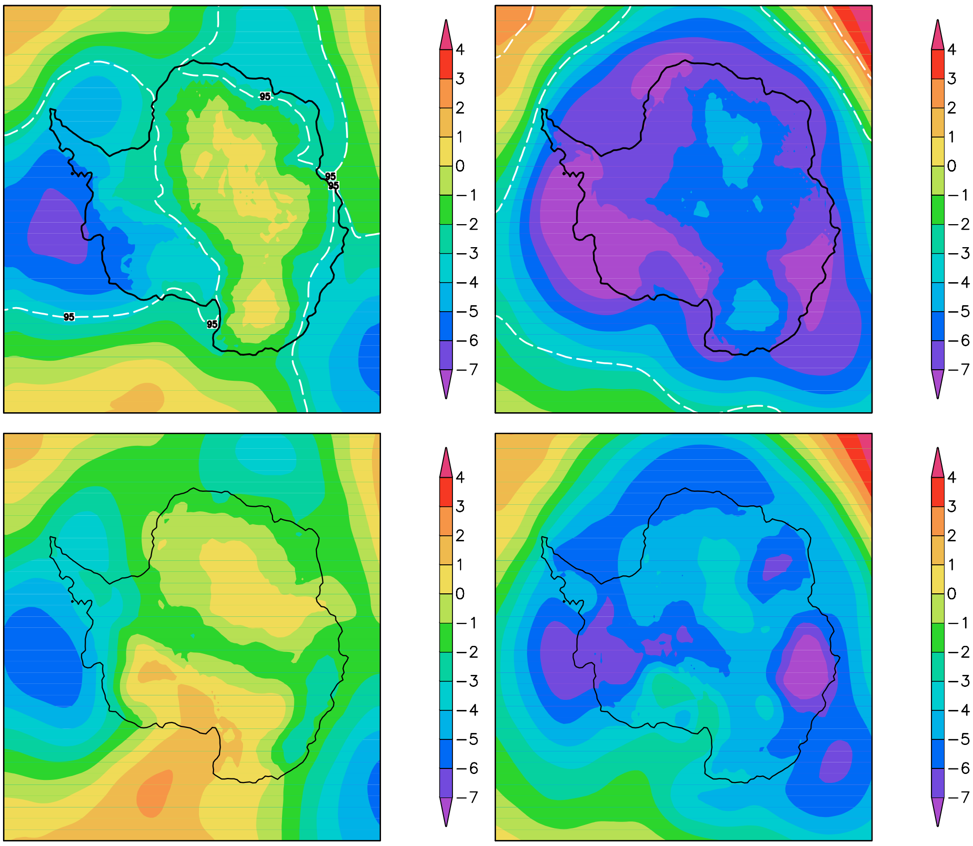

Figure 8.4: *MSLP (hPa) in austral summer (DJF), "AAO^{+1} minus AAO^{-}" (left), "AAO^{+2} minus AAO^{-}" (right). HIRHAM simulation (top panel). ERA40 (bottom panel). The white line denotes statistical significance at the 95 % confidence level.*

95% confidence level) have been marked by the white dashed line. Statistical significance were calculated with "Student-t" test (Bevington, 1969). Looking at the top panel of the HIRHAM simulation, the left picture presents the alternate areas of positive and negative biases whereas the right one shows the strong decrease in mean sea level pressure during the positive AAO phase over the entire continent and the adjacent part of the Southern Ocean. Over the Southern Ocean, the ERA40 data and HIRHAM simulation are in good agreement whereas over the continent, the differences become more visible. The area with the smallest positive changes between AAO^{+1} and AAO^{-} phases is located over Eastern Antarctica and stretches from north to south in the HIRHAM simulation. Meanwhile, from the Western to the Eastern part of Antarctica, the ERA40 data show a "negative breaking bridge". Apparently, it is connected with the coarse resolution of the re-analysis data. Fig. 8.5 to Fig. 8.7 show the AAO^{-} , AAO^{+1} and AAO^{+2} phases during the austral winter for the HIRHAM simulation and the ERA40 data.

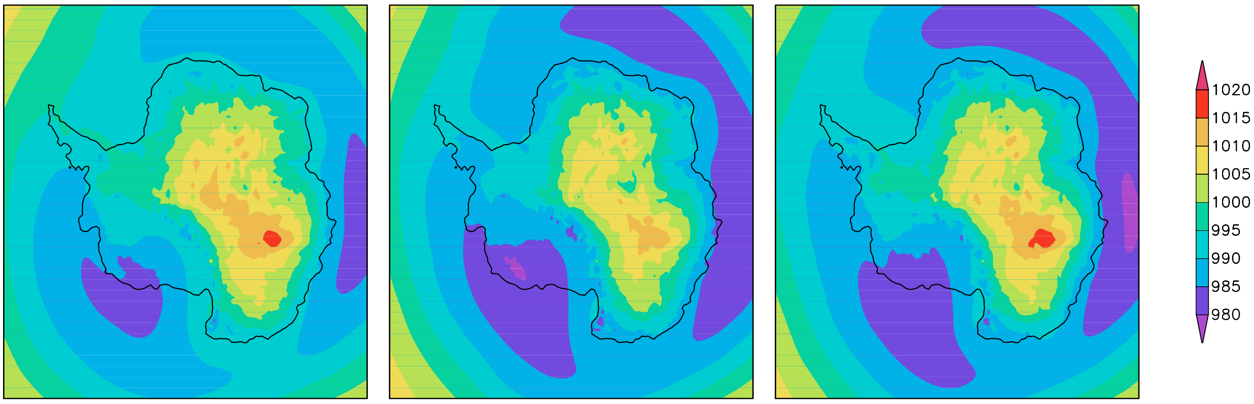

Figure 8.5: *Mean sea level pressure (hPa) in austral winter (JJA), HIRHAM simulation.*
Left – AAO^{-} years: 1963-1968, middle – AAO^{+1} years: 1982-1987, right – AAO^{+2} years: 1993-1998.

Relative to the summer season, the circumpolar vortex becomes stronger during the winter season. Also, the low pressure belt becomes deeper from negative to positive AAO phases. Looking at the MSLP structure during the positive and negative AAO index, one can see that Antarctic anticyclone become stronger thus, preventing inflow of air from the Southern Ocean. The horizontal patterns of the ERA40 and the HIRHAM simulation are in better agreement for "AAO^{+2} - AAO^{-} " than "AAO^{+1} - AAO^{-} ". Fig. 8.7 (top panel, left) shows the increasing

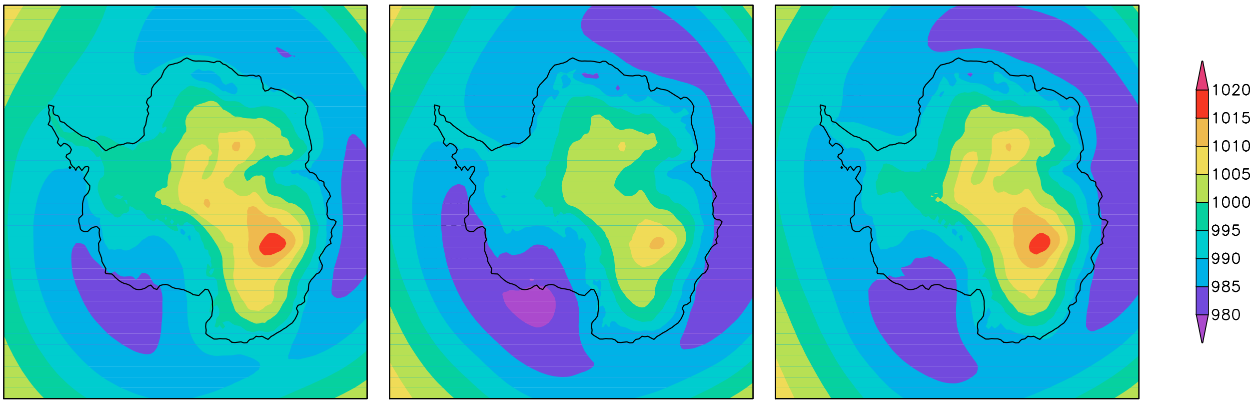

Figure 8.6: *Mean sea level pressure (hPa) in austral winter (JJA), ERA40.*
Left – AAO^{-} years: 1963-1968, middle – AAO^{+1} years: 1982-1987, right – AAO^{+2} years: 1993-1998.

MSLP over the continent; this structure clearly corresponds to the negative temperature trend in the HIRHAM simulation. Last years the AAO index was mostly in a positive phase and this explains the negative temperature trend over the Eastern Antarctic and warming over the Antarctic Peninsula. This conclusion agrees well with Thompson and Solomon (2002).

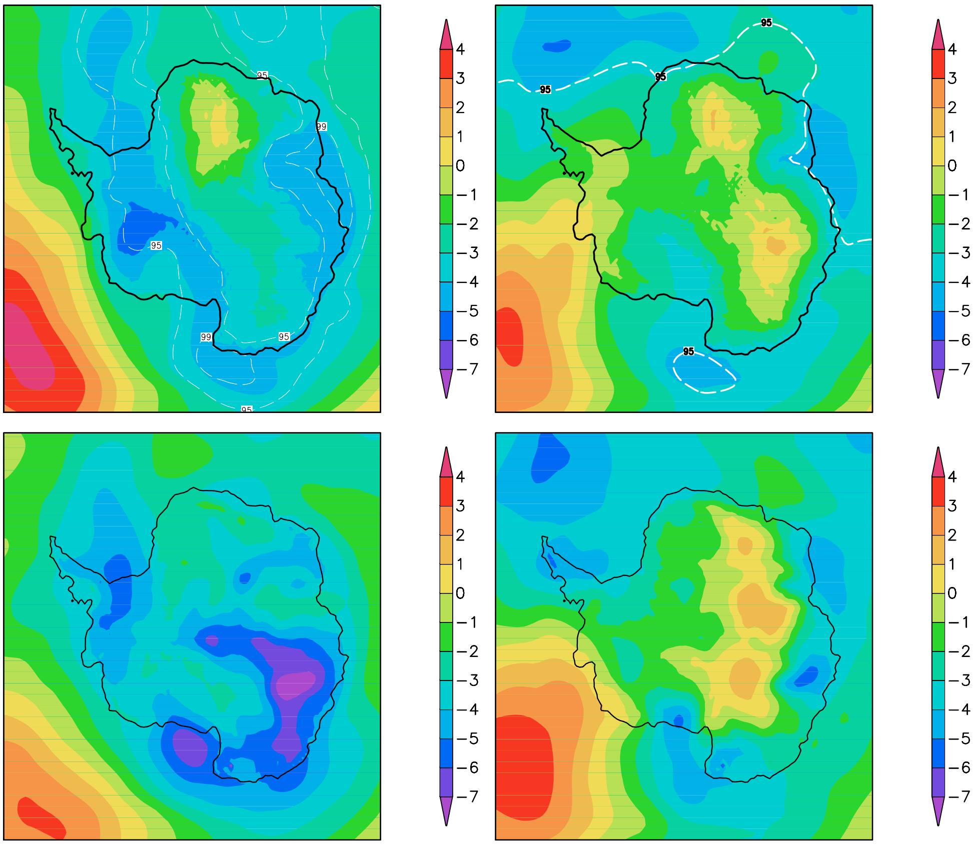

Figure 8.7: *MSLP (hPa) in austral winter (JJA), "AAO^{+1} minus AAO^{-}" (left), "AAO^{+2} minus AAO^{-}" (right). HIRHAM simulation (top panel). ERA40 (bottom panel). The white line denotes statistical significance at the 95 % confidence level.*

8.2 Temperature

Fig. 8.8 and Fig. 8.9 present the 2 *m* summer season temperature for the years AAO^{+1} and AAO^{-} . As expected, the temperature decreases gradually polewards. There are areas of regional cooling in the Eastern part of Antarctica and warming over the Southern Ocean.

The difference in the horizontal structure between positive and negative phases is not as evident as it was in the MSLP pattern. Fig. 8.10 shows the difference " AAO^{+1} - AAO^{-} " (left) and " AAO^{+2} - AAO^{-} " (right) for the HIRHAM simulation and ERA40 data, top and bottom panel, respectively.

The horizontal structure of these differences reveals the sequence of positive and negative temperature areas with the prevalence of the last one over Eastern Antarctica. This structure

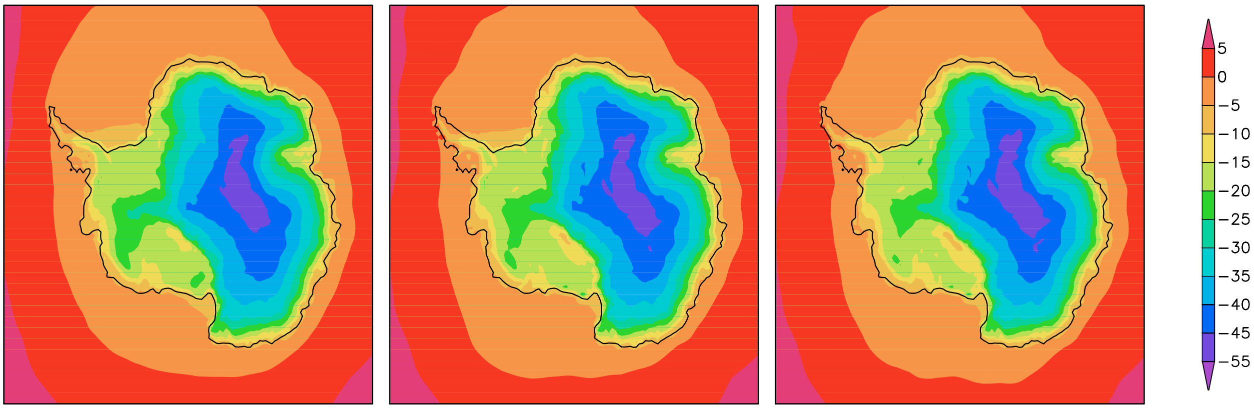

Figure 8.8: *2 m temperature (°C) in austral summer (DJF), HIRHAM simulation.*
Left – AAO$^-$ years: 1963-1968, middle – AAO^{+1} years: 1982-1987, right – AAO^{+2} years: 1993-1998.

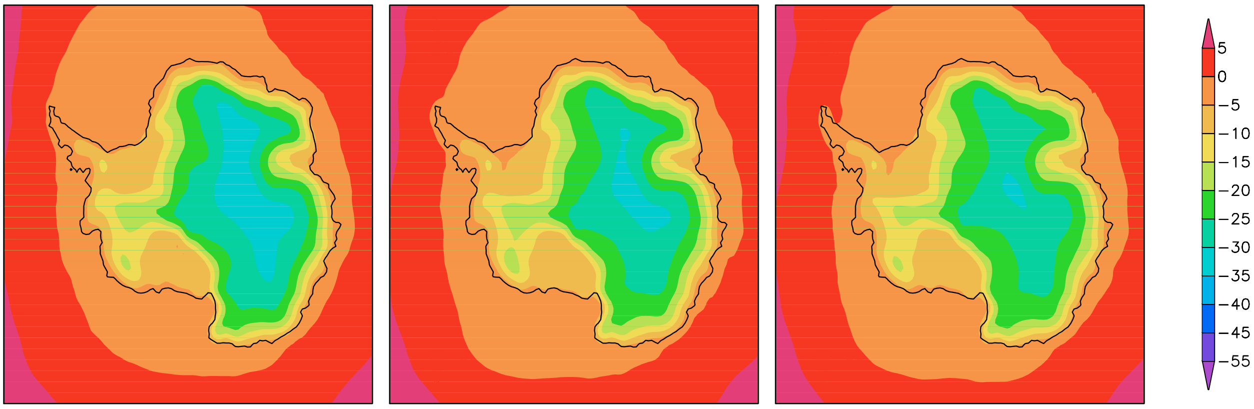

Figure 8.9: *2 m temperature (°C) in austral summer (DJF), ERA40.*
Left – AAO$^-$ years: 1963-1968, middle – AAO^{+1} years: 1982-1987, right – AAO^{+2} years: 1993-1998.

closely follows the temperature trend shown in Fig. 7.4. The ERA40 data show that the surface temperature during the positive phase was higher than during the negative one. This result can explain a doubtful positive temperature trend, which was shown in Fig. 7.4. Compared with the observations, the temperature trend of the HIRHAM simulation appears to be more realistic than the trend derived from the ERA40 data. Apparently, the ERA40 re-analysis have a gap in the global teleconnection representation. Fig. 8.11 to Fig. 8.13 show the 2 *m* temperature horizontal patterns during the wintertime in the HIRHAM simulation and ERA40 data. The area with the minimum temperature increased significantly and covered the entire continent. Fig. 8.13 presents a general background cooling over East Antarctica under AAO positive phase conditions. A notable feature is the zonally variable pattern over the Western Pacific Ocean, which is clearly linked to changes in the sea-ice cover shown in Fig. 8.14 (bottom panel). Strong cooling is found in the areas where sea-ice is prevalent during the positive AAO phases.

It is connected with the strengthening of the circumpolar vortex and the shifting of the latent

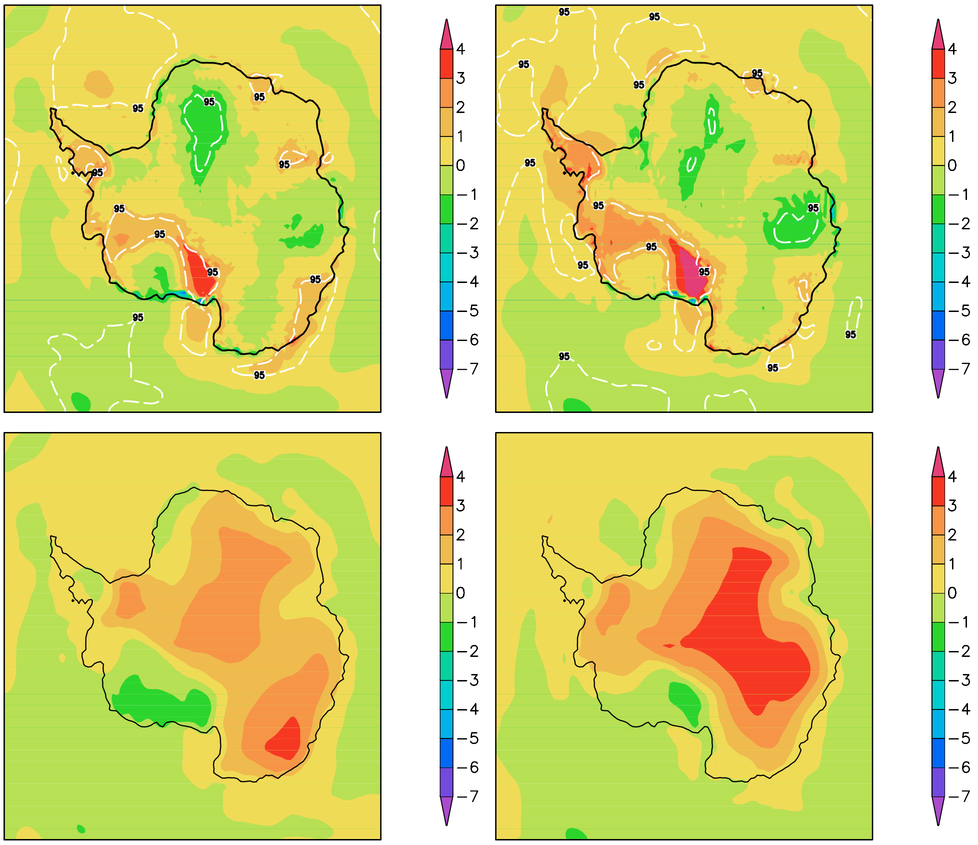

Figure 8.10: *2 m temperature (°C) in austral summer (DJF), "AAO^{+1} minus AAO^{-}" (left), "AAO^{+2} minus AAO^{-}" (right). HIRHAM simulation (top panel). ERA40 (bottom panel). The white line denotes statistical significance at the 95 % confidence level.*

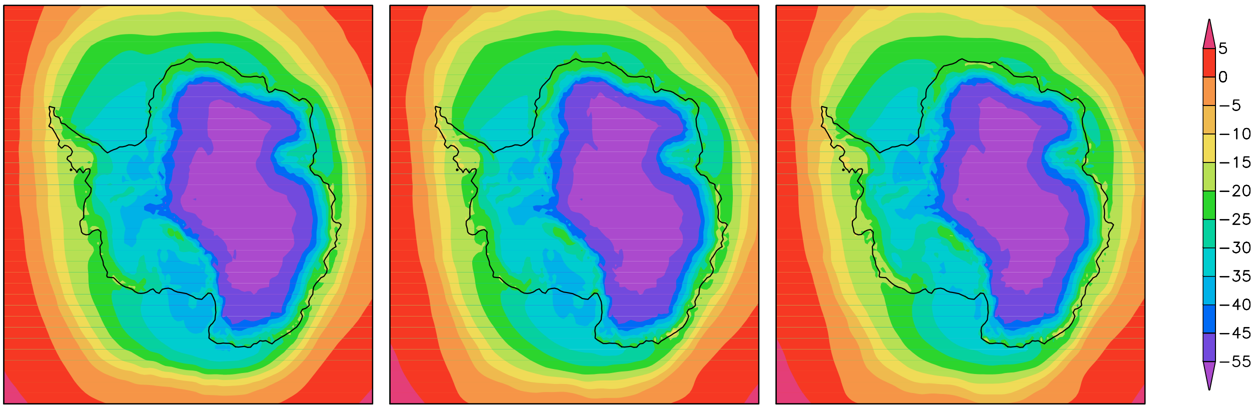

Figure 8.11: *2 m temperature (°C) in austral winter (JJA), HIRHAM simulation.*
Left – AAO^{-} years: 1963-1968, middle – AAO^{+1} years: 1982-1987, right – AAO^{+2} years: 1993-1998.

heat release zone. On the other hand, in Western Antarctica and in the Amundsen Sea sector, sea-ice reduction during the positive AAO phase can be observed and consequently, there is a positive difference between AAO^{+1} and AAO^{-} . The difference of "AAO^{+2} minus AAO^{-} " shows an even stronger warming during the austral winter in that area. Here, the ENSO influ-

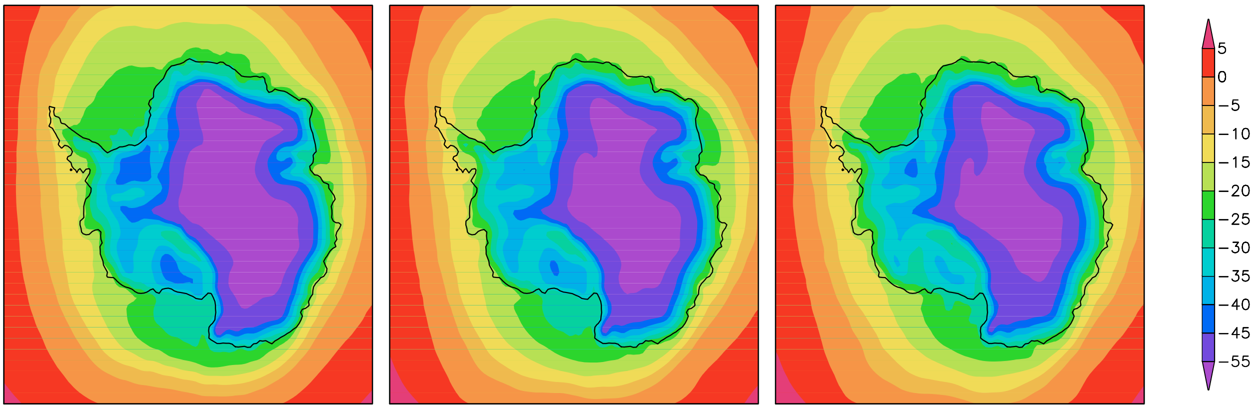

Figure 8.12: *2 m temperature (°C) in austral winter (JJA), ERA40.*
Left – AAO$^-$ years: 1963-1968, middle – AAO^{+1} years: 1982-1987, right – AAO^{+2} years: 1993-1998.

ence can also be taken into account, since this sector is strongly connected with El Niño / La Niña episodes. The mechanism of the sea-ice reduction in the Amundsen-Bellingshausen Seas sector via global teleconnection due to ENSO phenomena was studied in detail by Liu et al. (2002). The researcher figured out that during El Niño events, (i) the intensification (relaxation) of the Hadley Cell (warm air rises near the equator, flows north and south away from the equator at high altitudes, sinks near the poles, and flows back along the surface from both poles to the equator) in the eastern equatorial Pacific (tropical Atlantic) due to an increased (decreased) pole-to-equator meridional temperature gradient leads to (ii) an equatorward (poleward) shift of the subtropical jet. This results in an equatorward (poleward) shift of the storm track in the Ross/Amundsen Seas (the eastern Bellingshausen/Weddell sector). The reduced (enhanced) storm activity in the Ross/Amundsen sector (the eastern Bellingshausen/Weddell sector) leads to (iv) a strengthening (weakening) of the poleward segment of the regional Ferrel Cell and a weakening (strengthening) of the equatorward regional Ferrel Cell there indirectly by (a) changing the meridional eddy heat flux convergence/divergence, and (b) shifting the latent heat release zone. The changes of the regional Ferrel Cell cause anomalous southward (northward) mean meridional heat flux into the sea-ice zone in the Ross/Amundsen sector (the eastern Bellingshausen/ Weddell sector), which limits the growth (encourages) sea-ice there. In summary, the West Pacific sector appears to be a crucial region for communication between high latitudes and low latitudes during late austral winter. The Antarctic Peninsula shows the strongest positive temperature trend (in Fig. 7.4) which can be also connected with the reduction of sea-ice during the austral winter as shown in Fig. 8.14. Outside of the area where the ice is receding, the magnitude of the warming simply decreases gradually away from the Southern Ocean. The pattern of warming is consistent with the hypothesis that the amplification of the warming is largely due to ice-albedo feedback. Harangozo (2006) found that interannual variations in winter sea-ice extent in the West Antarctica Peninsula (WAP) region are largely determined by the atmospheric circulation. The meridional wind-sea-ice extent relationship in the WAP is

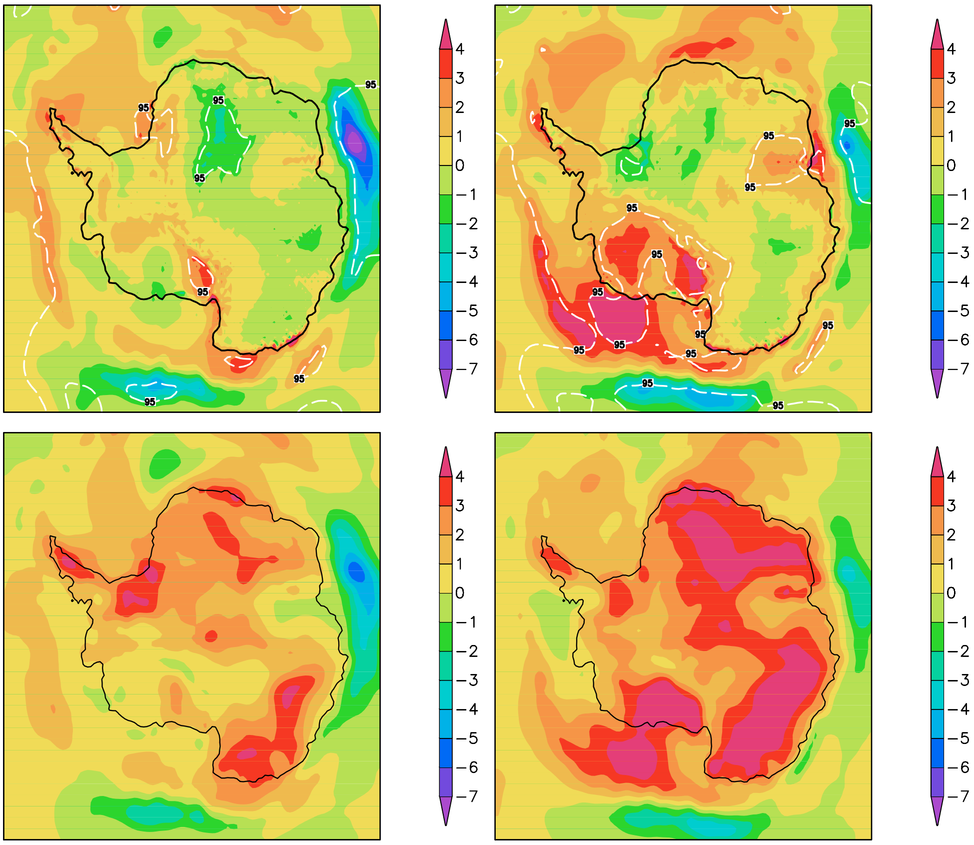

Figure 8.13: *2 m temperature (°C) in austral winter (JJA), "AAO^{+1} minus AAO^{-}" (left), "AAO^{+2} minus AAO^{-}" (right). HIRHAM simulation (top panel). ERA40 (bottom panel). The white line denotes statistical significance at the 95 % confidence level.*

stronger than in any other Antarctic regions. This is because in this region, wind-induced ice drift appears to be the dominant process controlling ice extent. In other Antarctic regions, other factors are equally important, notably ocean currents and considerable ice growth in the winter marginal ice zone. The north-south alignment of the WAP coast is also crucial to explaining the strong relationship because it prevents eastward ice drift by the prevailing westerly winds, as it occurs in other Antarctic regions. Taking into account the horizontal structure of the mean sea level pressure, surface temperature during AAO positive and negative phases and the difference between them, we concluded that recent cooling over the Eastern part of Antarctica and strong warming over the Antarctic Peninsula are closely connected with a global teleconnection pattern in mid-latitudes. Both ENSO and the AAO phases have been shown to affect temperatures in the Antarctic Peninsula. Thus, the negative surface temperature trend over Eastern Antarctica is caused by the strengthening of the circumpolar vortex and hence the decreases of the surface temperature in solstice seasons during AAO positive phases, when the blocking episodes most often occur and the surface temperature is extremely sensitive to circulation changes. In addition, changes in cloud cover and winds associated with blocking, will destroy the surface inversion, effectively adding to the magnitude of the surface temperature anomalies (Hirasawa

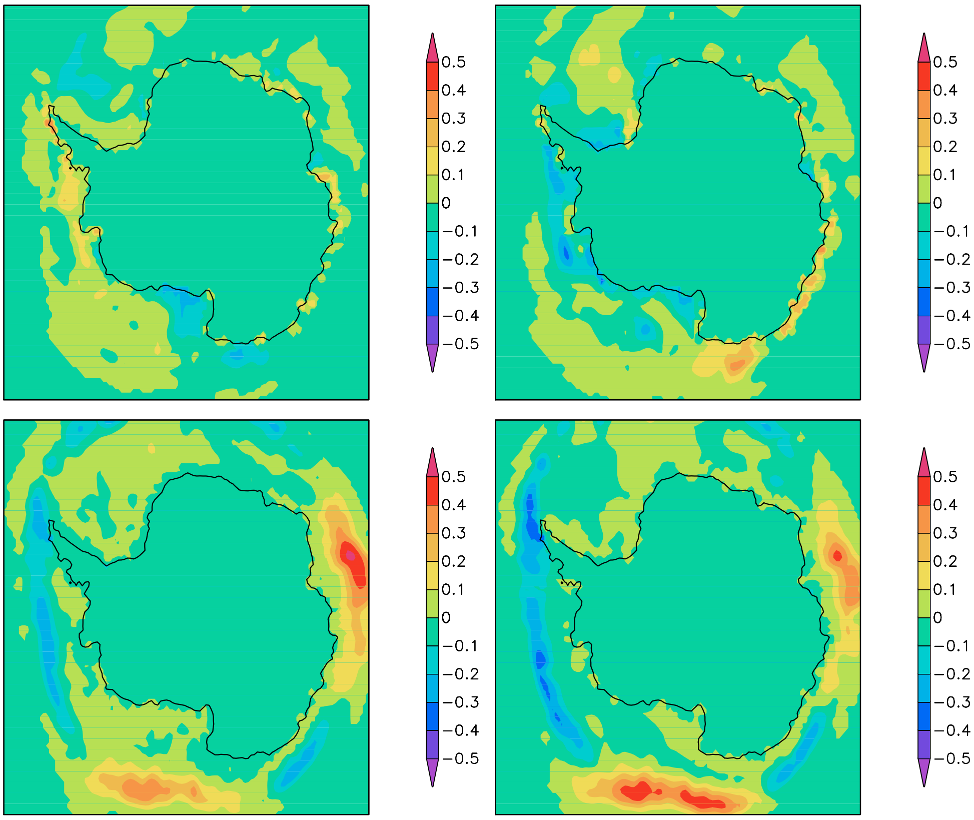

Figure 8.14: *Sea-ice cover in austral summer (DJF) (top panel) and in austral winter (JJA) (bottom panel). "AAO^{+1} minus AAO^{-}" (left), "AAO^{+2} minus AAO^{-}" (right). HIRHAM simulation.*

et al., 2000). Evidently, the surface cooling over 90 °E and 180 °E over the Southern Ocean strongly correlate with increasing sea-ice cover. This is because, the presence of sea-ice decreased the latent heat exchange between the warm Southern Ocean and the atmosphere. The model successfully reproduces strong relationships among the atmospheric circulation, sea-ice, and the surface air temperature that resemble observed patterns associated with interannual and decadal fluctuations.

8.3 Geopotential height

Coming from the surface layer to the first standard isobaric level which does not intersect with the Antarctic dome the 500 *hPa* geopotential level was investigated. Fig. 8.15 - Fig. 8.17 show the 500 *hPa* geopotential height during the austral summer for the negative and positive AAO phases, calculated for the HIRHAM simulation and the ERA40 data. The meridional gradient at the 500 *hPa* geopotential height has generally increased over the ocean, indicating a stronger mid-tropospheric polar vortex with a relatively weak north-south air exchange.

The tropospheric convergence above the continent is observed at this level. It can be seen that the HIRHAM simulation shows the strong anticyclone, strengthening from the negative to the

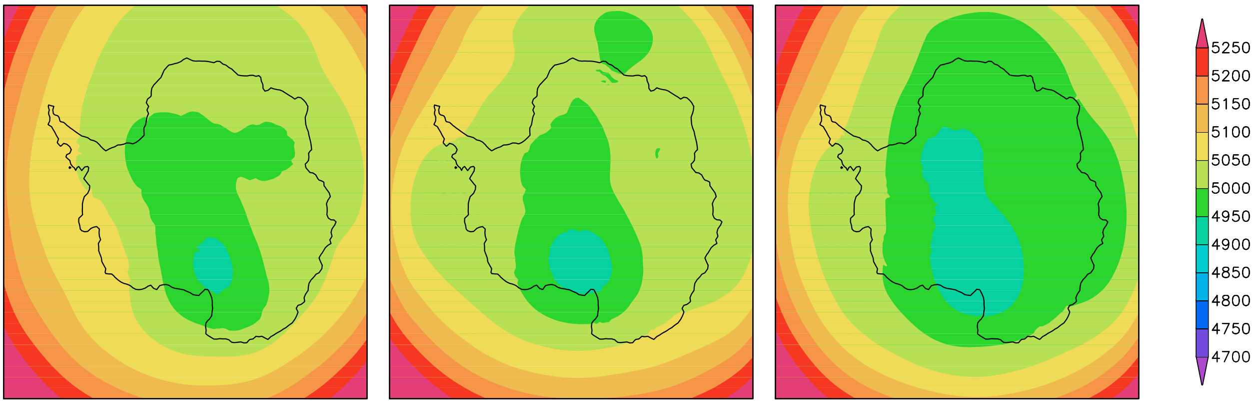

Figure 8.15: *500 hPa geopotential height (gpm) in austral summer (DJF), HIRHAM simulation. Left – AAO*$^-$ *years: 1963-1968, middle – AAO*$^{+1}$ *years: 1982-1987, right – AAO*$^{+2}$ *years: 1993-1998.*

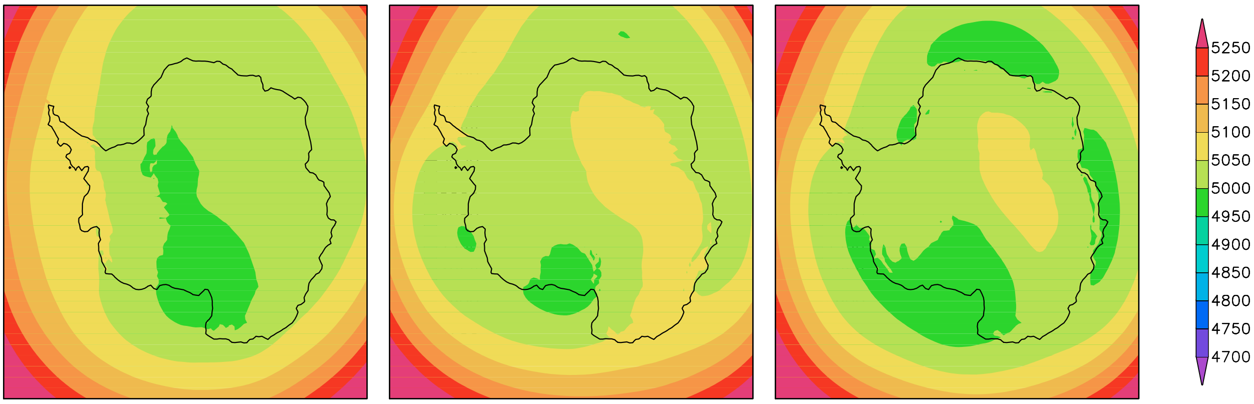

Figure 8.16: *500 hPa geopotential height (gpm) in austral summer (DJF), ERA40. Left – AAO*$^-$ *years: 1963-1968, middle – AAO*$^{+1}$ *years: 1982-1987, right – AAO*$^{+2}$ *years: 1993-1998.*

positive AAO phase. The area corresponds to the minimum geopotential height of 4900 *gpm* increasing from the AAO$^-$ to AAO^{+2} ; during AAO^{+2} it stretches along the Transantarctic Mountains whereas the ERA40 data show the opposite result. If during the AAO$^-$ years the simulation data and re-analysis reveal similar structure then during the AAO positive years the difference becomes more evident. ERA40 500 *hPa* geopotential height shows the zonal structure with an artificial maximum over the continent. Apparently, the surface air temperature anomalies over the Antarctic plateau are induced by an anomalous mid-tropospheric planetary-wave pattern which develops in response to the intensification of the stratospheric polar vortex. This is clearly seen through the model simulation, whereas the reverse situation is seen in the ERA40 data. Fig. 8.17 shows the difference of 500 *hPa* geopotential height between high-AAO years and low-AAO years over the integrated area, for the HIRHAM simulation and the re-analysis data. Looking at the difference "AAO^{+1} - AAO$^-$ " (left) one can say that the model simulation shows a similar pattern to the re-analysis data. There are two negative areas, one along the Eastern coast, another one over the Amundsen Sea and one positive area over Eastern Antarctica. Although the model simulation shows the difference between AAO plus

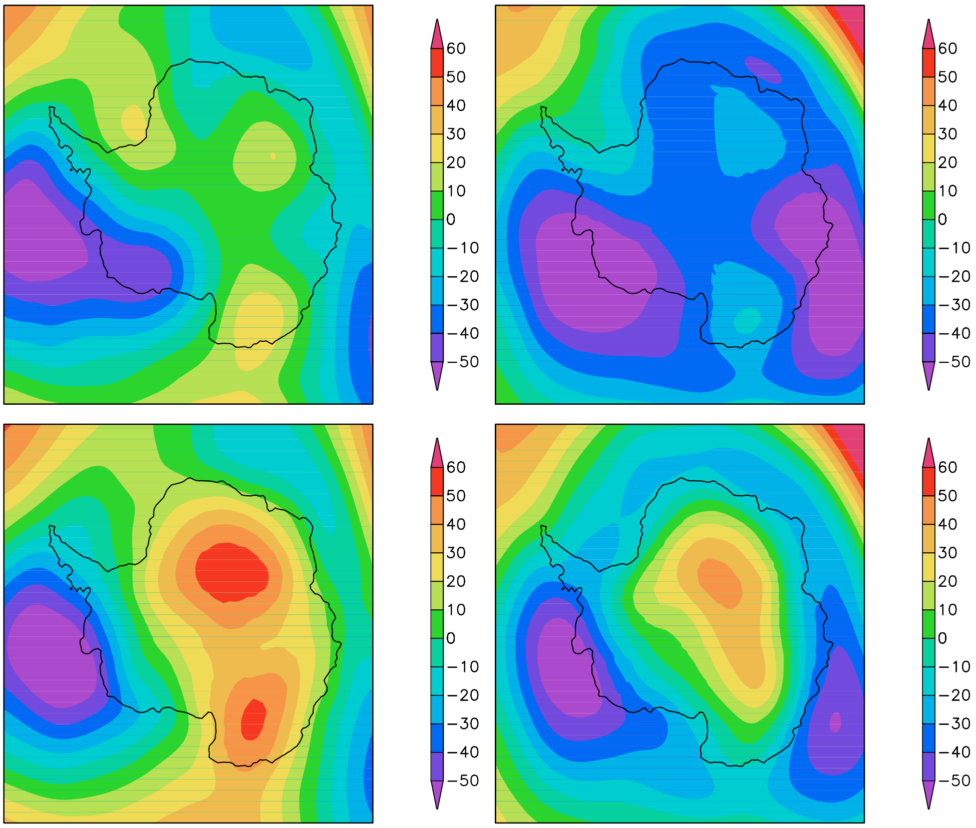

Figure 8.17: *500 hPa geopotential height (gpm) in austral summer (DJF), "AAO^{+1} minus AAO^{-}" (left), "AAO^{+2} minus AAO^{-}" (right). HIRHAM simulation (top panel). ERA40 (bottom panel).*

and AAO minus to be within 10 - 20 *gpm*, whereas ERA40 data reveal stronger difference up to 50 - 60 *gpm*. The right picture presents a different situation, the HIRHAM shows a more or less uniform structure with two minima in the Eastern and Western Pacific, which closely corresponds to the mean sea level pressure trend from 1978 to 1998. The ERA40 data reveal a wavenumber 3 pattern, the alternate blocks of positive and negative differences. Over the entire

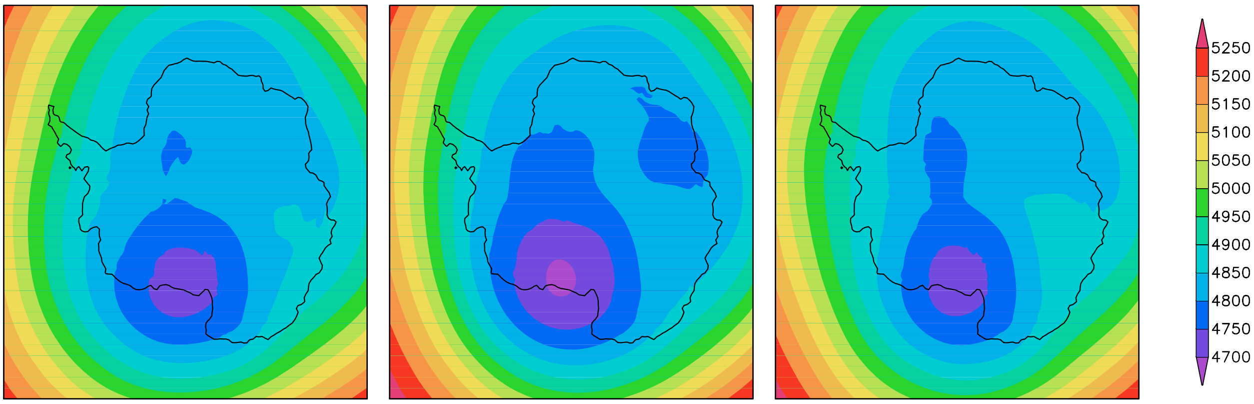

Figure 8.18: *500 hPa geopotential height (gpm) in austral winter (JJA), HIRHAM simulation.*
Left – AAO^{-} years: 1963-1968, middle – AAO^{+1} years: 1982-1987, right – AAO^{+2} years: 1993-1998.

continent the 500 *hPa* geopotential height during the positive AAO^{+2} phases was higher than during AAO^{-} . This structure shows that at this standard pressure level the ERA40 data do not have strong inter-annual or seasonal cycle variability.

The next intercomparison of the positive and negative AAO years for 500 *hPa* height was done for the wintertime. Fig. 8.18 to Fig. 8.20 show the austral winter 500 *hPa* horizontal structure and the difference between AAO phases. The HIRHAM simulation as well as the re-analysis data shows the evident zonal structure, with minimum values over the Ross Ice Shelf. The model output is in a better agreement with the driving data than what it was during the summertime, the average difference is 50 *gpm* over the most of the continent. The biggest variance can be observed during the AAO^{+2} . The strong meridional gradient is found in the simulation data and shown in Fig. 8.20 (left, top panel). The difference between AAO^{+1} and AAO^{-} shows the one maximum over the Pacific Ocean and two symmetrical minima along the Eastern coast and over Western Antarctica, which leads to the strengthening of the low pressure belt around the continent. The ERA40 data show the weakening of the circumpolar vortex with a small exception in the Western Pacific Ocean. The difference "AAO^{+2} minus AAO^{-} " (right) shows a weaker meridional gradient in both datasets. The simulation data and the re-analysis show the positive difference over the Eastern part of Antarctica, 10 to 20 *gpm* and 20 to 50 *gpm* in the HIRHAM output and ERA40 data, respectively. Apparently, the strong surface cooling during the positive AAO years is an issue relating to the changes of the atmospheric circulation which can be seen through the whole atmospheric layers. Therefore, these comparisons of positive and negative AAO phases may serve as a basis for the temperature and MSLP trend explanation.

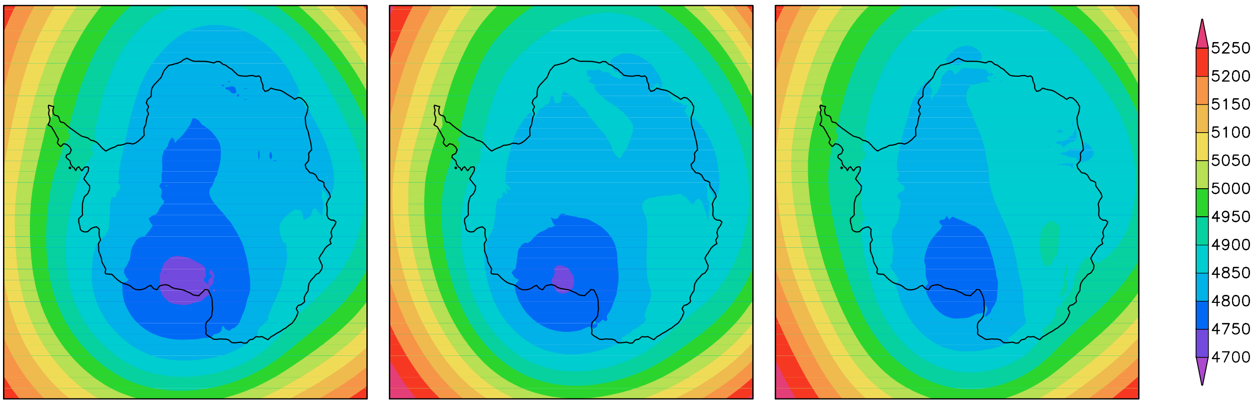

Figure 8.19: *500 hPa geopotential height (gpm) in austral winter (JJA), ERA40.*
Left – AAO^{-} years: 1963-1968, middle – AAO^{+1} years: 1982-1987, right – AAO^{+2} years: 1993-1998.

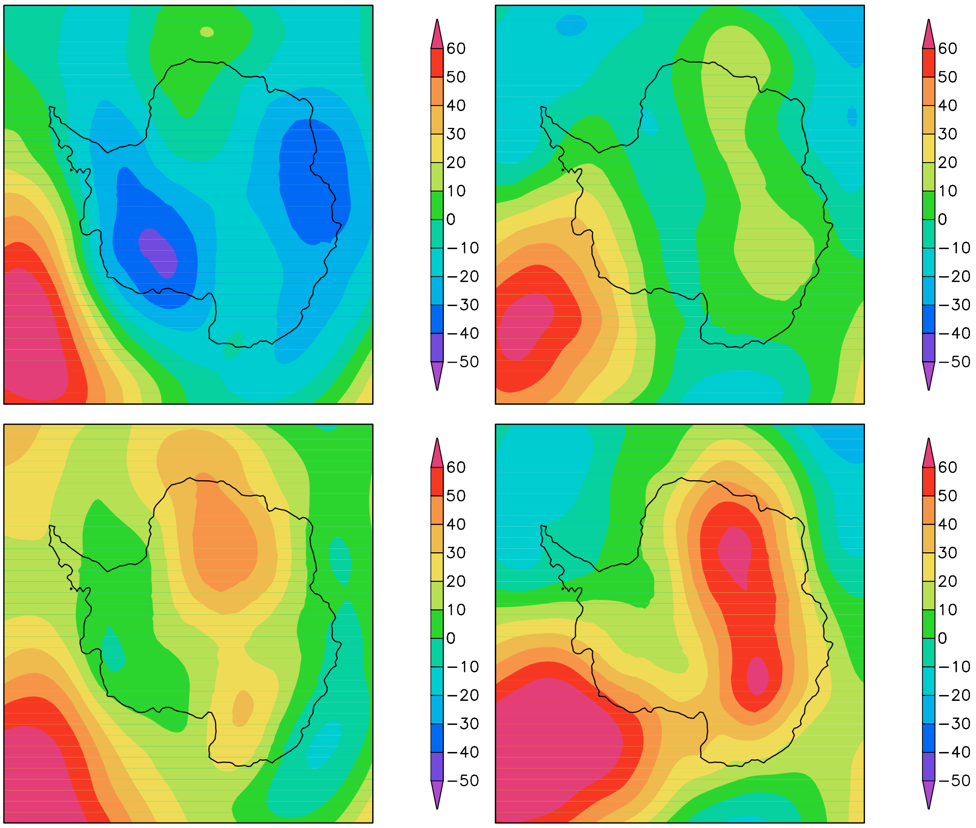

Figure 8.20: *500 hPa geopotential height (gpm) in austral winter (JJA), "AAO^{+1} minus AAO^{-}" (left), "AAO^{+2} minus AAO^{-}" (right). HIRHAM simulation (top panel). ERA40 (bottom panel).*

8.4 Precipitation and net mass balance

Fig. 8.21 shows the precipitation disparity between the positive and negative AAO years. The precipitation distribution is strongly connected with the synoptic-scale processes and the cyclonic activity in the coastal regions. During the wintertime, growing sea-ice closes the Southern Ocean around the continent, complicating the delivery of the relatively warm and humid air from the ocean to the continent. During the positive AAO phases, the circumpolar vortex becomes stronger, increasing the number of cyclones traveling towards the continent. As a consequence, the increasing precipitation rate can be observed over the coastline in Western Antarctica and along Wilkes Land. Over the central part of the continent the situation is reversed. The stronger anticyclone prevents the inflow of the warm air inland over the continent thereby decreasing the rare precipitation. The simulation result does not reveal big differences between AAO^{+1} and AAO^{+2} , the re-analysis data show the bigger disparity as can be seen in Fig. 8.21 (bottom panel). The ERA40 data show the changed areas spreading towards the inner part of the continent, for example Queen Maud Land, Wilkes Land and Marie Byrd Land.

The net mass balance intercomparison is shown in Fig. 8.22 - Fig. 8.24. The accumulation mass balance shows the biggest values along the coastline and a minimum over Eastern

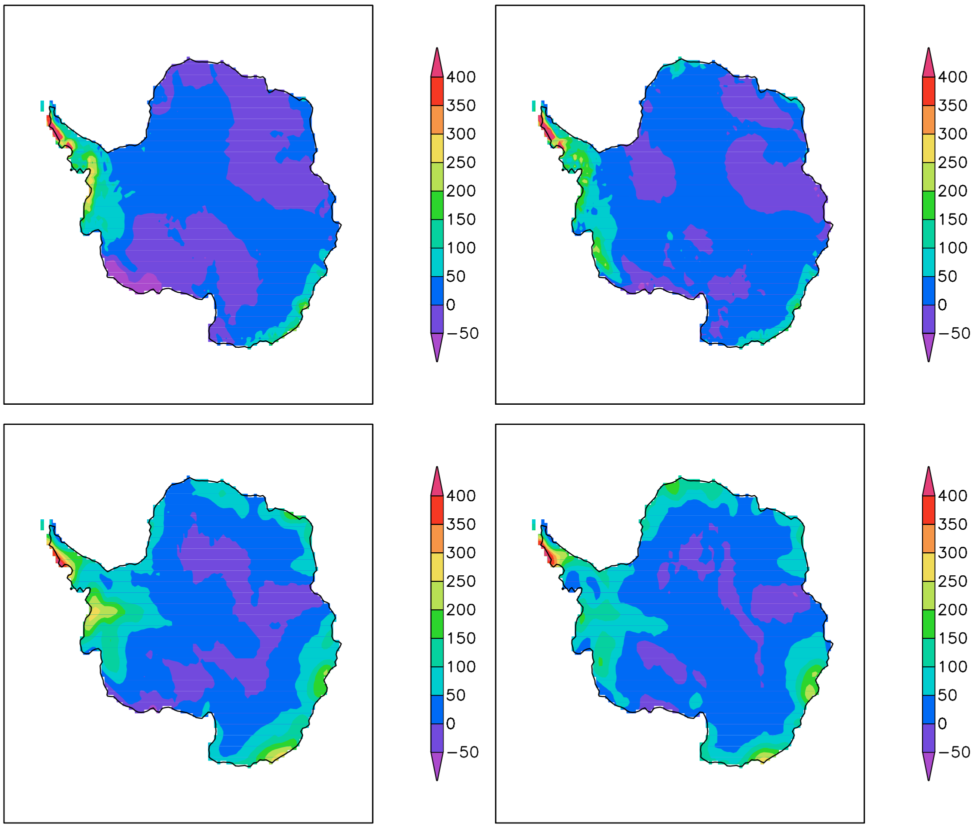

Figure 8.21: *Precipitation rate (mm/year), "AAO^{+1} minus AAO^{-}" (left), "AAO^{+2} minus AAO^{-}" (right). HIRHAM simulation (top panel). ERA40 (bottom panel).*

Antarctica. The areas with the negative mass balance or blue ice areas are present during the positive and negative AAO phases. The size of those areas only slightly changes with time, while the biggest changes take place along the coastline. The maximum difference between the AAO^{-} , AAO^{+1} and AAO^{+2} can be observed over Wilkes Land and the Antarctic Peninsula. The increasing precipitation rate and consequently the net mass balance over Antarctic

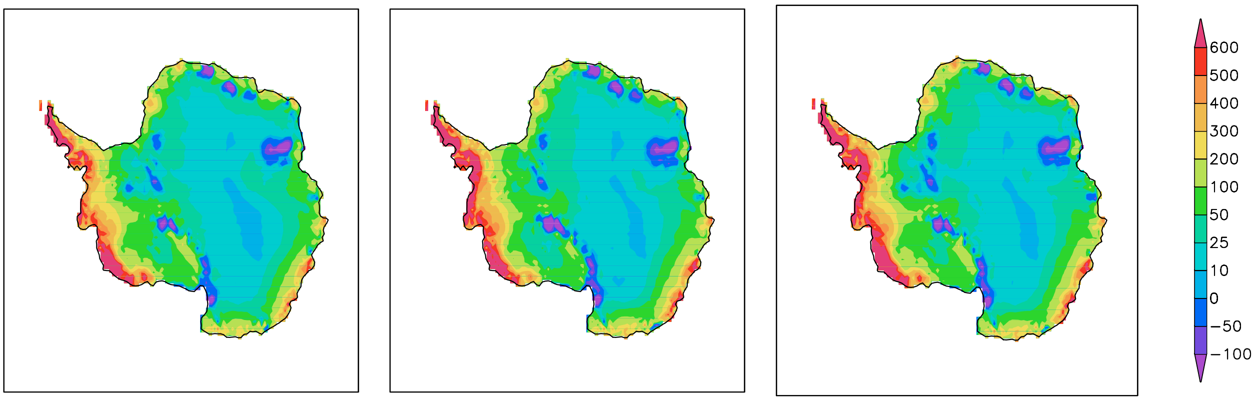

Figure 8.22: *Net mass balance (mm/year), HIRHAM simulation.*
Left – AAO^{-} years: 1963-1968, middle – AAO^{+1} years: 1982-1987, right – AAO^{+2} years: 1993-1998.

Peninsula during the positive AAO phases are connected with the reduction of sea-ice in the Bellingshausen Sea and the increase in the surface temperature. As has been explained before,

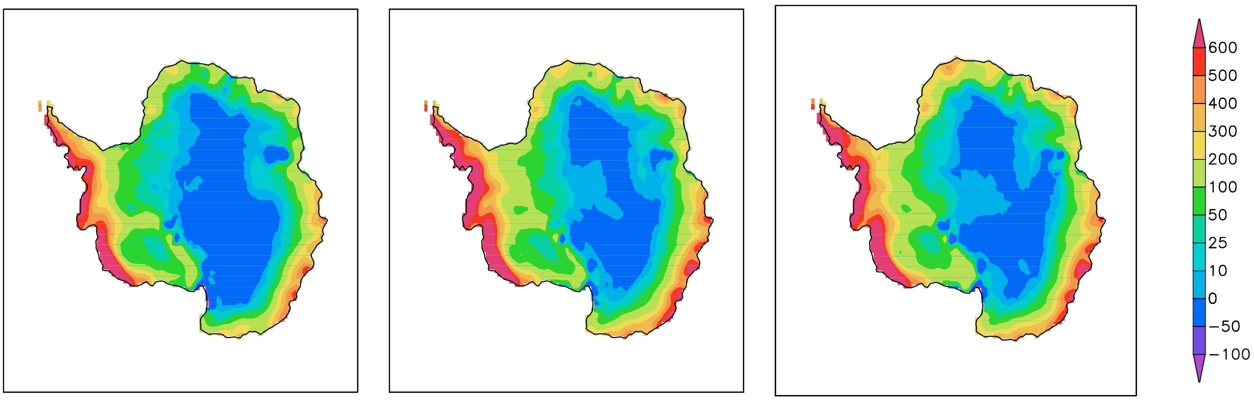

Figure 8.23: *Net mass balance rate (mm/year), ERA40.*
Left – AAO^{-} years: 1963-1968, middle – AAO^{+1} years: 1982-1987, right – AAO^{+2} years: 1993-1998.

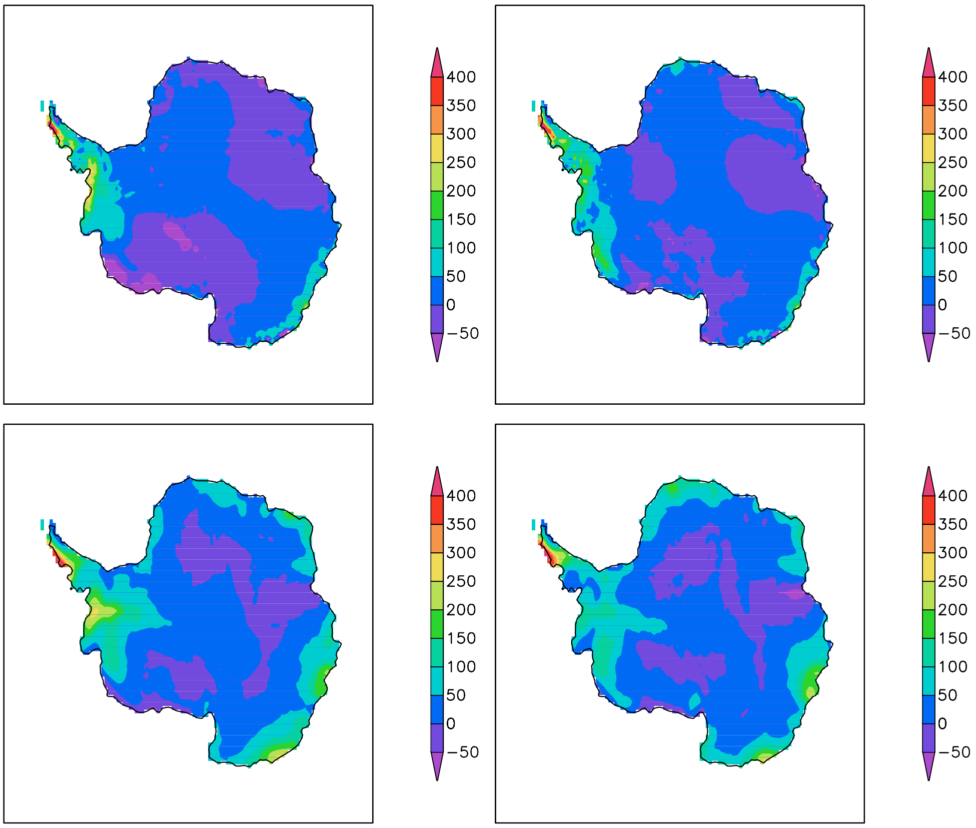

Figure 8.24: *Net mass balance (mm/year), "AAO^{+1} minus AAO^{-}" (left), "AAO^{+2} minus AAO^{-}" (right). HIRHAM simulation (top panel). ERA40 (bottom panel).*

most changes (for example sea-ice distribution) take place on the Western part of the Antarctic Peninsula rather than on the Eastern part. One can say the same about the net mass balance.

The high orography of this place acts as a barrier to cyclonic movement, thus it increases the precipitation rate and the net mass balance of the area. This is readily seen in Fig. 8.24.

To sum up, the global teleconnection plays an important role in the regional climate formation of the Antarctic continent. The AAO index shows a pressure gradient between the low and high southern latitudes. The positive AAO index means a strengthening of the circumpolar vortex around the continent, increasing both the westerly winds and the cyclonic activity in the high southern latitudes. Our investigation vividly shows the close connection between the main climate-formation variables (MSLP, surface temperature, etc.) and AAO phases. The model simulation shows the mismatch with the ERA40 driving data but closely follows the observational data. The recent surface cooling over the Eastern Antarctic can be explained by an increase in the number of years with a positive AAO index.

Chapter 9

Conclusions

The regional climate model HIRHAM was successfully applied to a pan-Antarctic area. Simulations for the years from 1958 to 1998 have been carried out using this model, with the ERA40 data used for the lateral and lower boundary forcing. The HIRHAM simulation results for 2 *m* air temperature, mean sea level pressure (MSLP), low level wind, 500 *hPa* geopotential height, short and longwave radiation, precipitation, evaporation and net mass balance have been compared with available observational, remote sensing and the ERA40, NCEP-NCAR re-analyses datasets.

The simulated MSLP shows the highest correlation index of 0.97 with the observation data among two re-analysis datasets. The 2 *m* air temperatures, simulated by the model at the 14 stations listed in Tab. 3.2 are very closed to the observational data. The summer averaged model 2 *m* air temperature underestimates the ERA40 data around the Eastern Antarctic by a maximum of 12 °*C*. Also the model cloud cover during the austral summer and winter is overestimated compared to the observational data in average by 16 %. Therefore, the model summer cold bias in 2 *m* air temperature is partly due to the overestimation of the cloud cover.

A series of sensitivity experiments using the HIRHAM model were conducted in order to identify the key processes responsible for the surface temperature and MSLP summer bias in the regional model climate simulations. The sensitivity cloud cover run showed an improvement in the simulated cloudiness of the model after modifying the tuning parameter. As in this case, the threshold relative humidity seems to not be an appropriate or insufficient solution to the problem. The revised stability function under the stable condition has slightly increased the downward heat flux during summer. Therefore, we found a small warming of 1 °*C* in the summer 2 *m* temperature. Two sensitivity runs were done where the flow relaxation parameter in the boundary zone is constant with height and a function of the horizontal grid points only. The twelve and eight points buffer zone have been applied to study the influence of the modified relaxation zone width on the MSLP and 2 *m* temperature. The twelve points thick buffer zone reduced the austral summer MSLP bias over the Antarctic Plateau by 2 - 3 *hPa*, which is almost 35 % of the MSLP summer bias found in the 40 years HIRHAM simulation. The surface temperature is a less dependent variable from the lateral boundary condition uncertainties than MSLP. Therefore, the 2 *m* temperature horizontal pattern does not show the big disparity by $\pm$ 1 $^{\circ}C$ between the control and both sensitivity runs. There is no key element responsible for temperature underestimation in the model, it is a more complex problem and relates to the feed back mechanisms presented in the HIRHAM model. The experiments described here underline the fact that in the Antarctic region a well-suited description of the boundary conditions and planetary boundary layer physics is most important.

The averaged winter surface temperature mean bias between the model simulation and re-analysis data or station data is ± 3 $^{\circ}C$. During winter, the underestimation of the surface temperature is partly cancelled by the warming effect of an overpredicted cloud amount. The simulated surface inversion depth is 15 - 20 $^{\circ}C$ which is in agreement with Phillpot and Zillman (1970). In winter, the model surface temperature has a fairly realistic representation and is in agreement with the satellite-derived surface temperature from Comiso (2000). In summer, the model underestimates the surface temperature by 12 $^{\circ}C$ compared to Comiso (2000). In this case, because the satellite data were derived based on a cloud-free case condition, the cloud cover representation plays a very important role.

The HIRHAM model was able to predict the observed temperature inversions; however, compared with the measured data during summertime the predicted surface temperature was too low. The horizontal and vertical structure of the simulated wind field clearly shows the katabatic wind phenomena. The modeled wind is lower than observational data by about 3 - 4 m/s. The simulated total water vapour (TWV) was compared to the TWV derived from the satellite data. The model field shows a good agreement with the remote sensing data, with an annual difference of 0.5 kg/m^2.

The averaged value of the net mass balance over the grounded ice sheet was compared with the compilation of observation, re-analysis and modeled datasets. The HIRHAM simulation slightly underestimates the accumulation rate. This is partly connected with overestimation of the horizontal size of the blue ice areas (places with the negative net mass balance). The reduction of these artificial areas can increase the net mass balance value. The decadal scale processes were studied based on trend calculations. The long-term run was divided into two 20 years parts (1958 - 1977 and 1978 - 1998). The 2 *m* temperature, 500 *hPa* temperature, MSLP, precipitation and net mass balance trends were calculated for both periods and over the years from 1958 to 1998. During the last two decades the strong surface cooling of 0.6 $^{\circ}C/decade$ can be observed over the Eastern Antarctica, this result is in a good agreement with the result of Chapman and Walsh (2005), who calculated the temperature trend based on the observational data. Over the period from 1958 to 1998 the 2 *m* temperature trend uncertainty was calculated. The uncertainty of the trend varies from ± 0.05 to 0.07 $^{\circ}C/decade$ over the Antarctic continent. The 500 *hPa* temperature shows a slight rise of about 0.5 $^{\circ}C/decade$ over the entire integration area. The MSLP trend reveals a big disparity between the first and second parts of the 40 year run. The overall trend shows the strengthening of the circumpolar vortex and continental anticyclone. The net mass balance as well as precipitation both show a positive trend over the Antarctic Peninsula region, along Wilkes Land and in Dronning Maud Land. The increasing precipitation rate was marked during the last 20 years in the HIRHAM simulation and ERA40 data. The Antarctic ice sheet grows over the Eastern part of Antarctica, but there is a small exceptions in Dronning Maud Land and Wilkes Land and sinks in the Antarctic Peninsula; this result is in good agreement with the satellite-measured altitude presented in Davis et al. (2005).

To better understand the horizontal structure of MSLP, 2 *m* temperature and net mass balance trends the influence of the Southern Annual Mode (SAM) on the Antarctic climate was investigated. The main meteorological parameters during the positive and negative Antarctic Oscillation (AAO) phases were compared to each other. The AAO index shows the phase of the SAM. A positive/negative AAO index means a strengthening/weakening of the circumpolar vortex, poleward/northward storm tracks and prevailing/weakening westerly winds. For a detailed investigation of global teleconnection, two positive and one negative periods of AAO phase were chosen. The first (negative) is denoted AAO^{-} and coveres the years 1963 to 1968, the second (positive) is denoted AAO^{+1} and covers the period from 1982 to 1987 and the third (positive) period is denoted AAO^{+2} and covers the years 1993 to 1998. Over recent decades the SAM has shifted into its positive phase, with decreasing MSLP values over the Antarctic and increasing values at mid-latitudes. The differences in MSLP between positive and negative AAO years during the winter months partly explain the surface cooling during the last decades. The same can be said about the difference in surface temperature patterns between AAO^{-} , AAO^{+1} and AAO^{+2} . The surface temperature trend pattern closely follows the difference between AAO plus and AAO minus. Another direct connection was found between the sea-ice reduction along the Western Antarctic Peninsula and surface temperature warming in this area. The reduction of the sea-ice increased the latent heat flux and supplied the Antarctic continent with relatively warm and humid air.

In summary, the presented results show that the HIRHAM model is able to simulate the regional climate of Antarctica with sufficient accuracy. Although, the HIRHAM simulated MSLP has the highest correlation coefficient with the observation data, the net mass balance pattern and trend are in good agreement with the satellite data presented by Davis et al. (2005). The temperature trend reveals the cooling over the Antarctic continent which is supported by Chapman and Walsh (2005) and the simulated surface inversion strength closely follows Phillpot and Zillman (1970). The HIRHAM model has the shortages in the correct simulation of the 2 *m* temperature in the summer and the total cloud cover all-the-year-round.

Numerical simulations with the HIRHAM model shows the strong connection between surface temperature decadale scale changes and AAO phases. Thus, numerical simulations may be a powerful tool for studying the teleconnection. As an outlook for the future, additional investigation should be made for understanding the influence of ENSO phenomena on the regional climate of Antarctica. Furthermore, the improved (for example albedo scheme) HIRHAM model should be applied toward studies of the critical questions of the Antarctic mass balance and the role of Antarctica in a changing climate.

Appendix A

Standard deviation

Standard deviation (SD) is the most common measure of statistical dispersion, measuring how spread out the values in a dataset are. If the data points are all close to the mean, then the SD is close to zero. If many data points are far from the mean, then the SD is far from zero. If all the data values are equal, then the SD is zero. The SD is measured in the same units as the values of the investigated parameter. SD was calculated as:

$$\sigma = \sqrt{\frac{\sum_{k=1}^{N} (X_k - \bar{X})^2}{N}} \qquad k = 1 \ldots N \tag{A.1}$$

where X_k is simulated pressure (2 *m* temperature, 500 *hPa* geopotential height, etc.), $\bar{X}$ is the mean value (calculated over the given period) and N is the months number included in statistic calculation. SD may serve as a measure of uncertainty. The reported SD of a group of repeated measurements should give the precision of those measurements. When deciding whether measurements agree with a theoretical prediction, the SD of those measurements is of crucial importance: if the mean of the measurements is too far away from the prediction (with the distance measured in SD), then we consider the measurements as contradicting the prediction. This makes sense since they fall outside the range of values that could reasonably be expected to occur if the prediction were correct and the SD appropriately quantified.

Fig. A.1 shows SD for MSLP during the austral summer and winter calculated over 40 years, for the HIRHAM and ERA40 datasets. As one can see, there are two permanent SD maxima in high Southern latitudes. One is above the central part of the Eastern part of the Antarctic continent and corresponds to the oscillation of the polar anticyclone. Another one is over the Amundsen Sea and persists through all seasons. The circumpolar vortex or low pressure system belt does not show a strong pressure variability.

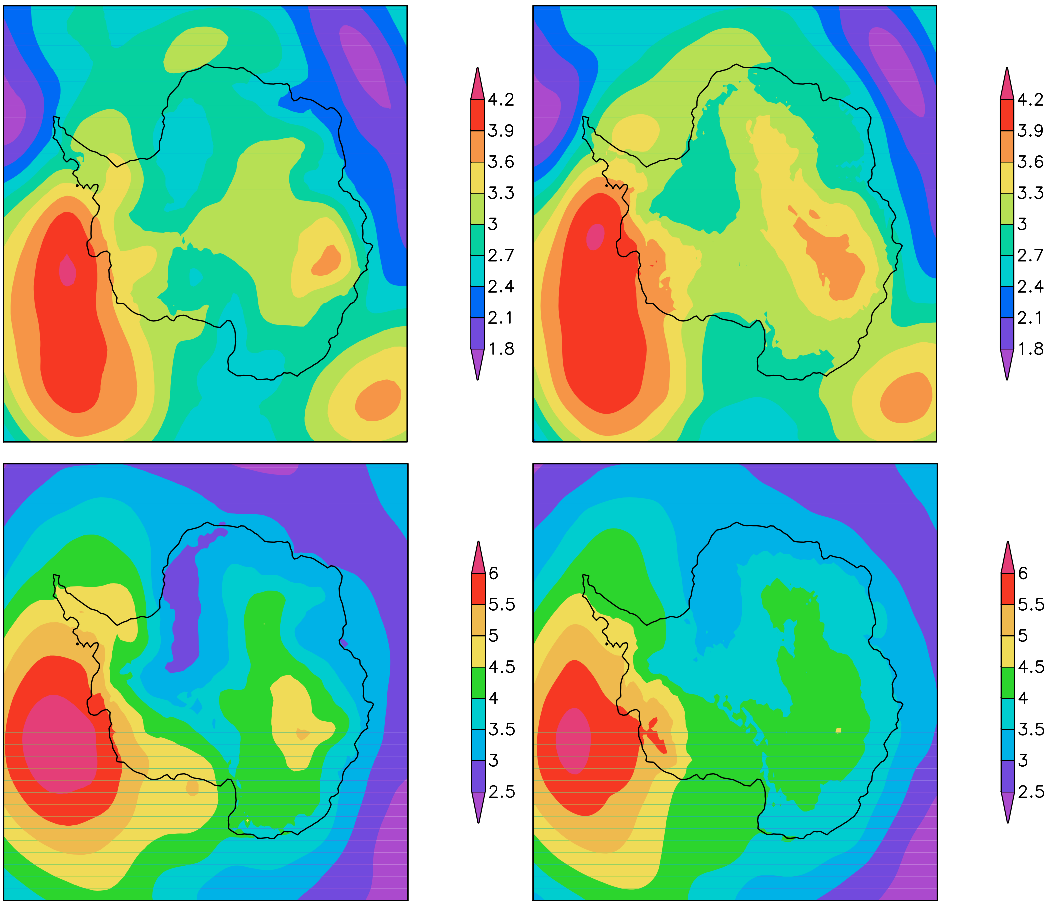

Figure A.1: *Standard deviation of MSLP (hPa) in austral summer (DJF) (top panel) and austral winter (JJA) (bottom panel) averaged over 1958 - 1998. ERA40 (left), HIRHAM simulation (right).*

Fig. A.2 shows the SD of 500 *hPa* geopotential height for the summer and winter seasons, respectively. The maximum over the Amundsen Sea shifted more to the north-west direction relative to the MSLP charts. The seasonal charts closely follow the surface MSLP maps. During the austral winter the circumpolar vortex becomes more visible relative to the summer season. The ERA40 data and HIRHAM simulations show very similar horizontal patterns.

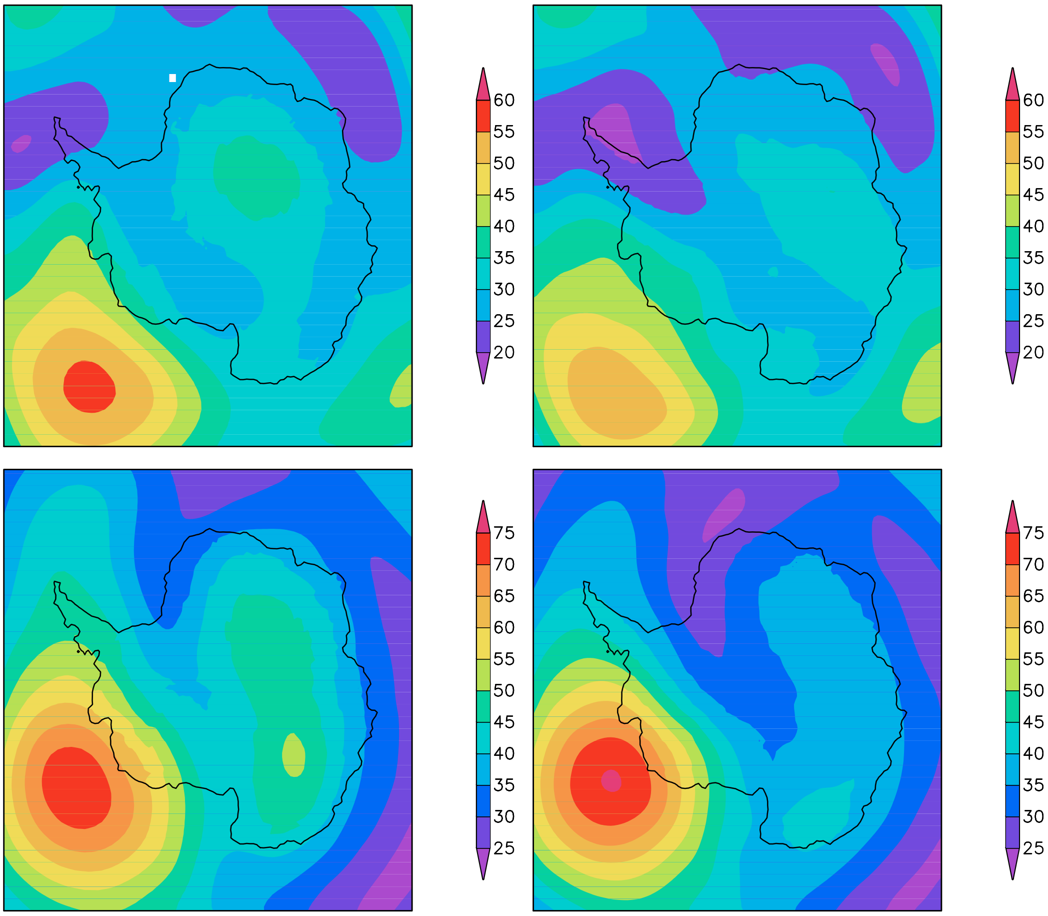

Figure A.2: *Standard deviation of 500 hPa geopotential height (m) in austral summer (DJF) (top panel) and austral winter (JJA) (bottom panel) averaged over 1958 - 1998. ERA40 (left), HIRHAM simulation (right).*

Fig. A.3 shows the SD of 2 *m* temperature for the winter and summer seasons, for the HIRHAM simulation and ERA40 data. During the summer months re-analysis data show a higher variability than model simulations. The horizontal pattern calculated for the model simulation shows the maximum value over the Ross Ice Shelf whereas over the continent the SD less significant. Both horizontal patterns closely follow the summer temperature trend presented in Fig. 7.2 (left). One may conclude that the main input to the negative temperature trends comes during the austral summer. The temperature SD during the austral winter is presented in Fig. A.3. The horizontal structure closely follows the winter sea-ice mask. The HIRHAM simulation shows two minima: one over the central part of the continent and another one over the Southern Ocean. The maximum changes are located close to the ice edge and in the Amundsen-Ross Seas sector. This result is in good agreement with re-analysis data. ERA40 data do not show such strong variability in SD. The biggest differences are over the Ross Ice Shelf and over the Antarctic Peninsula.

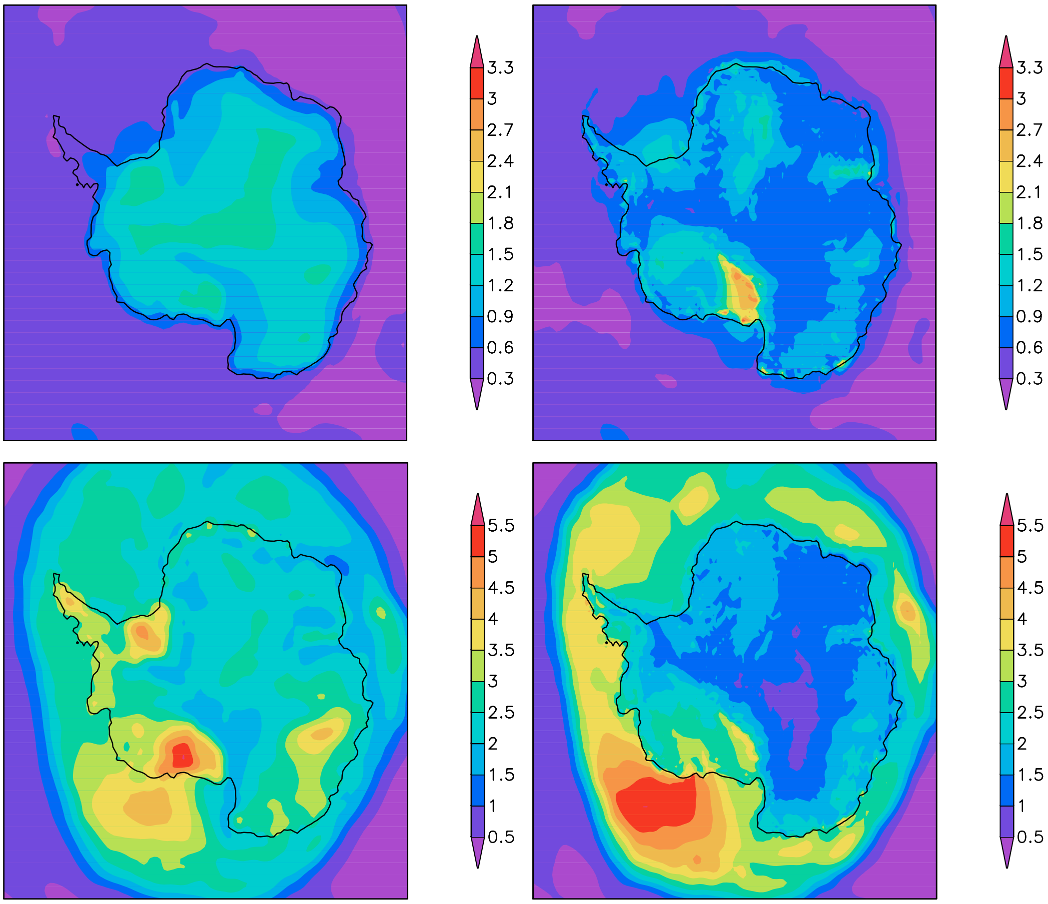

Figure A.3: *Standard deviation of 2 m temperature (°C) in austral summer (DJF) (top panel) and austral winter (JJA) (bottom panel) averaged over 1958 - 1998. ERA40 (left), HIRHAM simulation (right).*

Fig. A.4 shows the SD of the shortwave (top panel) and longwave (bottom panel) radiation during the austral summer (left) and winter (right) for the HIRHAM simulation. During the summertime the SD does not show big variability and minimum values can be observed over Eastern Antarctica. The high values are located over the Southern Ocean and the horizontal pattern does not reveal areas with a high SD rate, except for a few places along the coastline. During the winter season the polar night takes place, thus maximum variability of the SD was found in the 50 °S latitude zone. The longwave radiation is a more seasonally dependent variable than the shortwave radiation. During the austral summer the horizontal field shows more or less uniform structure with two maxima: one in the Western Antarctica along Coats Land and another one in Eastern Antarctica over Wilkes Land. During the austral winter (right) the SD follows the sea-ice mask. The biggest variability can be found in the Indian and Pacific Oceans. These changes are connected with the annual sea-ice mask variability and polynya presents (holes in the ice) for example the Weddell Sea.

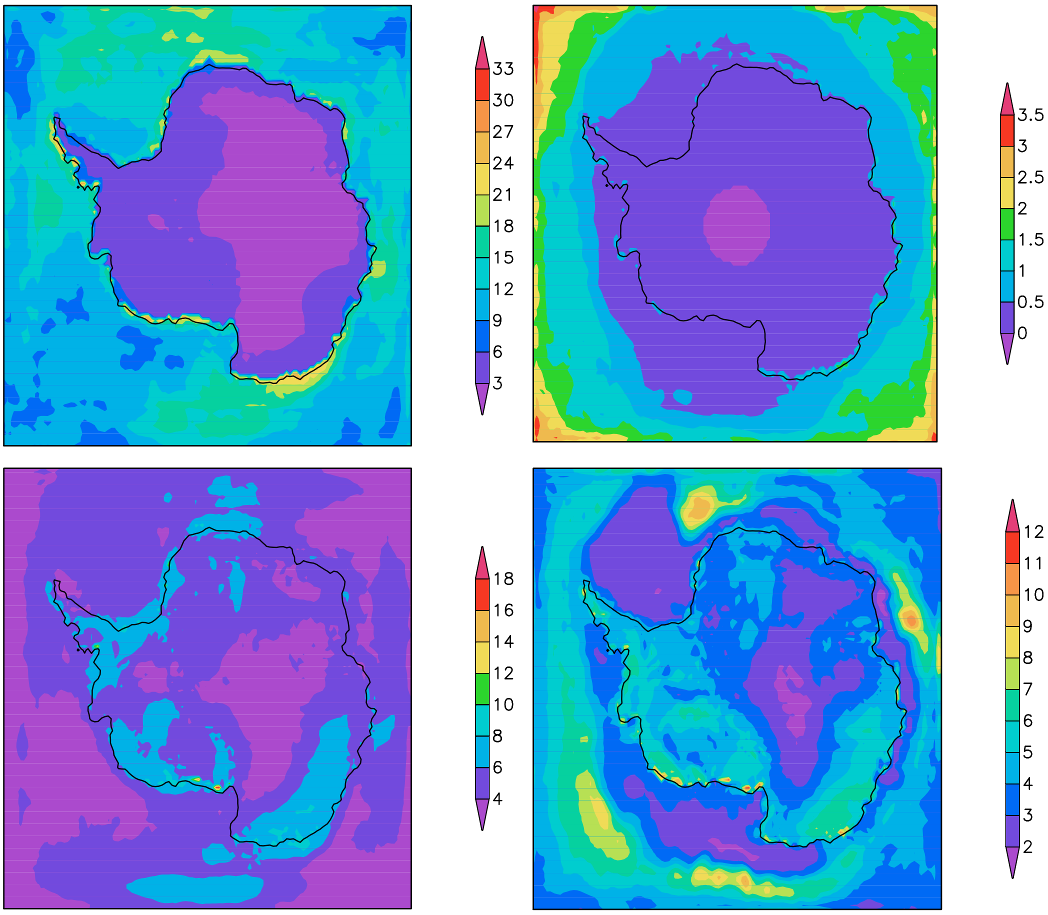

Figure A.4: *Standard deviation of the net surface shortwave radiation* (W/m^2) *(top panel) and net surface longwave radiation* (W/m^2) *(bottom panel) in austral summer (DJF) (left) and austral winter (JJA) (right) averaged over 1958 - 1998. HIRHAM simulation.*

Fig. A.5 shows the SD of the cloud cover during the austral summer (left) and winter (right) for the HIRHAM simulation. During the southern summer the maximum values are located along the coastline as far as cyclones can penetrate into the continent. During both seasons, the minimum SD is located along the steep Antarctic Plateau. During the southern winter, the positions of the maxima coincide with the edge of the sea-ice, since the relatively warm ocean surface supplies the atmosphere with warm and humid air which leads to cloud formation.

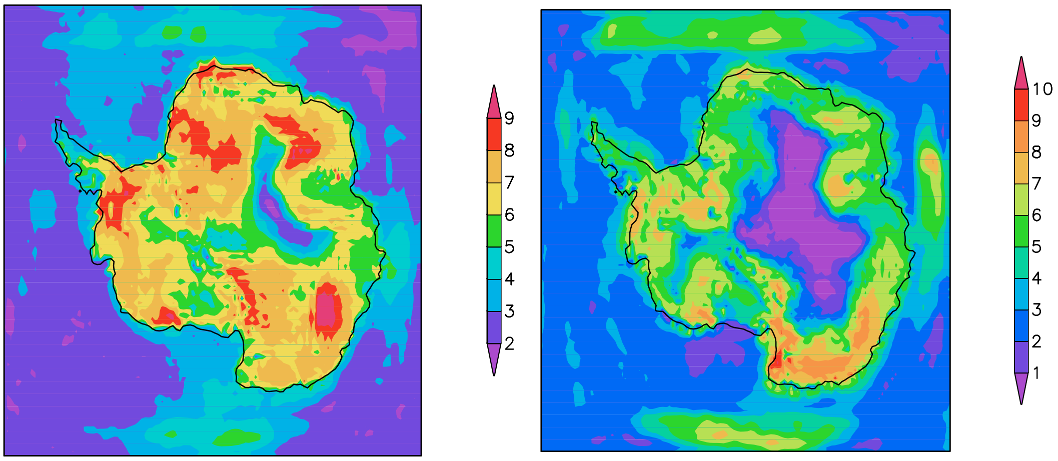

Figure A.5: *Standard deviation of cloud cover (%) in austral summer (DJF) (left) and austral winter (JJA) (right), averaged over 1958 - 1998. HIRHAM simulation.*

Fig. A.6 - Fig. A.7 show the SD of the precipitation and net mass balance over the 40 years for the HIRHAM and ERA40 simulations. One of the main components of the accumulation rate is precipitation. Precipitation in turn strongly depends on the synoptic-scale processes, storm track and intensity. That is why the highest SD can be found in the coastal area, since most of the cyclones can not penetrate deep inside the continent. There are two maxima present in model simulations and re-analysis data: one over the Western Antarctic Peninsulas and another one along Wilkes Land. The minimum value in SD can be found over the Antarctic Dome.

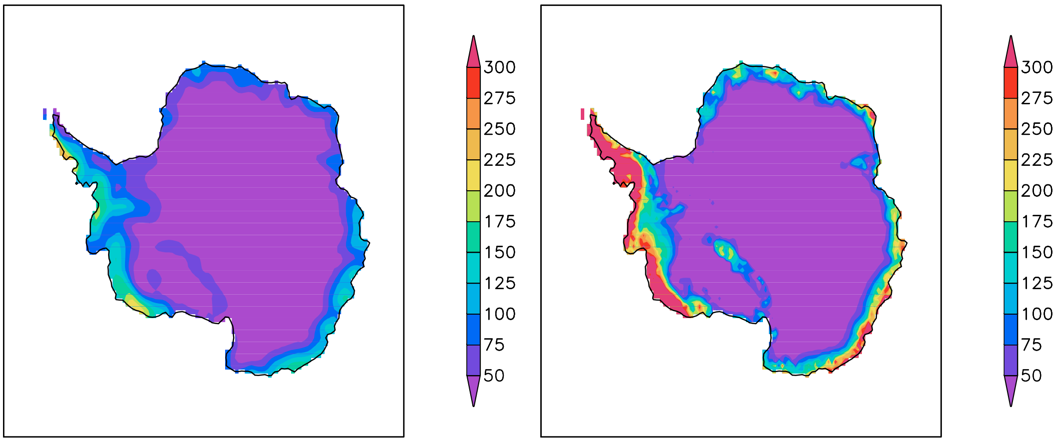

Figure A.6: *Standard deviation of precipitation (mm/year) averaged over 1958 - 1998. ERA40 (left), HIRHAM simulation (right).*

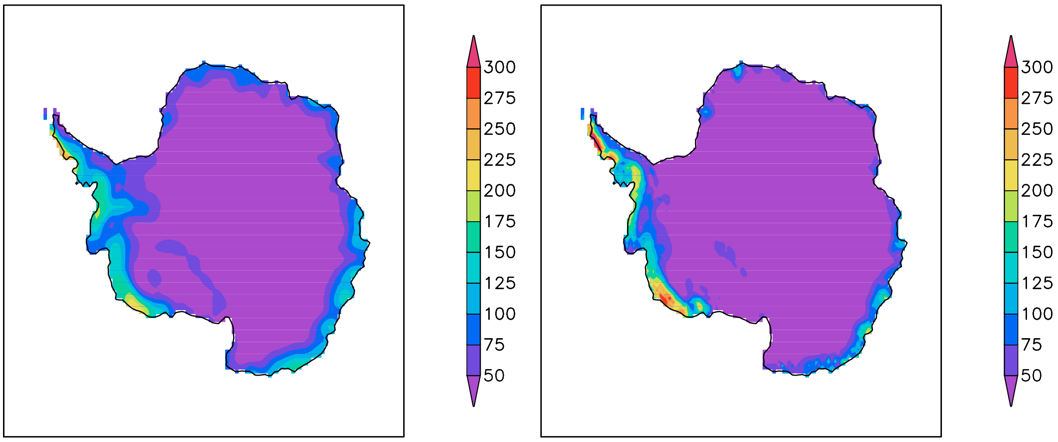

Figure A.7: *Standard deviation net mass balance (mm/year) averaged over 1958 - 1998. ERA40 (left), HIRHAM simulation (right).*

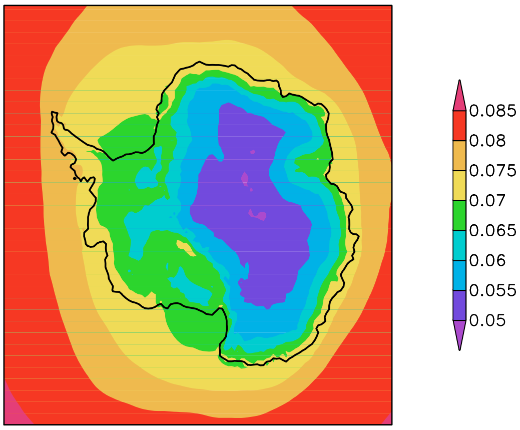

Figure A.8: *The trend uncertainty. 2 m temperature (°C/decade). 1958 - 1998. Calculation based on (Bevington, 1969).*

Appendix B

Model description

N	$A_{k+\frac{1}{2}}$	$B_{k+\frac{1}{2}}$	Lev	$Height$ (m)	$Pressure$ (hPa)	Lev	$Height$ (m)	$Pressure$ (hPa)
0	0.000	0.0000000						
1	2000.000	0.0000000	1	26195	10.0	1	26195	10.0
2	4000.000	0.0000000	2	22226	30.0	2	22226	30.0
3	6046.110	0.0003389	3	19927	50.4	3	19927	50.4
4	8267.927	0.0033571	4	18086	73.4	4	18086	73.4
5	10609.513	0.0130700	5	16306	102.7	5	16306	102.7
6	12851.100	0.0340771	6	14489	141.2	6	14489	141.2
7	14698.498	0.0706498	7	12639	190.9	7	12639	190.9
8	15861.125	0.1259166	8	10811	252.6	8	10811	252.6
9	16116.236	0.2011954	9	9048	325.9	9	9048	325.9
10	15356.924	0.2955196	10	7389	409.4	10	7389	409.4
11	13621.460	0.4054091	11	5862	500.6	11	5862	500.6
12	11101.561	0.5249322	12	4490	595.8	12	4490	595.8
13	8127.144	0.6461079	13	3289	690.4	13	3289	690.4
14	5125.141	0.7596983	14	2273	779.7	14	2273	779.7
15	2549.969	0.8564375	15	1455	858.6	15	1455	858.6
16	783.195	0.9287469	16	836	922.6	16	836	922.6
17	0.000	0.9432648	17	545	954.0	17	409	969.0
18	0.000	0.9580097	18	409	964.9	18	155	997.4
19	0.000	0.9729851	19	308	980.0	19	34	1011.1
20	0.000	0.9793752	20	212	990.8			
21	0.000	0.9858072	21	155	997.3			
22	0.000	0.9922814	22	97	1003.9			
23	0.000	0.99484476	23	56	1008.5			
24	0.000	0.9974205	24	34	1011.0			
25	0.000	1.0000000	25	12	1013.7			

Table B.1: *Height, standard pressure and the corresponding coordinate parameters of the vertical levels in HIRHAM. The 19 levels and 25 level versions of HIRHAM are shown.*

Appendix C

List of Abbreviations

AAO – Antarctic Oscillation Index
AMSU-B – Advanced Microwave Sounding Unit B
AVHRR – Advanced Very High Resolution Radiometer
AWS – Automatic Weather Station
BAS – British Antarctic Survey
ECHAM – climate model, developed from the **EC**MWF model + comprehensive parameterization package developed at **Ham**burg
ECMWF – European Center for Medium-Range Weather Forecasts
ENSO – El Niño-Southern Oscillation
EOF Empirical Ortogonal Function
GCM – Global Circulation Model
GIS Grounded Ice Surface
HIRHAM – **HIR**LAM + ECH**AM**
HIRLAM – **HI**gh **R**esolution **L**imited **A**rea **M**odel
INMI – Implicit normal mode initialization
IPCC – Intergovernmental Panel on Climate Change
NCAR – National Center for Atmospheric Research
NCEP – National Centers for Environmental Prediction
PBL – Planetary Boundary Layer
RCM – Regional Climate Model
READER – **RE**ference **A**ntarctic **D**ata for **E**nvironmental **R**esearch
SAM – Southern Annular Mode
SAO – Semi-Annual Oscillation
SD – Standard deviation
SST – Sea Surface Temperature
TWV – Total water vapour

Bibliography

Antic, S., Laprise, R., Denis, B., and de Elía, R. (2004). Testing the downscaling ability of a one-way nested regional climate model in regions of complex topography. *Clim. Dyn.*, 23:473–493.

Bevington, P. R. (1969). *Data reduction and error analysis for the physical sciences*. New York: McGraw-Hill, 1969.

Bintanja, R. (1999). On the glaciological, meteorological, and climatological significance of antarctic blue ice areas. *Rev. Geophys.*, 37:337–360.

Bintanja, R. (2001a). Characteristics of snowdrift over a bare ice surface in Antarctica. *J. Geophys. Res.*, 106:9653–9660.

Bintanja, R. (2001b). Snowdrift Sublimation in a Katabatic Wind Region of the Antarctic Ice Sheet. *J. Appl. Met.*, 40:1952–1966.

Bintanja, R. and Reijmer, C. H. (2001). Meteorological conditions over Antarctic blue-ice areas and their influence on the local surface mass balance. *J. Glaciol.*, 47:37–50.

Bintanja, R. and van den Broeke, M. R. (1996). The Influence of Clouds on the Radiation Budget of Ice and Snow Surfaces in Antarctica and Greenland in Summer. *Int. J. Climatol.*, 16:1281–1296.

Box, J. E. and Rinke, A. (2003). Evaluation of Greenland Ice Sheet Surface Climate in the HIRHAM Regional Climate Model Using Automatic Weather Station Data. *J. Clim.*, 16:1302–1319.

Brinkop, S. and Roeckner, E. (1995). Sensitivity of a general circulation model to parameterizations of cloud turbulence interactions in the atmospheric boundary layer. *Tellus Series A*, 47:197–220.

Bromwich, D. H. (1988). Snowfall in high southern latitudes. *Rev. Geophys.*, 26:149–168.

Bromwich, D. H. and Fogt, R. L. (2004). Strong Trends in the Skill of the ERA-40 and NCEP NCAR Reanalyses in the High and Midlatitudes of the Southern Hemisphere, 1958-2001. *J. Clim.*, 17:4603–4619.

Bromwich, D. H., Guo, Z., Bai, L., and Chen, Q.-S. (2004). Modeled Antarctic Precipitation. Part I: Spatial and Temporal Variability. *J. Clim.*, 17:427–447.

Cai, W., Whetton, P. H., and Karoly, D. J. (2003). The Response of the Antarctic Oscillation to Increasing and Stabilized Atmospheric CO_2. *J. Clim.*, 16:1525–1538.

Carrasco, J. F. and Bromwich, D. H. (1993). Mesoscale cyclogenesis dynamics over the southwestern Ross Sea, Antarctica. *J. Geophys. Res.*, 98:12973–12996.

Carroll, J. J. (1982). Long-term means and short-term variability of the surface energy balance components at the South Pole. *J. Geophys. Res.*, 87:4277–4286.

Chapman, W. and Walsh, J. (2005). A synthesis of Antarctic temperatures. *J. Clim.*. submitted.

Christensen, E. and van Meijgaard, E. (1992). On the construction of a regional climate model. Technical report, Dan. Meteorol. Inst., Copenhagen.

Christensen, J. H., Christensen, O. B., Deluisi, J. J.and Lopez, P. E., van Meijgaard, E., and Botzet, M. (1996). The HIRHAM4 regional atmospheric climate model. Technical report, Dan. Meteorol. Inst., Copenhagen.

Christensen, O. B., Christensen, J. H., Machenhauer, B., and Botzet, M. (1998). Very High-Resolution Regional Climate Simulations over Scandinavia–Present Climate. *J. Clim.*, 11:3204–3229.

Comiso, J. C. (2000). Variability and Trends in Antarctic Surface Temperatures from In Situ and Satellite Infrared Measurements. *J. Clim.*, 13:1674–1696.

Connolley, W. M. (1996). The Antarctic Temperature Inversion. *Int. J. Climatol.*, 16:1333–1342.

Connolley, W. M. and King, J. C. (1993). Atmospheric water-vapour transport to Antarctica inferred from radiosonde data. *Quart. J. Roy. Meteor. Soc.*, 119:325–342.

Cullather, R. I., Bromwich, D. H., and van Woert, M. L. (1998). Spatial and Temporal Variability of Antarctic Precipitation from Atmospheric Methods*. *J. Clim.*, 11:334–367.

Davies, H. C. (1976). A lateral boundary formulation for multi-level prediction models. *Quart. J. Roy. Meteor. Soc.*, 102:405–418.

Davis, C. H., Li, Y., McConnell, J. R., Frey, M. M., and Hanna, E. (2005). Snowfall-Driven Growth in East Antarctic Ice Sheet Mitigates Recent Sea-Level Rise. *Science*, 308:1898–1901.

Deardorff, J. W. (1980). Stratocumulus-capped mixed layers derived from a three-dimensional model. *Bound.-Lay. Meteorol.*, 18:495–527.

Denis, B., Laprise, R., Caya, D., and Côté, J. (2002). Downscaling ability of one-way nested regional climate models: the Big-Brother Experiment. *Clim. Dyn.*, 18:627–646.

Dethloff, K., Abegg, C., Rinke, A., Hebestadt, I., and Romanov, V. F. (2001). Sensitivity of Arctic climate simulations to different boundary layer parameterizations in a regional climate model. *Tellus Series A*, 53:1–26.

Dethloff, K., Rinke, A., Benkel, A., Køltzow, M., Sokolova, E., Kumar Saha, S., Handorf, D., Dorn, W., Rockel, B., von Storch, H., Haugen, J. E., Røed, L. P., Roeckner, E., Christensen, J. H., and Stendel, M. (2006). A dynamical link between the Arctic and the global climate system. *Geophys. Res. Let.*, 33:3703–3706.

Dethloff, K., Rinke, A., Lehmann, R., Christensen, J. H., Botzet, M., and Machenhauer, B. (1996). Regional climate model of the Arctic atmosphere. *J. Geophys. Res.*, 101:23401–23422.

Doran, P. T., Priscu, W. B., and Lyons, J. E. (2002). Antarctic climate cooling and terrestrial ecosystem response. *Nature*, 415:517–520.

Dorn, W. (2002). *Natural climate variations of the Arctic in a regional high-resolution atmosphere model.* PhD thesis, Alfred Wegener Institute for Polar and Marine Research,Potsdam.

Dutton, E. G., Stone, R. S., and Deluisi, J. J. (1989). South Pole surface radiation balance measurements, April 1986 to February 1988. Technical report.

Enomoto, H. and Ohmura, A. (1990). The influences of atmospheric half-yearly cycle on the sea ice in the Antarctic. *J. Geophys. Res.*, 95:9497–9511.

Fogt, R. and Bromwich, D. (2005). Decadal variability of the ENSO teleconnection to the high latitude South Pacific governed by coupling with the Southern Annular Mode. *J. Clim.*, 19:979–997.

Fortman, M. (2004). Influence of tropospheric aerosols on the Arctic climate (in German). Technical report, Reports on Polar and Marine Research, Alfred Wegener Institute for Polar and Marine Research, Bremerhaven, Germany.

Genthon, C., Kaspari, S., and Mayewski, P. (2005). Interannual variability of the surface mass balance of West Antarctica from ITASE cores and ERA40 reanalyses, 1958-2000. *Clim. Dyn.*, 24:759–770.

Giorgi, F. and Mearns, L. O. (1999). Introduction to special section: Regional climate modeling revisited. *J. Geophys. Res.*, 104:6335–6352.

Giovinetto, M. B., Yamazaki, K., Wendler, G., and Bromwich, D. H. (1997). Atmospheric net transport of water vapor and latent heat across 60degS. *J. Geophys. Res.*, 102:11171–11180.

Giovinetto, M. B. and Zwally, H. J. (2000). Spatial distribution of net surface accumulation on the Antarctic ice sheet. *Ann. Glaciol.*, 31:171–178.

Gong, D. and Wang, S. (1999). Definition of Antarctic oscillation index. *Geophys. Res. Let.*, 26:459–462.

Guo, Z., Bromwich, D., and Cassano, J. (2003). Evaluation of Polar MM5 Simulations of Antarctic Atmospheric Circulation. *Mon. Wea. Rev.*, 131:384–411.

Guo, Z., Bromwich, D. H., and Hines, K. M. (2004). Modeled Antarctic Precipitation. Part II: ENSO Modulation over West Antarctica(. *J. Clim.*, 17:448–465.

Hahn, C. J., Warren, S. G., and London, J. (1995). The Effect of Moonlight on Observation of Cloud Cover at Night, and Application to Cloud Climatology. *J. Clim.*, 8:1429–1446.

Harangozo, S. A. (2006). Atmospheric circulation impacts on winter maximum sea ice extent in the west Antarctic Peninsula region (1979-2001). *Geophys. Res. Let.*, 33:2502–2505.

Hines, K. M., Bromwich, D. H., and Marshall, G. J. (2000). Artificial Surface Pressure Trends in the NCEP-NCAR Reanalysis over the Southern Ocean and Antarctica. *J. Clim.*, 13:3940–3952.

Hines, K. M., Bromwich, D. H., Rasch, P. J., and Iacono, M. J. (2004). Antarctic Clouds and Radiation within the NCAR Climate Models(. *J. Clim.*, 17:1198–1212.

Hirasawa, N., Nakamura, H., and Yamanouchi, T. (2000). Abrupt changes in meteorological conditions observed at an inland Antarctic station in association with wintertime blocking. *Geophys. Res. Let.*, 27:1911–1914.

Hogan, A. (1997). A synthesis of warm air advection to the South Polar Plateau. *J. Geophys. Res.*, 102:14009–14020.

Hogan, R. J. and Illingworth, A. J. (2000). Deriving cloud overlap statistics from radar. *Quart. J. Roy. Meteor. Soc.*, 126:2903–2909.

Hudson, S. R. and Brandt, R. E. (2005). A Look at the Surface-Based Temperature Inversion on the Antarctic Plateau. *J. Clim.*, 18:1673–1696.

Karoly, D. J. (1989). Southern Hemisphere Circulation Features Associated with El Niño-Southern Oscillation Events. *J. Clim.*, 2:1239–1252.

Kerschgens, M., Pilz, U., and Raschke, E. (1978). A modified two-stream approximation for computations of the solar radiation budget in a cloudy atmosphere. *Tellus*, 30:429–435.

Key, J. R. (2002). The cloud and surface parameter retrieval (CASPR) system for polar AVHRR Users Guide. Technical report, Cooperative Institute forMeteorological Satellite Studies, University of Wisconsin-Madison.

Key, J. R. and Schweiger, A. J. (1998). Tools for atmospheric radiative transfer: Streamer and FluxNet. *Computers and Geosci.,*, 24:443–451.

King, J. C., Anderson, P. S., Smith, M. C., and Mobbs, S. D. (1996). The surface energy and mass balance at Halley, Antarctica during winter. *J. Geophys. Res.*, 101:19119–19128.

King, J. C. and Harangozo, S. A. (1998). Climate change in the western Antarctic Peninsula since 1945: observations and possible causes. *Ann. Glaciol.*, 27:571–575.

King, J. C. and Turner, J. (1997). *Antarctic meteorology and climatology*. Cambridge atmospheric and space science series, Cambridge, UK: Cambridge University Press, —c1997.

Kistler, R., Kalnay, E., Collins, W., Saha, S., White, G., Woollen, J., Chelliah, M., Ebisuzaki, W., Kanamitsu, M., Kousky, V., van den Dool, H., Jenne, R., and Fiorino, M. (2001). The NCEP-NCAR 50-Year Reanalysis: Monthly Means CD-ROM and Documentation. *Bull. Amer. Meteor. Soc.*, 82:247–268.

Kwok, R. and Comiso, J. C. (2002). Spatial patterns of variability in Antarctic surface temperature: Connections to the Southern Hemisphere Annular Mode and the Southern Oscillation. *Geophys. Res. Let.*, 29:50–1.

Liu, J., Yuan, X., Rind, D., and Martinson, D. G. (2002). Mechanism study of the ENSO and southern high latitude climate teleconnections. *Geophys. Res. Let.*, 29:24–1–24–4.

Louis, J.-F. (1979). A parametric model of vertical eddy fluxes in the atmosphere. *Bound.-Lay. Meteorol.*, 17:187–202.

Louis, J. F., Tiedtke, M., and Geleyn, J. F. (1982). A short history of the operational PBL parameterization at ECMWF . Technical report, ECMWF, Reading, UK.

Machenhauer, B., Windelband, M., Botzet, M., Christensen, J. H., Déqué, M., Jones, R., Ruti, P. M., and Visconti, G. (1998). Validation and analysis of regional present-day climate and climate change simulations over Europe. Technical report, Max Planck Inst. for Meteorol. Hamburg, Germany.

Mahesh, A., Walden, V. P., and Warren, S. G. (2001). Ground-Based Infrared Remote Sensing of Cloud Properties over the Antarctic Plateau. Part I: Cloud-Base Heights. *J. Appl. Met.*, 40:1265–1278.

Marbaix, P., Gallee.H., Brasseur.O., and Ypersele.J-P. (2003). Lateral Boundary Conditions in Regional Climate Models: A Detailed Study of the Relaxation Procedure. *Mon. Wea. Rev.*, 131:461–479.

Marshall, G. J. (2003). Trends in the Southern Annular Mode from Observations and Reanalyses. *J. Clim.*, 16:4134–4143.

Marshall, G. J. and Harangozo, S. A. (2000). An appraisal of NCEP/NCAR reanalysis MSLP data viability for climate studies in the South Pacific. *Geophys. Res. Let.*, 27:3057–3060.

Marshall, G. J., Lagun, V., and Lachlan-Cope, T. A. (2002). Changes in Antarctic Peninsula tropospheric temperatures from 1956 to 1999: a synthesis of observations and reanalysis data. *Int. J. Climatol.*, 22:291–310.

Maslanik, J., Fowler, C., Key, J., Scambos, T., Hutchinson, T., and Emery, W. (1997). AVHRR-based Polar Pathfinder products for modeling applications. *Ann. Glaciol.*, 25:388–392.

Meehl, G. A. (1991). A Reexamination of the Mechanism of the Semiannual Oscillation in the Southern Hemisphere. *J. Clim.*, 4:911–926.

Meinke, I., Geyer, B., Feser, F., and von Storch, H. (2006). The impact of spectral nudging on cloud simulation with a regional atmospheric model. *J. Atmos. Ocean Techn.*, 23:815–824.

Melsheimer, C. and Heygster, G. (2005). Retrieval of total water vapour over the arctic from space-borne microwave radiometer data. Technical report, Reports on Polar and Marine Research 520/2006: Proceedings of Arctic Climate Workshop, AWI British Antarctic Survey.

Miao, J., Kunzi, K., Heygster, G., Lachlan-Cope, T. A., and Turner, J. (2001). Atmospheric water vapor over Antarctica derived from Special Sensor Microwave/Temperature 2 data. *J. Geophys. Res.*, 106:10187–10204.

Misra, V., Dirmeyer, P. A., and Kirtman, B. P. (2003). Dynamic Downscaling of Seasonal Simulations over South America. *J. Clim.*, 16:103–117.

Monaghan, A., Bromwich, D., and Sheng-Hung, W. (2006). Recent trends in Antarctic snow accumulation from Polar MM5 simulations. *Phil. Trans. R. Soc.*, 364:1683–1708.

Morcrette , J. (1990). Impact of changes to the radiation transfer parameterizations plus cloud optical properties in the ECMWF model. *Mon. Wea. Rev.*, 118:847–873.

Morley, B. M., Uthe, E. E., and Viezee, W. (1989). Airborne lidar observations of clouds in the Antarctic troposphere. *Geophys. Res. Let.*, 16:491–494.

Noguer, M., Jones, R., and Murphy, J. (1998). Sources of systematic errors in the climatology of a regional climate model over Europe. *Clim. Dyn.*, 14:691–712.

Nylen, T. H., Fountain, A. G., and Doran, P. T. (2004). Climatology of katabatic winds in the McMurdo dry valleys, southern Victoria Land, Antarctica. *J. Geophys. Res.*, 109:D03114.

Ohmura, A., Wild, M., and Bengtsson, L. (1996). A Possible Change in Mass Balance of Greenland and Antarctic Ice Sheets in the Coming Century. *J. Clim.*, 9:2124–2136.

Parish, T. R. (1988). Surface winds over the Antarctic continent: A review. *Rev. Geophys.*, 26:169–180.

Parish, T. R. and Bromwich, D. H. (1991). Continental-Scale Simulation of the Antarctic Katabatic Wind Regime. *J. Clim.*, 4:135–146.

Pavolonis, M. J. and Key, J. R. (2003). Antarctic Cloud Radiative Forcing at the Surface Estimated from the AVHRR Polar Pathfinder and ISCCP D1 Datasets, 1985-93. *J. Appl. Met.*, 42:827–840.

Phillpot, H. and Zillman, J. (1970). The surface temperature inversion over the Antarctic continent. *J. Geophys. Res.*, 75:4161–4169.

Pohlmann, H. and Greatbatch, R. J. (2006). Discontinuities in the late 1960's in different atmospheric data products. *Geophys. Res. Let.*, 33:L22803.

Räisänen, P. (1999). Effect of vertical resolution on cloudy-sky radiation calculations: Tests with two schemes. *J. Geophys. Res.*, 104:27407–27420.

Renfrew, I. A. and Anderson, P. S. (2002). The surface climatology of an ordinary katabatic wind regime in Coats Land, Antarctica. *Tellus Series A*, 54:463–484.

Rinke, A. and Dethloff, K. (2000). On the sensitivity of a regional Arctic climate model to initial and boundary conditions. *Clim.Res.*, 14:101–113.

Rinke, A., Dethloff, K., and Christensen, J. H. (1999). Arctic winter climate and its interannual variations simulated by a regional climate model. *J. Geophys. Res.*, 104:19027–19038.

Rinke, A., Dethloff, K., Christensen, J. H., Botzet, M., and Machenhauer, B. (1997). Simulation and validation of Arctic radiation and clouds in a regional climate model. *J. Geophys. Res.*, 102:29833–29848.

Rinke, A., Maslowski, W., Dethloff, K., and Clement, J. (2006). Influence of sea ice on the atmosphere: A study with an Arctic atmospheric regional climate model. *J. Geophys. Res.*, 111:L16103.

Robock, A. (1980). The seasonal cycle of snow cover, sea ice and surface albedo. *Mon. Wea. Rev.*, 108:267–285.

Roeckner, E., Arpe, K., Bengtsson, L., Brinkop, S., Dumenil, L., Esch, M., Kirk, E., Lunkeit, F., Ponater, M., Rockel, B., Sausen, R., Schlese, U., Schubert, S., and Windelband, M. (1992). Simulation of the present-day climate with the echam model: impact of model physics and resolution. Technical report, MPI 93, Max Planck Inst. for Meteorol., Hamburg, Germany.

Roeckner, E., Arpe, K., Bengtsson, L., Christoph, M., Claussen, M., Dümenil, L., Esch, M., Giorgetta, M., Schlese, U., and Schulzweida, U. (1996). The atmospheric general circulation model echam-4: Model description and simulation of present-day climate. Technical report, MPI 218, Max Planck Inst. for Meteorol., Hamburg, Germany.

Rossow, W. B. and Schiffer, R. A. (1999). Advances in Understanding Clouds from ISCCP. *Bull. Amer. Meteor. Soc.*, 80:2261–2288.

Rossow, W. B., Walker, A. W., Beuschel, D. E., and Roiter, M. D. (1996). International Satellite Cloud Climatology Project (ISCCP) documentation of cloud data. Technical report, World Climate Research Programme, WMO.

Saha, S. K. (2006). *The influence of an improved soil scheme on the Arctic climate in a regional climate model.* PhD thesis, Alfred Wegener Institute for Polar and Marine Research,Potsdam.

Shapiro, R. (1970). Smoothing, Filtering, and Boundary Effects. *Rev. Geophys. Space Phys.*, 8:359–387.

Simmonds, I. and Keay, K. (2000). Mean Southern Hemisphere Extratropical Cyclone Behavior in the 40-Year NCEP-NCAR Reanalysis. *J. Clim.*, 13:873–885.

Simmonds, I. and Law, R. (1995). Associations between Antarctic katabatic flow and the upper level winter vortex. *Int. J. Climatol.*, 15:403–421.

Sinisalo, A., Moore, J. C., van de Wal, R. S. W., Bintanja, R., and Jonsson, S. (2003). A 14 year mass-balance record of a blue-ice area in Antarctica. *Ann. Glaciol.*, 37:213–218.

Stearns, C. R. and Wendler, G. (1988). Research results from Antarctic automatic weather stations. *Rev. Geophys.*, 26:45–61.

Stephens, G. L. (1978). Radiation Profiles in Extended Water Clouds. II: Parameterization Schemes. *J. Atmos. Sci.*, 35:2123–2132.

Sundqvist, H. (1978). A parameterization scheme for non-convective condensation including prediction of cloud water content. *Quart. J. Roy. Meteor. Soc.*, 104:677–690.

Temperton, C. (1988). Implicit normal mode initialization. *Mon. Wea. Rev.*, 116:1013.

Thompson, D. W. and Solomon, S. (2002). Interpretation of recent Southern Hemisphere climate change. *Science*, 296:895–899.

Thompson, D. W. J. and Wallace, J. M. (2000). Annular Modes in the Extratropical Circulation. Part I: Month-to-Month Variability*. *J. Clim.*, 13:1000–1016.

Tiedtke, M. (1989). A comprehensive mass flux scheme for cumulus parameterization in large-scale models. *Mon. Wea. Rev.*, 117:1779–1800.

Turner, J., Colwell, S. R., Marshall, G. J., Lachlan-Cope, T. A., Carleton, A. M., Jones, P. D., Lagun, V., Reid, P. A., and Iagovkina, S. (2004). The SCAR READER Project: Toward a High-Quality Database of Mean Antarctic Meteorological Observations. *J. Clim.*, 17:2890–2898.

Turner, J., Colwell, S. R., Marshall, G. J., Lachlan-Cope, T. A., Carleton, A. M., Jones, P. D., Lagun, V., Reid, P. A., and Iagovkina, S. (2005). Antarctic climate change during the last 50 years. *Int. J. Climatol.*, 25:279–294.

Turner, J., Connolley, W. M., Lachlan-Cope, T. A., and Marshall, G. J. (2006). The performance of the Hadley Centre Climate Model (HadCM3) in high southern latitudes. *Int. J. Climatol.*, 26:91–112.

Turner, J., Connolley, W. M., Leonard, S., Marshall, G. J., and Vaughan, D. G. (1999). Spatial and temporal variability of net snow accumulation over the Antarctic from ECMWF re-analysis project data. *Int. J. Climatol.*, 19:697–724.

Turner, J., Marshall, G. J., and Lachlan-Cope, T. A. (1998). Analysis of synoptic-scale low pressure systems within the Antarctic Peninsula sector of the circumpolar trough. *Int. J. Climatol.*, 18:253–280.

Turner, J. C. and Pendlebury, S. (2004). *The International Antarctic Weather Forecasting Handbook*. British Antarctic Survey.

Uppala, S. M., Kållberg, P. W., Simmons, A. J., Andrae, U., da Costa Bechtold, V., Fiorino, M., Gibson, J. K., Haseler, J., Hernandez, A., Kelly, G. A., Li, X., Onogi, K., Saarinen, S., Sokka, N., Allan, R. P., Andersson, E., Arpe, K., Balmaseda, M. A., Beljaars, A. C. M., van de Berg, L., Bidlot, J., Bormann, N., Caires, S., Chevallier, F., Dethof, A., Dragosavac, M., Fisher, M., Fuentes, M., Hagemann, S., Hólm, E., Hoskins, B. J., Isaksen, L., Janssen, P. A. E. M., Jenne, R., McNally, A. P., Mahfouf, J. F., Morcrette, J. J., Rayner, N. A., Saunders, R. W., Simon, P., Sterl, A., Trenberth, K. E., Untch, A., Vasiljevic, D., Viterbo, P., and Woollen, J. (2005). The ERA-40 re-analysis. *Quart. J. Roy. Meteor. Soc.*, 131:2961–3012.

Van de Berg, W., Van den Broeke, M., Reijmer, C., and Van Meijgaard, E. (2005). Characteristics of the Antarctic surface mass balance (1958-2002) using a Regional Atmospheric Climate Model. *Ann. Glaciol.*, 41:97–104.

van de Berg, W. J., van den Broeke, M. R., Reijmer, C. H., and van Meijgaard, E. (2006). Reassessment of the Antarctic surface mass balance using calibrated output of a regional atmospheric climate model. *J. Geophys. Res.*, 111:L11104.

van den Broeke, M., van de Berg, W. J., van Meijgaard, E., and Reijmer, C. (2006). Identification of Antarctic ablation areas using a regional atmospheric climate model. *Journal of Geophysical Research (Atmospheres)*, 111:18110–18124.

van den Broeke, M. R. (2000). On the Interpretation of Antarctic Temperature Trends. *J. Clim.*, 13:3885–3889.

van den Broeke, M. R., van de Wal, R. S. W., and Wild, M. (1997). Representation of Antarctic Katabatic Winds in a High-Resolution GCM and a Note on Their Climate Sensitivity. *J. Clim.*, 10:3111–3130.

van Lipzig, N. (1999). *The surface mass balance of the Antarctic ice sheet: a study with a regional atmospheric model*. PhD thesis, Utrecht University.

van Lipzig, N. P. M., van Meijgaard, E., and Oerlemans, J. (2002). The spatial and temporal variability of the surface mass balance in Antarctica: results from a regional atmospheric climate model. *Int. J. Climatol.*, 22:1197–1217.

van Loon, H. (1967). The Half-Yearly Oscillations in Middle and High Southern Latitudes and the Coreless Winter. *J. Atmos. Sci.*, 24:472–486.

Vaughan, D. G., Bamber, J. L., Giovinetto, M., Russell, J., and Cooper, A. P. R. (1999). Reassessment of Net Surface Mass Balance in Antarctica. *J. Clim.*, 12:933–946.

Viterbo, P., Beljaars, A., Mahfouf, J.-F., and Teixeira, J. (1999). The representation of soil moisture freezing and its impact on the stable boundary layer. *Quart. J. Roy. Meteor. Soc.*, 125:2401–2426.

von Storch, H., Langenberg, H., and Feser, F. (2000). A spectral nudging technique for dynamical downscaling purposes. *Mon. Wea. Rev.*, 128:3664–3673.

Weatherly, J. W., Walsh, J. E., and Zwally, H. J. (1991). Antarctic Sea ice variations and seasonal air temperature relationships. *J. Geophys. Res.*, 96:15119–15130.

Wendler, G., André, J. C., Pettré, P., Gosink, J., and Parish, T. (1993). Katabatic Winds in Adélie Coast. In Bromwich, D. H. and Stearns, C. R., editors, *Antarctic Meteorology and Climatology: Studies Based on Automatic Weather Stations*, page 23.

Wendler, G., Stearns, C., Weidner, G., Dargaud, G., and Parish, T. (1997). On the extraordinary katabatic winds of Adélie Land. *J. Geophys. Res.*, 102:4463–4474.

Yamanouchi, T. and Charlock, T. P. (1995). Comparison of Radiation Budget at the TOA and Surface in the Antarctic from ERBE and Ground Surface Measurements. *J. Clim.*, 8:3109–3109.

List of Figures

List of Tables

Acknowledgements

This work was completed at the Alfred Wegener Institute for Polar and Marine Research at the Potsdam Research Unit under the supervision of Prof. Klaus Dethloff. I am indebted to Prof. Klaus Dethloff for his encouragement and continuous support. His expertise in physics and his world view inspired and motivated me in an invaluable way.

I would like to thank my co-supervisor Dr. Annette Rinke for the collaboration we have established. I am grateful to I. Hebestadt and S. Erxleben for technical support.

Much gratitude to S. Debatin, C. Melsheimer and J. Comiso for providing me necessary data.

Along my graduate life I have had the chance of meeting an incredible number of people who have supported me in one way or another.

I would like to thank my first teacher Слуцкер Татьяну Моисеевну. Танечка в моём сердце ты навсегда останешся моей первой учительницей.

Prof. Tarakanov, thank you very much for being supportive during my university study. Спасибо Вам и Олегу Георгиевичу Богаткину, за безумно интересные лекции и за ещё более интересные встречи после них.

Many thanks to my best friend and my first supervisor Анискиной Ольге Георгиевне. Оля, спасибо от всего сердца за твоё безграничное терпение и поддержку. Очень трудно подобрать слова чтобы передать всю мою благодарность тебе, но я постараюсь и сделаю это при следуюшей личной встречи в ”Сладкоежке”.

Jürgen, sorry ... dear Юрий, many thanks to you. I wish you all the best and thanks a lot for being such a nice guy. Looking forward to our Russian conversation.

Many thanks to my friends and colleagues E.Sokolova, S. Brandt, C. Ritter and F. Otto for helping me in various aspects of this work. Your help was very valuable to me.

Special thanks to Robert Walker. Dear Robert, your corrections and support did helped me to finish this work. See you one day in Australia.

I thank all my friends, who have been supporting me during last 3 years.

Carsten, my dear friend, thanks a lot for everything. Thanks for bringing fun and happiness to my life. With you, I understoond what does ”the best friend” mean, and I will miss our ”info-point-strawberry-smoothie” meetings. Dont forget in 10 years, at 18 oclock

Dear Marcel, this work would not be completed without your unlimited support. Thanks for understanding, love and patience. Thank you very much for the ”officially” best time in Potsdam-Drewitz.

I am very sorry that I am not able to mention all people who have given a contribution to this thesis. I am sure that some people will be missing to be mentioned. I would like to thank all of You.

Erklärung

Hiermit bestätige ich, dass ich diese Doktorarbeit selbstsändig verfasst und keine anderen als die angegebenen Quellen und Hilfsmittel verwendet habe.
Ich versichere, dass diese Arbeit noch nicht an anderer Stelle zur Erlangung eines Doktorgrades eingereicht worden ist.

Potsdam, December 2007 (Ksenia N Glushak)